

A 3-D Magnetotelluric Study of the Slave Craton Lithosphere, NW Canada

by

Sean Bettac

A thesis submitted in partial fulfillment of the requirements for the degree of

Master of Science

in

Geophysics

Department of Physics

University of Alberta

© Sean Bettac, 2019

Abstract

Archean cratons are comprised of thick, stable continental lithosphere that has persisted for billions of years owing to their isopycnicity (i.e. near neutral buoyancy) and higher viscosity than the surrounding mantle. These regions host diamonds at depths greater than 150 km due to the relatively cold temperatures found in the depth range where pressure is high enough for diamonds to be stable. Because of this, understanding the deep structure of cratonic lithosphere is important for regional diamond exploration. In this thesis previously collected magnetotelluric (MT) data were used to produce a 3-D resistivity model of the Slave craton's lithosphere. The resolution of this resistivity model was rigorously tested. Important features of the model and their implications include:

(1) A region of low resistivity ($< 10 \Omega\text{m}$) at a depth of 100 km beneath the Lac de Gras kimberlite field in the central Slave craton, which was interpreted as a layer of high density saline fluids that were emplaced from a Mesozoic subduction event. Phlogopite and grain boundary sulphides also remain as possible interpretations for the cause of the low resistivity ($< 10 \Omega\text{m}$). However, none of these proposed interpretations are without their flaws. Fluids in the mantle would be positively buoyant and reactive suggesting that it would be difficult to retain fluids from the Mesozoic over long time periods. Large quantities of phlogopite would be required ($> 20\%$ volume fraction) to produce the low resistivity observed ($< 10 \Omega\text{m}$), which is not strongly supported by observations in xenoliths and there is little experimental work on grain boundary sulphides in the mantle. This region of low resistivity was previously observed at depths of 80 - 120 km by Jones et al. (2003). Previous interpretations of this conductor invoked graphite films as an explanation, but it is unlikely that graphite films are stable at these depths. The spatial correlation between the low resistivity layer and the Lac de Gras kimberlite field

could be the result of kimberlite magmas following zones of weakness in the lithosphere as a result of the metasomatism caused by the slab-derived fluids.

(2) The resistivity model also showed that beneath the entire Slave craton the lithosphere-asthenosphere boundary (LAB) is at a depth of at least 200 km. Determining the depth to the LAB is important as this can determine the size of the diamond stability field within the lithosphere, which is used in regional diamond targeting.

(3) The upper mantle resistivity can be interpreted as requiring a low water content on the order of 10 - 150 ppm by weight in the depth range 100 -170 km. Below these depths the lithosphere appears to be dry (< 5 ppm). The dry base of the lithosphere may act as a resistant boundary preventing the cratonic root from being eroded by the underlying asthenosphere.

Acknowledgements

I would like to thank my supervisor, Martyn Unsworth. He provided feedback on my work continuously throughout my degree and was always helpful in advising me in regards to the modelling and interpretations presented in this thesis. Without his guidance, this project would not have been possible. I would also like to thank Graham Pearson for providing helpful advice regarding my interpretation of lithospheric structures. His expertise in petrology and fluid interactions in the mantle was greatly appreciated. Bruce Kjaarsgaard also provided helpful comments throughout this project.

I would also like to thank my the other members in my research group including Benjamin Lee, Darcy Cordell, Enci Wang, Theron Finley and Cedar Hanneson for their continuous support. I would like to particularly thank Benjamin Lee and Darcy Cordell for always listening to my newest ideas on our daily coffee runs and providing advice in many aspects of my daily work. Completing my Master's degree would have been much more difficult without their support. Lastly, I am grateful to Jim Craven for providing the magnetotelluric data in the Slave craton and being helpful resource whenever needed.

I would also like to acknowledge the St. Joes Rangers for their support through this project. Specifically, Connor MacDonald, Tyler Henry and Peter Steer were supportive throughout this project.

I would also like to acknowledge my family for their support through this project as it would have not been possible without them.

Lastly, I would like to acknowledge that this research was supported by the Diamond Exploration and Research Training School (DERTS). The DERTS program provided funding throughout this project, which allowed me to focus on research rather spending time as a TA or working part time to support myself.

Table of Contents

List of Tables	xi
List of Figures.....	xii
Chapter 1 : Introduction.....	1
Chapter 2 : Slave Craton Geology	6
2.1 Introduction.....	6
2.2 Crustal Geology	8
2.3 Lithospheric Composition from Xenoliths.....	8
2.4 Lithospheric Thickness from Xenoliths.....	8
2.5 Igneous Intrusions in the Slave Craton: Kimberlite Magmatism and the Mackenzie Dyke Swarm.	9
Chapter 3 : Previous Non-MT Studies	11
3.1 Introduction.....	11
3.2 Seismic Tomography Studies.....	11
3.2.1 Early P-wave Seismic Tomography Studies	11
3.2.2 Recent Seismic Tomography Studies.....	12
3.3 Receiver Functions.....	12
3.3.1 Shear Receiver Functions.....	12
3.4 Rayleigh Wave Analysis.....	13
3.5 Gravity Studies.....	14
3.6 Aeromagnetic Studies	15
3.7 Geophysical Methods for Diamond Exploration	16
Chapter 4 : The Theory of Magnetotellurics	19
4.1 Introduction to Magnetotellurics.....	19
4.2 Maxwell's Equations	19
4.2.1 Theory of Magnetotellurics of a 1-D Earth.....	20
4.2.2 Magnetotelluric Impedance of a 1-D Earth.....	21
4.2.3 Impedance Phase.....	22
4.3 Magnetotelluric Impedance of a 2-D Earth.....	22
4.3.1 The Transverse Electric and Transverse Magnetic modes.....	23
4.4 Dimensionality Analysis.....	24
4.4.1 Rotation of the Impedance Tensor	24
4.4.2 The Phase Tensor	25

4.5	Vertical Magnetic Field (Tipper)	26
4.6	Static Shifts	26
4.7	Magnetotelluric Impedance of a 3-D Earth.....	27
4.8	Mantle Conduction Mechanisms	27
4.8.1	Ionic Conduction.....	28
4.8.2	Small Polaron Hopping.....	29
4.8.3	Proton Conduction	29
4.8.4	Sources of Enhanced Mantle Conductivity.....	30
4.9	Mixing Laws	30
4.9.1	Archie's Law	30
4.9.2	The Multiphase Archie's Law	31
4.10	Summary	32
Chapter 5 : Magnetotelluric Data and Previous Studies in the Slave Craton.....		33
5.1	Introduction.....	33
5.2	Magnetotelluric Data.....	33
5.3	LITHOPROBE Studies and SNORCLE Data	34
5.3.1	The Electric Lithosphere Asthenosphere Boundary.....	35
5.3.2	The Electric Moho	36
5.4	The Central Slave Mantle Conductor.....	37
5.4.1	2-D Resistivity Models	37
5.4.2	A 3-D Resistivity Model of the Slave Craton	39
5.4.3	Central Slave Mantle Conductor Interpretation	40
5.5	The Slave to Bear Province (S2B) Profile	41
5.5.1	S2B: Slave Crustal Structure.....	41
5.5.2	S2B: Slave Mantle Structure.....	42
5.6	3-D Inversion of the Slave Craton Magnetotelluric Data	44
5.7	A Case Study of the CSMC in the Slave Craton.....	44
5.8	Future Work.....	45
Chapter 6 :2-D Inversion of Magnetotelluric Data from the Central Slave Craton Revisited.....		47
6.1	Introduction.....	47
6.2	Dimensionality Analysis	48
6.3	Classification of Apparent Resistivity and Phase Sounding Curves.....	50
6.3.1	Spatial Distribution of the Groups of MT Curves.....	54

6.4	2-D Inversion	55
6.5	Model Fit.....	58
6.5.1	R.M.S. Misfit and Static Coefficients	58
6.5.2	MT Data Pseudosections:.....	59
6.6	Parameter Optimization	60
6.6.1	Effect of Varying the Regularization Parameter (τ).....	60
6.6.2	Effect of Varying Static Shift Parameters	61
6.6.3	Effect of Varying Error Floors.....	62
6.6.4	Effect of Varying Starting Model	64
6.7	Comparison with the Previous 2-D Resistivity Model in the Slave Craton.....	65
6.8	Can a 3-D Analysis of the Slave Craton Data Improve on Previous 2-D Results?.....	66
6.9	Conclusions:.....	67
Chapter 7 :3-D Inversion of MT Data from the Slave Craton		68
7.1	Introduction.....	68
7.2	Magnetotelluric Data for the Slave Craton	68
7.3	Preferred 3-D Resistivity Model (s92p21r8) of the Slave Craton.....	71
7.3.1	Preferred Inversion Parameters	71
7.3.2	Preferred Resistivity Model Data Fit	73
7.4	The 3-D Resistivity Model (s92p21r8)	77
7.5	Investigating the Inversion Parameters for the Preferred Resistivity Model (s92p21r8).....	82
7.5.1	Effect of Varying the Error Floors	82
7.5.2	Effect of Varying the Resistivity of the Starting Model	83
7.5.2.1	Investigating the 100 Ω m and 1000 Ω m Starting Models with a Simple Three-Layer Synthetic	86
7.5.3	Effect of Varying the Covariance Parameter	89
7.6	Investigating the Preferred Resistivity Model (S92p21r8) Using Sensitivity Tests	91
7.6.1	Forward Modelling	91
7.6.1.1	Resolution Test of the C1 Conduit Structures.....	92
7.6.1.2	Resolution Test of C2	96
7.6.1.3	Resolution Test of C3	99
7.6.1.4	Resolution Test of C4	103
7.6.2	Synthetic Inversion tests	105
7.6.2.1	Resolution Test of the Geometry of C1	105

7.6.2.2	Investigation of the Depth to C3	108
7.7	Other Inversions	109
7.7.1	Initial Inversions	109
7.7.2	Focussed Inversions	110
7.7.3	Comparing the ModEM and WSINV3DMT Inversion Algorithms for a Data Subset.....	110
7.7.4	Comparison of the ModEM and WSINV3DMT Inversion Algorithm	111
7.8	Model Discussion.....	115
7.8.1	Crustal Structure (Depth of 0 - 40 km)	115
7.8.2	Upper Mantle Structure (Depth of 40 - 200 km).....	118
7.8.3	Deep Mantle Structure (Depths greater than 200 km, Figure 7.5).....	120
7.9	Conclusions.....	121
	Chapter 8 : Interpretation	122
8.1	Introduction.....	122
8.2	Lithospheric Thickness	122
8.3	Conduction Mechanisms for the Central Slave Mantle Conductor.....	125
8.3.1	Option 1: Graphite	126
8.3.1.1	Evidence in Favour of Graphite	126
8.3.1.2	Evidence Against Graphite	127
8.3.1.3	Summary of Graphite as a Conduction Mechanism.....	127
8.3.2	Option 2: Sulphide Minerals	128
8.3.2.1	Evidence in Favour of Sulphide Minerals.....	128
8.3.2.2	Evidence Against Sulphides.....	128
8.3.2.3	Summary of Sulphide Minerals as a Conduction Mechanism	129
8.3.3	Option 3: Hydrogen Diffusion in Nominally Anhydrous Minerals	129
8.3.3.1	Evidence Against Hydrogen Diffusion in Nominally Anhydrous Minerals	130
8.3.3.2	Evidence in Favour of Hydrogen Diffusion in Nominally Anhydrous Minerals.....	130
8.3.3.3	Summary of Hydrogen Diffusion in NAMs.....	132
8.3.4	Option 4: Hydrous Minerals (Amphibole and Phlogopite).....	132
8.3.4.1	Evidence Against Phlogopite	133
8.3.4.2	Evidence in Favour of Phlogopite.....	134
8.3.4.3	Modelling the Conductivity of Phlogopite Bearing Peridotite.....	135
8.3.4.4	Summary of Hydrous Minerals as a Conduction Mechanism.....	137
8.3.5	Option 5: High-Density Fluids.....	138

8.3.5.1	Carbonate-Rich Melts	138
8.3.5.1.1	Evidence in Favour of Hydrous Carbonate-Rich Melts	139
8.3.5.1.2	Evidence Against Hydrous Carbonate-Rich Melts	140
8.3.5.1.3	Summary of Hydrous Carbonate-Rich Melts as a Conduction Mechanism	140
8.3.5.2	Brines	141
8.3.5.2.1	Evidence in Favour of Brines.....	141
8.3.5.2.2	Evidence Against Brines.....	144
8.3.5.2.3	Summary of Brines as a Conduction Mechanism	144
8.4	Cause of the CSMC	144
8.5	Upper Mantle Conductors and Diamondiferous Kimberlites	147
8.6	Comparison to Previous Teleseismic Studies	148
8.7	Comparison to Body Wave Tomography Studies.....	149
8.8	Estimating Mantle Water Content in the Slave Craton.....	153
8.9	Water-Content Estimations for Representative Sites	153
8.9.1	Station S99-018a (Figure 8.9a).....	155
8.9.2	Station Sno-108 (Figure 8.9b).....	155
8.9.3	Station S99-022a (Figure 8.9c).....	155
8.9.4	Water Concentration Estimates at 100 and 150 km Depth	156
8.9.5	Discussion of Water Estimates	158
8.10	Conclusions.....	160
Chapter 9 : Conclusions.....		162
9.1	Introduction.....	162
9.2	Water Content in the Upper Mantle.....	162
9.3	Cause of the Central Slave Mantle Conductor (CSMC)	162
9.4	Relationship Between Upper Mantle Conductors and Diamondiferous Kimberlites	163
9.5	The Lithosphere-Asthenosphere Boundary.....	163
9.6	Future Work.....	164
References.....		166
Appendix.....		184
A.1	Initial 3-D Resistivity Models of the Slave Craton.....	184
A.2	Varying Parameters in the initial 3-D inversions.....	184
A.2.1	Effect of Varying Covariance	184
A.3	Focussed Resistivity Models of the Slave Craton.....	186

A.4	Varying Parameters.....	187
	A.4.1 Effect of Varying Starting Models.....	187
	A.4.2 Effect of Varying Covariance	188
A.5	Investigating the Resolution of Upper Mantle Conductors.....	190

List of Tables

Table 7.1: Mesh parameters for the preferred resistivity model (s92p21r8) and other inversions investigated. N = cell number where $N = 1$ corresponds to the surface layer and increases with increasing depth. All values in the table are in kilometres (km). The formulas for thicknesses in specific intervals are shown in the dz rows for each inversion model.

List of Figures

Figure 1.1: Simplified model of a diamondiferous lithospheric root adapted from Helmstaedt and Gurney (1995). The grey shaded region represents the region of the lithospheric root which is in the correct temperature and pressure regime to bear diamonds.

Figure 2.1: A cross-section of the Slave craton containing the three mantle domains described by Grütter et al. (1999) and the two crustal domains as described by Bleeker et al. (2007). Lithospheric thickness decreases from the south to north based upon xenolith studies. Details regarding the mantle and crustal geology are described in text. Age estimates are given for each unit. (From Heaman and Pearson, 2010).

Figure 2.2: The four kimberlite domains in the Slave craton described in text. (From Heaman et al., 2003).

Figure 3.1: 1D velocity model obtained from inverting for Rayleigh wave data. (From Chen et al., 2007). The starting velocity model is marked as a dashed line (ak135).

Figure 3.2: (a) Long wavelength Bouguer gravity anomalies in the Slave craton (From Poudjom Djomani et al., 2005a). The gravity data is contoured in milligals where cool colours are gravity lows and warm colours are gravity highs. (b) Contour map of the total elastic thickness obtained from inverting topographic and Bouguer gravity data in the Slave craton (From Poudjom Djomani et al., 2005a). The Central Slave Mantle Conductor described by Jones et al. (2003) is outlined in yellow. Kimberlites are indicated as stars on both maps.

Figure 3.3: Aeromagnetic map of the Slave craton. (From Percival et al., 2012). TF = Thelon Front; GBA = Great Bear Arc.

Figure 4.1: The reference coordinate system is denoted by xy and the rotated coordinate system is denoted by $x'y'$. The new coordinate system has been rotated by θ relative to the original coordinate system.

Figure 5.1: The distribution of magnetotelluric surveys in the Slave craton and their associated bandwidths. WBIF = West-Indin Bay Fault. GSLZ = Great Slave Lake Shear Zone.

Figure 5.2: (a) 1-D average responses of the Slave craton (dashed line) and for comparison the MT responses obtained by Schultz et al. (1993) (pluses) for the Superior Craton for their 1-D resistivity model. (b) 1-D best fit resistivity models for the average response curves. The solid black line is the layered Earth model, the light solid line is the smooth Earth model and the thick

dashed line is the layered Earth model that fit the response curves for Schultz et al. (1993). (Modified from Jones et al., 2003).

Figure 5.3: (a) MT response curves obtained from the lake bottom MT station at Lac de Gras. The smooth black line is the model response and the black dots are the measured MT data. (b) The best fit smooth resistivity models for the data. One model is smooth over its entirety while the other model allows for a tear in the resistivity at the base of the lithosphere (200 km). (Modified from Jones et al., 2003).

Figure 5.4: Magnetotelluric sites collected on the Slave craton with profiles 1, 2, 3 and 4 corresponding to profiles A, B, C and D (Adapted from Jones et al., 2003).

Figure 5.5: On the left hand side is a horizontal slice of the 3-D resistivity model at 140 km depth. The solid black arrows are observed induction vectors and the white arrows are calculated induction arrows. The induction arrows plotted are for a periods of 620 s. On the right hand side are three vertical slices through the 3-D model along profiles A, B and C. (Adapted from Jones et al., 2003).

Figure 5.6: On the left hand side is the resistivity model for the whole S2B profile to depths of ~300 km with faded out regions representing the depth of maximum penetration beneath a given site. On the right hand side are the preferred models for three focussed inversions that used a finer discretization to increase resolution in the upper 60 km of the model. The extent of the focussed inversions relative to the model for the whole S2B profile is indicated by the red, yellow and magenta boxes respectively. Modified from Spratt et al. (2009).

Figure 5.7: The interpretation of the three focussed inversions spliced together for the upper 60 km of the S2B profile. The red line shows the depth extent of the Phanerozoic sedimentary cover and the yellow line marks the crust mantle boundary. (From Spratt et al., 2009).

Figure 6.1: The profile of magnetotelluric stations used in the 2-D inversion. The green line shows the four segments that were stitched together to create a continuous profile, which are labelled 1 - 4. Magnetotelluric stations on each segment were rotated such that the x component of the MT data were perpendicular to the line segment and stations used in the inversions are coloured as red circles. Black circles represent other existing magnetotelluric data that were not utilized in the 2-D inversions. Purple diamonds show existing or previously active diamond mines. NU = Nunavut. NWT = Northwest Territories.

Figure 6.2: Phase tensor map slices for the decades 1 - 10000s. A beta skew greater than 3° is an indication of 3-D structure. WBIF = West-Bay-Indin fault zone. NU = Nunavut NWT = Northwest Territories. Further details are given in text.

Figure 6.3: The distribution of groups of sounding curves in the Slave province. Coloured circles correspond to groups of curves with distinct data characteristics. An insert map is shown on the right hand side of North America with a black box that contains the study area. WBIF = West-Bay Indin fault zone.

Figure 6.4: Examples of MT curves measured at stations on the Slave craton and displayed with rotation angles of 0° (left column) and 45° (right column) Descriptions of each group of curves are given in text. The XY and YX components are shown as red and blue circles respectively. Red and blue lines are the XX and YY components respectively. The classification is based upon XY and YX information exclusively.

Figure 6.5: Examples of MT curves measured at stations on the Slave craton and displayed with rotation angles of 0° (left column) and 45° (right column) Descriptions of each group of curves is given in the text. The XY and YX components are shown as red and blue circles respectively. Red and blue lines are the XX and YY components respectively. The classification is based upon XY and YX information exclusively.

Figure 6.6: The preferred 2-D resistivity model obtained from magnetotelluric data along the profile of Jones et al. (2003). The profile consists of four segments stitched together with the x axis rotated to be perpendicular to each segment. Rotation angles for each segment are labelled with a positive angle indicating a clockwise rotation. LdG = Lac de Gras. Three significant features are visible: R1 - a near surface resistor, R2 a moderately resistive feature in the upper mantle and CSMC the Central Slave Mantle Conductor (CSMC). The resistivity model was produced by jointly inverting the TE and TM modes with a starting model of $100 \Omega\text{m}$ and has an r.m.s. misfit of 1.89. The regularization parameter was set to $\tau = 3$ and the damping and variance were set to 1000 and 10% respectively to correct for static shifts present in the data.

Figure 6.7: (a) The r.m.s. misfit of each MT station along the profile for the preferred model. An r.m.s. misfit of 1 is considered an ideal data fit. (b) Static shift coefficients of each MT station determined by the 2-D inversion for the preferred model. The means of the static shift coefficients for the TE and TM are given as a red and blue dashed line respectively. A static shift

coefficient of 1 corresponds to no shift in the modelled apparent resistivity while a positive or negative value scales the modelled apparent resistivity response up or down respectively.

Figure 6.8: Pseudosections of the measured magnetotelluric data and the response of the preferred inversion model. The top panel shows the apparent resistivity pseudosections for the (a) TM mode data, (b) TE mode data, (c) TM mode inversion response and (d) TE inversion response. The bottom panel shows the phase pseudosections for the TM mode data, (b) TE mode data, (c) TM mode modelled response and (d) TE modelled response. Increasing apparent resistivity will correspond to a phase less than 45° and a decreasing apparent resistivity will correspond to a phase greater than 45° .

Figure 6.9: Pseudosections of residuals between the observed and modelled magnetotelluric data for the preferred model for the (a) TM mode apparent resistivity, (b) TE mode apparent resistivity, (c) TM mode phase and (d) TE mode phase. Residuals are given as the difference between observed and modelled apparent resistivity and phases that is scaled by the error. For the preferred model, the residuals were calculated using a 5% error floor.

Figure 6.10: (a) Inversion convergence curve for $\tau = 4$ showing the r.m.s. misfit for each iteration. The smooth decrease in r.m.s. misfit indicated the inversion for the preferred model is stable. (b) The L-Curve plotting r.m.s. misfit against model smoothness. The best τ value is chosen to be 4 based upon the inflection point of the L-Curve and is indicated by a red dot in (b). The resistivity models produced by varying τ , are shown for values of (c) 100, (d) 25, (e) 10, (f) 4, (g) 1 and (h) 0.25. Higher τ values result in smoother models and lower τ values result in rougher models. The preferred model is shown in (f) with $\tau = 4$.

Figure 6.11: Resistivity models produced by varying the variance and damping coefficients for (a) a variance of 100% and damping of 1000, (b) a variance of 10% and a damping of 2500, (c) a variance of 10% and a damping of 10000 and (d) a variance of 10% and a damping of 1000. The main resistivity features were recovered with each combination of parameters suggesting a robust model. The preferred model is shown in (d).

Figure 6.12: Resistivity models obtained from setting the error floor to (a) 5%, (b) 10% and (c) 20%. The main resistivity feature is recovered in each model, however, larger error floors produce a smearing effect on the conductor. The preferred model is shown in (a), which is the least prone to smearing seen in models with higher error floors.

Figure 6.13: Resistivity models obtained from setting the resistivity of the starting model to (a) 1 Ωm , (b) 10 Ωm , 100 Ωm , 1000 Ωm and 10000 Ωm . The main features are recovered in all starting models with the exception of the 1 Ωm starting model, which is likely a result of starting with a resistivity that is too far from the average resistivity of the region. The preferred model is shown in (c).

Figure 6.14: (a) The preferred magnetotelluric model and (b) the model published by Jones et al. (2003). Red numbers in the preferred model correspond to the same stations as those labelled in the model of Jones et al. (2003). Distance is not labelled on panel (b) as it is not available in Jones et al. (2003).

Figure 7.1: Pseudosections of apparent resistivity and phase for a 0° rotation are shown along Profiles A - E. These profiles correspond to the same profiles, which will show the preferred resistivity model (s92p21r8) in Section 7.4. Apparent resistivity is shown for the (a) YX, (b) XY, (e) XX and (f) YY components and phase is shown for the (c) YX, (d) XY, (g) XX and (h) YY components. White areas correspond to stations and periods with no data.

Figure 7.2: The misfit convergence for the preferred resistivity model (s92p21r8). The inversion converged to an r.m.s. misfit of 0.92 after 247 iterations.

Figure 7.3: Examples of data fits for the preferred resistivity model (s92p21r8). The locations of the MT stations are shown on the map by red dots.

Figure 7.4: Examples of data fit for from the preferred resistivity model (s92p21r8). The locations of the MT stations are shown on the base map by red dots.

Figure 7.5: Model results are shown as five representative resistivity profiles across the Slave craton. The profiles are labelled as (a) Profile A, (b) Profile B, (c) Profile C, (d) Profile D and (e) Profile E and are shown in (f) on the base map. The pink line is the Electric Moho and black dots on the base map represent MT station locations. LdG = Lac de Gras; EK = Ekati; GK = Gacho Kue; D = Diavik; J = Jericho; YK = Yellowknife.

Figure 7.6: (a) R.M.S. misfit as a function of period for each station individual station (light blue lines), averaged r.m.s. misfit (red line) and overall model r.m.s. misfit (black dashed line). (b) Map view of station locations with each coloured circles representing the overall r.m.s misfit of the station. The model is shown at depths of (c) 60 km, (d) 100 km, (e) 160 km and (f) 220 km. On the 100 km depth slice diamond mines (pink diamonds), known kimberlite locations (yellow stars) and teleseismic sites with an observed reduction in shear wave velocities are also plotted.

Figure 7.7: Horizontal slices of inversion models produced by varying the error floor applied to the diagonal and off-diagonal components of the magnetotelluric impedance tensor. (a) Horizontal model slice at 100 km depth using an error floor of (a) 5% and (b) 10%. The preferred model uses an error floor of 10% and is shown in (b).

Figure 7.8: Vertical slices of inversion models produced by varying the error floor applied to the diagonal and off-diagonal components of the magnetotelluric impedance tensor. Stations along the vertical slices are highlighted in red in (a). Depth slices using an error floor of (b) 5%. and (c) 10 %. The preferred model uses an error floor of 10% and is shown in (c).

Figure 7.9: Horizontal slices of inversion models produced by varying the resistivity of the starting model. Horizontal model slices at 100 km depth produced using a starting model with resistivity of (a) 1 Ωm , (b) 10 Ωm , (c) 100 Ωm , (d) 1000 Ωm and (e) 100000 Ωm . The preferred model used a resistivity of 1000 Ωm and is shown in (d).

Figure 7.10: Model depth slices produced by varying the starting model used in the inversion. Stations along the depth slices are highlighted in red on the base map. Resistivity models are shown that were produced using starting models of (a) 1 Ωm , (b) 10 Ωm , (c) 100 Ωm , (d) 1000 Ωm and 10000 Ωm . The preferred model is used a starting model of 1000 Ωm and is shown in (d). NU = Nunavut. NWT = Northwest Territories.

Figure 7.11: (a) Resistivity depth curves for each magnetotelluric station obtained from inverting the MT data produced from the three-layer synthetic with a 100 Ωm starting model. Each depth curve plotted in black corresponds to a station in the model. The solid red line is the average resistivity between all stations and the red dotted line corresponds to one standard deviation above or below the average resistivity. (b) The true synthetic three-layer model (solid black line) compared with the average resistivity obtained when inverting with a 100 Ωm starting model (red line) plus or minus one standard deviation (red dashed line). (c) Resistivity depth curves for each magnetotelluric station obtained from inverting the MT data produced from the three-layer synthetic with a 1000 Ωm starting model. Each depth curve plotted in black corresponds to a station in the model. The solid red line is the average resistivity between all stations and the red dotted line corresponds to 1 standard deviation above or below the average resistivity. (d) The true synthetic three-layer model (solid black line) compared with the average resistivity obtained when inverting with a 1000 Ωm starting model (red line) plus or minus one standard deviation (red dashed line).

Figure 7.12: Horizontal slices of inversion models produced by varying the covariance parameter for inverting the magnetotelluric data. Horizontal model slices at 100 km depth produced using a covariance parameter of (a) 0.1, (b) 0.3, (c) 0.4, (d) 0.5 and (e) 0.6 and (f) 0.9. The preferred model uses a covariance of 0.3 and is shown in (b).

Figure 7.13: Model depth slices produced by varying the covariance parameter for the preferred resistivity model. Stations along the depth slices are highlighted in red on the base map. Resistivity models are shown that were produced using a covariance parameter of (a) 0.1, (b) 0.3, (c) 0.4, (d) 0.5, (e) 0.6, and (f) 0.9. The preferred model uses a covariance parameter of 0.3 and is shown in (d). NU = Nunavut. NWT = Northwest Territories.

Figure 7.14: A resolution test to investigate conductor C1 (a) Profile B from Figure 7.5, which has been modified to replace the conduits that branch from C1 with a resistivity of 1000 Ωm . (b) Apparent resistivity and phase curves for the stations STG004 and STG007 are shown as examples of how the data fits change between the modified and preferred solutions. The sites STG004 and STG007 are indicated as red triangles in (a) and are labelled in map view in (c-f). Removing the conduits causes an overestimation of the apparent resistivity and an underestimation of the phase in the modified solution. (c) The r.m.s. misfit of the preferred solution shown as coloured circles. (d) The r.m.s. misfit of the modified solution shown as coloured circles. (e) P-values returned from the KS test shown as coloured circles comparing the preferred model and a modified model that removed the conduit structures from C1. The KS test returns a p-value of 0.0078 where a p-value less than 0.05 is considered statistically significant suggesting that the conduits are robust. (f) The r.m.s. misfit ratio between the modified solution and the preferred solution as coloured circles. A ratio greater than 1.0 indicates that the r.m.s. misfit has increased in the modified solution shown in (d) relative to the preferred solution shown in (c). Notably, the r.m.s. misfit ratio increases at all sites along Profile B further suggesting that the conduits are required to fit the data. These observations are taken as evidence that the conduits are robust structures in the model and are required by the data.

Figure 7.15: A resolution test to investigate conductor C2 (a) Profile D from Figure 7.5, which has been modified to replace C2 with a resistivity of 1000 Ωm . (b) Apparent resistivity and phase curves for the stations Snare and s2b-002 are shown as examples of how the data fits change between the modified and preferred solutions. The sites s2b002mg and Snare are indicated as red triangles in (a), but Snare has been projected onto the profile. Snare and s2b002 are labelled in

map view in (c-f). (c) The r.m.s. misfit for each site of the preferred solution shown as coloured circles. (d) The r.m.s. misfit for each site of the modified solution shown as coloured circles. (e) P-values returned from the KS test shown as coloured circles comparing the preferred model and a modified model, which removed C2. The KS test returns a p-value of 0.689 where a p-value less than 0.05 is considered statistically significant suggesting that C2 may not be robust. (f) The r.m.s. misfit ratio between the modified solution and the preferred solution as coloured circles. A ratio greater than 1.0 indicates that the r.m.s. misfit has increased in the modified solution shown in (d) relative to the preferred solution shown in (c). Removing C2 does not appear to cause the data fits to become significantly worse in s2b-002 and Snare as the modified solutions generally remain within the error bars. The r.m.s. misfit ratio in (d) increases at most sites near Profile D, however, only by a factor of about 10%. These observations are taken as evidence that C2 may not be a robust feature in the model.

Figure 7.16: A resolution test to investigate conductor C3 (a) Profile C from Figure 7.5, which has been modified to replace C3 with a resistivity of 1000 Ωm . (b) Apparent resistivity and phase curves for the stations STG014 and prov are shown as examples of how the data fits change between the modified and preferred solutions. The site STG014 is indicated as a red triangle in (a) and prov is not located on profile C and thus is not shown. STG014 and STG007 are labelled in map view in (c-f). (c) The r.m.s. misfit for each site of the preferred solution shown as coloured circles. (d) The r.m.s. misfit for each site of the modified solution shown as coloured circles. (e) P-values returned from the KS test shown as coloured circles comparing the preferred model and a modified model, which removed C3. The KS test returns a p-value of 1.43E-05 where a p-value less than 0.05 is considered statistically significant suggesting that C3 is robust. (f) The r.m.s. misfit ratio between the modified solution and the preferred solution as coloured circles. A ratio greater than 1.0 indicates that the r.m.s. misfit has increased in the modified solution shown in (d) relative to the preferred solution shown in (c). Removing C3 worsens the data fit appreciably, but seems to only affect the lake bottom and STG stations, which have the longest periods in the data set. This is taken as evidence that the C3 is a robust feature, but is likely only being constrained by a subgroup of data with the longest periods in the data set.

Figure 7.17: A resolution test to investigate conductor C4 (a) Profile E from Figure 7.5, which has been modified to replace C4 with a resistivity of 1000 Ωm . (b) Apparent resistivity and phase curves for the stations Ash-004 and Ash-006 are shown as examples of how the data fits change

between the modified and preferred solutions. The sites Ash-004 and Ash-006 are indicated as red triangles in (a) and are labelled in map view in (c-f). (c) The r.m.s. misfit for each site of the preferred solution shown as coloured circles. (d) The r.m.s. misfit for each site of the modified solution shown as coloured circles. (e) P-values returned from the KS test shown as coloured circles comparing the preferred model and a modified model, which removed C4. The KS test returns a p-value of 1.0 where a p-value less than 0.05 is considered statistically significant suggesting that C4 is not robust. (f) The r.m.s. misfit ratio between the modified solution and the preferred solution as coloured circles. A ratio greater than 1.0 indicates that the r.m.s. misfit has increased in the modified solution shown in (d) relative to the preferred solution shown in (c). Removing C4 does not appear to cause the data fits to become significantly worse in s2b-002 and Snare as the modified solutions generally remain within the error bars. This is taken as evidence that the C4 is not a robust feature.

Figure 7.18: Synthetic test recovering a mantle conductor with the same spatial extent as the CSMC proposed by Jones et al. (2003). A black line in each panel outlines the extent of the input model. The thickness of the conductor is 40 km at depths of 80 - 120 km. The panels show (a) the 1 Ωm input model, (b) the 10 Ωm input model, (c) the recovered model for the 1 Ωm input model with the current station distribution, (d) the recovered model for the 10 Ωm input model with the current station distribution, (e) the recovered model for the 1 Ωm input model with the proposed station distribution and (f) the recovered model for the 10 Ωm input model with the proposed station distribution.

Figure 7.19: (a) Resistivity depth curves for each magnetotelluric station in the preferred 3-D resistivity model. The depth to the top of the conductor is given by the inflection point of the resistivity depth curve in agreement with Comeau et al. (2016). (b) Results from a synthetic inversion showing the change in resistivity character when encountering a conductive halfspace. The average resistivity is given for all MT stations in the model (red line) compared to the true two layer model (black line). All recovered resistivity curves in the synthetic model are shown as light blue lines. The top of the halfspace is defined by the inflection point.

Figure 7.20: Map slices comparing models obtained from the WSINV3DMT and ModEM inversion algorithms for a subset of the Slave magnetotelluric data at depths of (a,e) 43 km, (b,f) 62 km, (c,g) 90 km and (d,h) 130 km. The starting model was 1000 Ωm and similar features are

visible at each depth between the WSINV3DMT and ModEM models. The overall r.m.s. misfit for the WSINV3DMT and ModEM inversions are 1.02 and 1.67, respectively.

Figure 7.21: Comparison of depth slices for the models obtained with the WSINV3DMT and ModEM inversion algorithms for a subset of the Slave magnetotelluric data. Depth slices were extracted beneath the magnetotelluric sites, which are indicated as red dots on the base map. The starting model was 1000 Ωm and similar features are visible at each depth in both the WSINV3DMT and ModEM models. The r.m.s. misfit for the WSINV3DMT and ModEM inversions are 1.02 and 1.67 respectively.

Figure 7.22: Comparison of depth slices for the WSINV3DMT and ModEM inversion algorithms for a subset of the Slave magnetotelluric data. Depth slices are extracted beneath the magnetotelluric sites, which are indicated as red dots on the base map. The starting model was 100 Ωm and similar features are visible at each depth between the WSINV3DMT and ModEM models. The r.m.s. misfit for the WSINV3DMT and ModEM inversions are 1.02 and 1.67 respectively.

Figure 7.23: Map slices comparing the WSINV3DMT and ModEM inversion algorithms for a subset of the Slave magnetotelluric data for depths of (a,e) 43 km, (b,f) 62 km, (c,g) 90 km and (d,h) 130 km. The starting model was 1000 Ωm and similar features are visible at each depth between the WSINV3DMT and ModEM models. The r.m.s. misfit for the WSINV3DMT and ModEM inversions are 1.02 and 1.67 respectively.

Figure 8.1: (a) A summary of depth estimates for the lithosphere-asthenosphere boundary (LAB) from various studies as described in text. The light blue circle with an arrow pointing downwards indicates that the depth is a minimum estimate. The depth estimate obtained from this study is indicated by a red star. (b) The locations of the studies with a specific location listed in (a) on the base map. Studies that are 1-D estimates or estimates for the whole Slave craton are not included on the base map. See text for further details of each study.

Figure 8.2: Estimated water content from electrical resistivity for STG008 overlying the CSMC in the Slave craton using the methodology of Rippe et al. (2013). The panels from left to right are: (a) the electrical resistivity profile (blue line) and the electrical resistivity of dry olivine from the SEO3 model (black line) (Constable, 2006). (b) The geotherm predicted for the Slave craton (Mathers, 2012) (blue line) and the solidus of dry peridotite (red line). (c) The Water content predicted by Wang et al. (2006) (pink line), Yoshino et al. (2009) (green line) and Karato (1990)

(blue dashed line). Water solubility limit (black line) (Lizarralde et al., 1995; Bell et al., 2003). Water content required for hydrous melt (red line). (d) Predicted melt fractions using resistivity relationships of Wang et al. (2006) (pink line), Yoshino et al. (2006) (green line) and Karato (1990) (blue dashed line).

Figure 8.3: Resistivity contours calculated using the Modified Archie's Law (Glover, 2010) plotting phlogopite volume fraction against temperature (K). Each panel models a different depositional geometry including (a) well-connected ($m = 1$), (b) partially connected ($m = 1.5$) and (c) disconnected ($m = 2$). This model is used to constrain the phlogopite volume fraction required to produce the observed resistivities in the CSMC under different depositional geometries. Red lines are the upper and lower resistivity bound of the CSMC. The temperature range is defined from the geotherm of Mathers (2012).

Figure 8.4: Grey dashed lines are isocontours of the conductivity of different volume fractions of an olivine - hydrous carbonatite melt mixture for melt fractions between 0.01 vol% and 10 vol%. For comparison, the conductivity of dry olivine and 0.1 wt% hydrous olivine under different oxygen buffers (NNO = NiNiO: Yoshino et al., 2006 and MMO = MoMoO₂: Yoshino et al., 2009) are plotted as thick grey and blue lines respectively. The red line represents the conductivity of the Central Slave Mantle Conductor from Jones et al. (2001a). (Modified from Yoshino et al., 2018).

Figure 8.5: The conductivity of interconnected brines in olivine modelled using the upper Hashin Shtrickman bound (Hashin and Shtrickman, 1963). The conductivity of the brines used the conductivity relationship from Guo and Keppler (2019). The conductivity of interconnected brines are shown for volume fractions of 1, 0.1 and 0.01 and concentrations of 1M and 0.1M or equivalently 5.5wt% and 0.55 wt%. The panels show the conductivity as a function of temperature and pressure for (a) 1% volume fraction and 5.5 wt% brine, (b) 0.1 wt% volume fraction and 5.5 wt% brine, (c) 0.01 wt% and 5.5 wt% brine, (d) 1% volume fraction and 0.55 wt% brine, (e) 0.1% volume fraction and 0.55 wt% brine and (f) 0.01% volume fraction and 0.55 wt% brine.

Figure 8.6: The suggested relationship between Mesozoic subduction events and the CSMC and MLD located in the central Slave craton. (a) A slab subducts at a low angle beneath the Slave craton during the Mesozoic and releases high density fluids that percolate upwards through the lithosphere stalling at mid-lithosphere depths. (b) The high density fluids remain trapped beneath

the Slave craton simultaneously producing a MLD and the CSMC. (Adapted from Weiss et al., 2015).

Figure 8.7: (a) Interpreted seismic reflection section from Cook et al. (1997) combined with the seismic model produced with PRFs by Bostock (1998) beneath the southern Slave craton. The seismic discontinuities H, X and L are labelled on the seismic section and are described in text. (b) The preferred electrical resistivity model for Profile A from Figure 7.5. There is no clear correlation between the H, X and L seismic discontinuities and the electrical resistivity for Profile A. YK = Yellowknife. The vertical scale on the seismic model in (a) is the same vertical scale as the vertical scale in (b). (Modified from Snyder and Grütter, 2010)

Figure 8.8: P and S wave model depth slices and MT model depth slices for 100 km, 160 km and 220 km. Yellow triangles are the teleseismic station locations. Thick black lines are the Great Slave Lake Shear Zone (NE SW trending) and the Bathurst fault (NW SE trending). Red colours are slower than average velocities and blue colours are faster than average velocities.

Figure 8.9: Estimated water content from electrical resistivity for example three stations in the Slave craton using the methodology of Rippe et al. (2013). (A) S99-018a near Lac de Gras, (B) Sno-108 in the south western Slave craton and (C) S99-022a near the Jericho diamond mine. The locations of these MT stations are labelled as red dots on the base map. The panels from left to right are: (a) the electrical resistivity profile (blue line) and the electrical resistivity of dry olivine from the SEO3 model (black line) (Constable, 2006). (b) The geotherm predicted for the Slave craton (blue line) and the solidus of dry peridotite (red line). (c) The Water content predicted by Wang et al. (2006) (pink line), Yoshino et al. (2009) (green line) and Karato (1990) (blue dashed line). Water solubility limit (black line) (Lizarralde et al., 1995; Bell et al., 2003). Water content required for hydrous melt (red line). (d) Predicted melt fractions using resistivity relationships of Wang et al. (2006) (pink line), Yoshino et al. (2006) (green line) and Karato (1990) (blue dashed line).

Figure 8.10 Water content estimations at a depth of 100 km depth for each site using the methodology of Rippe et al. (2013). The water content estimates are represented as coloured circles for (a) the Wang et al. (2006) model, (b) the Yoshino et al. (2009) model, (c) the Karato (1990) model, (d) the minimum water content estimated of the three aforementioned models and (e) the maximum water content estimated without exceeding the solubility (Lizarralde et al., 1995; Bell et al., 2003) from the three models.

Figure 8.11 Water content estimates at a depth of 150 km depth for each site using the methodology of Rippe et al. (2013). The water content estimates are represented as coloured circles for (a) the Wang et al. (2006) model, (b) The Yoshino et al. (2009) model, (c) the Karato (1990) model, (d) the minimum water content estimated of the three aforementioned models and (e) the maximum water content estimated without exceeding the solubility (Lizarralde et al., 1995; Bell et al., 2003) from the three models. (f) Horizontal depth slices at 100 km to show the correlation between upper mantle conductors and above average water content estimates. Notably water contents estimated beneath the upper mantle conductors C2 and the CSMC predict much higher water contents than water content predicted beneath resistive mantle.

Figure 8.12 (a) Apparent resistivity data generated from a theoretical model containing a lower crustal conductor and the asthenosphere. (b) Phase data generated from a theoretical model containing a lower crustal conductor and the asthenosphere. (c) A theoretical model containing a lower crustal conductor and the asthenosphere (thick black line) and the inversion models recovered using a smooth model (smooth light grey line) and a sharp 7-layer inversion (sharp light grey line). (From Jones, 1999).

Figure A.1 Horizontal slices of inversion models produced by varying the covariance parameter for early inversions. Horizontal model slices at 75 km depth produced using a covariance parameter of (a) 0.1, (b) 0.3, (c) 0.6, (d) 0.9. The preferred model uses a covariance of 0.3 and is shown in (b). NU = Nunavut. NWT = Northwest Territories. BC = British Columbia. YK = Yukon. SK = Saskatchewan. AB = Alberta.

Figure A.2 Model depth slices produced by varying the covariance parameter for early inversions. Stations along the depth slices are highlighted in red on (a) the base map. Resistivity models are shown that were produced using a covariance parameter of (b) 0.1, (c) 0.3, (d) 0.6, and (e) 0.9. The preferred model uses a covariance parameter of 0.3 and is shown in (c). NU = Nunavut. NWT = Northwest Territories.

Figure A.3 Model depth slices produced by varying the starting model used in the inversion. Stations along the depth slices are highlighted in red on the base map. Resistivity models are shown that were produced using starting models of (a) 1 Ωm , (b) 10 Ωm , (c) 100 Ωm , (d) 1000 Ωm and 10000 Ωm . The preferred model is used a starting model of 1000 Ωm and is shown in (d). NU = Nunavut. NWT = Northwest Territories.

Figure A.4 Horizontal slices of inversion models produced by varying the covariance parameter for inverting the magnetotelluric data. Horizontal model slices at 100 km depth produced using a covariance parameter of (a) 0.3, (b) 0.4, (c) 0.5, (d) 0.6 and (e) 0.9. The preferred model uses a covariance of 0.3 and is shown in (a).

Figure A.5 Model depth slices produced by varying the covariance parameter used in the inversion. Stations along the depth slices are highlighted in red on (a) the base map. Resistivity models are shown that were produced using starting models of (b) 0.4, (c) 0.6, (d) 0.3, (e) 0.9 and (f) 0.5. The preferred model is used a covariance parameter of 0.3 and is shown in (d). NU = Nunavut. NWT = Northwest Territories.

Figure A.6 Synthetic inversion recovering four upper mantle conductors. A black line in each panel outlines the extent of the input model.

Chapter 1 : Introduction

Canada is currently the worlds second largest exporter of rough diamonds with an estimated economic value exceeding 2.6 billion Canadian dollars in 2017 (Natural Resources Canada, 2017). However, many of Canada's producing diamond mines have closed (e.g., Snap Lake and Jericho) or will be closing in the next decade (e.g., Diavik and Victor) and thus further exploration is needed to maintain Canadian output. Diamond exploration is similar to that of any resource, namely that "one must understand the source and holding reservoir of the commodity being sought" (Snyder and Grütter, 2010). For diamonds the reservoir is primarily the cratonic lithosphere and the deposit is kimberlite pipes, which act as a transport mechanism for bringing diamonds to the surface from deep within the Earth (> 150 km depth) (e.g., Helmstaedt and Gurney, 1995). Archean cratons are comprised of thick, stable continental lithosphere that has persisted for billions of years owing to their isopycnicity (i.e. near-neutral buoyancy) and higher viscosities than the surrounding mantle (Jordan, 1978; Eaton and Perry, 2013; Snyder et al., 2014; Snyder et al., 2017). These regions host diamonds due to their cold geotherms (see Figure 1.1), which coincide with the diamond stability field (Day, 2012) and thus mapping cratonic lithosphere may help regional diamond exploration and improve the chances of finding new diamond deposits (Helmstaedt and Gurney, 1995; Snyder et al., 2004; Jones and Craven, 2004; Jones et al., 2009b; Evans et al., 2011).

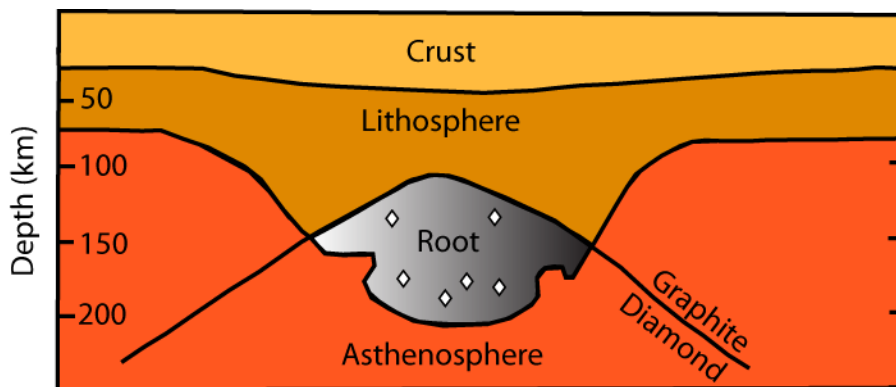


Figure 1.1: Simplified model of a diamondiferous lithospheric root adapted from Helmstaedt and Gurney (1995). The grey shaded region represents the region of the lithospheric root which is in the correct temperature and pressure regime to bear diamonds.

The Slave craton is a 400 x 600 km block of Archean aged lithosphere in Northwest Canada that contains many of the country's diamond mines. There is a large amount of available geophysical and geological data in the Slave craton and, as such, it presents an excellent opportunity to study cratonic lithospheric structure in relation to the emplacement of diamondiferous kimberlite pipes (Power et al., 2004; Snyder et al., 2014). Results from past studies have found the Slave craton to be distinctive from other cratons. Xenoliths have revealed a uniquely stratified mantle in the central Slave craton where ultradepleted harzburgite overlies a more fertile lherzolite to a depth of ~160 km (Griffin et al., 1999). On the other hand, seismic studies have imaged several prominent mantle discontinuities suggesting that the Slave craton was built through the stacking and underthrusting of ancient proto-continental lithosphere (Snyder et al., 2008; Chen et al., 2009; Snyder et al., 2014; Snyder et al., 2017). The integration of geophysical, geological and petrological data in previous studies has elucidated complex internal structures with evidence of metasomatic overprinting (e.g., Snyder et al., 2014; Snyder et al., 2017), but there are still uncertainties in structural and chemical boundaries that need to be addressed.

Magnetotelluric data collected during the LITHOPROBE program in the late 1990s and early 2000s discovered a large mantle conductor in the central Slave craton, which was coined the Central Slave Mantle Conductor (CSMC) at depths of 80 - 120 km with an internal resistivity of no more than 30 Ωm (Jones et al., 2001a; Jones et al., 2003). One longstanding uncertainty is the origin of the (CSMC), which is especially intriguing due to its apparent overlap with the Lac de Gras diamondiferous kimberlite field (Jones et al., 2001a; Jones et al., 2003; Jones and Craven, 2004). The CSMC was once thought to be a unique feature among cratons, but MT experiments have now defined upper mantle conductors in the Kaapvaal Craton (Evans et al., 2011), Sask Craton (Jones et al., 2005), Superior Craton (Ferguson et al., 2005), Sao Francisco Craton (Pinto et al., 2010), and Gawler Craton (Thiel and Heinson, 2013). The existence of extensive upper mantle conductors in cratonic lithosphere was a surprising discovery as these regions are characterized by cooler geotherms and are not expected to contain abundant conducting phases such as partial melt or fluids (Selway, 2018). Jones et al. (2005) speculated that upper mantle conductors are genetically related to the formation of diamondiferous kimberlites, but this is difficult to prove without first understanding the nature of these conductors. The varied geological history and composition of the aforementioned cratons suggests there is likely no single mechanism that will produce an upper mantle conductor (see

Selway (2018) for a review of upper mantle conductors) and thus each region must be interpreted individually in accordance to its geologic history.

The MT method uses low frequency radio waves to image the electrical resistivity of the Earth (e.g., Chave and Jones, 2012) and is valuable as it provides information that is complementary to deep probing seismic experiments, which yield information regarding elastic properties. The depth of investigation for MT data can be on the order of hundreds of kilometres, particularly in resistive regions such as cratons and is thus an ideal tool for studying cratonic lithosphere where diamonds form. This project used magnetotellurics to better characterize the lithosphere of the Slave craton in the Northwest Territories, Canada to aid in delineating regions that may contain diamondiferous kimberlite pipes. Specifically, this thesis presents a 3-D resistivity model of the Slave craton that utilizes all available MT data from LITHOPROBE (Jones et al., 2003; Jones et al., 2001a) and the Slave to Bear Province (S2B) profile (Spratt et al., 2009) to map the electrical structure of the lithosphere in the Slave craton. In addition, the apparent spatial overlap between the CSMC and the diamondiferous Lac de Gras kimberlites discovered by Jones et al. (2003) will be investigated using the newly produced 3-D magnetotelluric model. This contribution improves upon previous publications as past results were either 2-D models (Jones et al., 2001a; Jones et al., 2003; Spratt et al., 2009), which are susceptible to artefacts caused by galvanic distortion and show only limited cross-sections of the Earth (e.g., Türkoğlu et al., 2009), or 3-D algorithms that down weighted the diagonal components of the impedance tensor which removed 3-D information from the data set (Snyder et al., 2014). The 3-D resistivity model produced by Snyder et al. (2014) also did not use all available data to satisfy memory requirements for the inversion. Furthermore, MT models in the Slave craton can be interpreted more reliably today than two decades ago when the first resistivity models were published due to significant advances in mineral physics experiments. For example, recently it was thought that only graphite and semi-conduction in mantle minerals were the prominent conduction mechanisms in the mantle (Selway, 2014), but recent laboratory experiments have found that graphite may not be electrically conductive under mantle conditions (Zhang and Yoshino, 2017; Watson et al., 2010) and recent experiments have shown that hydrous minerals (Wang et al., 2012; Hu et al., 2018; Li et al., 2016; Li et al., 2017), carbonatite melts (Gaillard et al., 2008; Yoshino et al., 2018) and brines (Guo and Keppler, 2019) are

Chapter 1 : Introduction

conductive in the shallow upper mantle. Thus, it is also worthwhile revisiting past interpretations of the CSMC in light of these new mineral physics experiments.

Chapter 2 reviews the geology of the Slave craton. The regional crustal and mantle structure are discussed including a brief description of the assembly of the Slave craton. The timing and distribution of kimberlite magmatism is also discussed.

Chapter 3 gives a brief overview of the existing MT data collected in the Slave craton. The results of previous MT studies are discussed, which includes studies that delineated the electric Moho, the depth to the asthenosphere, and the discovery of the Central Slave Mantle Conductor.

Chapter 4 reviews the MT method. Apparent resistivity and phase relationships are derived from Maxwell's equations along with the skin depth equation. Additionally, the methods of determining strike direction in a 2-D Earth are discussed, including how to remove the effects of distortion in MT data.

Chapter 5 reviews geophysical studies completed in the Slave craton with the exception of MT studies, which were discussed in Chapter 3. This includes, gravity, seismic and aeromagnetic studies. This also includes a section on kimberlite pipe scale exploration in comparison to regional exploration for diamonds.

Chapter 6 presents 2-D MT inversions for the Slave data and compares these to previous publications in the Slave craton from Jones et al. (2003).

Chapter 7 presents 3-D MT inversion results and reviews the models obtained with different parameters, which were tested and optimized. The preferred resistivity model (s92p21r8) is presented along with synthetic testing of the robustness of key resistivity features. The main resistivity features are described with a comparison to previous MT studies.

Chapter 8 discusses the interpretation of the preferred resistivity model (s92p21r8) for the Slave craton. Possible causes for the Central Slave Mantle Conductor are discussed and the relationship between upper mantle conductors and diamondiferous kimberlites is considered. The s92p21 resistivity model is compared to previous seismic studies to determine if there are any correlations between the models. Water content in the mantle is estimated to be on the order of 10 - 150 ppm for 100 - 170 km and below these depths appears to be dry (< 5 ppm). The

Chapter 1 : Introduction

lithosphere-asthenosphere boundary (LAB) was determined to be at a depth of 210 ± 10 km, which was found agree with estimates determined from previous MT, seismic and xenolith studies for the LAB depth.

Chapter 9 summarizes the results of this thesis and reiterates important findings from the new 3-D MT model.

Chapter 2 : Slave Craton Geology

2.1 Introduction

The Slave craton is located in north western Canada and is one of the stable nuclei of the Precambrian core of North America known as Laurentia (Hoffman et al., 1989). The Slave craton is one of ~35 Archean cratons found worldwide (Bleeker, 2003). Presently, it is one of several cratons that were together by Proterozoic collisional orogens, which comprises the North American Craton, also known as Laurentia (Hoffman et al., 1989). However, similarities between the Slave, Darwhar, Zimbabwe and Wyoming cratons suggest that at one time its history the Slave was a component of a greater supercraton known as Sclavia (Bleeker, 2003). Thus, the Slave craton can be considered an exotic fragment of the earlier supercraton Sclavia. The Slave craton is also of particular economic interest as diamondiferous kimberlites have episodically erupted since the late Phanerozoic (Heaman et al., 2003). This chapter will briefly describe the origin of the Slave craton including its crustal and mantle structure and the distribution of kimberlites in the Slave Province. A simplified cross section through the Slave craton is given in Figure 2.1 and descriptions of the major crustal and mantle features are given in this chapter.

2.2 Crustal Geology

The exposed crust in the Slave craton covers an area of ~700 by 500 km and exhibits a marked dichotomy between the western and eastern sides of the craton. The western side contains the Central Slave Basement Complex, which is overlain by the Central Slave Cover Group that is composed of primarily quartzite and banded iron formations (Bleeker et al., 1999). The Central Slave Basement Complex (CSBC) also hosts the Acasta gneisses that have been dated as some of the oldest rocks on Earth at ~ 4030 Ma (Bowring and Williams, 1999). The eastern side of the Slave crust is characterized by more isotopically juvenile rocks that are dated to be ~ 2600 Ma (Davis et al., 2003). This east-west division is also observed in as an isotopic boundary which shows a change in Pb and Nd isotope compositions in granitoids between the juvenile crust to the east and the more ancient crust to the west (Thorpe et al., 1992; Davis et al., 2003). The Slave province can be broadly categorized into five sub provinces, which are the Central Slave Superterrane, Hackett River Terrane, Contwyto Terrane, Snare River Terrane and Bathurst Block (Percival et al., 2012).

2.3 Lithospheric Composition from Xenoliths

The Slave mantle displays a decoupling from the crust and has three distinct NE-SW trending domains, which were first proposed by Grütter et al. (1999) based upon G10 garnet distributions. The central domain is dominated by depleted G10 garnets, which also coincides with the ultradepleted hazburgite layer first described by Griffin et al. (1999) and the Lac de Gras kimberlite field. The northern domain is characterized by a rapid decrease in G10 garnets accompanied by an increase in eclogitic garnets. The southern domain similarly has a drop off in G10 garnets, but the transition is much more gradual than seen in the northern domain. The geometry of the mantle domains has been used as evidence for the mantle lithosphere forming by subcretion of SE-vergent subduction (Davis et al., 2003).

2.4 Lithospheric Thickness from Xenoliths

The base of the lithosphere in xenoliths is expressed as a rapid increase in Fe, Ca, Al, Ti, Zr and Y accompanied with a decrease in the magnesium number of olivine (O'Reilly and Griffin, 2010). The Slave craton contains an abundance of xenolith suites from kimberlites that have been emplaced over the last ~500 Ma (Heaman et al., 2003). Such xenolith suites can provide a snapshot of the depth to the lithosphere asthenosphere boundary at the time of kimberlite

emplacement where studies in the Slave craton suggest thicknesses on average greater than 200 km. Xenolith studies in the northwest Slave craton from the Jericho pipe have found the LAB to be at a depth of 190 km (Kopylova and Russell, 2000). In the southeast of the Slave craton estimates suggest a depth to the LAB of 220 - 250 km (Kopylova and Caro, 2004) and in the southwest Slave the minimum thickness of the lithosphere is 160 - 190 km (Carbno and Canil, 2002); while beneath Lac de Gras the lithosphere was found to be 200 km thick (Pearson et al., 1999; Griffin et al., 1999). The 200 km depth estimate from the Lac de Gras kimberlites likely represents the best present estimate of lithosphere thickness as these are the youngest kimberlites and the thickness of cratonic roots can vary over time due to convective instabilities in the mantle (Conrad, 2000; Morency et al., 2002).

2.5 Igneous Intrusions in the Slave Craton: Kimberlite Magmatism and the Mackenzie Dyke Swarm

Kimberlite magmatism in the Slave craton spans from the Cambrian (~542 Ma) for the oldest kimberlite clusters to the Eocene (47.5 - 56 Ma) for the most recent Lac de Gras kimberlite cluster (Heaman et al., 2003). The kimberlites in the Slave craton can be roughly divided into four domains that are distinctly spatially and temporally similar to one another (see Figure 2.2).

- Domain I is in the western most part of the Slave province and is dominated by Silurian-Ordovician aged kimberlites.
- Domain II is in the south eastern part of the Slave province and contains primarily Cambrian aged kimberlites, which contains the Gacho Kue and Snap Lake mines.
- Domain III is in the Central Slave and is defined by Cretaceous and Eocene aged kimberlites (48 - 74 Ma). These kimberlites are mostly clustered around Lac de Gras and contain the first two diamond mines opened in Canada, Diavik and Ekati.
- Domain IV is in the northern Slave province, which contains two distinct ages of kimberlites: the first group is Jurassic in age including the Jericho mine and the second group further north is Permian in age.

Prior to kimberlite magmatism the Mackenzie dyke swarm, one of the largest dyke swarms on Earth, penetrated the Slave craton and much of the Canadian Shield at ~ 1.27 Ga (Ernst et al., 1995). The large volume and short time span of emplacement for the Mackenzie swarm has been

taken as evidence for the dykes originating from a hotspot (Lecheminant and Heaman, 1989), who proposed the origin of the dyke swarm to be the result of a mantle plume, which became impinged beneath present day Victoria Island. Numerical modelling has also proven that the observed change in orientation of the dyke swarm is consistent with paleo stress regimes resulting from an impinged mantle plume (Hou et al., 2010).

Chapter 3 : Previous Non-MT Studies

3.1 Introduction

This chapter will focus on previous geophysical studies in the Slave craton that are complementary to magnetotelluric studies that will be discussed in Chapter 5. This includes, seismic body wave tomography, receiver functions, surface wave tomography, gravity and magnetics. In addition to these methods, a section describing near surface geophysical methods for kimberlite exploration is given to provide context between regional-and deposit-scale diamond exploration.

3.2 Seismic Tomography Studies

3.2.1 Early P-wave Seismic Tomography Studies

Banks et al. (2000) analyzed 14 broadband seismic stations distributed throughout the Slave craton for the purpose of mapping the upper mantle structure and to investigate if a relationship between mantle structure and kimberlite genesis exists. The P-wave tomography model imaged a low-velocity anomaly ($> 0.5\%$ slowness) in a depth range of 350 - 600 km below the Lac de Gras kimberlite field. It was speculated that a genetic relationship could exist between this anomaly and the diamondiferous kimberlites of Lac de Gras, however, further work would be required to prove such a speculation. The seismic tomography model constrained lithospheric thickness to be 250 ± 50 km, which agreed well with previous results from xenoliths (Kopylova et al., 1998) and magnetotelluric data (Jones et al., 2003). Two robust low-velocity features were also imaged lying between the Central Slave Basement Complex and the Hackett river arc. These were speculated to be trapped wedges of seismically slow fertile mantle, which had a lherzolitic composition that differed from the surrounding seismically fast harzburgitic rocks. However, it was noted that more xenolith studies would be required to validate this speculation.

Snyder et al. (2004) published a P-wave tomography model, which incorporated the stations used in tomography modelling by Banks et al. (2000) in addition to the newly acquired POLARIS stations. This produced a model that was more detailed in the Central Slave area while retaining the major features found by Banks et al. (2000) such as higher velocities in the southwest portion of the craton. The new model found a major transition at depths of 170 - 230 km in mantle, which were coincident with the northeast southwest trending G10 garnet mantle domain mapped

by Grütter et al. (1999). Strong lateral variations seen in the north-south cross section suggest that previously mapped mantle discontinuities are not laterally continuous, "but rather the tops and bottoms of irregular blobs" (Snyder et al., 2004). Furthermore, the seismic tomography model did not image laterally continuous layering suggesting that the Slave mantle has finer scale structure than tomographic imaging is able to resolve. However, the lack of layering may also be attributed to poor depth resolution of seismic tomography.

3.2.2 Recent Seismic Tomography Studies

Recently, the highest resolution tomography model of the Slave craton mantle to date was published by Esteve et al. (2019), which improved upon previous contributions by including (1) a higher station density and (2) an S-wave model in addition to a P-wave model of the mantle. The results of Esteve et al. (2019) found alternating patterns of fast and slow anomalies in the Central Slave craton. The Central Slave craton was also found to be relatively slower than the eastern and northern regions of the Craton, which was attributed to prevalent metasomatism in the region. The Lac de Gras kimberlite field was found to overlap with steep V_p and V_s velocity gradients. This correlation was suggested to not be a cause for the Eocene kimberlites, but could possibly be related to kimberlite magma ascent from the asthenosphere. However, it is not clear if this is guaranteed to be related to kimberlite genesis as the Coronation field to the west does not coincide with steep velocity gradients. Lastly, Esteve et al. (2019) did not find any evidence of a sharp LAB due to large vertical smearing in the model.

3.3 Receiver Functions

Seismic body waves are either longitudinal (P-waves) or transverse (S-waves) of which the S wave can be further categorized as S_H (horizontally polarized) or S_V (vertically polarized). When these waves encounter an interface with an isotropic velocity change, a conversion will occur as either S_V to P (Sp wave) or P to S_V (Ps wave). The depth to the interface is determined from the difference in arrival time between the P wave and Ps waves constitute PRFs and similarly the difference in arrival time between S wave and Sp waves constitute SRFs (Selway et al., 2015).

3.3.1 Shear Receiver Functions

Chen et al. (2009) used Ps converted waves to image seismic discontinuities in the lithosphere of the Slave craton. There were two seismic discontinuities observed: (1) The Moho at a depths

ranging between 34 and 41 km along the profile and (2) a mid-lithosphere discontinuity (MLD) at a depth of ~100 km. The MLD only appeared in the SV component of the receiver function and was absent in the SH component suggesting the seismic discontinuity is not a consequence of anisotropy. The shear wave velocity reduction across the MLD was 9 - 21% and appeared to coincide with the Central Slave Mantle Conductor. Chen et al. (2009) interpreted the coincidence of these two features to be the expression of an ancient metasomatic boundary between two subducting plates dating back to the Paleoproterozoic. It was suggested that the metasomatic alteration front concentrated graphite and phlogopite, which may also explain the conductive and seismic boundaries respectively.

3.4 Rayleigh Wave Analysis

Chen et al. (2007) used Rayleigh wave phase and amplitude data collected by the POLARIS broadband seismic network to determine the velocity structure of the upper mantle of the Slave craton. Chen et al. (2007) inverted for periods between 20 and 142 s to produce a 1D phase velocity model and was the most reliable in the depth range of 28 - 200 km.

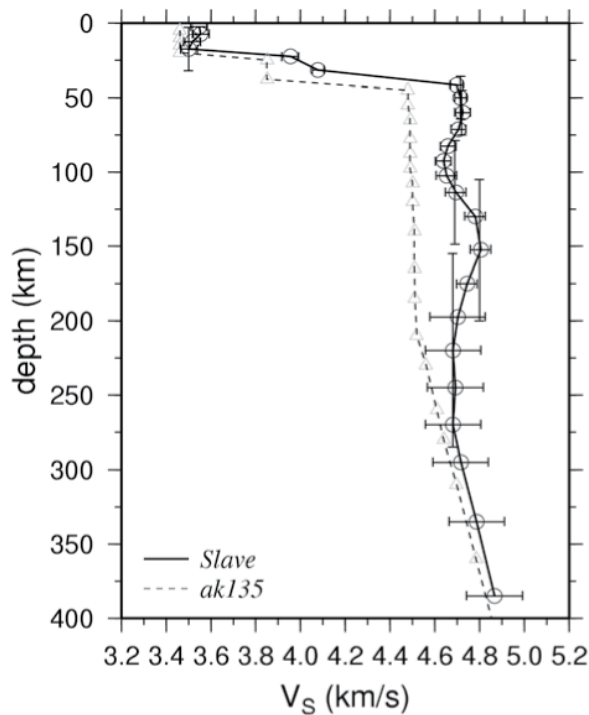


Figure 3.1: 1D velocity model obtained from inverting for Rayleigh wave data. (From Chen et al., 2007). The starting velocity model is marked as a dashed line (ak135).

Chen et al. (2007) found velocities in the cratonic lithosphere of 4.7 ± 0.2 km/s, which extended to depths between 50 and 150 - 200 km. A velocity reduction within the cratonic lid is also visible at the depth of ~ 100 km, but it was found that this feature was highly sensitive to starting parameters and thus was not interpreted. Lastly, a negative gradient was found below the high velocity cratonic lid, which reached a minimum of 4.68 km/s at a depth of ~ 275 km. The reduction in shear wave velocities was inferred to be the base of the lithosphere. However, Chen et al. (2007) noted that their model was unable to resolve features uniquely below the depths of ~ 200 km. For this reason the authors assigned a large uncertainty to their LAB depth estimate of 220 ± 65 km, which is within uncertainty of the 160 - 190 km estimate derived from xenolith studies (Kopylova et al., 1999)

3.5 Gravity Studies

Poudjom Djomani et al. (2005b) mapped the relationship between gravity and topography to obtain effective elastic thickness (T_e) in the Slave craton for the purpose of delineating possible prospective regions for diamond exploration. The Bouguer anomaly map of the Slave craton found anomalies in the range of -20 to 100 mGal with an average value of 50 mGal. High gravity anomalies are restricted to the northwest corner of the Slave province, which coincides with the Mackenzie Plume that penetrated the region at ~ 1.27 Ga. The Slave craton itself is dominated by gravity lows with the most pronounced lows found in the south eastern corner of the craton.

Poudjom Djomani et al. (2005b) combined the Bouguer gravity results with topographic data and inverted for T_e in the Slave craton. T_e values ranged from 20 - 60 km with low values found generally in the Central Slave. A major feature found was a north south trending low in T_e that separated two zones of strong lithosphere on either side. Poudjom Djomani et al. (2005b) noted that the majority of kimberlites in the Slave craton are found over the steep gradient in T_e and suggested that this feature was a major zone of weakness in the lithosphere. Furthermore, it was proposed that the low T_e values represented a suture or zone of weakness that could influence kimberlite ascent pathways and thus mapping such anomalies can add significant value to regional diamond targeting. Lithospheric controls on kimberlite emplacement were further explored by Poudjom Djomani et al. (2005a).

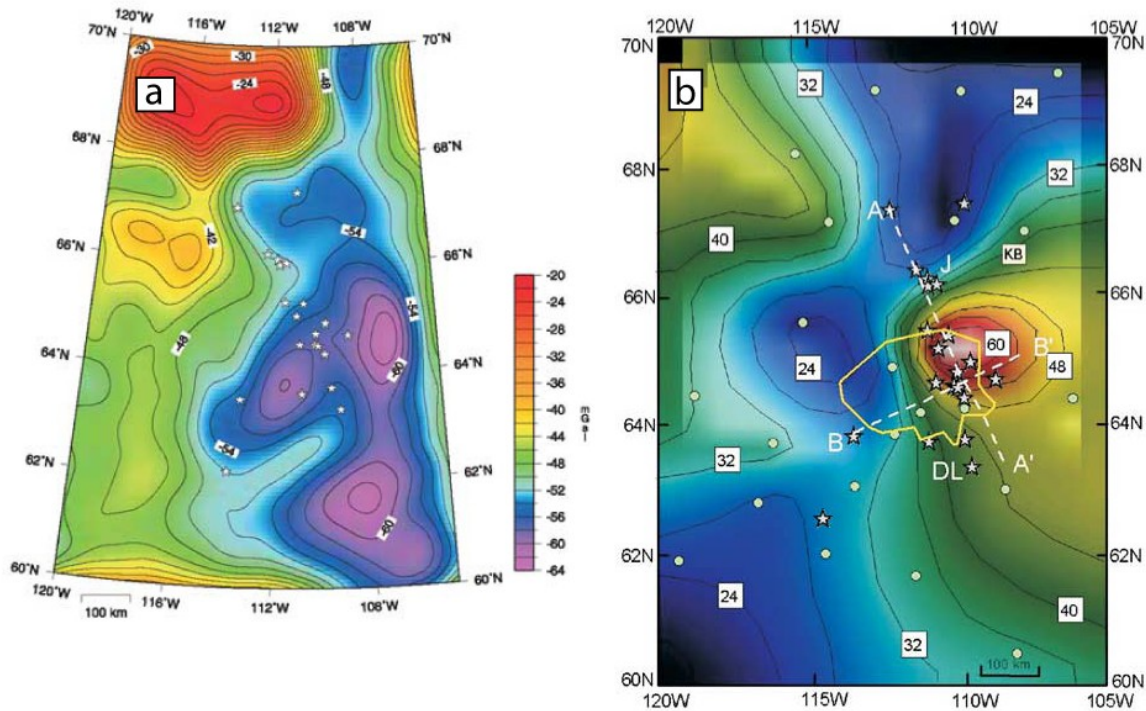


Figure 3.2: (a) Long wavelength Bouguer gravity anomalies in the Slave craton (From Poudjom Djomani et al., 2005a). The gravity data is contoured in milligals where cool colours are gravity lows and warm colours are gravity highs. (b) Contour map of the total elastic thickness obtained from inverting topographic and Bouguer gravity data in the Slave craton (From Poudjom Djomani et al., 2005a). The Central Slave Mantle Conductor described by Jones et al. (2003) is outlined in yellow. Kimberlites are indicated as stars on both maps.

3.6 Aeromagnetic Studies

High quality aeromagnetic data were collected over most of the Slave Province. The results show the majority of the Slave province to be generally homogeneous with the exception of the Thelon Front to the east and the western Slave. The Thelon Front is a magmatic arc and coincides well with a strong magnetic high. To the west of the Thelon Front there is a strong magnetic low, which overlaps with a region of variable geology and thus cannot be correlated with a specific geologic structure. For this reason, the magnetic low is thought to simply be part of a dipolar signal that is a consequence of the magnetic high from the magmatic arc to the east (Thomas, 1992). The western Slave contains pockets of magnetic highs that are attributed to the mineral assemblages found in granulite facies, particularly titanomagnetite which has a high magnetic susceptibility (Pehrsson et al., 2000). Finally, the Mackenzie dykes are visible as linear northwest trending features in parts of the Slave (Percival et al., 2012).

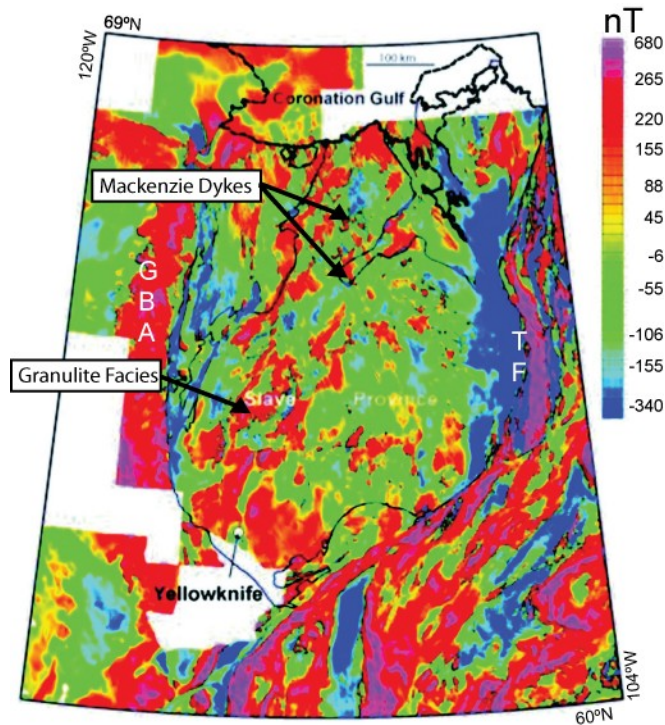


Figure 3.3: Aeromagnetic map of the Slave craton. (From Percival et al., 2012). TF = Thelon Front; GBA = Great Bear Arc.

3.7 Geophysical Methods for Diamond Exploration

Geophysical methods can aid in prospecting for diamonds in two ways: (1) direct detection of kimberlite pipes, which are the source for diamonds or (2) evaluation of lithospheric-scale structure to infer regions that are more conducive to formation of diamonds. The latter has so far been the focus of this thesis and does not need further elaboration as numerous geophysical studies have already been reviewed for regional targeting. Thus, this section will discuss the former and briefly review geophysical methods used for pipe-scale exploration.

Exploration for kimberlites typically begins with programs that bulk sample indicator minerals, which define large prospective regions, but mineral trains rarely terminate at individual kimberlite pipes (Power et al., 2004). Therefore, once a prospective region is found, geophysical surveys are employed to determine the location of individual kimberlite pipes. Since kimberlite rock is a combination of the parent magma and the ingested host rock, it generally has distinct physical properties relative to the host rock which can be measured in geophysical surveys, which can include density, magnetic susceptibility, resistivity and seismic velocities (Power et al., 2004; Kjarsgaard, 2007). Magnetism is usually the first geophysical technique applied for

kimberlite exploration due to its low cost and high sensitivity to near surface structure (Macnae, 1995; Power and Hildes, 2004). Kimberlites are typically seen as magnetic highs, however, depending upon the remnant magnetization it is also possible for the pipes to be magnetic lows or exhibit dipolar responses (Power et al., 2004). The shape of the magnetic anomaly will also vary with latitude where pipes will appear circular in high latitudes and become more asymmetric at latitudes closer to the equator (Keating and Sailhac, 2004). In some cases the magnetite that is responsible for the magnetic signature of the pipe will be weathered extensively to the point that the kimberlite pipe is no longer detectable with magnetic methods (Macnae, 1979). In these cases airborne time domain electromagnetic methods have proven effective for finding kimberlite pipes that would not otherwise have been found using only magnetic methods (Macnae, 1979). Time domain EM is effective because electrical resistivity of kimberlite pipes is typically lower than the surrounding rock as a result of clay alteration in the crater facies allowing for effective kimberlite mapping (Macnae, 1979; Macnae, 1995; Jansen and Witherly, 2004; Power et al., 2004; Fournier et al., 2017). Still, one must be careful when interpreting magnetic and time-domain EM geophysical methods as these surveys can generate false positives. Examples of features that can produce similar geophysical anomalies as kimberlites are boulder trains and topographic depressions filled with glaciofluvial sediments (Power and Hildes, 2007). Once potential targets have been identified using magnetic and time domain methods, higher resolution geophysical methods can be employed to more effectively map the geometry of the prospective kimberlite pipes. Reflection seismic has in some rare cases been applied to image the geometry of kimberlites or dykes. For example, the Snap Lake dyke was delineated to depths of 1200 m using reflection seismic although seismic surveys have not been used extensively in the majority of the Slave craton (Power et al., 2004; Reed and Witherly, 2007). Audiomagnetotellurics have in some rare cases been used to produce 3-D pipe-scale models although this is not a common practice as data acquisition is much slower and laborious than other geophysical techniques (La Terra and Menezes, 2012). However, MT provides the advantage that it can image deeper than other geophysical methods and can more accurately constrain depths with its frequency dependence (see Chapter 4) than potential field methods. Kimberlites have contrasting dielectric permittivity to the surrounding host rock as a result of bound water in overlying clays. Thus, kimberlites will have clear reflective boundaries when conducting a GPR survey (Power et al., 2004). Still it is common for false positives to result

from GPR surveys. Consequently GPR is most effective if used after drill holes have confirmed the presence of kimberlite (Power et al., 2004). The aforementioned geophysical methods all have some degree of non-uniqueness and thus exploration is most effective when two or more geophysical methods are combined for interpretation.

Chapter 4 : The Theory of Magnetotellurics

4.1 Introduction to Magnetotellurics

In the last chapter, previous studies regarding the lithosphere in the Slave craton were reviewed to summarize our current knowledge of the mantle from studies other than magnetotellurics. This chapter will give an overview of the magnetotelluric method in preparation for the discussion of magnetotelluric studies in the Slave craton in chapter 5. The magnetotelluric theory will also provide a framework for the results and interpretations of the electrical lithosphere of the Slave craton discussed in future sections. Magnetotellurics is a passive electromagnetic method used for determining resistivity in the Earth that began with the theoretical formulation first proposed by Cagniard (1953). Magnetotelluric data, once processed, consists of apparent resistivity and phase curves, which act as inputs for inversions. Inversions provide resistivity models of the Earth that are able to reproduce the input data and are used to make inferences about the subsurface geology as resistivity varies by many orders of magnitude in the Earth (e.g., Simpson and Bahr, 2005). This section outlines the magnetotelluric method including the propagation of electromagnetic waves in conductors, the derivation of apparent resistivity and phase curves and conduction mechanisms expected in the mantle.

4.2 Maxwell's Equations

The behaviour of electric and magnetic fields denoted as \mathbf{E} and \mathbf{B} , respectively, can be described in full by Maxwell's four fundamental equations as first formulated by Maxwell (1861). These equations are given below for a conductor that does not contain any free charges in terms of \mathbf{E} and \mathbf{B}

$$\nabla \cdot \mathbf{E} = 0 \quad (\text{Gauss' Law}) \quad (4.1)$$

$$\nabla \cdot \mathbf{B} = 0 \quad (\text{no name}) \quad (4.2)$$

$$\nabla \times \mathbf{E} = -\frac{\partial \mathbf{B}}{\partial t} \quad (\text{Faraday's Law}) \quad (4.3)$$

$$\nabla \times \mathbf{B} = \mu_0 \sigma \mathbf{E} + \mu_0 \epsilon_0 \frac{\partial \mathbf{E}}{\partial t} \quad (\text{Ampere's Law}) \quad (4.4)$$

where μ_0 is the magnetic permeability of free space (H/m), ϵ_0 is the electric permittivity of free space (F/m) and σ is the conductivity (S/m). For magnetotellurics it is assumed that $\mu = \mu_0$ and $\epsilon = \epsilon_0$, which is generally an accurate assumption for materials typically found in the Earth.

Equations (4.1) and (4.2) describe the fields for electrostatic and magnetostatic charge configurations respectively. Gauss' Law (4.1) describes the electric field of static charge distributions. Equation (4.2) simply states that magnetic monopoles have not been observed.

Equations (4.3) and (4.4) describe fields for the more general case of electrodynamics. Faraday's Law (4.3) describes how a changing magnetic field produces a perpendicular electric field. Similarly, Ampere's Law (4.4) describes how a changing electric field produces a perpendicular magnetic field. Thus, these two equations prove that the behaviour of electric and magnetic fields are intrinsically coupled to one another, which naturally leads to the existence of electromagnetic waves (Maxwell, 1861).

4.2.1 Theory of Magnetotellurics of a 1-D Earth

The electric field in Faraday's Law (4.3) is coupled to the magnetic field, however, it can be decoupled by taking the curl of both sides of (4.3) and applying a common vector identity:

$$\nabla \times \nabla \times \mathbf{E} = \nabla(\nabla \cdot \mathbf{E}) - \nabla^2 \mathbf{E} = -\frac{\partial(\nabla \times \mathbf{B})}{\partial t} \quad (4.5)$$

Substituting Ampere's Law (4.4) and Gauss' Law (4.1) into (4.5) yields a modified wave equation

$$\nabla^2 \mathbf{E} = \mu_0 \sigma \frac{\partial \mathbf{E}}{\partial t} + \mu_0 \epsilon_0 \frac{\partial^2 \mathbf{E}}{\partial t^2} \quad (4.6)$$

The form of the solution for the propagating wave is assumed to be harmonic in time thus the solution for $\mathbf{E}(x,y,z,t)$ takes the form of $\mathbf{E}(x,y,z)e^{-i\omega t}$ where ω is angular frequency (rads/s). Substituting the harmonic solution into (4.6) results in

$$\nabla^2 \mathbf{E}(x,y,z) = -i\omega\mu_0\sigma\mathbf{E}(x,y,z) + \omega^2\mu_0\epsilon_0\mathbf{E}(x,y,z) \quad (4.7)$$

Under the conditions typically found in the subsurface the real term in (4.7) can be discarded as it is many orders of magnitude smaller than the imaginary term which simplifies to a diffusion equation of the form

$$\nabla^2 \mathbf{E}(x,y,z) = -i\omega\mu_0\sigma\mathbf{E}(x,y,z) \quad (4.8)$$

Further, the source of electromagnetic waves is assumed to be very far away and thus the wave front can be approximated as being a plane wave, which mathematically is shown as

$$\frac{\partial E}{\partial x} = \frac{\partial E}{\partial y} = 0 \quad (4.9)$$

Secondly, it is assumed that the wave is polarized, which if we consider downward propagation into the earth to be the positive z axis then the electric field simplifies to

$$\mathbf{E} = (E_x, 0, 0) \quad (4.10)$$

Thus, (4.8) simplifies to the second order differential equation

$$\frac{\partial^2 E_x(z)}{\partial z^2} = -i\omega\mu_0\sigma E_x \quad (4.11)$$

where the solution to (4.11) is of the form

$$E_x(z) = E_0 e^{-\sqrt{\frac{\omega\mu_0\sigma}{2}}z} e^{i\sqrt{\frac{\omega\mu_0\sigma}{2}}z} \quad (4.12)$$

Finally, the skin depth of the propagating electric field denoted by δ is defined as the depth where the magnitude is reduced to $1/e$. This can be written as

$$\frac{|E_x(z = \delta)|}{|E_x^s|} = \frac{1}{e} = e^{-\sqrt{\frac{\omega\mu_0\sigma}{2}}\delta} \quad (4.13)$$

and the solution to (4.13) is the skin depth which is

$$\delta = \sqrt{\frac{2}{\mu\sigma\omega}} \approx \frac{500}{\sqrt{\sigma f}} \quad (4.14)$$

such that f is frequency (Hz). Therefore, lower frequencies penetrate deeper into the Earth and higher frequencies attenuate quickly resulting in near surface observations.

4.2.2 Magnetotelluric Impedance of a 1-D Earth

In a 1D Earth the electric and magnetic fields are related to each other by the complex impedance in the form of

$$\begin{bmatrix} E_x(\omega) \\ E_y(\omega) \end{bmatrix} = \begin{bmatrix} 0 & Z(\omega) \\ -Z(\omega) & 0 \end{bmatrix} * \begin{bmatrix} H_x(\omega) \\ H_y(\omega) \end{bmatrix} \quad (4.15)$$

The complex impedances in the off diagonal elements of the impedance tensor are of equal magnitude but opposite signs. From (4.15) the complex impedance can be written as

$$Z_{xy} = \frac{E_x}{H_y} \quad (4.16)$$

The complex impedance then relates the apparent electrical resistivity of the Earth through the following relationship

$$\rho_a = \frac{1}{\omega\mu} \left| \frac{E_x}{H_y} \right|^2 = \frac{1}{\omega\mu} |Z_{xy}|^2 \quad (4.17)$$

The electrical resistivity observed is not the true resistivity of the Earth due to the diffusive nature of the signal, but is rather a weighted average of every layer encountered before the signal attenuates as dictated by the skin depth equation (4.14).

4.2.3 Impedance Phase

When electromagnetic waves propagate in a conductor, the electric and magnetic fields are no longer in phase with each other. Their phase difference is defined by

$$\varphi = \tan^{-1} \left(Z_{xy}(\omega) \right) = \tan^{-1} \left(\frac{E_x(\omega)}{H_y(\omega)} \right) \quad (4.18)$$

The phase lag between the electric and magnetic fields is important for interpretation as decreasing phase corresponds to increasing apparent resistivity and an increasing phase corresponds to a decreasing apparent resistivity. This relationship is also useful for checking the quality of incoming field data as there may be problems if the phase increases with increasing apparent resistivity or vice versa. For 1D and 2-D magnetotelluric data the phase is always in the range $0^\circ \leq \varphi \leq 90^\circ$, however, for 3-D data the phase can exceed these boundaries as a result of galvanic distortion.

4.3 Magnetotelluric Impedance of a 2-D Earth

In the case of a 2-D Earth the impedance can be represented as a second order tensor

$$\begin{bmatrix} E_x \\ E_y \end{bmatrix} = \begin{bmatrix} 0 & Z_{xy} \\ Z_{yx} & 0 \end{bmatrix} \begin{bmatrix} H_x \\ H_y \end{bmatrix} \quad (4.19)$$

In an ideal 2-D geometry the Earth only varies in depth and perpendicular to geoelectric strike. In this case, there exists a rotation angle such that the diagonal components of the impedance tensor are reduced to 0 indicating that only the orthogonal components of the electric and magnetic fields are related. In a real data set the Earth is always 3-D to some extent, however, if the diagonals are small, then it is still reasonable to continue with a 2-D analysis. There are thus

two apparent electrical resistivities describing resistivity parallel and perpendicular to geoelectric strike, which are

$$\rho_{xy} = \frac{1}{\omega\mu} |Z_{xy}|^2 \quad (4.20)$$

$$\rho_{yx} = \frac{1}{\omega\mu} |Z_{yx}|^2 \quad (4.21)$$

These apparent resistivities are formally known as the Transverse Electric (TE) and Transverse Magnetic (TM) modes assuming that the data has been rotated perpendicular to strike.

4.3.1 The Transverse Electric and Transverse Magnetic modes

For a 2-D geometry the electric and magnetic fields can be described by two decoupled partial differential equations

$$\frac{\partial^2 E_x}{\partial y^2} + \frac{\partial^2 E_x}{\partial z^2} + E_x i\omega\mu\sigma(y, z) = 0 \quad (4.22)$$

$$\frac{\partial^2 B_x}{\partial y^2} + \frac{\partial^2 B_x}{\partial z^2} + B_x i\omega\mu\sigma(y, z) = 0 \quad (4.23)$$

Equation (4.22) is the Transverse Electric (TE) mode and (4.23) is the Transverse Magnetic mode (TM). In the TE mode the electric field is parallel to the geoelectric strike direction and is dominated by inductive effects. As a result the TE mode is not very sensitive to resistors because induction does not effectively produce electric fields in resistive bodies. Additionally, inductive effects are frequency dependent and are sensitive to the rate of change of magnetic fields. Thus, inductive effects disappear at low frequencies because the magnetic fields change rate of change is insufficient to produce a measurable electric field.

In comparison, in the TM mode the electric field is perpendicular to the geoelectric strike direction and is dominated by both galvanic and inductive effects. Electric fields are discontinuous at conductive boundaries and therefore cause electric charges build up at the boundaries. As such, the TM mode can sense resistors and conductors effectively because the build up of charges occurs on all boundaries assuming that there is a change in conductivity

across the boundary. Further, charge build occurs at all frequencies including direct current, which differentiates galvanic effects from inductive effects which are frequency dependent.

4.4 Dimensionality Analysis

4.4.1 Rotation of the Impedance Tensor

Magnetotelluric data often requires a rotation after acquisition to ensure the TE and TM modes are orthogonal to one another. The rotation matrix is defined as

$$R = \begin{pmatrix} \cos \theta & -\sin \theta \\ \sin \theta & \cos \theta \end{pmatrix} \quad (4.24)$$

where θ defines the angle of rotation from the original coordinate system xy to the new coordinate system $x'y'$ in the clockwise direction (see Figure 1.1). The rotated impedance tensor in the desired coordinate system $x'y'$ is given as

$$Z' = R^T(\theta)ZR(\theta) \quad (4.25)$$

In a 2-D analysis the rotation angle θ should minimize the diagonal components of the impedance tensor resulting in a decoupling of the TE and TM modes.

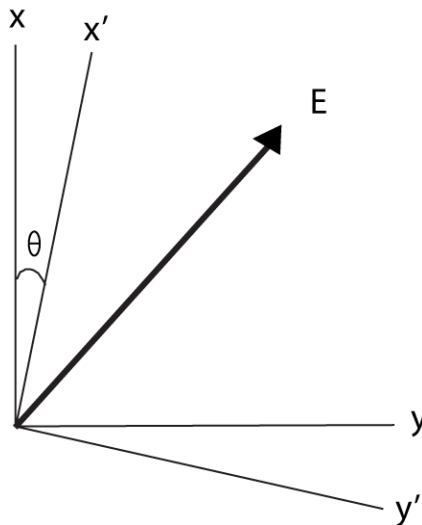


Figure 4.1: The reference coordinate system is denoted by xy and the rotated coordinate system is denoted by $x'y'$. The new coordinate system has been rotated by θ relative to the original coordinate system.

4.4.2 The Phase Tensor

The phase tensor provides an alternate means of determining the geoelectric strike by relying on the phase information instead of the measured impedance as described in previous sections. Caldwell et al. (2004) first developed the phase tensor and proved it is a valuable tool for understanding the dimensionality of the Earth as it is unaffected by galvanic distortion. The complex impedance can be broken down to its real and imaginary components and is defined as

$$Z = X + iY \quad (4.26)$$

where X and Y are the real and imaginary components respectively. Thus, the phase tensor is mathematically defined as

$$\varphi = X^{-1}Y = \begin{bmatrix} \varphi_{11} & \varphi_{12} \\ \varphi_{21} & \varphi_{22} \end{bmatrix} \quad (4.27)$$

The eigenvectors of the phase tensor constitute the major and minor axes of an ellipse giving a geometrical representation to the tensor. A second important property of the phase tensor is the skew, which is defined as

$$\beta = \tan^{-1} \left(\frac{\varphi_{12} - \varphi_{21}}{\varphi_{11} + \varphi_{22}} \right) \quad (4.28)$$

For a 1D Earth the shape of the tensor is a circle and $\beta = 0$ where its radius is related to the conductivity of the Earth. A higher conductivity will result in a larger radius for the circle. In a 2-D Earth the tensor is represented as an ellipse with $\beta = 0$, but for practical purposes a skew angle a β of up to 3° can still be valid for a 2-D analysis (Caldwell et al., 2004; Booker, 2014). However, this is not necessarily sufficient evidence to assume a 2-D geometry because local symmetries in 3-D structures can result in a small skew angle (Booker, 2014). Conversely, a non-zero skew angle can be an indication of 3-D structure. Additionally, assuming a 2-D Earth, the ellipse's major axis is either parallel or perpendicular to the geoelectric strike. Given that the tensor is unaffected by galvanic distortion the phase tensor's orientation is a more robust method for determining the subsurface strike direction than decomposing the impedance tensor (e.g., McNeice and Jones, 2001; Groom and Bailey, 1989). In a 3-D case the tensor is also an ellipse, with $\beta > 0^\circ$ such that the principal axis of the tensor is rotated clockwise by the skew angle (see Figure 1 of Caldwell et al. (2004) for an illustration of the phase tensor).

4.5 Vertical Magnetic Field (Tipper)

By Amperes' Law (4.4) an electric field will generate an orthogonal magnetic field and thus, the electric field flowing along geoelectric strike in a conductor creates a magnetic field about the conductor. The tipper is a transfer function that relates the vertical magnetic field to the two orthogonal horizontal fields' components. This relationship can be written as

$$H_z = [T_{zx} \ T_{zy}] \begin{bmatrix} H_x \\ H_y \end{bmatrix} \quad (4.29)$$

such that T_{zx} and T_{zy} relate the vertical magnetic field to the x and y horizontal components of the magnetic fields. The tipper is has good resolution for the horizontal extent of a conductor, however, it has poor vertical resolution and as such is unreliable for determining depth. The tipper is useful for sensing conductors because the rotating magnetic fields are more easily induced in a conductor rather than a resistor. The tipper is a complex quantity similar to the impedance tensor and the real part of the tipper yields induction arrows where the components are written as

$$I_x = \frac{H_z}{H_x} \quad (4.30)$$

$$I_y = \frac{H_z}{H_y} \quad (4.31)$$

such that the induction vector magnitude is

$$I = \sqrt{I_x^2 + I_y^2} \quad (4.32)$$

The sign of the induction vector will reverse when crossing a conductor where the magnitude of the induction arrow directly above a conductor is zero as the magnetic field has no vertical component. The induction vectors on either side of a conductor will either point towards it (Parkinson convention) or point away from it (Weise convention) depending upon the chosen convention. Thus, displaying induction vectors is most useful in exploration for determining the geometries of linear bodies and can aid in defining their geoelectric strike angle.

4.6 Static Shifts

Static shifts in magnetotelluric data cause the apparent resistivity curves to be shifted by an unknown multiplicative constant that preserves the shape of the curve and the phase, but distorts

the resistivity magnitudes. This phenomenon is caused by measuring a horizontal electric field that is not representative of the regional electric field as a result of localized charge build up on a local heterogeneity is at or near surface (e.g., Jones, 1988). Thus, the measured apparent resistivity of magnetotelluric data is written as

$$\rho_m = s\rho \quad (4.33)$$

where s is the static shift coefficient and ρ is the resistivity of the regional structure of interest. Therefore, the static shifted skin depth equation is

$$\delta = 500\sqrt{spT} \quad (4.34)$$

which if uncorrected will cause the depth of an interface to be wrong by a factor of \sqrt{s} . Therefore, it is important to accurately estimate the static shift coefficients to avoid erroneous interpretations of magnetotelluric data.

4.7 Magnetotelluric Impedance of a 3-D Earth

For a 3-D Earth the impedance is a full tensor given as

$$\begin{bmatrix} E_x \\ E_y \end{bmatrix} = \begin{bmatrix} Z_{xx} & Z_{xy} \\ Z_{yx} & Z_{yy} \end{bmatrix} \begin{bmatrix} H_x \\ H_y \end{bmatrix} \quad (4.35)$$

where all entries are non-zero values. In a 3-D Earth both the parallel and orthogonal components of the electric and magnetic field are related to one another (i.e. the xy and yx components). The diagonals of the impedance tensor are typically noisier, but this is typical behaviour for magnetotelluric data as the impedances are smaller and thus there is a smaller signal to noise ratio than for the off-diagonal components (Simpson and Bahr, 2005). An apparent electrical resistivity corresponding to each component of the impedance tensor and can be written in the general form of

$$\rho_{ij} = \frac{1}{\omega\mu} |Z_{ij}|^2 \quad (4.36)$$

4.8 Mantle Conduction Mechanisms

The mechanism for conducting electricity in materials depends on whether the compound is metallic or non-metallic, its phase (i.e. solid, liquid or gas) and its chemical composition (Chakraborty, 2008). The most common mantle minerals by volume are olivine, orthopyroxene,

clinopyroxene and garnet (Selway, 2014), all of which are ferromagnesian silicates. In these solids, conduction is governed by the migration of point defects that diffuse through the crystal lattice of the mineral (Chakraborty, 2008; Yoshino, 2010; Yang, 2011; Selway, 2014). The point defects can be ions (e.g., Mg⁺), a vacancy or an electron. These conduction mechanisms control the quantity of available charge carriers and their ease of mobility, which in turn controls the conductivity. For conditions in the mantle, minerals act as semiconductors and the conductivity is described by an Arrhenius relation

$$\sigma = \sigma_0 * e^{-\frac{\Delta H}{RT}} \quad (4.37)$$

where σ_0 is an empirical constant, ΔH is the activation enthalpy, R is the ideal gas constant and T is the temperature (K). The Arrhenius relations find temperature and composition (related to activation enthalpy) to be the dominant parameters that control conductivity. If multiple conduction mechanisms are present, then the net effect is the superposition of each mechanism

$$\sigma = \sigma_1 * e^{-\frac{\Delta H_1}{RT}} + \sigma_2 * e^{-\frac{\Delta H_2}{RT}} + \sigma_3 * e^{-\frac{\Delta H_3}{RT}} \quad (4.38)$$

where $\sigma_{1,2,3}$ and $\Delta H_{1,2,3}$ are the empirical constants and activation enthalpies for their respective conduction mechanisms (Yoshino et al., 2009; Yang, 2011). Thus, the summation of the contribution from each type of point defect yields the bulk conductivity, however, only certain mechanisms will dominate in specific temperature ranges as a result of their differing activation energies (Yoshino et al., 2009; Yoshino, 2010; Selway, 2014). Additionally, since conduction mechanisms are related to composition, inferences can be drawn from the bulk conductivity structure in the Earth (e.g., The Central Slave Mantle Conductor) assuming the in-situ pressure and temperature are known. The following section provides an overview of conductivity mechanisms that commonly occur in mantle minerals, which are (1) ionic conduction via the diffusion of ions, (2) polaron hopping via electron hopping and (3) proton conduction.

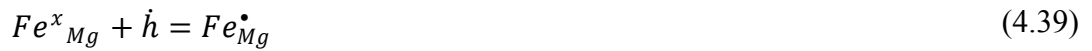
4.8.1 Ionic Conduction

Yoshino (2010) describes ionic conduction in mantle minerals to be facilitated by the creation of cation vacancies (usually from the removal of a magnesium or iron ion) that migrates through the crystal lattice. These vacancies are only able to diffuse assuming that there is a sufficiently high activation energy for the vacancy to overcome its energy barrier. Consequently, ionic conduction

only becomes the dominant conduction mechanism at high temperatures (typically greater than 1000 °C) (e.g., Schilling, 1997) because it requires a large activation energy (~2 eV) for the cation vacancies to escape their respective energy well (see Chakraborty (2008) for a discussion of the role of potential wells).

4.8.2 Small Polaron Hopping

Yoshino (2010) outlines polaron hopping as a conduction mechanism where electrons are exchanged between the ferrous and ferric iron (Fe^{2+} and Fe^{3+} respectively) (see Figure 3 from Yoshino (2010) for the shape of a polaron structure). This can be written succinctly as



where Fe_{Mg} indicates a ferromagnesian ion, \dot{h} is an electron hole, the x indicates a neutral charge and the \bullet represents a positive charge. When a ferrous iron transforms to a ferric iron by receiving an electron, it creates a region with excess positive charge that induces repulsive forces on nearby cations and attractive forces on nearby anions. This contrasts the behaviour of metals where removing an electron creates a “vacuum” that attracts surrounding charge carriers (Chakraborty, 2008). The net effect of the disturbance from the presence of excess positive charge in the lattice produces a “small polaron” structure. The strains induced by the small polaron structure cause an increase in the activation energy and hinders the mobilization of the electrons. Consequently, the activation energy for small polaron hopping is relatively high (> 1 eV) but smaller than the required energy for ionic conduction. The degree of small polaron conduction in ferromagnesian minerals in the mantle is thus controlled by the quantity of iron and the ratio of $\frac{Fe^{3+}}{Fe^{2+}+Fe^{3+}}$ which tends to increase with increasing oxygen fugacity.

4.8.3 Proton Conduction

Proton conduction is the process in which “charge transfer occurs by proton hopping amongst point defects” (Yoshino, 2010). Yoshino (2010) described protons as highly mobile in solids owing to their low bonding energy and their size, which is significantly smaller in comparison to magnesium or iron ions that carry charge in ionic conduction. The combination of these traits permits for relatively unrestricted motion of protons in solids and consequently this mechanism has the lowest activation energy (< 1eV) compared to the previously mentioned polaron hopping

(> 1 eV) and ionic conduction (>2 eV). Hence, proton conduction is the dominant mechanism in olivine at low temperature (< 1000 K) (Yoshino et al., 2009; Yoshino, 2010). Additionally, Karato (1990) proved that even trace amounts of water (a source of protons) can significantly enhance conductivities of olivine in the mantle. Therefore, proton conduction in hydrous mantle minerals is important to consider because (1) mantle minerals have the ability to store water in their crystal lattices (Kohlstedt, 1996), which changes their electrical properties and (2) it is the dominant mechanism in typical cratonic lithospheric conditions (Selway, 2014).

4.8.4 Sources of Enhanced Mantle Conductivity

The Central Slave Mantle Conductor is orders of magnitude more conductive than the surrounding lithosphere beneath the Slave craton. As such, an additional conducting phase must be present that is not found elsewhere in the lithosphere of the Slave craton. There are four categories of conducting phases that could raise the conductivity of the mantle appreciably compared to the country rock: (1) dissolved water in nominally anhydrous minerals (NAMs), (2) grain boundary graphite or sulphides, (3) hydrous minerals (e.g., phlogopite or amphibole) or (4) free fluids such as brines or melts. These conduction mechanisms will be considered in more detail in the interpretation section in Chapter 8.

4.9 Mixing Laws

Magnetotellurics infers bulk resistivity, which is a weighted average of the contribution of all conducting phases in the Earth at a given depth. Thus, a means of estimating the bulk conductivity of mixtures of conducting phases is required for quantitative interpretation of conductors in the mantle. The bulk conductivity of a mixture of two phases can be modelled by Archie's Law (Archie, 1942) and in a system with more than two conducting phases can be modelled using the more robust multiphase Archie's Law (Glover, 2010). These bulk resistivity models are discussed in the following sections of this thesis.

4.9.1 Archie's Law

Archie (1942) formulated a relationship between the saturation of oil in sandstone and the bulk resistivity of the rock. This relationship is known as Archie's Law and is given as

$$\rho = \rho_w S^{-n} \varphi^{-m} \quad (4.40)$$

where ρ is the bulk resistivity, ρ_w is the resistivity of the conducting phase, S is the saturation defined as the fraction of pore space filled with the fluid, n is the saturation exponent, ϕ is the porosity and m is the cementation factor which is typically between 1 and 2. Archie's law was originally derived for determining the saturation of oil in a rock, however, it can also be used to model the bulk resistivity of an arbitrary conducting phase (e.g., partial melt) within a rock in a two phase system. It should be noted that Archie's Law is invalid at low porosities, in the presence of clay as clays or if there is conduction through the grains of the rock. In these circumstances a different means of modelling bulk resistivity is required such as the multiphase Archie's Law (Glover, 2010).

4.9.2 The Multiphase Archie's Law

The multiphase Archie's Law (Glover, 2010) describes the bulk resistivity of an arbitrary number of conducting phases which is given as

$$\sigma_{\text{bulk}} = \sum_{i=1}^N \sigma_i \phi_i^{m_i} \quad (4.41)$$

where N is the number of phases, ϕ_i is the volume percent of the phase, m is a coefficient bound by $1 \leq m \leq 2$ representing the degree of interconnection in the material and σ_i is the conductivity of the phase. The extremes of m represent a parallel circuit and a series circuit for $m = 1$ and $m = 2$ respectively while intermediate values represent intermediate degrees of interconnection. Thus, (4.41) can be used in a forward modelling exercise to relate the bulk conductivity of the Earth to the required proportions of conducting phases that are in the mantle. These predictions are of course predicated upon being correct about the conducting phases present, however, this issue can be constrained using petrological studies from xenoliths (e.g., Pearson et al., 1999) and models of seismic velocity (e.g., Chen et al., 2009).

4.10 Summary

The magnetotelluric method uses measurements of naturally occurring electromagnetic waves to determine a model of the resistivity structure of the Earth. Naturally occurring materials have conductivities that vary by many orders of magnitude, which help to constrain interpretation of subsurface geologic structures. Thus, combining resistivity values obtained from magnetotelluric inversions with an understanding of conduction mechanisms in the mantle allows for inferences to be made regarding conducting phases and lithospheric scale structure.

Chapter 5 : Magnetotelluric Data and Previous Studies in the Slave Craton

5.1 Introduction

The previous chapter reviewed the theory of magnetotellurics, which provides the background to understand previous magnetotelluric (MT) studies, which will be the focus of this chapter. Chapter 5 begins with an overview of the MT data previously collected in the Slave craton, and is followed by a review of the previous publications on magnetotelluric data in the Slave craton. Reviewing these studies is important for (1) understanding what is currently known about the resistivity structure of the Slave craton and (2) identifying areas which are not well understood and may need additional data collection. This includes a review of previous studies and interpretations of the Central Slave Mantle Conductor (CSMC), which is of particular interest due to its spatial coincidence with the Lac de Gras kimberlite field. At the end of this chapter, the areas that need further work are highlighted which provides the motivation for the remainder of this thesis.

5.2 Magnetotelluric Data

The available MT data is a combination of legacy data collected by the Slave Northern Cordillera Lithospheric Evolution (SNORCLE), a component of the LITHOPROBE project, which collected MT data over all of Canada (Jones et al., 2001a; Jones et al., 2003) and the Slave to Bear Province (S2B) profile that crossed the Wopmay orogen (Spratt et al., 2009). The S2B data consists of 20 broadband MT (BBMT) sites with the data from every fourth BBMT station being merged with a long period MT (LMT) station to provide deeper soundings. The SNORCLE data is a combination of three different MT surveys conducted between 1996 and 1999, which are described by Jones et al. (2003).

- The first MT survey consisted of BBMT stations collected along an east-west, all-weather road beginning near Yellowknife and ending in the southeastern region of the Slave craton.
- The second survey collected LMT sites by float plane and helicopter in the southeast portion of the craton.
- The last survey deployed lake bottom LMT sites, which recorded for one year to obtain high-quality data up to periods of ~8000 s.

The total number of MT stations is 147 with 127 from SNORCLE and 20 stations from the S2B profile. Figure 5.1 shows the data distribution and bandwidth for each magnetotelluric survey. In total, 92 stations out of 147 were used in the final 3-D inversion model, which is discussed in greater detail in Chapter 7. The reduction in stations was required to produce the highest quality model inside the craton boundaries over the area of interest that is, the diamondiferous kimberlite fields.

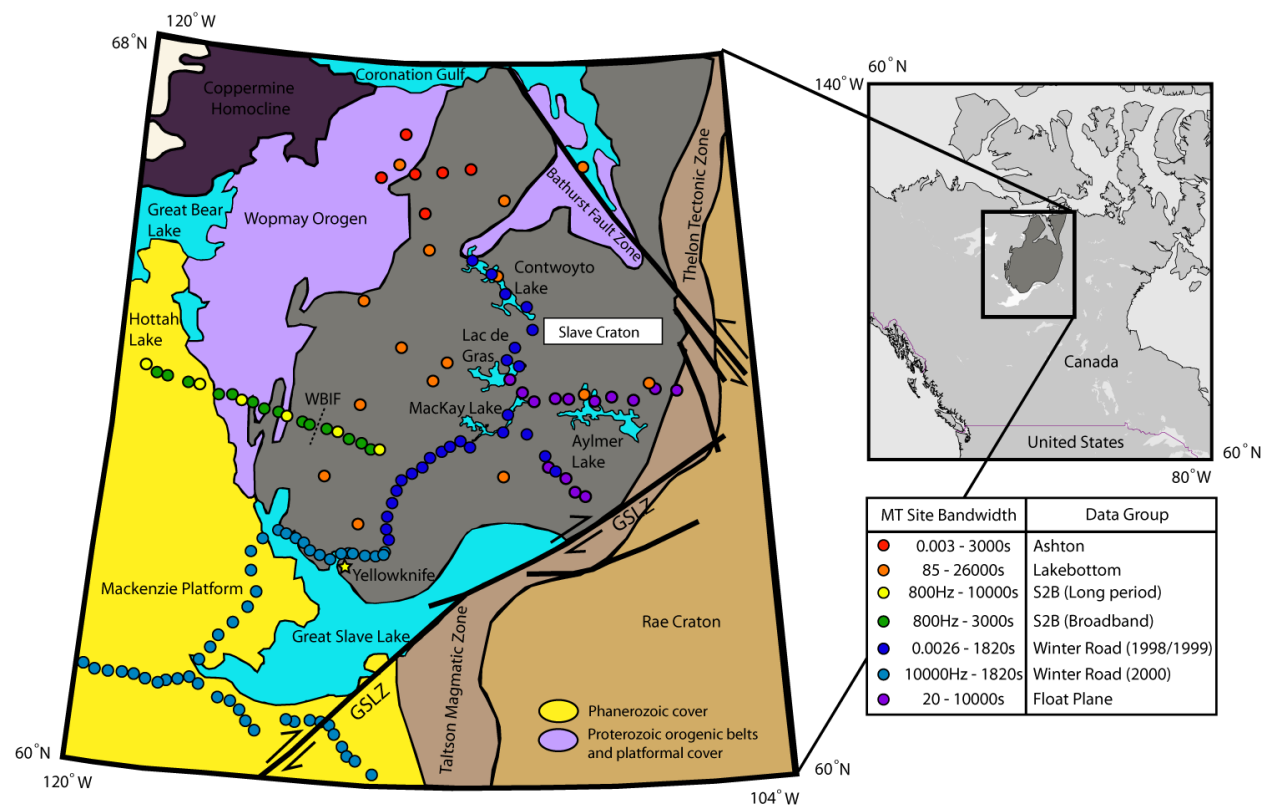


Figure 5.1: The distribution of magnetotelluric surveys in the Slave craton and their associated bandwidths. WBIF = West-Indin Bay Fault. GSLZ = Great Slave Lake Shear Zone.

5.3 LITHOPROBE Studies and SNORCLE Data

The first MT data in the Slave craton were collected during LITHOPROBE's SNORCLE (Slave northern Cordillera lithospheric evolution) program in the late 1990s as previously discussed. These early magnetotelluric studies were significant for delineating three key features: (1) the electric Moho, (2) the depth to the electric lithosphere-asthenosphere boundary (LAB) and (3) the Central Slave Mantle Conductor. These findings will be discussed in detail in the following section.

5.3.1 The Electric Lithosphere Asthenosphere Boundary

Jones et al. (2003) averaged the MT responses from 138 sites on the Slave craton to obtain a representative 1-D average phase and apparent resistivity response curve. Skin depth arguments suggested that the depth of penetration for the model would be greater than 300 km, which is sufficient to fully penetrate the lithosphere and determine the depth of the asthenosphere. Smooth and sharp boundary resistivity models were fit to the average responses curves to determine the depth of the lithosphere asthenosphere boundary. Both models found the LAB to occur at a depth of 260 km. This was in agreement with the petrologically-defined LAB depth of 260 km in the southern portion of the Slave craton (Kopylova et al., 2002), but much greater than petrological estimates in the northern part of the Slave craton of 190 - 200 km at Jericho (Kopylova et al., 1997) and Lac de Gras (Pearson et al., 1999). The discrepancy in LAB depth between MT and xenolith estimates of the LAB depth was suggested to be a result of the majority of the MT stations being in the southern portion of the Slave craton where the lithosphere is thicker which would thus bias the thickness obtained from the 1-D model upwards.

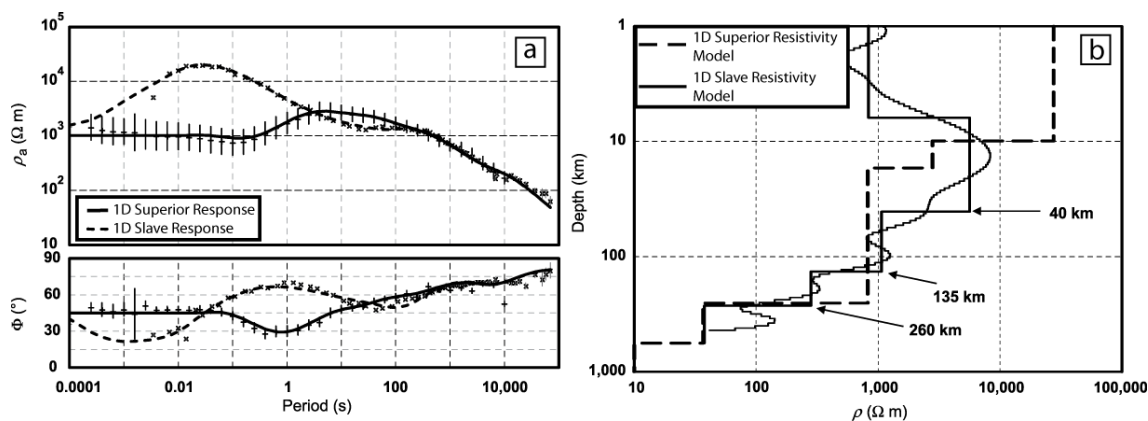


Figure 5.2: (a) 1-D average responses of the Slave craton (dashed line) and for comparison the MT responses obtained by Schultz et al. (1993) (pluses) for the Superior Craton for their 1-D resistivity model. (b) 1-D best fit resistivity models for the average response curves. The solid black line is the layered Earth model, the light solid line is the smooth Earth model and the thick dashed line is the layered Earth model that fit the response curves for Schultz et al. (1993). (Modified from Jones et al., 2003).

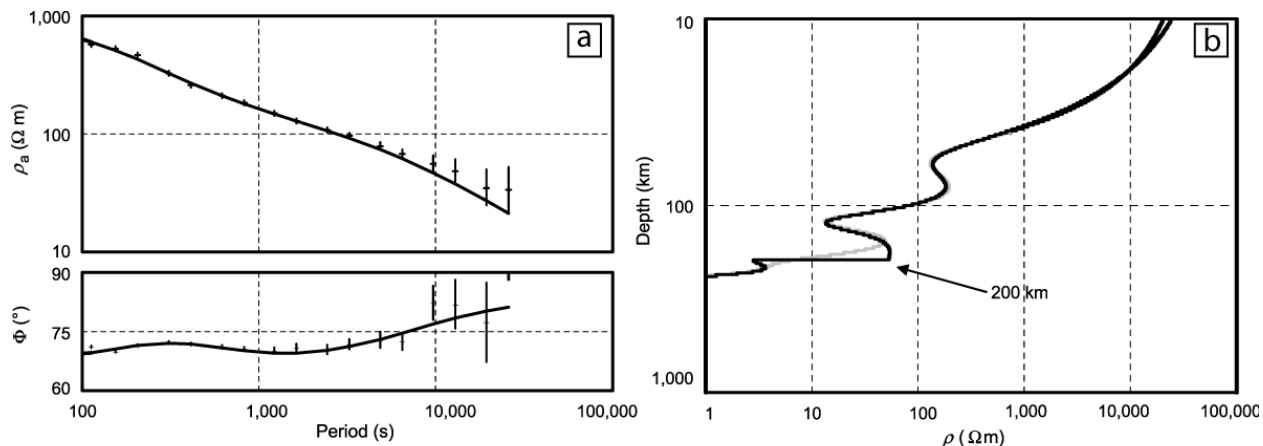


Figure 5.3: (a) MT response curves obtained from the lake bottom MT station at Lac de Gras. The smooth black line is the model response and the black dots are the measured MT data. (b) The best fit smooth resistivity models for the data. One model is smooth over its entirety while the other model allows for a tear in the resistivity at the base of the lithosphere (200 km). (Modified from Jones et al., 2003).

Jones et al. (2003) obtained a second estimate of the depth to the LAB in the northern part of the Slave craton by fitting a 1-D resistivity model to the response curve from a lake bottom MT site collected at Lac de Gras. Other available MT sites were not used because they did not record sufficiently long periods to penetrate through the underlying CSMC to sample the asthenosphere. In comparison, the lake bottom site recorded data for one year and yielded high-quality data up to ~ 8000 s, which was sufficient to sample depths of $\sim 250 - 300$ km. Two resistivity models were fit to the response curve: one of which was continuously smooth while the other had a tear in the resistivity at the petrologically defined LAB (~ 200 km). The smooth model based upon Parker's D+ placed the depth to the LAB at 210 km, which is similar to the petrologically defined depth of 200 km (Pearson et al., 1999).

5.3.2 The Electric Moho

Jones and Ferguson (2001) inverted MT data collected in the southwest corner of the Slave craton for frequencies in the range of 1000 - 0.01 Hz. The MT data were fit to a 1-D conductivity model and it was found that the data was best fit with a four-layer model. The first layer was ~ 1 km thick with low conductivity followed by a second layer with higher conductivity that extended from depths of 2-3 km. The third layer was highly resistive ($> \sim 40000 \Omega \cdot m$) and the last layer was moderately resistive with a resistivity of $\sim 4000 \Omega \cdot m$. The boundary between the third and fourth layer was found to be at a depth of 35.8 ± 1.4 km, which is consistent with Moho

depths found from previous seismic reflection (Cook et al., 1999), refraction (Viejo et al., 1999) and teleseismic (Bostock, 1998) studies in the region. Thus, Jones and Ferguson (2001) concluded that the interface corresponded to the Moho, which was a significant finding for the LITHOPROBE initiative since a change in resistivity at the same depth as the seismically defined Moho had not been observed anywhere else in the world at the time. The non-conducting lower crust ($\sim 40000 \Omega\text{m}$) in the Slave craton allows for the subtle electrical contrast between the crust and mantle to be visible.

5.4 The Central Slave Mantle Conductor

5.4.1 2-D Resistivity Models

Jones et al. (2003) constructed four 2-D resistivity profiles from the MT data collected on the Slave craton. A map view of the profiles and their associated resistivity sections are shown in Figure 5.4. Profile 1 is 150 km long and is located in the southwest corner of the Slave craton with Yellowknife roughly in the centre of the profile. Profile 2 consists of four individual segments that are stitched together that follow a winter road that start at the end of Profile 1 in the southern part of the Slave craton, passes through the Lac de Gras region and then ends in the north following Contwyto Lake in a northwest direction. Profile 3 is in the southeast part of the Slave craton and profile 4 runs directly east starting from the northern part of Aylmer Lake and ends at the eastern most edge of the craton.

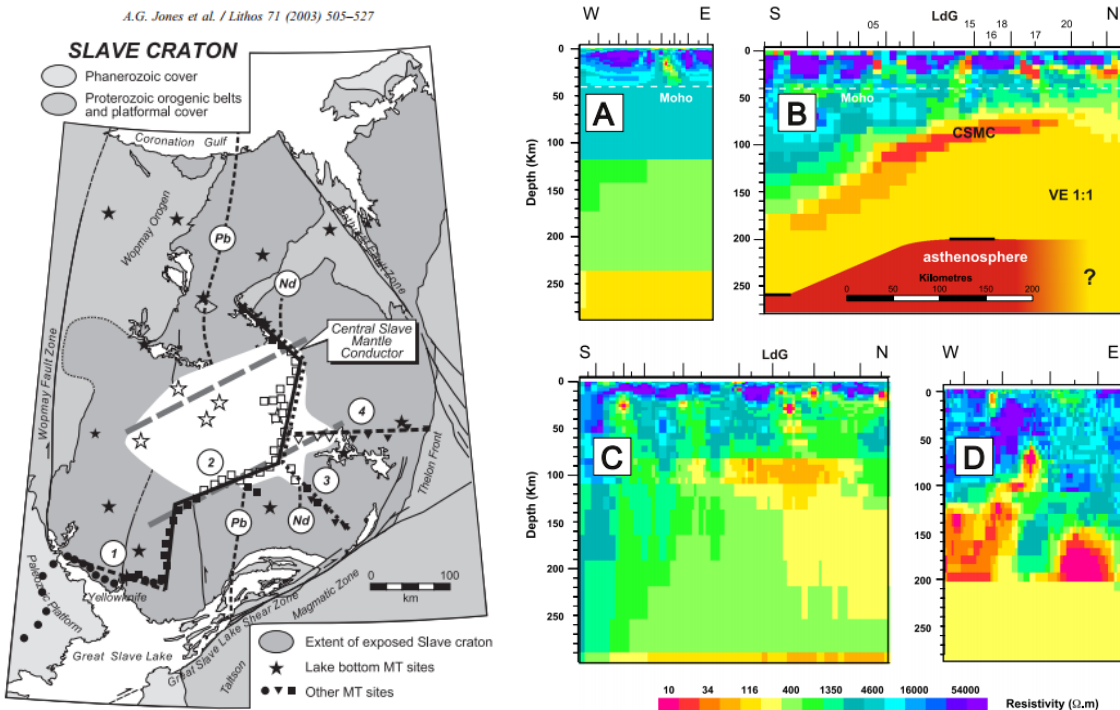


Figure 5.4: Magnetotelluric sites collected on the Slave craton with profiles 1, 2, 3 and 4 corresponding to profiles A, B, C and D (Adapted from Jones et al., 2003).

Profile 1 has a crustal conductor that may be associated with mineralization. The crust and mantle were found to be highly resistive and a crustal discontinuity that is visible was interpreted to be the electric Moho as discussed previously by Jones and Ferguson (2001). The LAB is also visible at 250 km depth, which is in agreement with the depth found by 1-D modelling.

Profile 2 shows the Central Slave Mantle Conductor (CSMC), which is at depths of 80 - 100 km and has a resistivity of no greater than $\sim 30 \Omega m$. The asthenosphere drawn on Profile 2 was not imaged in the resistivity model due to the strongly attenuating CSMC, but is based upon 1-D modelling from the Lac de Gras lake bottom site as discussed previously.

Profile 3 found a conducting anomaly at similar depths to Profile 2, which is also interpreted to be part of the CSMC.

Profile 4 found evidence for a deep mantle conductor on the far east side of the line, but it was interpreted to be an artefact based upon the induction vectors for the eastern sites presented by Jones et al. (2001b).

5.4.2 A 3-D Resistivity Model of the Slave Craton

Jones et al. (2003) presented a preliminary 3-D resistivity model using a trial and error approach to fit observed MT data and magnetic transfer functions. Only select MT stations were chosen as inputs for the model and there were plans to construct a 3-D model using all available data in the future. Forward modelling found that a NE-SW trending conductor fit the data well, particularly at long periods (>1000 s). The NE-SW trending conductor can be identified as the CSMC, which corroborates the results of the 1-D and 2-D modelling that were also completed by Jones et al. (2003). Jones et al. (2003) also compared the data fits when placing a $50 \Omega\text{m}$ halfspace or a $500 \Omega\text{m}$ halfspace beneath the preferred model at a depth of 230 km. It was found that the $50 \Omega\text{m}$ halfspace gave a superior data fit suggesting that mantle resistivity decreases at this depth, which is consistent with the transition to the asthenosphere. These results agree within error for the depth to the asthenosphere found in 1-D modelling.

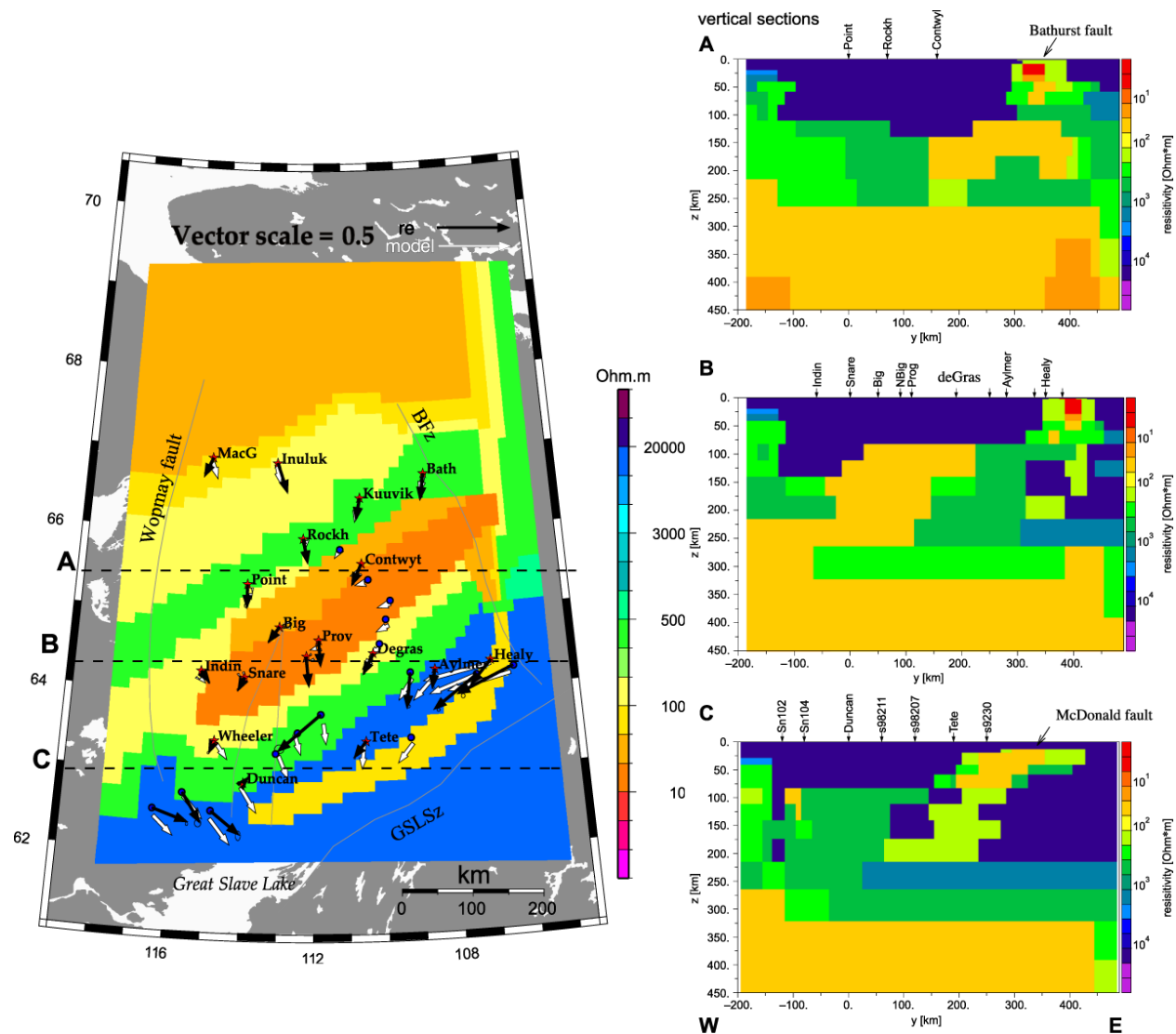


Figure 5.5: On the left hand side is a horizontal slice of the 3-D resistivity model at 140 km depth. The solid black arrows are observed induction vectors and the white arrows are calculated induction arrows. The induction arrows plotted are for a periods of 620 s. On the right hand side are three vertical slices through the 3-D model along profiles A, B and C. (Adapted from Jones et al., 2003).

5.4.3 Central Slave Mantle Conductor Interpretation

As mentioned in previous sections, the Central Slave Mantle Conductor (CSMC) was discovered beneath the Lac de Gras kimberlite field with a resistivity no greater than $30 \Omega\text{m}$ (Jones et al., 2001a; Jones et al., 2003). A spatial overlap between the ultra-depleted hazburgitic mantle domain mapped by Griffin et al. (1999) and the G10 garnet geochemical zone mapped by Grütter et al. (1999) was also found to coincide with the CSMC. Considering the coincidence of these features, Jones et al. (2003) interpreted the CSMC to be of an ancient origin and related to the

subcretion of exotic lithosphere at approximately 2630 Ma (see Davis et al. (2003) for more detail on this interpretation). Thus, the origin of the conductor was not attributed to recent kimberlite magmatism in the Eocene. It was proposed that large volumes of carbon would have been subducted in this process, which could lead to graphite films being deposited during the construction of the Slave craton in the Neoproterozoic (~2.7 Ga). Further evidence for graphite was taken from the rapid increase in resistivity beneath the CSMC, which was interpreted to be the transition from conductive graphite to diamonds which are highly resistive. Jones and Craven (2004) further proposed that regional diamond exploration should focus on regions with (1) old lithosphere, (2) thick lithosphere and (3) lithosphere that is abundant in carbon. It was further suggested that regions in the upper mantle with high conductivity may be more prospective for diamond exploration as these areas have more carbon (in the form of graphite), which is required to form diamonds. However, it was noted that the prospectivity of these regions would still be predicated upon kimberlites reaching the surface.

5.5 The Slave to Bear Province (S2B) Profile

The MT data in on the S2B profile were collected approximately 10 years after the SNORCLE data set. The goal of the S2B survey was to delineate the electrical structure of the lithosphere of the transition between the Wopmay orogen, which includes the Hottah Terrane and the Slave craton to the east. Spratt et al. (2009) produced a resistivity model for the entire profile (Figure 5.6) and also combined three focussed resistivity models that provided higher resolution for crustal structures (Figure 5.7).

5.5.1 S2B: Slave Crustal Structure

Spratt et al. (2009) found the crust-mantle boundary of the Slave craton to be at a depth of 32 – 35 km. The electrical boundary between the upper mantle and the crust is typically not visible due to conducting phases in the crust masking the subtle contrast between the two layers, but the Slave craton crust is highly resistive allowing for the subtle contrast to be detected (e.g., Jones and Ferguson, 2001). The inversions also revealed two notable crustal-scale conductive structures: the first conductor was situated beneath site 008 while the second conductor was situated slightly west of site 006 and dipped east to a depth of at least 30 km (see Figure 5.7). The conductor beneath site 008 was highly localized and shallow extending to only ~2 km in depth with a resistivity of ~10 Ωm . Spratt et al. (2009) noted that metasedimentary rocks could

be an explanation for the anomaly. However, the conductor is limited to a small area while metasedimentary rocks were widespread in the region. The inconsistency between metasedimentary coverage and the extent of the conductor were used as evidence to reject this conduction mechanism. The preferred explanation for the conductor was a localized structure of interconnected sulphides, which provided a more likely explanation considering the size of the feature. The second conductor below site 006 has a resistivity of ($\sim 10 \Omega\text{m}$) in the upper 10 km but extends to depths of at least 30 km where its resistivity decreases to $\sim 100 - 300 \Omega\text{m}$. Spratt et al. (2009) found that the location of the edge of the conductor near surface coincided with the West-Bay-Indin fault zone and for this reason it was suggested that sulphide mineralization may have occurred along the fault plane. This could explain the reason for enhanced conductivity being visible deep into the crust as mineralization would occur along the whole extent of the fault.

5.5.2 S2B: Slave Mantle Structure

The Slave craton upper mantle was found to be highly resistive and the most westward part of the Slave mantle did not coincide with the Wopmay fault zone, but rather was 50 km west of the fault. This suggests that the Slave mantle was underthrust beneath the Wopmay orogen and that a decoupling between the crust and mantle has occurred. Secondly, there was no evidence of the Central Slave Mantle Conductor, which was found further east underneath the Lac de Gras kimberlite field (Jones et al., 2001a; Jones et al., 2003). As such, it was suggested that the western boundary of the CSMC lies further east than the eastern edge of the S2B profile. Spratt et al. (2009) remarked that the absence of the CSMC may have implications to regional diamond exploration, but the role of upper mantle conductors is still not clear as the Kaapvaal Craton has many of the world's premiere diamond mines and does not have a similar conductor.

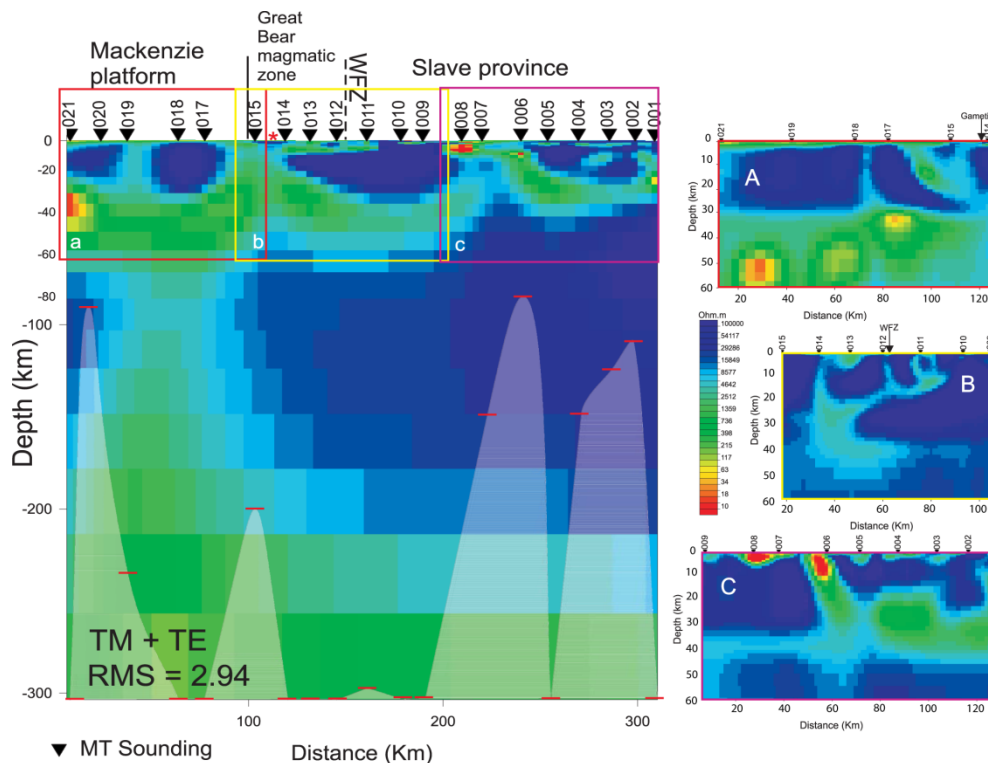


Figure 5.6: On the left hand side is the resistivity model for the whole S2B profile to depths of ~300 km with faded out regions representing the depth of maximum penetration beneath a given site. On the right hand side are the preferred models for three focussed inversions that used a finer discretization to increase resolution in the upper 60 km of the model. The extent of the focussed inversions relative to the model for the whole S2B profile is indicated by the red, yellow and magenta boxes respectively. Modified from Spratt et al. (2009).

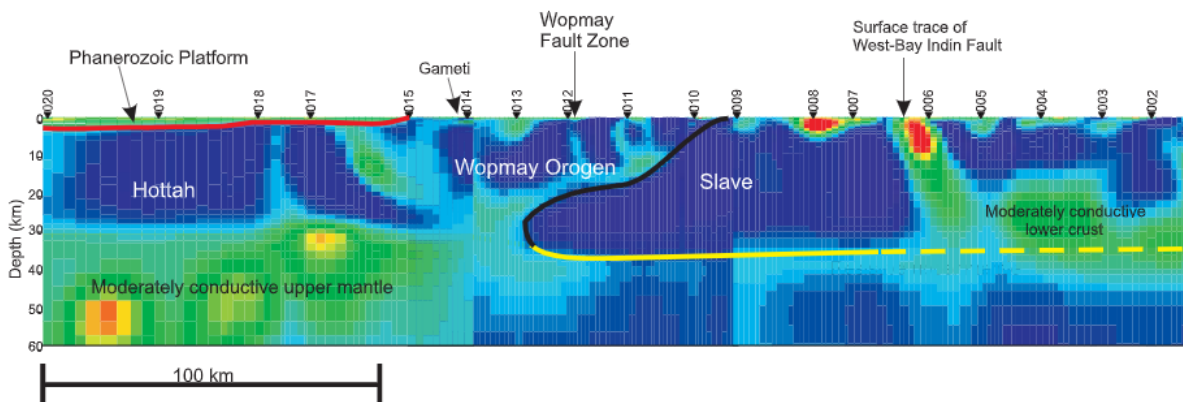


Figure 5.7: The interpretation of the three focused inversions spliced together for the upper 60 km of the S2B profile. The red line shows the depth extent of the Phanerozoic sedimentary cover and the yellow line marks the crust mantle boundary. (From Spratt et al., 2009).

5.6 3-D Inversion of the Slave Craton Magnetotelluric Data

Snyder et al. (2014) produced a 3-D MT model of the Slave craton by inverting only the off-diagonal components of the impedance tensor for 53 MT sites from the data collected in earlier MT studies (Jones et al., 2003; Spratt et al., 2009). Their model found three regions of anomalously high conductivity ($< 10 \Omega\text{m}$) in the Slave lithosphere. The largest anomaly lies beneath Aylmer Lake and Lac de Gras in the east - central craton which at its shallowest is 52 km and at its deepest is 102 km. This is the Central Slave Mantle Conductor described by Jones et al. (2003). The second anomalous zone is 200 km north of Lake Contwyto and underlies the Jericho mine at a depth of 80 km. The third anomaly was found east of Yellowknife at a depth of 85 - 100 km at 64° N latitude. As a whole, the Slave craton exhibited enhanced conductivity at depths of 100 - 120 km in the model, which was taken as evidence of extensive metasomatic overprinting of primary lithospheric structures.

Snyder et al. (2014) rejected graphite as an interpretation for the Central Slave Mantle Conductor as oxygen fugacity trends documented in mantle xenoliths from beneath the Lac de Gras field were too oxidizing for graphite to be stable shallower than ~ 135 km depth (Creighton et al., 2010). The mantle below Lac de Gras has anomalously high $\text{Fe}^{3+} / \text{Fe}^{2+}$ ratios which were imparted by the passage of oxidizing fluids. It was noted that there is not any experimental data on olivine subjected to oxidizing fluids that can explain a nominal value of $10 \Omega\text{m}$, however, these resistivities are consistent with a small polaron hopping mechanism. It was further speculated that olivine exposed to highly oxidizing fluids could increase conductivity, but there were no existing laboratory experiments to support this hypothesis.

5.7 A Case Study of the CSMC in the Slave Craton

Selway (2014) gave an extensive review on the causes of enhanced conductivity in tectonically stable regimes and considered the CSMC in the Slave craton as a case study. It was argued that there were only two possible mechanisms in cratonic lithosphere that could appreciably raise conductivity: (1) conduction through grain boundary graphite and (2) semi-conduction through nominally anhydrous minerals (NAMs). Selway (2014) noted that the depth of the CSMC was 80 - 100 km and at these depths hydrogen diffusion in NAMs is unable to account for the observed resistivity of $\leq 30 \Omega\text{m}$ and thus graphite was argued to be a more likely conduction mechanism. However, the previous genetic relationship and Archean age attributed to the CSMC and the ultradepleted zone in the central Slave craton by Jones et al. (2003) was

found to be problematic as depleted zones are by definition poor in carbon, which is required for the formation of graphite films. Additionally, temperatures in the upper mantle during the assembly of the Slave craton in the Archean would have been too high to be conducive to the formation of graphite films. Thus, the Archean age and subduction origin of the CSMC in previous interpretations was rejected.

An alternative explanation was proposed where the conductor was the result of more recent kimberlite magmatism. Kimberlites and carbonatites are spatially and temporally related to one another and carbon-rich fluid inclusions have been observed in the central Slave craton. Studies have shown that such melts are able to entirely wet grain boundaries owing to their low interstitial angles and will release carbon as vapour at depths of 80 -100 km, which is in the range of the CSMC. These melts are also known to deposit grain boundary graphite films and thus it is possible that carbon-rich melts related to recent kimberlite eruptions in the central Slave craton deposited graphite films in the depth range of 80 -100 km. Selway (2014) suggested that the source of the carbon could still be from subduction as proposed by Jones et al. (2003), however, this carbon became remobilized during kimberlite emplacement rather than being deposited concurrently with subduction events.

5.8 Future Work

Considering the previously discussed MT studies in the Slave craton, there is value in reanalyzing the Slave data due to (1) computational limitations in previous contributions and (2) advancements in mineral physics experiments for interpreting magnetotelluric data. The Slave to Bear Province (S2B) MT study (Spratt et al., 2009) and the LITHOPROBE studies (Jones et al., 2001a; Jones and Ferguson, 2001; Jones et al., 2003) were limited to being 1-D or 2-D, which rely on additional assumptions about the geology (e.g., Türkoğlu et al., 2009). As well, the 3-D MT model produced by Snyder et al. (2014) used a decimated station distribution of 53 stations out of ~100 stations available and inverted only the off-diagonal components of the impedance tensor. Thus, an improvement on previous studies could be achieved by inverting for the full impedance tensor and using all available MT stations. A second reason to reanalyze MT data in the Slave craton is that there have been significant advancements in mineral physics experiments, which allow for more reliable interpretations of MT data at upper mantle conditions. It was previously thought that in cratonic lithosphere only graphite and semi-conduction in nominally

anhydrous minerals could raise mantle conductivity (Selway, 2014), but recent laboratory experiments have now found that hydrous minerals (Wang et al., 2012; Hu et al., 2018; Li et al., 2016; Li et al., 2017), carbonatite melts (Gaillard et al., 2008; Yoshino et al., 2018), and NaCl brines (Guo and Keppler, 2019) are conductive in the shallow upper mantle. Furthermore, laboratory experiments have raised doubts on whether graphite films remain connected in the mantle (Watson et al., 2010; Zhang and Yoshino, 2017). Thus, the remainder of the focus of this thesis will be to (1) produce a 3-D MT model that inverts the full impedance tensor with a dense station distribution and (2) to re-evaluate past interpretations of the CSMC in light of new mineral physics experiments.

Chapter 6 : 2-D Inversion of Magnetotelluric Data from the Central Slave Craton Revisited

6.1 Introduction

In this chapter, magnetotelluric inversion models previously published by Jones et al. (2003) and Jones et al. (2001a) are investigated. The data considered are Profile 2 from Jones et al. (2003) which crossed the Central Slave Mantle Conductor. This reanalysis is important because it can (1) investigate the validity of previously published models and (2) determine if a 3-D MT inversion is required for a specific data set.

This chapter begins with a dimensionality analysis using phase tensor analysis, followed by a classification of the MT data on the basis of curve type. This chapter then presents the 2-D inversion model derived from the Profile 2 data and discusses the inversion procedure including the influence of varying the parameters that control the inversion. Finally, at the end of this chapter, the new model is compared with the inversion models published by Jones et al. (2003).

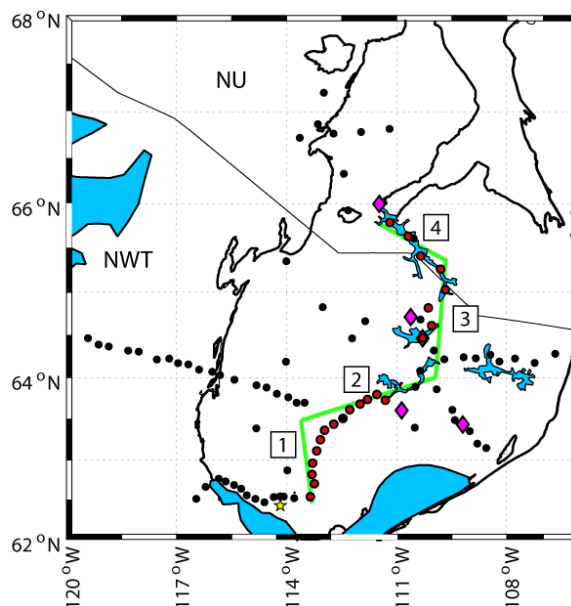


Figure 6.1: The profile of magnetotelluric stations used in the 2-D inversion. The green line shows the four segments that were stitched together to create a continuous profile, which are labelled 1 - 4. Magnetotelluric stations on each segment were rotated such that the x component of the MT data were perpendicular to the line segment and stations used in the inversions are coloured as red circles. Black circles represent other existing magnetotelluric data that were not utilized in the 2-D inversions. Purple diamonds show existing or previously active diamond mines. NU = Nunavut. NWT = Northwest Territories.

6.2 Dimensionality Analysis

Phase tensors are a useful tool for evaluating the geoelectric strike and dimensionality of the magnetotelluric impedance tensor, which then provides information about the subsurface resistivity structure beneath the study area (Caldwell et al., 2004). The geoelectric strike direction is not needed in a 3-D analysis. However, determining the dimensionality of the MT data is valuable as it may reveal trends and show if the data set requires a 3-D analysis. The phase tensors are generally plotted as coloured ellipses where the minimum and maximum phase angles determine the orientation of the major and minor axes of the ellipse. The colour fill denotes the beta skew (β), which represents the rotation of the ellipse's major axis away from an identically shaped ellipse that would arise from a symmetrical phase tensor (see Figure 4.2 for a graphical explanation of the phase tensor). For practical purposes $\beta < 3^\circ$ can be treated as 1-D or 2-D while $\beta > 3^\circ$ is generally considered evidence of a 3-D resistivity structure (Booker et al., 2014). The dimensionality of the Slave MT data set was investigated by plotting map slices of the phase tensor at periods from 1 - 10000 s (Figure 6.2). The skew angle for periods of 1 - 10 s are generally less than 3° with the exception of a few scattered MT stations that have skew angles greater than 3° . There is no clear trend between the MT stations with high skew angles suggesting that the high skew angles are caused by local near surface distortion, but as a whole periods of 1 - 10 s are 1-D / 2-D in nature. At 30 s the phase tensors east of the S2B profile begin to show very high skew angles and by 100 s the majority of stations in the southern and easternmost portion of the Slave craton display high skew angles suggesting a 3-D resistivity structure. Interestingly, these regions coincide spatially with the southernmost part of the CSMC as defined by Jones et al. (2003) and also correspond spatially to the location where previous 3-D inversions detected anomalously conductive mantle (Snyder et al., 2014). The only region in the MT data set which appears to not be strongly 3-D at long periods is the S2B profile, which maintains low skew angles up to periods of 1000 s. Overall, high skew values at periods greater than 30 s support the need for performing a 3-D inversion to image the lithosphere, as a 2-D MT analysis would not be able to compensate for 3-D effects such as galvanic distortion. However, we will proceed with a 2-D analysis to investigate previously published resistivity models. Since segments 3 and 4 of the profile are not strongly 3-D, this suggests that there may be some validity to this exercise.

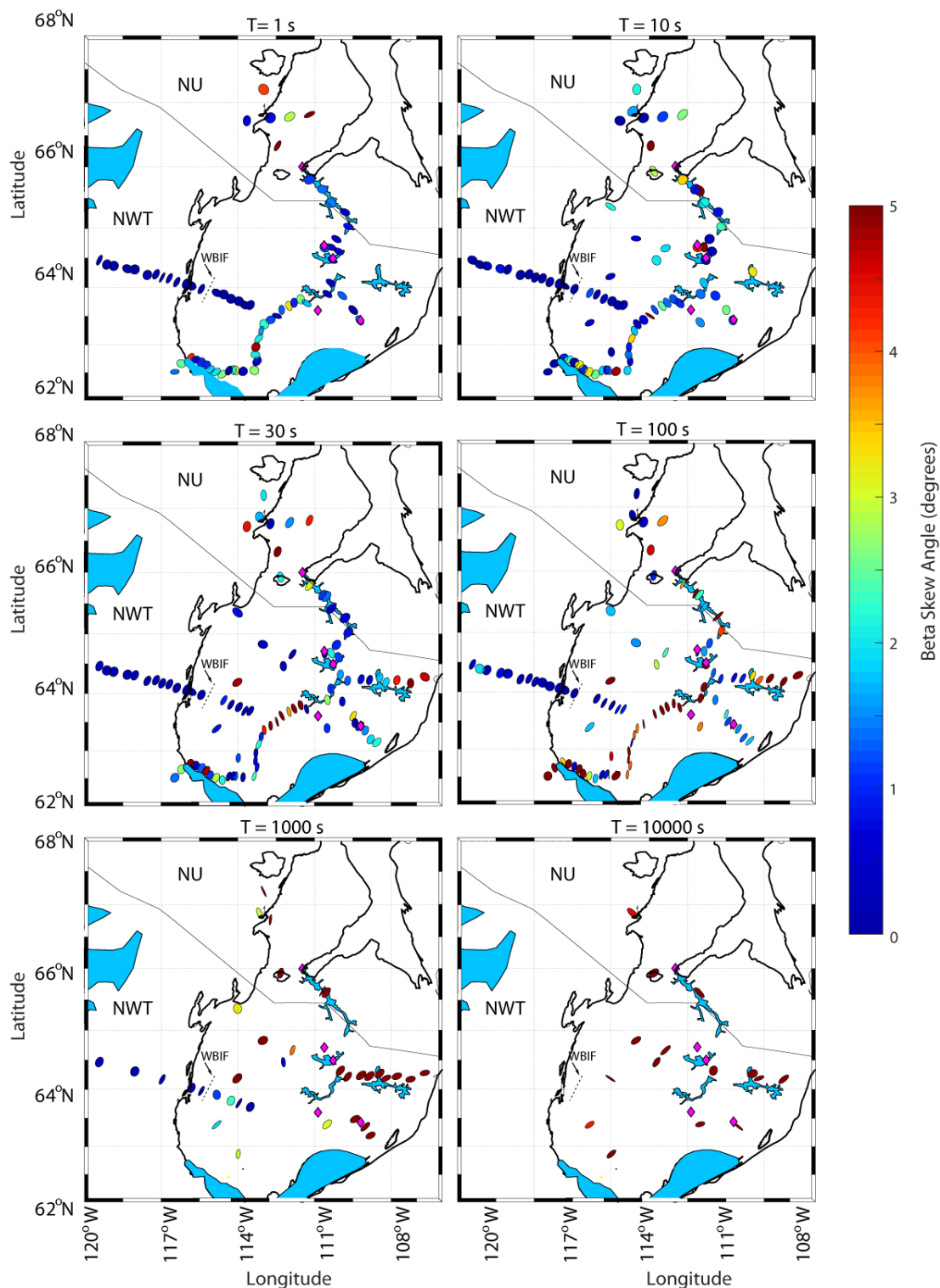


Figure 6.2: Phase tensor map slices for the decades 1 - 10000s. A beta skew greater than 3° is an indication of 3-D structure. WBIF = West-Bay-Indin fault zone. NU = Nunavut NWT = Northwest Territories. Further details are given in text.

6.3 Classification of Apparent Resistivity and Phase Sounding Curves

Before analyzing a MT data set it is useful to characterize the magnetotelluric data where the data was divided into groups with similar characteristics. This exercise is useful for revealing trends in the data before inversion, and qualitatively helps find regions where the absence or presence of conductivity anomalies may be expected. To ensure the robustness of this analysis, the MT data were examined in coordinate systems with rotation angles of both 0° and 45° . The distribution of the groups in the Slave craton is shown in Figure 6.3.

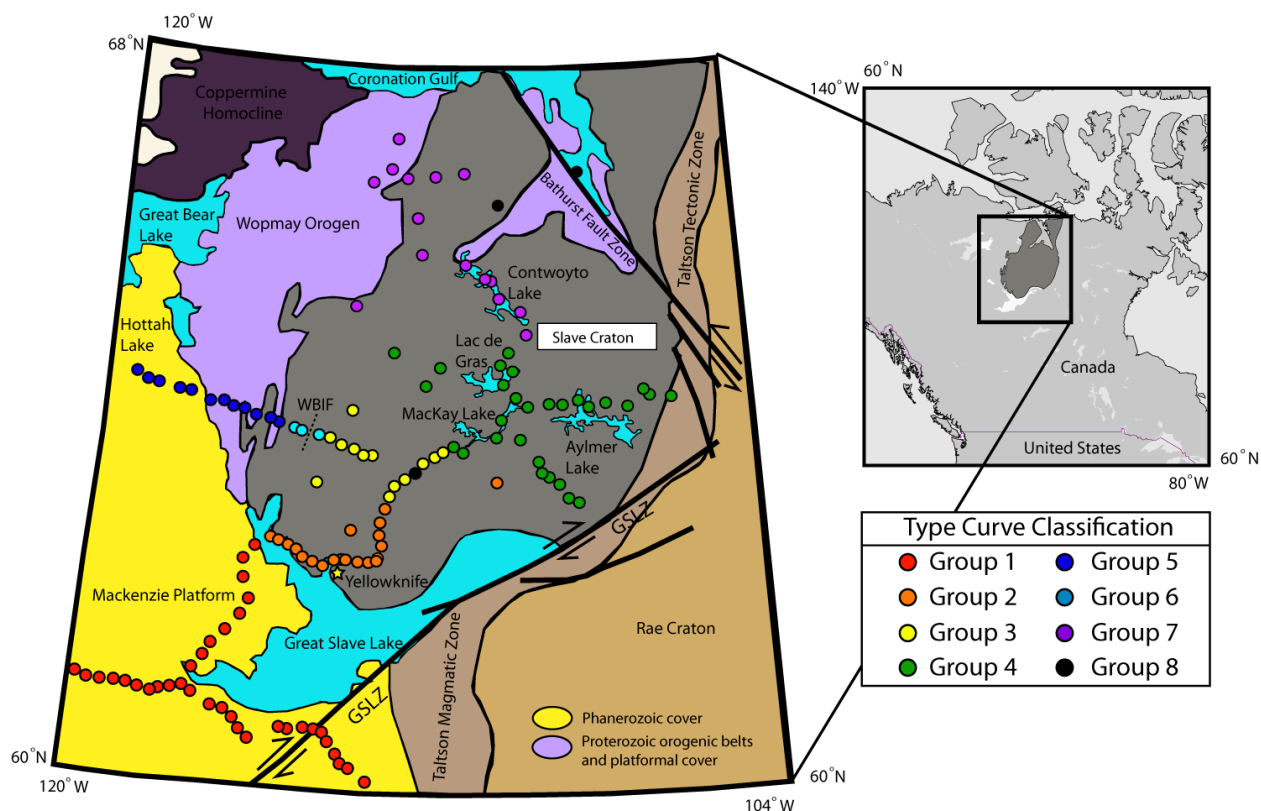


Figure 6.3: The distribution of groups of sounding curves in the Slave province. Coloured circles correspond to groups of curves with distinct data characteristics. An insert map is shown on the right hand side of North America with a black box that contains the study area. WBIF = West-Bay Indian fault zone.

The groups of sounding curves identified in the study area are described below, and an example of each group is shown in Figure 6.4 and Figure 6.5 for rotation angles of both 0° and 45° respectively. If an MT curve differs significantly between a rotation angle of 0° and 45° , it suggests that the dimensionality of the subsurface is at minimum 2-D or maybe 3-D. If there is no variation with rotation angle, then this suggests that the subsurface resistivity structure is 1-D.

Group 1: This group of apparent resistivity curves are relatively 1-D and only show a split in a few cases at periods greater than 1 s. The apparent resistivity at short period is $\sim 100 \Omega\text{m}$ and decreases up to a period of ~ 1 s where the apparent resistivity then steadily increases to $\sim 1000 \Omega\text{m}$ at a period is 100 s.

Group 2: There is very little split between the XY and YX components of the impedance and the apparent resistivity magnitude only varies between 1000 and 10000 Ωm . The character of the curves suggests a quasi 1-D subsurface structure. The apparent resistivity at short periods is around 1000 Ωm and increases gradually up to a period of around 1s where the apparent resistivity then begins to decrease gradually towards 1000 Ωm again.

Group 3: The apparent resistivity at periods less than 1 s is around 10000 Ωm and gradually decreases to around 100 Ωm at periods greater than 1 s.

Group 4: The apparent resistivity at short periods is in the range 1000 - 10000 Ωm at periods of 100 - 10s and then gradually decreases to 100 - 1000 Ωm at periods of greater than 100 s.

Group 5: The apparent resistivity at short periods is around 500 Ωm and decreases to 100 Ωm where it then increases steadily to over $\sim 1000 \Omega\text{m}$ at a period of 1 s. For periods greater than 1 s, the apparent resistivity decreases gradually to a value on the order of hundreds of Ωm at a period of around 100 s.

Group 6: The apparent resistivity at periods less than 1 s is very low between 1 Ωm and 0.1 Ωm . The shape of the curve is very similar to group 5 curves, but with much lower overall apparent resistivities.

Group 7: The apparent resistivity at short period is in the range 1000 Ωm to 10000 Ωm and then beginning at a period of 0.1 s it steadily decreases until reaching a value of 100 Ωm at long periods.

Group 8: These apparent resistivity curves do not fit into the other categories and can be considered as outliers. They are highly 3-D as they contain out of quadrant phases. These curves are likely being affected by local galvanic distortion.

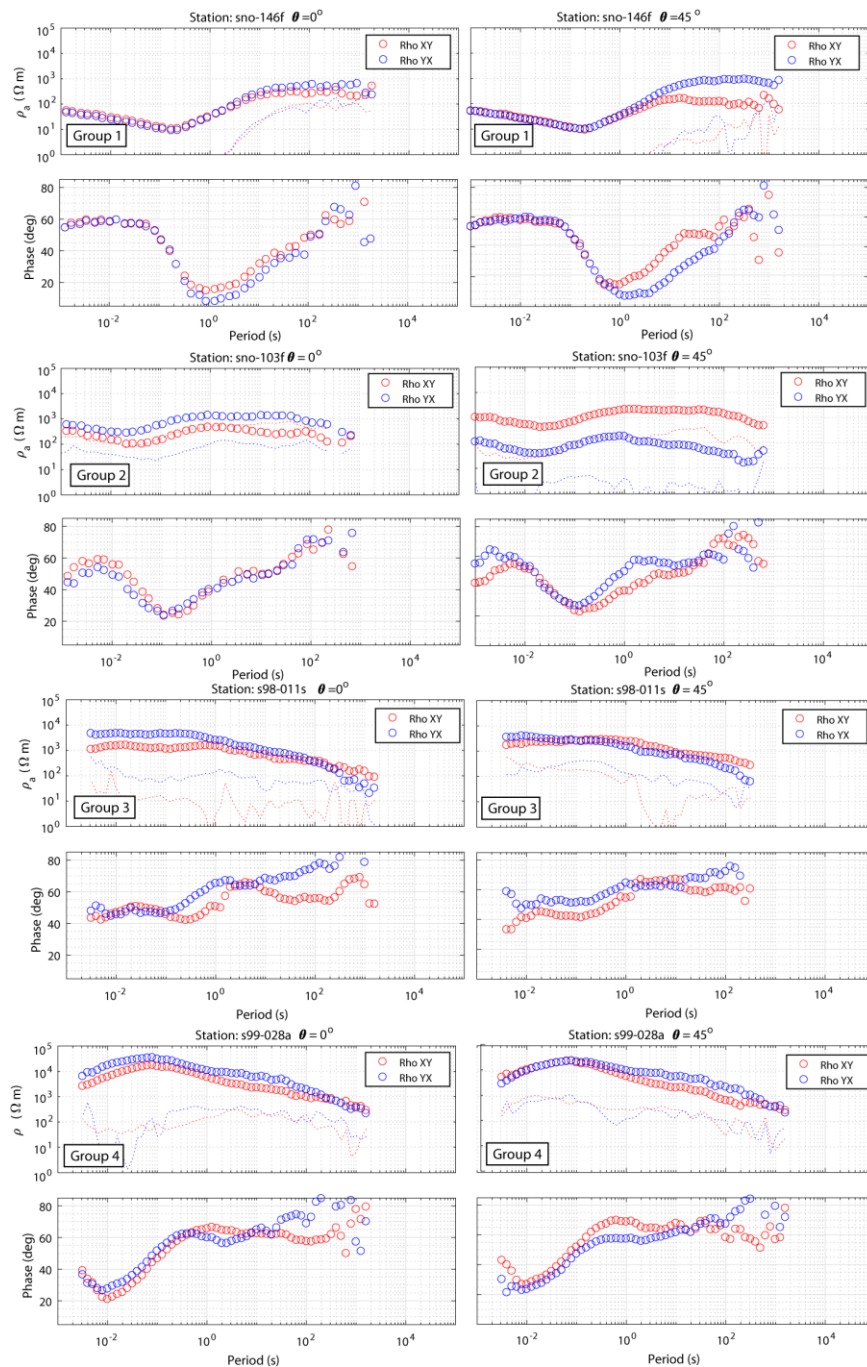


Figure 6.4: Examples of MT curves measured at stations on the Slave craton and displayed with rotation angles of 0° (left column) and 45° (right column). Descriptions of each group of curves are given in text. The XY and YX components are shown as red and blue circles respectively. Red and blue lines are the XX and YY components respectively. The classification is based upon XY and YX information exclusively.

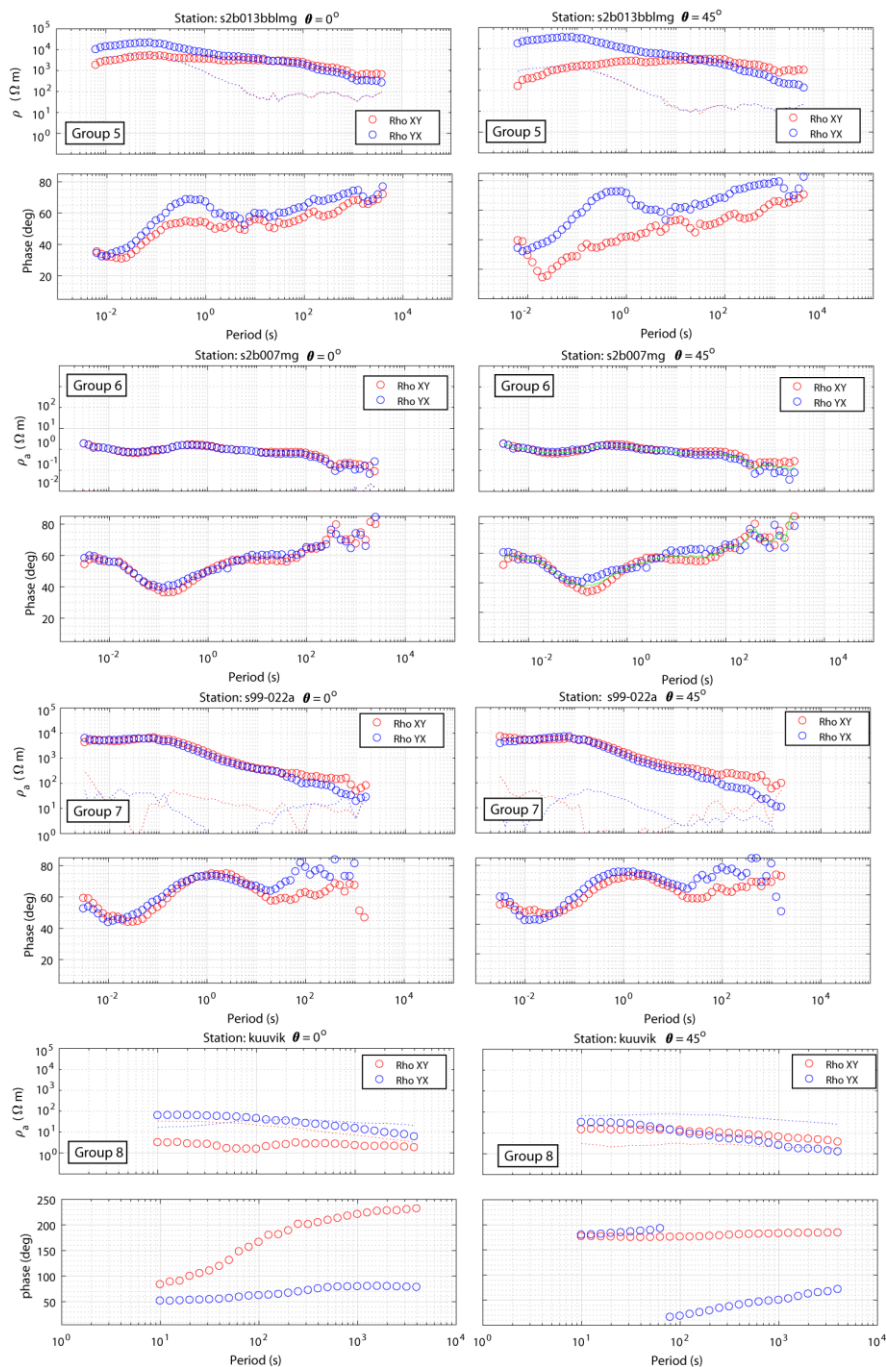


Figure 6.5: Examples of MT curves measured at stations on the Slave craton and displayed with rotation angles of 0° (left column) and 45° (right column). Descriptions of each group of curves is given in the text. The XY and YX components are shown as red and blue circles respectively. Red and blue lines are the XX and YY components respectively. The classification is based upon XY and YX information exclusively.

6.3.1 Spatial Distribution of the Groups of MT Curves

The classification of groups corresponded to different regions within the Slave craton and their distribution seems to be related to the resistivity structure reported in previous publications. These spatial relationships are also evident from the distribution of phase tensors (Figure 6.2) and some of the sounding curves (Figure 6.3).

- Group 1 curves are only found outside of the Slave craton and within the Fort Simpson Sedimentary Basin (i.e. The Mackenzie Platform) (see Figure 6.3), which explains the uniform character of the curves at frequencies above 1 Hz.
- Group 2 curves occur in the southernmost part of the Slave craton and suggest a relatively 1-D resistivity structure with at least four layers (assuming 1-D geometry). This subset of the Slave MT data corresponds to profile 1 from Jones et al. (2003), which found a relatively 1-D resistivity structure with four distinct layers: (1) a highly resistive crust, (2) a resistive upper mantle, (3) a moderately resistive sub-continental lithosphere and (4) the asthenosphere. The phase tensors generally have skew angles less than 3° until periods of 100s supporting a structure that is not highly 3-D.
- Group 3 curves are found in the southern central Slave craton at $\sim 64^\circ$ N on the east end of the S2B profile. The character of the curves shows a highly resistive resistivity structure near the surface followed by a rapid decrease in resistivity at long periods. Snyder et al. (2014) described an anomalous region of low resistivity at $\sim 64^\circ$ N suggesting that Group 3 curves are indicative of the presence of an upper mantle conductor beneath the resistive crust. Interestingly, Spratt et al. (2009) did not report a conductor on the east end of the S2B profile, however, model resolution at the edge of a profile is lower than in the centre and the maximum depth of penetration on the east end of the profile was calculated to be ~ 100 km, which could potentially be at a similar depth to the mantle conductor. Phase tensors with high skew angles correlate well spatially with Group 3 curves, which may be an indication of the mantle conductor described by Snyder et al. (2014).
- Group 4 curves are generally found in the central Slave craton and show that the apparent resistivity is very high near the surface, but the apparent resistivity decreases continuously starting at a period of 0.1 - 1 s suggesting the presence of a deeper conductor. This region corresponds spatially to the location of the Central Slave Mantle

Conductor (Jones et al., 2001a; Jones et al., 2003; Snyder et al., 2014) and thus the character of the groups of curves is an indication of the anomalous upper mantle conductor.

- Group 5 curves are found on the S2B profile west of the Slave craton boundary ($\sim 116^\circ\text{N}$). The distinct character of the curves is an indication of the transition from the Slave craton to the Wopmay Orogen as described by Spratt et al. (2009). The distinct character of the curves is also likely a consequence of the Phanerozoic sedimentary cover described by Spratt et al. (2009), which does not overlie the Slave craton to the east.
- Group 6 curves are only found in the centre of the S2B profile and have the same general shape as the surrounding curves, but with very low apparent resistivities (10 - 0.01 Ωm). These sites correspond to the location of the shallow near surface conductor described by Spratt et al. (2009), which was interpreted to be sulphide mineralization in the West-Bay-Indin fault zone, which is labelled in Figure 6.3.
- Group 7 curves are found in the northern region of the Slave craton and have similar character to some of the group 4 curves in the Central Slave craton (63°N - 65°N), but the decrease in apparent resistivity at long periods is not as steep decreasing to ~ 1000 Ωm rather than 10 - 100 Ωm in group 4 curves. The decrease in apparent resistivity suggests an increase in mantle conductivity, but perhaps not as significant as in the central Slave craton. Snyder et al. (2014) described an upper mantle conductor beneath Jericho, which corresponds spatially to the group 7 curves.
- Finally, the distribution of group 8 curves does not have a spatial significance as it is comprised of data that did not fit into any characterization of the other groups. These curves are dominated by galvanic effects and have out of quadrant phases suggesting a 3-D resistivity structure.

6.4 2-D Inversion

The profile extends approximately 500 km from the southwest of the Slave craton to the northeast and contains the same 23 broadband magnetotelluric stations as profile 2 from Jones et al. (2003). The dimensionality of the profile shows that a 2-D inversion is suitable for data up to a period of ~ 100 s as the data has low skew angles (see Figure 6.2). The resistivity model was determined by inverting the MT data with the algorithm of Rodi and Mackie (2001). The

resistivity model was obtained by inverting the transverse electric (TE) and transverse magnetic (TM) modes simultaneously with a frequency band of 0.01 s - 1000 s. The TE and TM mode correspond to the XY and YX components of the magnetotelluric impedance such that the x direction is parallel to strike and the y direction is perpendicular to strike. Tipper data were not included in the inversions as Jones et al. (2001a) and Jones et al. (2003) did not use tipper data and this analysis aims to follow the same procedure as previous publications. A dense mesh was used for the preferred model with 119 columns and 67 rows. The cells extended to 450 km in both horizontal and vertical directions, which is based upon three skin depths for an EM wave in a 100 Ωm halfspace. This model size prevents the diffusing signal from reaching the edge of the halfspace, which can cause artefacts at the boundaries. The preferred resistivity model assumes a perpendicular strike along each separate line segment with strike angles of 29° , 140° , 67° and 79° used for segments 1 - 4 respectively where a positive angle indicates a clockwise rotation. This procedure is chosen as it follows the methodology of Jones et al. (2003). The segments are shown in map view in Figure 6.1 and are labelled in Figure 6.6 with their respective strike angles. The inversion ran for 200 iterations before converging to a solution and had a final r.m.s. misfit of 1.89. The inversion began from a 100 Ωm halfspace and error bars of 5% were applied to the data. A regularization parameter $\tau = 3$ was applied for smoothing and static shifts coefficients were computed by the inversion algorithm. The investigation of these parameters is discussed in detail in section 6.6.

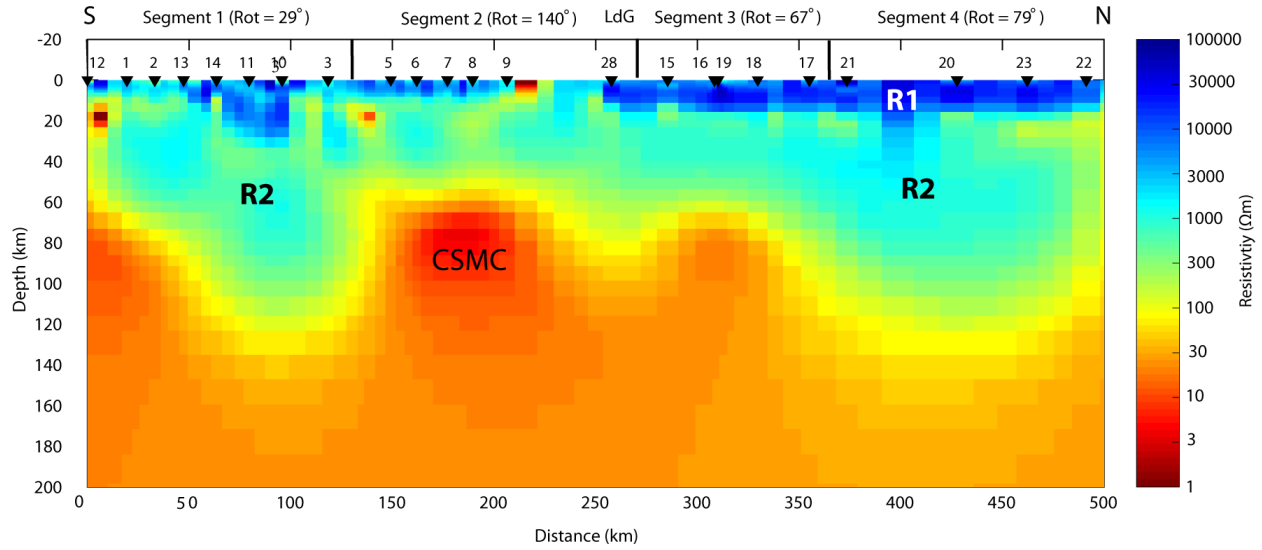


Figure 6.6: The preferred 2-D resistivity model obtained from magnetotelluric data along the profile of Jones et al. (2003). The profile consists of four segments stitched together with the x axis rotated to be perpendicular to each segment. Rotation angles for each segment are labelled with a positive angle indicating a clockwise rotation. LdG = Lac de Gras. Three significant features are visible: R1 - a near surface resistor, R2 a moderately resistive feature in the upper mantle and CSMC the Central Slave Mantle Conductor (CSMC). The resistivity model was produced by jointly inverting the TE and TM modes with a starting model of 100 Ωm and has an r.m.s. misfit of 1.89. The regularization parameter was set to $\tau = 3$ and the damping and variance were set to 1000 and 10% respectively to correct for static shifts present in the data.

6.5 Model Fit

6.5.1 R.M.S. Misfit and Static Coefficients

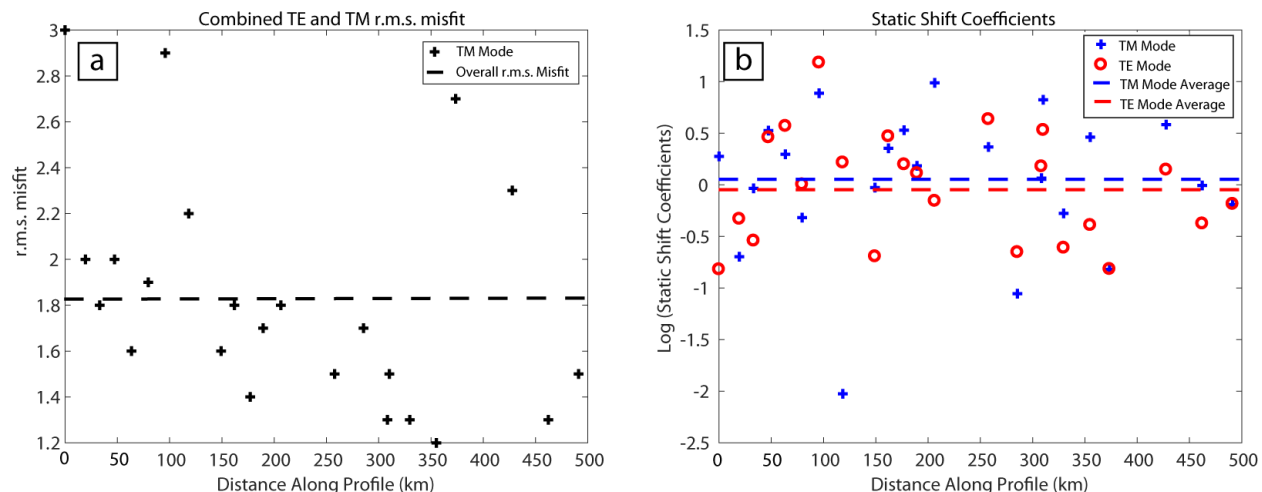


Figure 6.7: (a) The r.m.s. misfit of each MT station along the profile for the preferred model. An r.m.s. misfit of 1 is considered an ideal data fit. (b) Static shift coefficients of each MT station determined by the 2-D inversion for the preferred model. The means of the static shift coefficients for the TE and TM are given as a red and blue dashed line respectively. A static shift coefficient of 1 corresponds to no shift in the modelled apparent resistivity while a positive or negative value scales the modelled apparent resistivity response up or down respectively.

The mean of the static shift coefficients for the TE and TM modes are -0.0371 and 0.0389 respectively and the standard deviation of the static shift coefficients for the TE and TM modes are 0.5366 and 0.6932 respectively. The standard deviations are less than 1 for both modes, which reveals that the majority of MT stations only required a shift in apparent resistivity of less than 1 order of magnitude. The average value for the static shift coefficients is close to zero for both modes indicating that there is no significant upward or downward bias in the apparent resistivity curves. This distribution of static shift coefficients justifies the choice of variance being 10% in the preferred inversion model because the sum of the statics is close to zero. However, choosing a variance of 10% rather than zero is preferred as it allows the inversion to have more freedom in applying the statics to account for the possibility of some minor bias being present in the data. The r.m.s. misfit is generally between 1 and 2 indicating a good fit for the model and there are no large outliers that could negatively affect the data fit and reduce the model reliability.

6.5.2 MT Data Pseudosections:

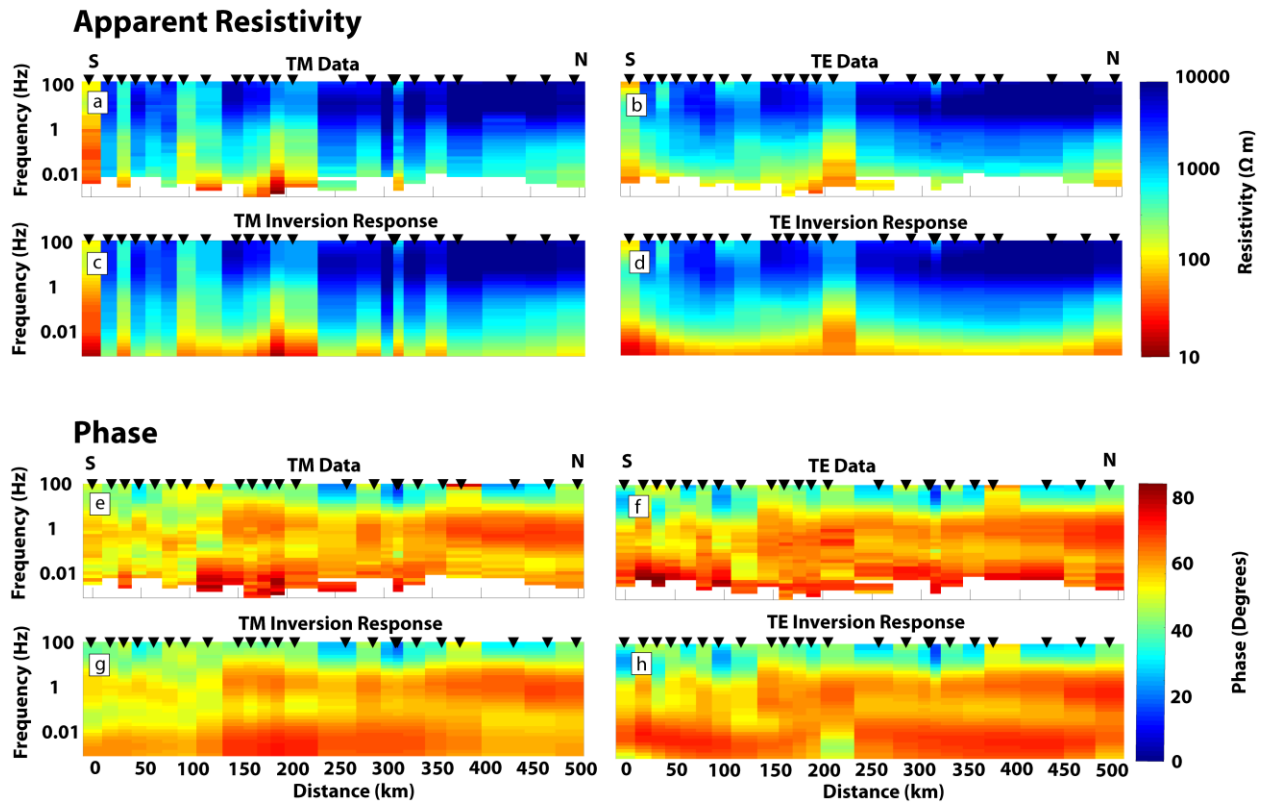


Figure 6.8: Pseudosections of the measured magnetotelluric data and the response of the preferred inversion model. The top panel shows the apparent resistivity pseudosections for the (a) TM mode data, (b) TE mode data, (c) TM mode inversion response and (d) TE inversion response. The bottom panel shows the phase pseudosections for the TM mode data, (b) TE mode data, (c) TM mode modelled response and (d) TE modelled response. Increasing apparent resistivity will correspond to a phase less than 45° and a decreasing apparent resistivity will correspond to a phase greater than 45° .

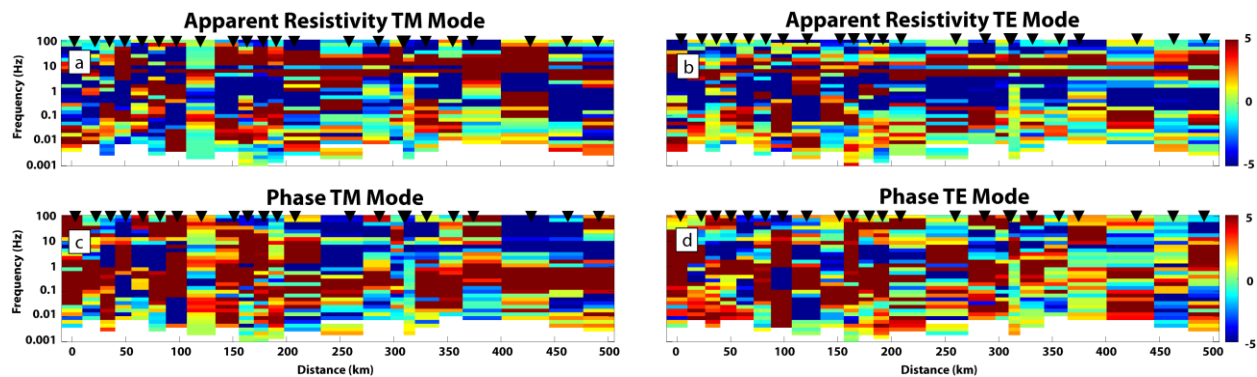


Figure 6.9: Pseudosections of residuals between the observed and modelled magnetotelluric data for the preferred model for the (a) TM mode apparent resistivity, (b) TE mode apparent resistivity, (c) TM mode phase and (d) TE mode phase. Residuals are given as the difference between observed and modelled apparent resistivity and phases that is scaled by the error. For the preferred model, the residuals were calculated using a 5% error floor.

High phases in these pseudosections represent resistivity values that decrease with depth and conversely low phases represent resistivity that increases with depth. The TE and TM pseudosections show high apparent resistivities from the surface to periods of at least 100 s (Figure 6.8(a,b)), which is consistent with the low porosity crystalline rocks that comprise the Slave craton's crust and upper mantle. At periods greater than 100 s the apparent resistivity of the centre of the TM profile decreases to resistivities on the order of 1 - 10 Ωm (Figure 6.8(a)). The TE mode also reflects the presence of a deeper conductor, but is less spatially uniform than the TM mode (Figure 6.8(b)). The decrease in resistivity at long periods is likely evidence of the CSMC, which is present in the preferred model and in the resistivity model of Jones et al. (2001a) and Jones et al. (2003). The phase pseudosections also reflect any changes in the apparent resistivities with increasing resistivities corresponding to decreasing phases and vice versa. The phase pseudosections increase to values greater than 30° at periods greater than 1 s, which is a reflection of the decreasing resistivity with depth (Figure 6.8(e,f)). Figure 6.9 shows the residual pseudosections for the preferred model, which is a difference between the observed and predicted data that is scaled by error. There are no clear trends to suggest some regions of the model are being fit better than other portions.

6.6 Parameter Optimization

6.6.1 Effect of Varying the Regularization Parameter (τ)

The Rodi and Mackie (2001) inversion algorithm determines the smoothest resistivity model that fits the MT data to a specified statistical tolerance. Depending on the degree to which

the inversion smooths or regularizes, a range of models can be obtained and this is controlled by the user specified parameter, τ . It is important to look at a range of values for τ to determine a value which optimizes the trade-off between over fitting the data (low τ values) and over smoothing the model (high τ values). If there is too much weight on smoothing the model (high τ values), then the inversion will not fit the MT data satisfactorily resulting in a higher r.m.s. misfit. If the inversion does not put enough weight on smoothing the model (low τ values), then there is a risk of fitting noise resulting in models that are spatially rough, but with a lower r.m.s. misfit. An ideal model will have a τ value that finds a balance between model smoothness and data misfit, which is determined from an L curve. A range of inversions were implemented using τ values in the range 0.1 and 100, which are plotted as L-curve in Figure 6.10(a). From this exercise it was found that $\tau = 4$ corresponded to the best trade off between data fit and model smoothness. All other parameters were held constant to isolate the different degrees of smoothing from changing the τ parameter.

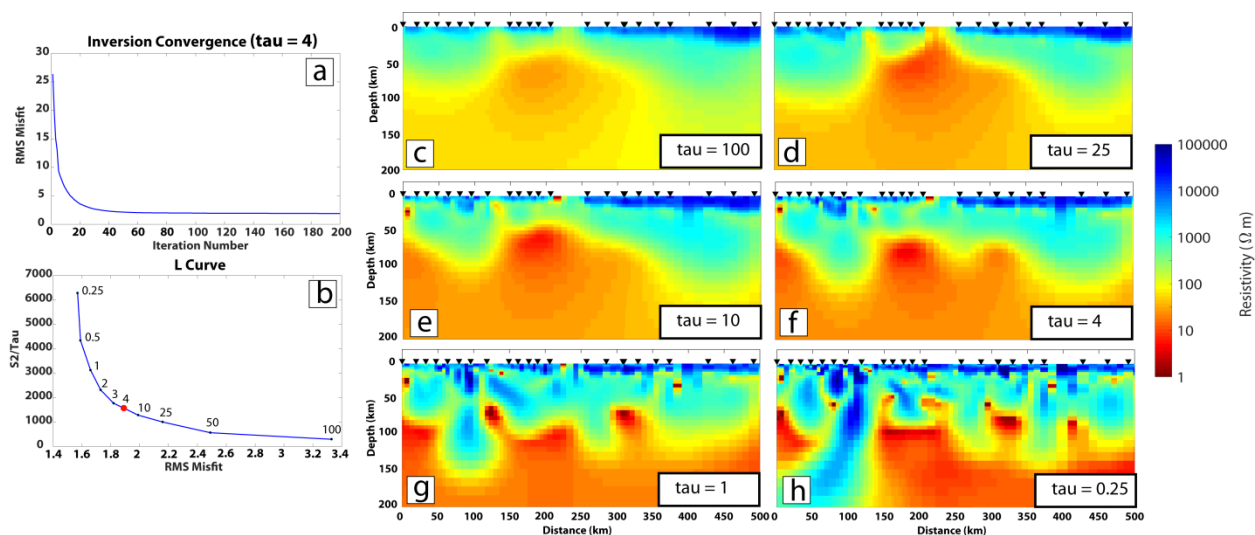


Figure 6.10: (a) Inversion convergence curve for $\tau = 4$ showing the r.m.s. misfit for each iteration. The smooth decrease in r.m.s. misfit indicated the inversion for the preferred model is stable. (b) The L-Curve plotting r.m.s. misfit against model smoothness. The best τ value is chosen to be 4 based upon the inflection point of the L-Curve and is indicated by a red dot in (b). The resistivity models produced by varying τ , are shown for values of (c) 100, (d) 25, (e) 10, (f) 4, (g) 1 and (h) 0.25. Higher τ values result in smoother models and lower τ values result in rougher models. The preferred model is shown in (f) with $\tau = 4$.

6.6.2 Effect of Varying Static Shift Parameters

Static shifts cause the apparent resistivity to be scaled by an unknown multiplicative constant (e.g., Jones, 1988). The shifts are the result of localized galvanic effects that reduce or

increase the measured electric field strength in the region, which causes the MT curves to shift down or up, but does not change their shape. There are two parameters available in the Rodi and Mackie (2001) inversion algorithm to control how statics shift coefficients are determined: damping and variance. The damping values range from 0 to 10000 with a variance that can range from 0 to 100%. A lower value of the variance forces the sum of the static coefficients to be closer to 0 (i.e. it is assumed there is no bias in the average static coefficient). A larger damping parameter forces statics to remain fixed until later iterations in the inversion while a small value allows for statics to be changeable early in the inversion. Changing the damping parameter between 1000 and 10000 does not change the model appreciably (Figure 6.11(a-c)). In contrast, changing the variance between 10 and 100 has an appreciable effect on the model and pulls the CSMC closer to surface (Figure 6.11d in comparison to Figure 6.11(a-c)). Still, a high variance does not seem justified as the static shift coefficients do not show any upwards or downward bias (see Figure 6.7).

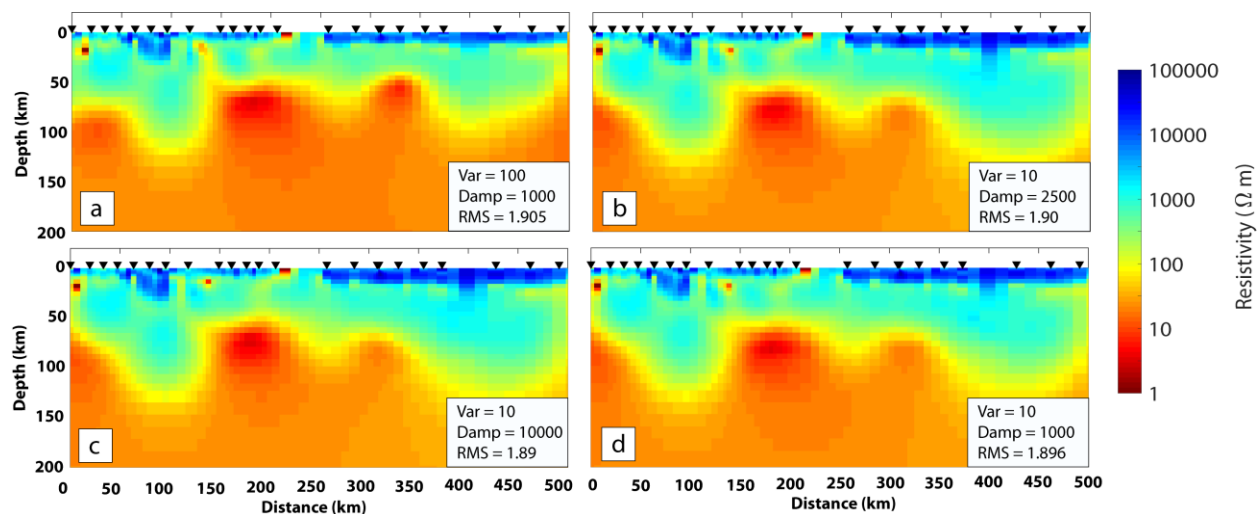


Figure 6.11: Resistivity models produced by varying the variance and damping coefficients for (a) a variance of 100% and damping of 1000, (b) a variance of 10% and a damping of 2500, (c) a variance of 10% and a damping of 10000 and (d) a variance of 10% and a damping of 1000. The main resistivity features were recovered with each combination of parameters suggesting a robust model. The preferred model is shown in (d).

6.6.3 Effect of Varying Error Floors

The error floor defines a minimum error bar for each apparent resistivity and phase data point in the inversion. Thus, the error bar is changed for a data point if it is smaller than the error floor and data points with error bars larger than the error floor remain unchanged. Larger error

floors are typically required in noisier data sets whereas smaller error floors can be used for data sets that are less contaminated with noise. A larger error floor also gives the inversion more freedom to deviate from the apparent resistivity and phase data points and in some cases large error floors can be used as a means of compensating for static shifts (e.g., Jones et al., 2003).

Error floors for apparent resistivity were tested for values of 5, 10 and 20% while the error floor for phase remained fixed at 5%. Each error floor produces the same main resistivity features, however, the higher error floors produce a smearing effect. The models with error floors of 10 and 20% produced non-physical smearing of the CSMC (Figure 6.12(b,c)), which brought the conductor towards the surface of the models. In comparison, the model with an error floor of 5% (Figure 6.12a) produced a geologically reasonable model, which did not have any smearing of the CSMC. For this reason, the 5% error floor was chosen as the preferred model over higher error floors.

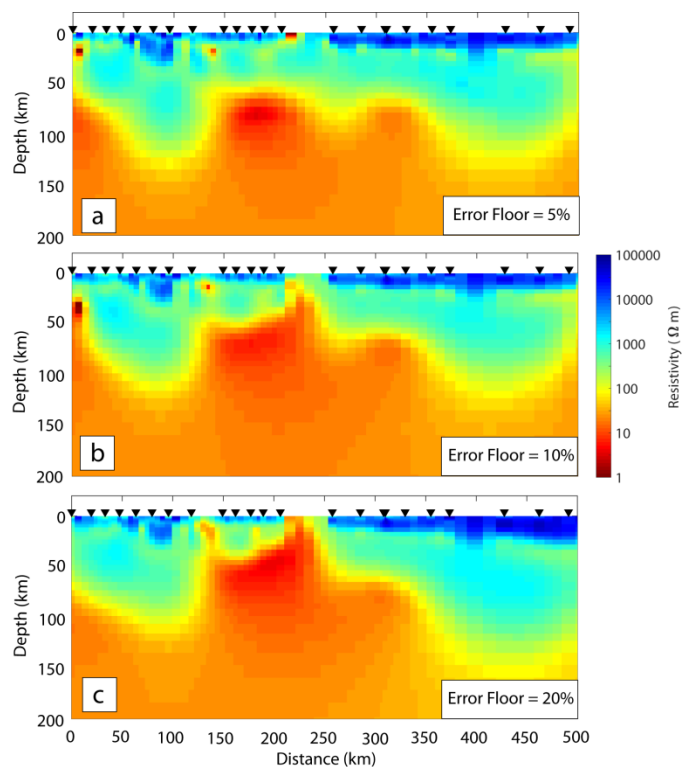


Figure 6.12: Resistivity models obtained from setting the error floor to (a) 5%, (b) 10% and (c) 20%. The main resistivity feature is recovered in each model, however, larger error floors produce a smearing effect on the conductor. The preferred model is shown in (a), which is the least prone to smearing seen in models with higher error floors.

6.6.4 Effect of Varying Starting Model

An inversion searches for smooth variations with respect to a specified starting model and ideally will recover similar resistivity features irrespective of the starting model. Figure 6.13 shows that the CSMC is recovered using all tested starting models with the exception of the 1 Ωm starting model. The 1 Ωm starting model has a satisfactory r.m.s. misfit, however, the model can be rejected because it (1) is an outlier relative to the other resistivity models and (2) appears to be geologically unreasonable. The resistivity models produced for starting models of 100 and 1000 Ωm are the most consistent of the four resistivity models that were able to recover the CSMC. These two models are preferred to the 10 and 10000 Ωm as they are (1) consistent, which suggests they are more robust models and (2) they do not contain any near surface conductors that appear to be smeared upwards. As well, these models are more consistent with the previous resistivity model from Jones et al. (2003). The 100 Ωm starting model was chosen as the preferred model on the basis of having a lower r.m.s. misfit (1.89 versus 1.91), however, it should be noted that the models are almost indistinguishable suggesting a 1000 Ωm could also be an acceptable starting model.

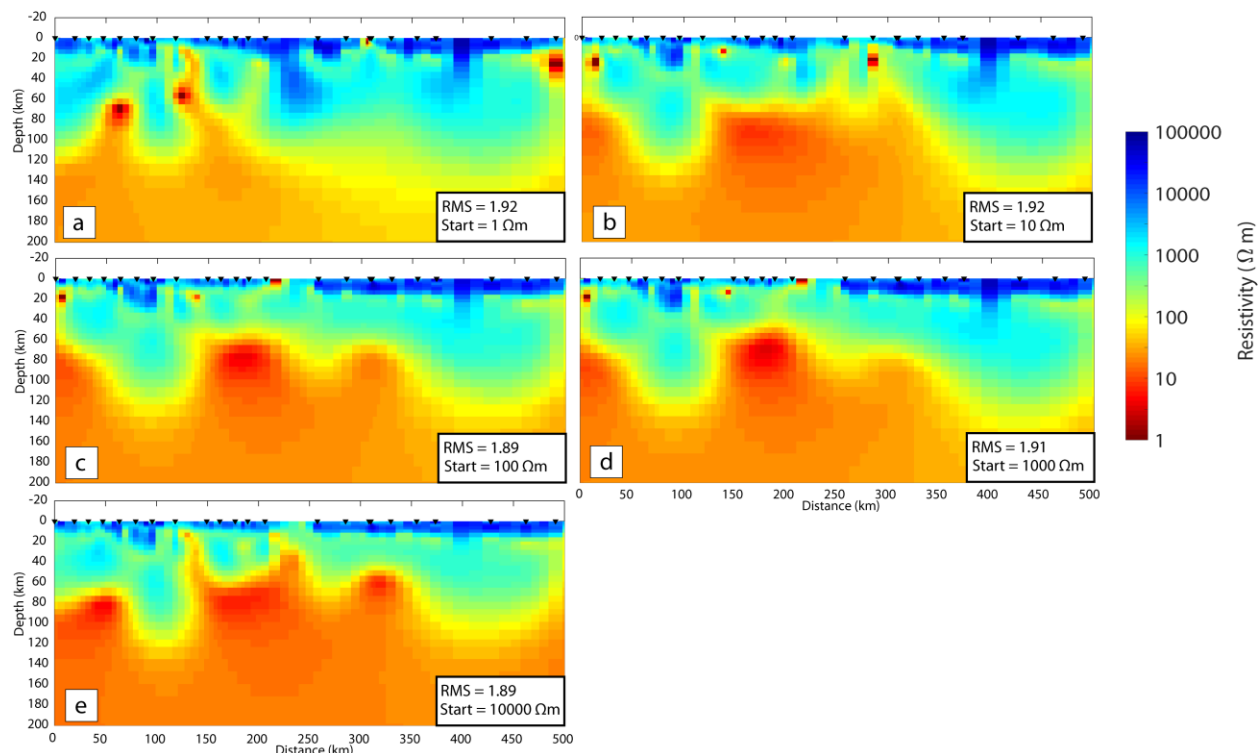


Figure 6.13: Resistivity models obtained from setting the resistivity of the starting model to (a) 1 Ωm , (b) 10 Ωm , 100 Ωm , 1000 Ωm and 10000 Ωm . The main features are recovered in all starting models with the exception of the 1 Ωm starting model, which is likely a result of starting with a resistivity that is too far from the average resistivity of the region. The preferred model is shown in (c).

6.7 Comparison with the Previous 2-D Resistivity Model in the Slave Craton

The preferred inversion model is broadly similar to those previously published using the same data. Specifically, both the new and previously published models have a prominent upper mantle conductor that was called the Central Slave Mantle Conductor (CSMC) by Jones et al., (2001) and Jones et al., (2003). However, the geometry of the CSMC in the new model is different to that in Jones (2003). In the new model, the conductor does not have a well defined northwest dip that is apparent in the model of Jones et al. (2003). A dipping geometry occurred for some values of τ , but those τ values did not correspond to the best trade off between smoothness and data misfit (see Figure 6.10). As such, the dipping geometry may be dependent upon choice of regularization parameter rather than being a representation of the true geometry of the CSMC. The shallower regions of the crust and mantle above the CSMC were also similar in the new model and that of Jones et al. (2003). The crust was highly resistive and the mantle above the CSMC was moderately resistive. In general, the major resistivity features determined

by Jones et al. (2003) were reproduced, which provides confidence to move onto inverting the data in 3-D, which is the subject of Chapter 7. The advantages of a 3-D inversion are described in the following section.

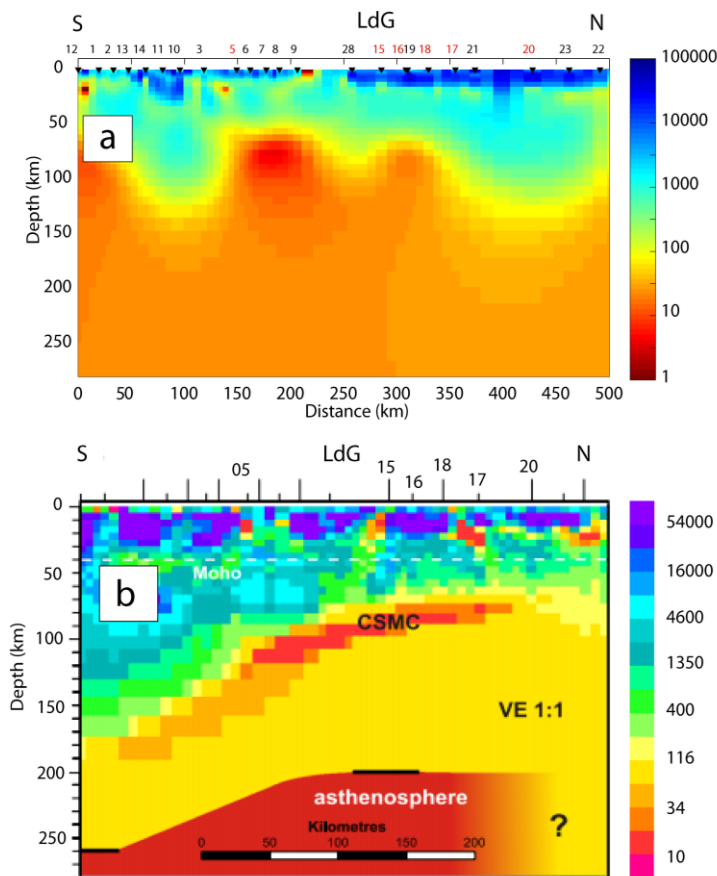


Figure 6.14: (a) The preferred magnetotelluric model and (b) the model published by Jones et al. (2003). Red numbers in the preferred model correspond to the same stations as those labelled in the model of Jones et al. (2003). Distance is not labelled on panel (b) as it is not available in Jones et al. (2003).

6.8 Can a 3-D Analysis of the Slave Craton Data Improve on Previous 2-D Results?

After completing this analysis, there is compelling evidence that a 3-D inversion could improve upon the previously published 2-D inversions by Jones et al. (2003). First, the 2-D inversion stitched together four profiles under the assumption that strike was perpendicular to each profile segment. This assumption may hold some validity as the MT data are laterally slow varying, but it is unlikely that this assumption holds true for the entire profile. Strike angle determination is not required in a 3-D inversion, which removes this uncertainty. Second, Jones et al. (2003) justified a 2-D analysis based upon the dimensionality of the Slave data being quasi

1-D, however, a phase tensor analysis (see Figure 6.2), which was not available at the time of publication reveals that in reality the magnetotelluric data along profile 2 becomes 3-D ($\beta > 3^\circ$) at periods as short as ~ 30 s negating a 2-D analysis (Booker, 2014). Third, a 3-D inversion can include the long period lake bottom sites that are off the main profiles, which will provide additional constraints on the structure of the lithosphere. Therefore, there is ample reason to proceed with a 3-D analysis of the magnetotelluric data in the Slave craton.

6.9 Conclusions:

The major features in the resistivity model of Jones et al. (2003) can be reproduced using a 2-D inversion with the rotation angle varying along the profile. However, there are some noticeable differences between the two resistivity models, which should be considered (see Figure 6.14). These differences may have arisen as different values were used for some control parameters in the two inversions. Namely, the rotation angles assigned to the MT stations along each segment were not specified in Jones et al. (2003) and thus it is unlikely that the exact same rotation angles were used in their study. Secondly, Jones et al. (2003) accounted for static shifts by assigning 25% error bars to the apparent resistivity whereas in this study the inversion solved directly for static shift coefficients (see section 6.5.1). Finally, the τ parameter chosen for the model published by Jones et al. (2003) was not specified and it is possible that the L-curve for the preferred model resulted in a different τ parameter than Jones et al. (2003). These differences may be able to account for the discrepancies between the resistivity models.

A 2-D analysis cannot account for the 3-D geometries that are present in the lithosphere as shown by the high skew angles in the phase tensors (Figure 6.2). A 3-D analysis will provide improvements to the existing 2-D resistivity model as it can (1) account for galvanic distortion present in the MT data and (2) will incorporate off-profile data from the lake bottom sites adding further constraints to the resistivity model that cannot be included in the 2-D models. The 3-D analysis and resistivity modelling will be the focus of Chapter 7.

Chapter 7 : 3-D Inversion of MT Data from the Slave Craton

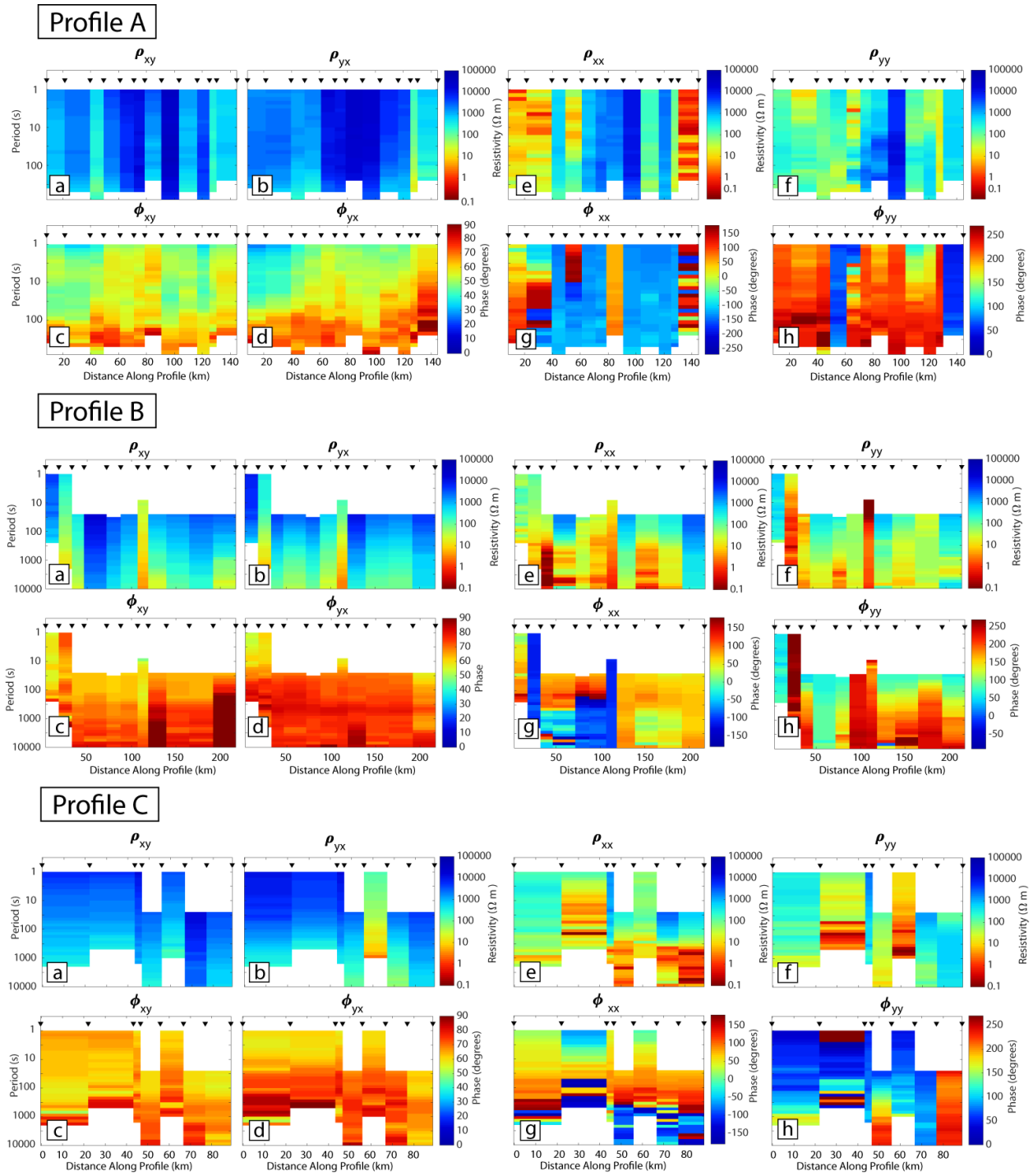
7.1 Introduction

This chapter begins by reviewing the magnetotelluric data previously measured on the Slave craton, and then introduces the preferred 3-D resistivity model (s92p21r8) and data fit. The main conductive and resistive features in the preferred model are then identified and described. The dependence of the final model on the inversion settings is then described. These include starting model resistivity, error floors and covariance, which controls the degree of spatial smoothing applied to the inversion model. This chapter only considers the effect of varying these control parameters on the preferred 3-D resistivity model (s92p21r8), but many more inversions were tested and details can be found in the Appendix. The reliability of the preferred model is then investigated using a combination of synthetic forward modelling and synthetic inversions. This chapter then investigates a comparison of inversion models produced using the WSINV3DMT algorithm (Siripunvaraporn et al., 2005) and the ModEM algorithm (Kelbert et al., 2014). This test was conducted to demonstrate that there are only minor differences between the models produced by these two inversion algorithms proving that the preferred resistivity model (s92p21r8) produced using ModEM is robust. Finally, the chapter concludes with a discussion of the preferred resistivity model (s92p21r8). The preferred resistivity model (s92p21r8) presented in this chapter will provide the basis for the interpretation in Chapter 8.

7.2 Magnetotelluric Data for the Slave Craton

This section introduces the MT data, which is important as these data will be used in the inversion to produce the preferred resistivity model (s92p21r8). The data are shown as apparent resistivity and phase pseudosections for five profiles in the data set. MT data are typically presented as interpolated map view slices when a 2-D grid at the surface is available. However, the data in this study are not uniformly distributed, making interpolation ineffective. The MT data are shown as five profiles labelled A - E on Figure 7.1

Chapter 7 : 3-D Inversion of MT Data from the Slave craton



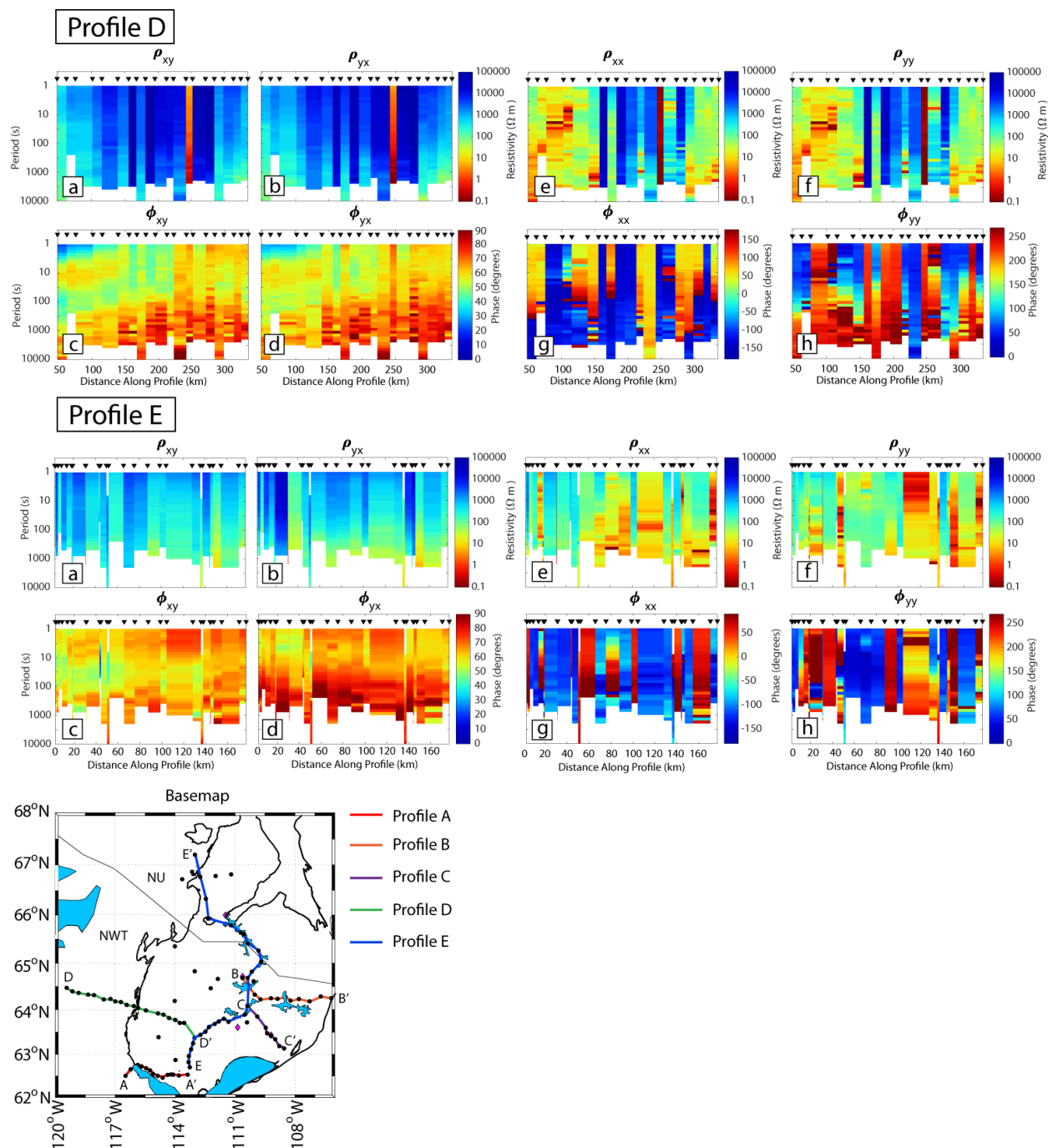


Figure 7.1: Pseudosections of apparent resistivity and phase for a 0° rotation are shown along Profiles A - E . These profiles correspond to the same profiles, which will show the preferred resistivity model (s92p21r8) in Section 7.4. Apparent resistivity is shown for the (a) YX, (b) XY, (e) XX and (f) YY components and phase is shown for the (c) YX, (d) XY, (g) XX and (h) YY components. White areas correspond to stations and periods with no data.

7.3 Preferred 3-D Resistivity Model (s92p21r8) of the Slave Craton

A 3-D resistivity model was produced by inverting the full magnetotelluric impedance tensor using the ModEM inversion algorithm (Kelbert et al., 2014) using the data described in Section 7.2. The final resistivity model described in this section was produced after a long process of trial-and-error to determine the optimal set of parameters to use in the inversion. Readers that are interested to learn more about the process leading up to the final resistivity model are referred to the Appendix, which contains supplemental information regarding the parameters that were investigated. The parameters chosen for the preferred resistivity model (s92p21r8) will be introduced briefly, and are then discussed in detail in Section 7.5. This section begins with a discussion of the data fit (Section 7.3.2) and then shows the preferred resistivity model (s92p21r8) and describes its major features (Section 7.4).

7.3.1 Preferred Inversion Parameters

The ModEM inversion package was implemented to solve for resistivity structure using finite difference methods and a non-linear conjugate gradient algorithm to converge on a model (Kelbert et al., 2014). The mesh used a total of 88 by 96 by 80 cells in the x, y and z directions respectively. A detailed description of the mesh dimensions used in the preferred model is shown in Table 7.1. This also includes the mesh parameters of the preliminary inversions, which are briefly described in Section 7.7.1 and 7.7.2.

	Preferred Inversion (s92p21r8)	Initial Inversion	Focussed Inversion	WSINV3DMT ModEM Inversion
Cell width in x-direction in core (km)	10	10	10	5
Cell width in y-direction in core (km)	10	10	10	5
x-pad (# of cells)	13	13	13	13
y-pad (# of cells)	13	13	13	13
x-pad Geometric Factor	1.5	1.5	1.5	1.5
y-pad Geometric Factor	1.5	1.5	1.5	1.5
Surface Layer Thickness (km)	0.1	0.1	0.1	0.1
Cell Thickness in z-direction (km)	$0.1*(1.2)^N$ (0 -35 km)	$0.1*(1.3)^N$	$0.1*(1.2)^N$	$0.1*(1.2)^N$
Cell Thickness in z-direction for a non-uniform mesh	5 (35 - 200 km)	N/A	5 (27 - 130 km)	N/A
	$5*(1.2)^N$ (> 200 km)	N/A	(> 130 km)	N/A
Max Depth (km)	3024	611	1780	2200
Max Width (km)	5800	5800	5800	5800

Table 7.1: Mesh parameters for the preferred resistivity model (s92p21r8) and other inversions investigated. N = cell number where N = 1 corresponds to the surface layer and increases with increasing depth. All values in the table are in kilometres (km). The formulas for thicknesses in specific intervals are shown in the dz rows for each inversion model.

Topography was not included in the mesh as the elevation in the study area is between 109 and 539 m above sea level and these variations are insignificant compared to the depth of investigation. A 1000 Ωm halfspace was used for the starting model, and this value reflects the higher than average resistivities found in the crust of the Slave craton. A covariance parameter of 0.3 was chosen for spatial smoothing of the resistivity model, which was found to result in a good trade-off between model smoothness and data fit in the inversions. Lastly, an error floor of

10 % was assigned for the impedance tensor. The following sections will discuss the effect of varying the error floors, starting model and covariance and show the reasoning for choosing the preferred model parameters. Impedance data in the period range 1 - 10000 s were inverted to focus on lithospheric structure. The inversion for the preferred resistivity model (s92p21r8) converged after 247 iterations to an overall root mean square (r.m.s.) misfit of 0.92 (Figure 7.2).

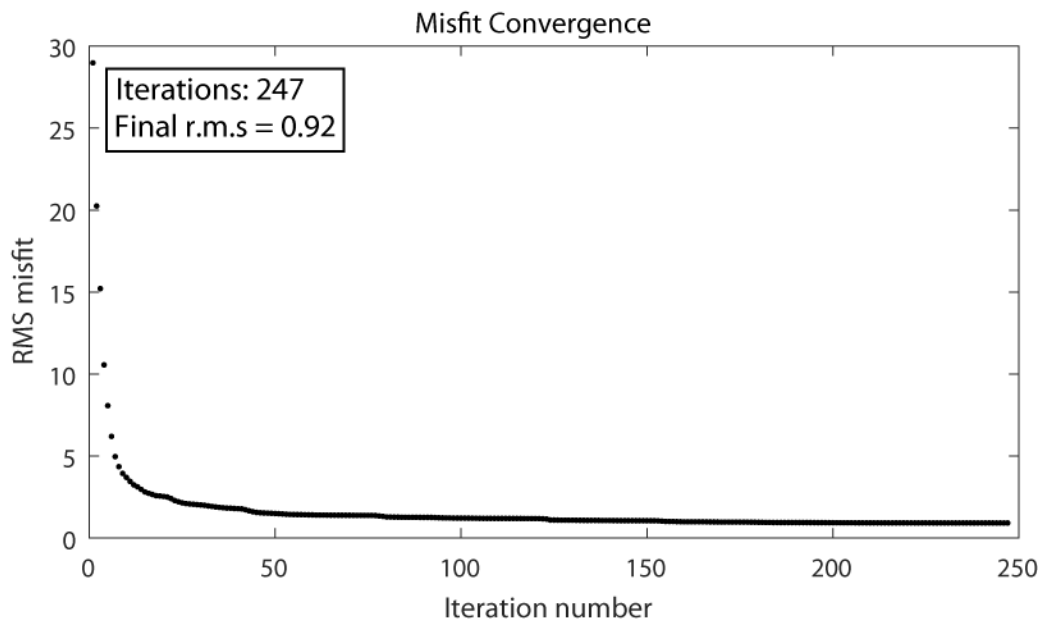


Figure 7.2: The misfit convergence for the preferred resistivity model (s92p21r8). The inversion converged to an r.m.s. misfit of 0.92 after 247 iterations.

7.3.2 Preferred Resistivity Model Data Fit

The data were fit well with only one station exceeding an r.m.s misfit of 2.0 and the stations with higher misfits had out-of-quadrant phases or were on the edge of the survey area (Figure 7.6b). In general, the data are fit very well as the r.m.s. misfits are below or near the ideal r.m.s misfit of 1.0 for most stations. Plotting the r.m.s. misfit by period for each station reveals there is not any significant scatter in fit between stations until long periods, however, this is expected as the data becomes noisier at longer periods (Figure 7.6a). Examples of data fits for the preferred resistivity model (s92p21r8) are shown in Figure 7.3 and Figure 7.4. The model response for the apparent resistivity and phase generally stays within the error bars for the diagonal and off-diagonal components demonstrating a satisfactory data fit for the model. The error bars are larger in the diagonal components of the apparent resistivity and phase, but this is a typical behaviour for magnetotelluric data as the impedances are smaller and thus there is a smaller signal to noise ratio than for the off-diagonal components. Overall, these sites can be

taken as representative of the major regions in the model, which shows that the data are being fit well across the entirety of the model. This is in agreement with the r.m.s misfit map shown in Figure 7.6(b).

Chapter 7 : 3-D Inversion of MT Data from the Slave craton

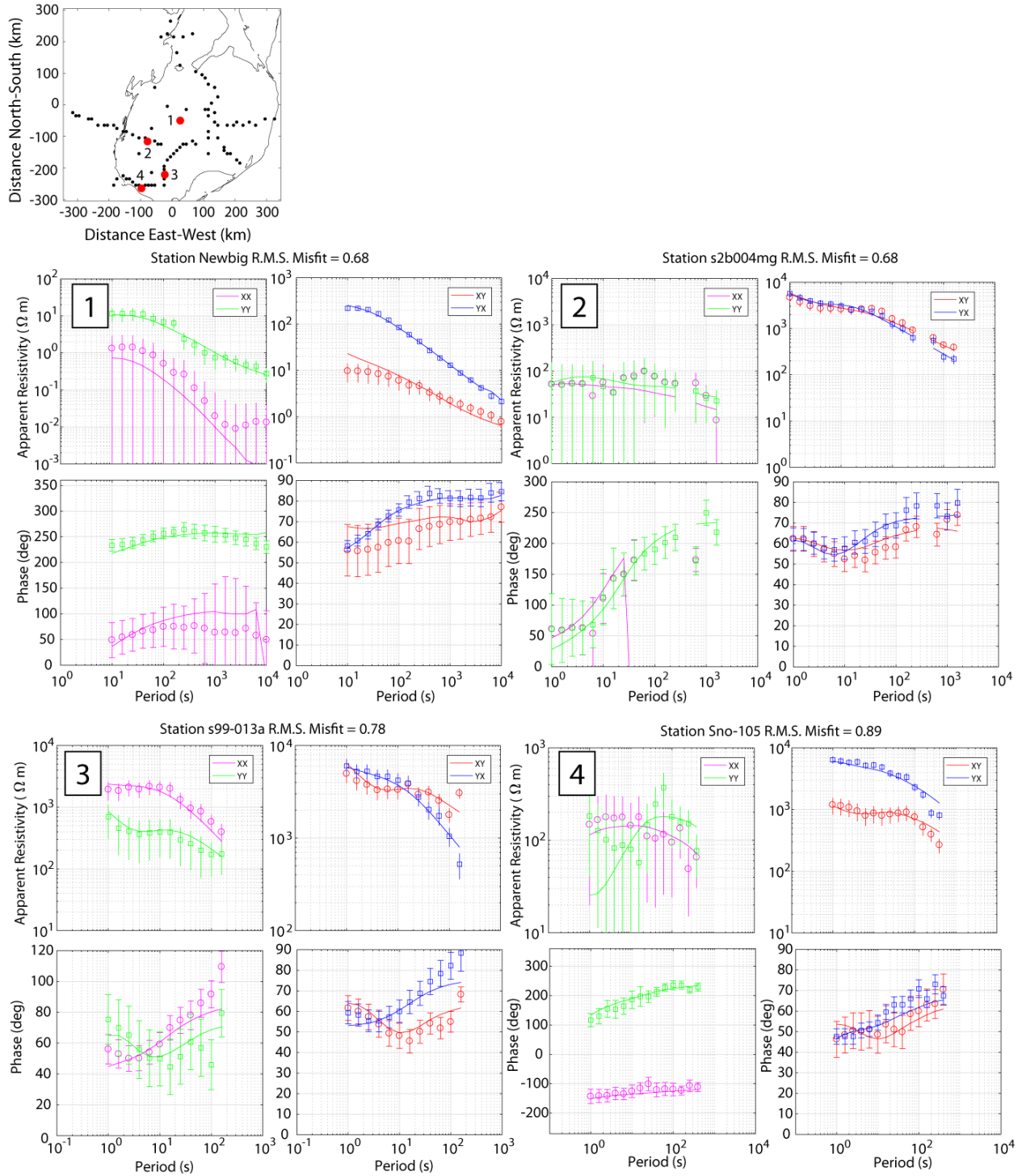


Figure 7.3: Examples of data fits for the preferred resistivity model (s92p21r8). The locations of the MT stations are shown on the map by red dots.

Chapter 7 : 3-D Inversion of MT Data from the Slave craton

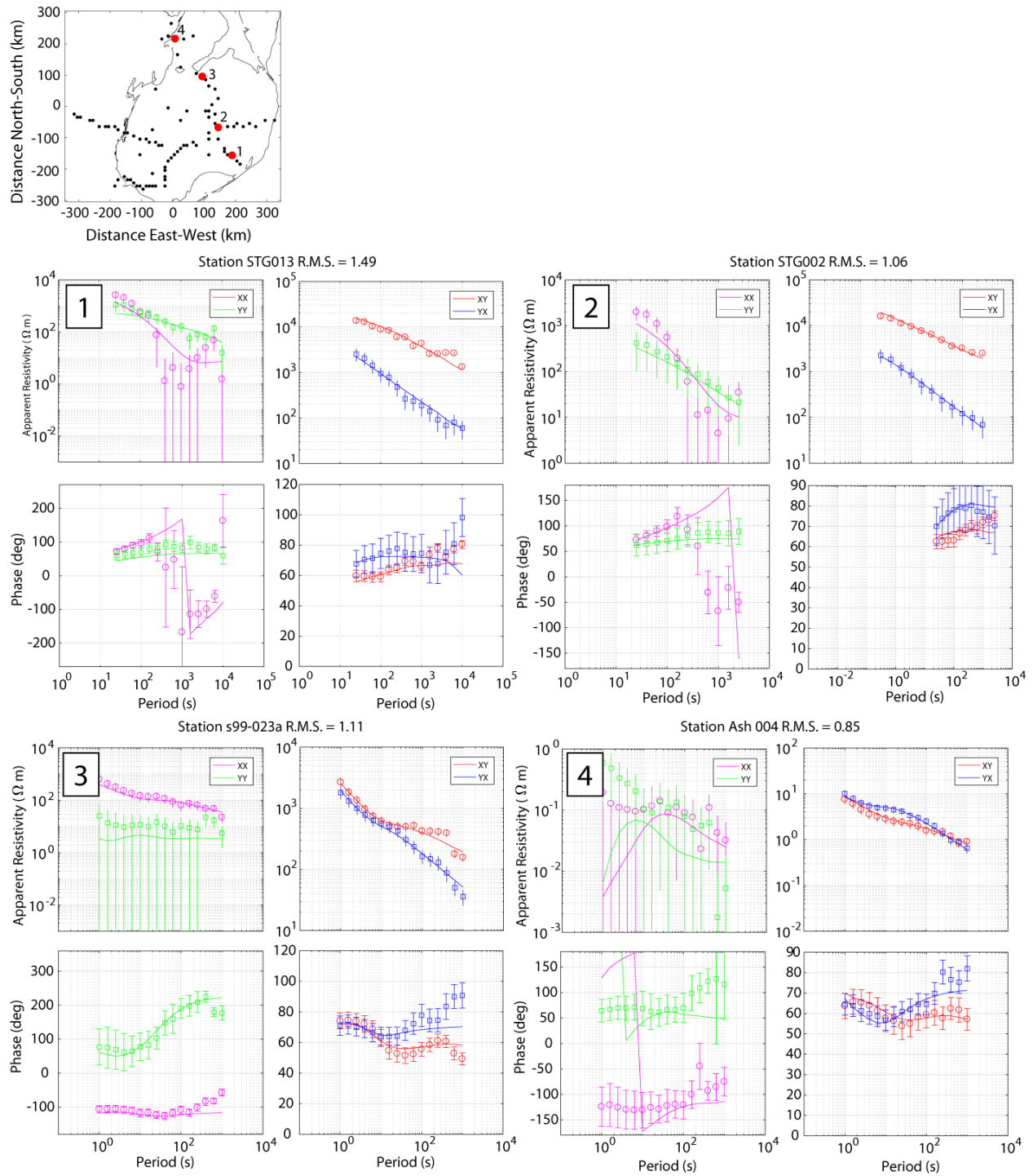


Figure 7.4: Examples of data fit for from the preferred resistivity model (s92p21r8). The locations of the MT stations are shown on the base map by red dots.

7.4 The 3-D Resistivity Model (s92p21r8)

The resistivity model is presented as five representative profiles (Figure 7.5) that were extracted beneath the MT stations in the model and depth slices at four representative depths (60, 100, 160 and 220 km) (Figure 7.6(c-f)). Irregular profiles are shown rather than projecting stations onto straight profiles as the MT station distribution in the model is non-uniform and the resistivity of regions directly beneath MT stations are better resolved than regions that are laterally offset from the stations. The preferred resistivity model (s92p21r8) (Figure 7.5 and Figure 7.6) contains four primary conductive anomalies in the mantle and four primary crustal conductors with resistivities in the range of 1 - 100 Ωm . These major features are described in this section.

Upper Mantle Conductor (C1)

An upper mantle conductor with resistivity in the range 1 - 10 Ωm is located at a depth of approximately 100 km on profile B in Figure 7.5, and is labelled C1. In map view C1 is centred beneath Aylmer Lake and extends as far west as Lac de Gras (Figure 7.6d). Several conduit-like structures with resistivities of $\sim 100 \Omega\text{m}$ branch from C1 and extend upwards to crustal depths with the westernmost branch coinciding with Lac de Gras and the additional two branches penetrating the crust beneath Aylmer Lake (Profile B, Figure 7.5). The westernmost conductive branch can be seen to intersect profile E and is also labelled as C1 (Profile E, Figure 7.5).

Upper Mantle Conductor (C2)

An upper mantle conductor is observed on profile D in Figure 7.5(d), and is denoted as C2. The top of this feature is at a depth of ~ 100 km and it has a resistivity of around 10 Ωm . The top of C2 is relatively flat and except at its western edge where it appears to extend upwards and connect with a near surface crustal conductor.

Deep Mantle Conductor (C3)

A prominent decrease in resistivity is observed at a depth of 200 km on all profiles and reaches a minimum resistivity at a depth of 250 km (Figure 7.5(a-e)). This conductor is labelled as C3 and extends across the entirety of the Slave craton with a resistivity in the range 50 - 100 Ωm . It appears to be less resistive in the southern part of the craton than in the north.

Upper Mantle Conductor (C4)

C4 is the shallowest upper mantle conductor in the preferred resistivity model (s92p21r8) and is located in the northern Slave craton. C4 has a resistivity of around 100 Ωm at a depth of \sim 70 km (Figure 7.6e).

Crustal Conductor (C5)

C5 is a crustal conductor at a depth of 20 km located east of Yellowknife on profile A in Figure 7.5. The conductor has a resistivity of around 100 Ωm .

Crustal Conductor (C6)

C6 is a crustal conductor beneath Gacho Kue at a depth of 20 km on Profile C in Figure 7.5. The conductor has a resistivity of around 1 - 10 Ωm .

Crustal Conductor (C7)

C7 is a crustal conductor on the east end of Profile D at a depth of 20 km in Figure 7.5. The conductor has a resistivity of around 10 Ωm .

Crustal Conductor (C8)

C8 is a crustal conductor, which lies at a depth of 20 - 40 km between Ekati and Jericho on Profile E in Figure 7.5. C8 has a resistivity of around 10 Ωm and lies primarily beneath Lake Contwoyto.

Crustal Conductor (C9)

C9 is a crustal conductor on Profile D between sites s2b-008 and s2b-009, which extends from the surface to a depth of about 3 - 5 km. C9 has a resistivity of around 1 Ωm .

The Electric Moho

A decrease in resistivity is observed at depths of \sim 30 - 40 km from very high resistivities ($>$ 10000 Ωm) to moderate resistivities (1000 - 10000 Ωm) along Profile A and E in Figure 7.5.

This change in resistivity is the electrical contrast between the crust and mantle otherwise known as the Electric Moho.

The preferred resistivity model (s92p21r8) will be discussed in detail in Section 7.8 including comparisons with previous studies and descriptions of more subtle resistivity structures that are also present in the model. The following sections of this chapter will focus on testing the reliability of the major features in the preferred resistivity model (s92p21r8), which is a necessary step before interpreting these features or comparing them with other studies.

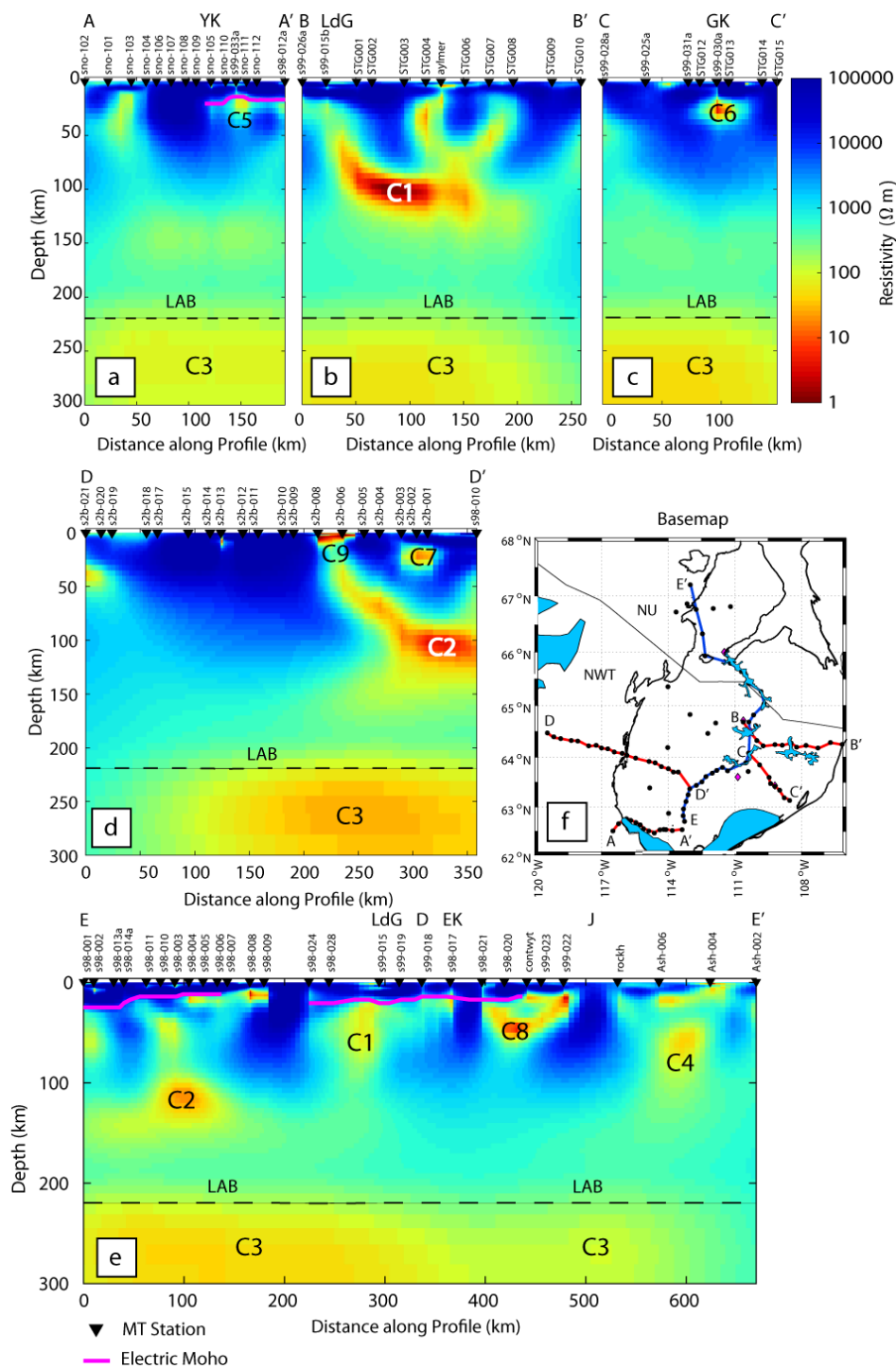


Figure 7.5: Model results are shown as five representative resistivity profiles across the Slave craton. The profiles are labelled as (a) Profile A, (b) Profile B, (c) Profile C, (d) Profile D and (e) Profile E and are shown in (f) on the base map. The pink line is the Electric Moho and black dots on the base map represent MT station locations. LdG = Lac de Gras; EK = Ekati; GK = Gacho Kue; D = Diavik; J = Jericho; YK = Yellowknife.

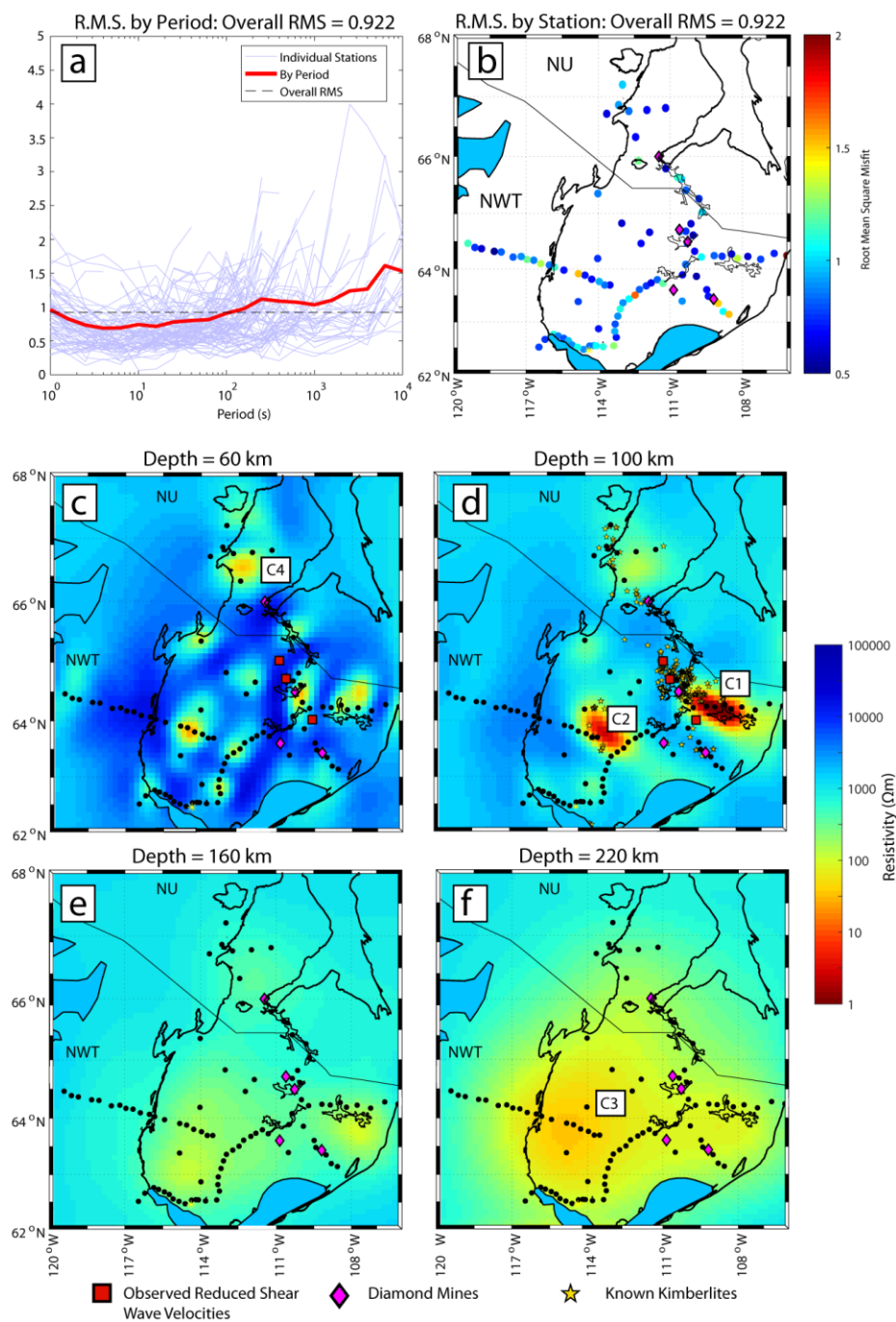


Figure 7.6: (a) R.M.S. misfit as a function of period for each station individual station (light blue lines), averaged r.m.s. misfit (red line) and overall model r.m.s. misfit (black dashed line). (b) Map view of station locations with each coloured circles representing the overall r.m.s misfit of the station. The model is shown at depths of (c) 60 km, (d) 100 km, (e) 160 km and (f) 220 km. On the 100 km depth slice diamond mines (pink diamonds), known kimberlite locations (yellow stars) and teleseismic sites with an observed reduction in shear wave velocities are also plotted.

7.5 Investigating the Inversion Parameters for the Preferred Resistivity Model (s92p21r8)

7.5.1 Effect of Varying the Error Floors

As outlined earlier in Section 6.6.3, the error floor defines a minimum error bar for each data point. A data points error bar is changed to the minimum error floor value if it is less than the assigned error floor and data points with error bars larger than the error floor remain unchanged. In the ModEM inversion (Kelbert et al., 2014) the error floor is applied to the impedance tensor, which differs from the Rodi and Mackie (2001) 2-D inversion which applies the error floors to the apparent resistivity and phase separately. Error floors of 5% and 10% were applied uniformly to the off-diagonal and diagonal components of the impedance tensor. An error floor of 10% (Figure 7.7b and Figure 7.8b) is preferable to the 5% error floor (Figure 7.7a and Figure 7.8a) as the r.m.s. misfit is closest to the ideal data fit of 1.0 suggesting that this error floor is in the ideal range. The main difference between resistivity models between the error floors is that the mantle conductors are spatially larger with the 5% error floor than the 10% error floor. However, the models are very similar overall and the main resistivity features were recovered using both error floors suggesting the model is robust.

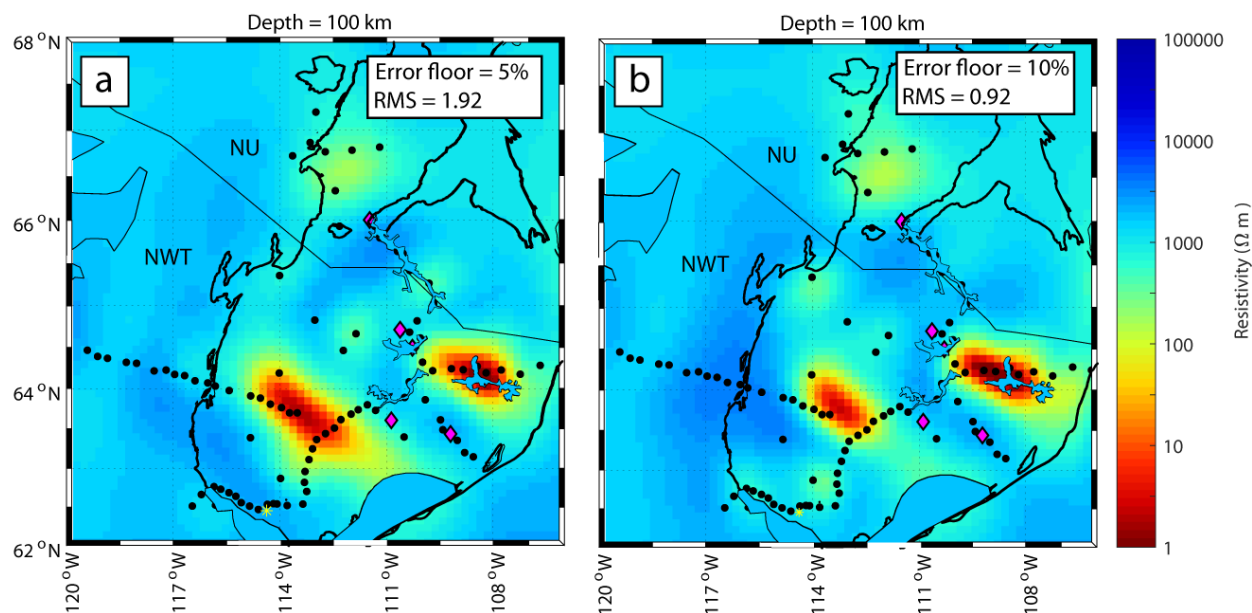


Figure 7.7: Horizontal slices of inversion models produced by varying the error floor applied to the diagonal and off-diagonal components of the magnetotelluric impedance tensor. (a) Horizontal model slice at 100 km depth using an error floor of (a) 5% and (b) 10%. The preferred model uses an error floor of 10% and is shown in (b).

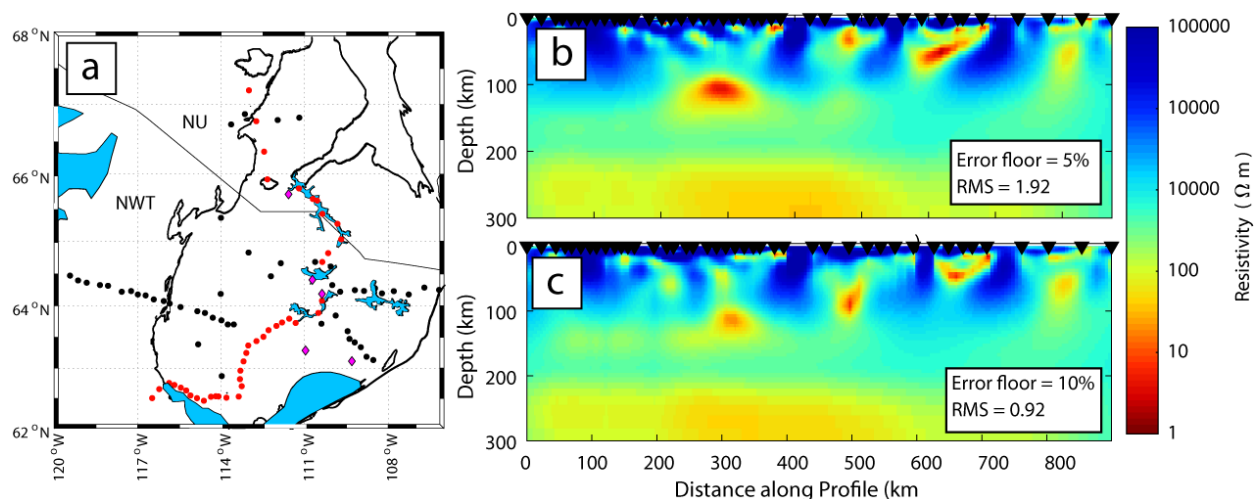


Figure 7.8: Vertical slices of inversion models produced by varying the error floor applied to the diagonal and off-diagonal components of the magnetotelluric impedance tensor. Stations along the vertical slices are highlighted in red in (a). Depth slices using an error floor of (b) 5% and (c) 10%. The preferred model uses an error floor of 10% and is shown in (c).

7.5.2 Effect of Varying the Resistivity of the Starting Model

An inversion searches for a resistivity model that fits the data. The algorithm used in this thesis uses an iterative process that starts from an initial resistivity halfspace, which will be referred to as the starting model in this section. It is important to investigate different starting models as the inversion will attempt to not significantly deviate from the chosen starting model and thus the starting model will influence the final resistivity model. The resistivity of the starting model for the preferred inversion model (Figure 7.5 and Figure 7.6) was tested for five orders of magnitude for 1, 10, 100, 1000 and 10000 Ωm to test the effect on the final inversion model. The resistivity models produced from this exercise show that using starting models of 1 and 10000 Ωm (Figure 7.10a and e) show a strong bias towards the initial resistivity model and have relatively high overall r.m.s. misfits (1.82 and 2.45 for 1 and 10000 Ωm respectively). These models were rejected as they do not fit the data well as indicated by the high r.m.s. misfits and they do not appear to deviate significantly from the starting model. These poor results could be a result of the ModEM inversion algorithm encountering a local minimum in the data fit due to these starting models being far away from the average resistivity value of the measured data. Indeed, resistivity values in the crust of the Slave craton exceed 100000 Ωm (e.g., Jones and Ferguson, 2001), which suggests that a very low resistivity starting model of 1 Ωm is insufficient to model this geological environment. On the other hand, a resistivity of 10000 Ωm for the

starting model may be too far away from the low resistivities found in the CSMC ($\sim 10 \Omega\text{m}$) causing the inversion difficulty in finding a suitable resistivity model to accommodate this contrast in resistivity.

The resistivity model produced using a $10 \Omega\text{m}$ starting model has an overall r.m.s. misfit of 1.32 (Figure 7.10b), which suggests the data are being fit well as values less than 1.5 are typically considered acceptable. However, similar to the resistivity models produced from starting models with resistivities 1 and $10000 \Omega\text{m}$, there is a strong bias towards the starting model and there is no clear structure beneath depths of around 100 km. There is no reason to expect the entirety of the cratonic lithosphere to have resistivities on the order of $\sim 10 \Omega\text{m}$ below depths of 100 km. C1 and C2 have resistivities in the range of 1 - $10 \Omega\text{m}$, but they do not cover the whole craton. Indeed, resistivity measurements on xenoliths (Bagdassarov et al., 2007) and laboratory experiments predict resistivities greater than $1000 \Omega\text{m}$ at these depths assuming a mantle composition of olivine, orthopyroxene, clinopyroxene and garnet. Therefore, the $10 \Omega\text{m}$ resistivity model is rejected.

The 100 and $1000 \Omega\text{m}$ models are preferable compared to the 1, 10 and $100000 \Omega\text{m}$ models as they have (1) low overall r.m.s. misfits (0.92 and 1.02 for the 1000 and $100 \Omega\text{m}$ starting models respectively), (2) the final resistivity models show structures deeper than ~ 100 km and (3) do not appear to be as heavily biased towards the value of the starting model (Figure 7.10c and d). Interestingly, the $1000 \Omega\text{m}$ model is able to achieve a similar data fit to the $100 \Omega\text{m}$ model, but finds more prominent upper mantle conductors than the $1000 \Omega\text{m}$ starting model. Additionally, a decrease in resistivity is clearly detectable at depths greater than 200 km in the $1000 \Omega\text{m}$ starting model while a similar boundary does not appear in the $100 \Omega\text{m}$ starting model. For these reasons, the difference between the 100 and $1000 \Omega\text{m}$ starting model was further investigated using synthetics in Section 7.5.2.1. It is also worth noting that the 100 and $1000 \Omega\text{m}$ starting models produced the most realistic resistivity models in the 2-D inversions (Section 6.6.4).

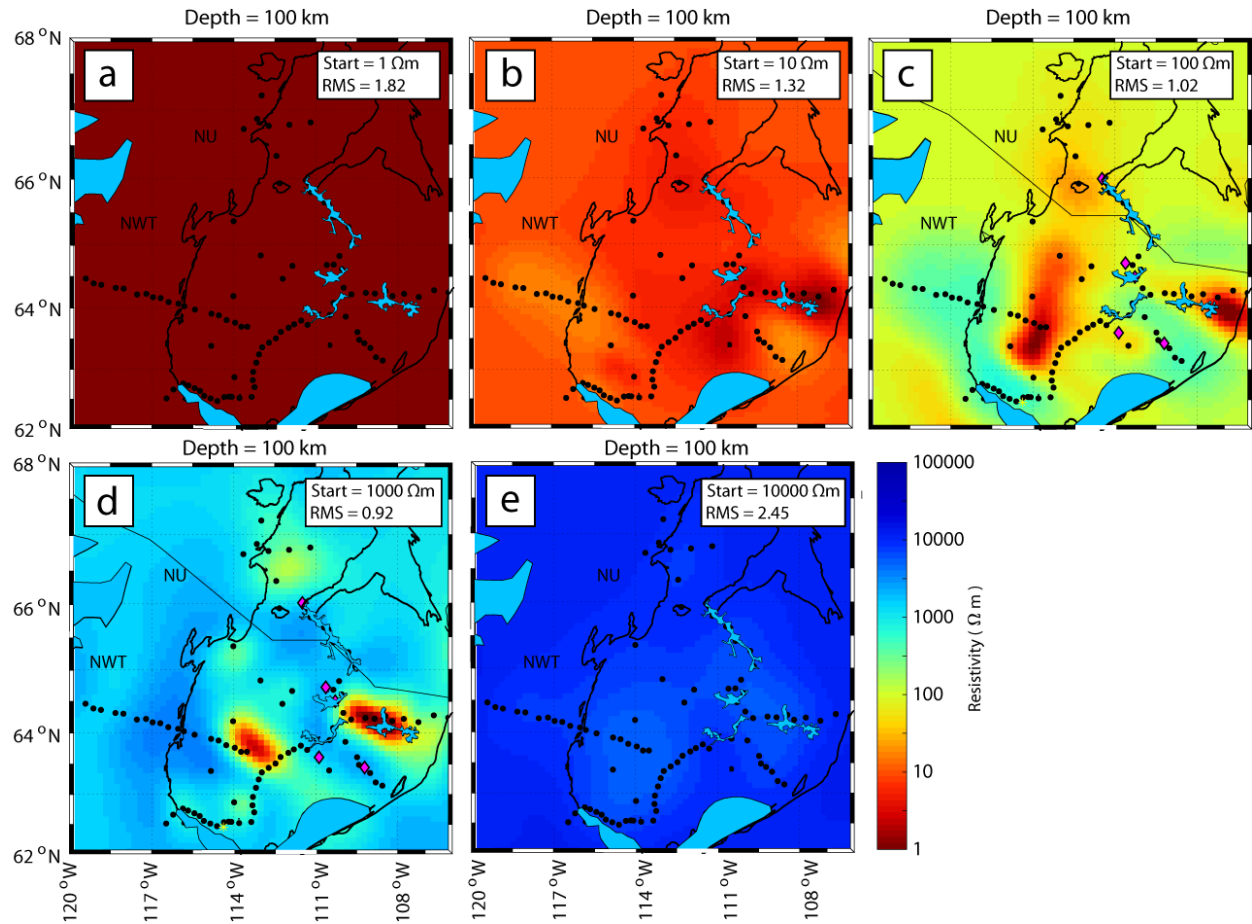


Figure 7.9: Horizontal slices of inversion models produced by varying the resistivity of the starting model. Horizontal model slices at 100 km depth produced using a starting model with resistivity of (a) 1 Ωm , (b) 10 Ωm , (c) 100 Ωm , (d) 1000 Ωm and (e) 100000 Ωm . The preferred model used a resistivity of 1000 Ωm and is shown in (d).

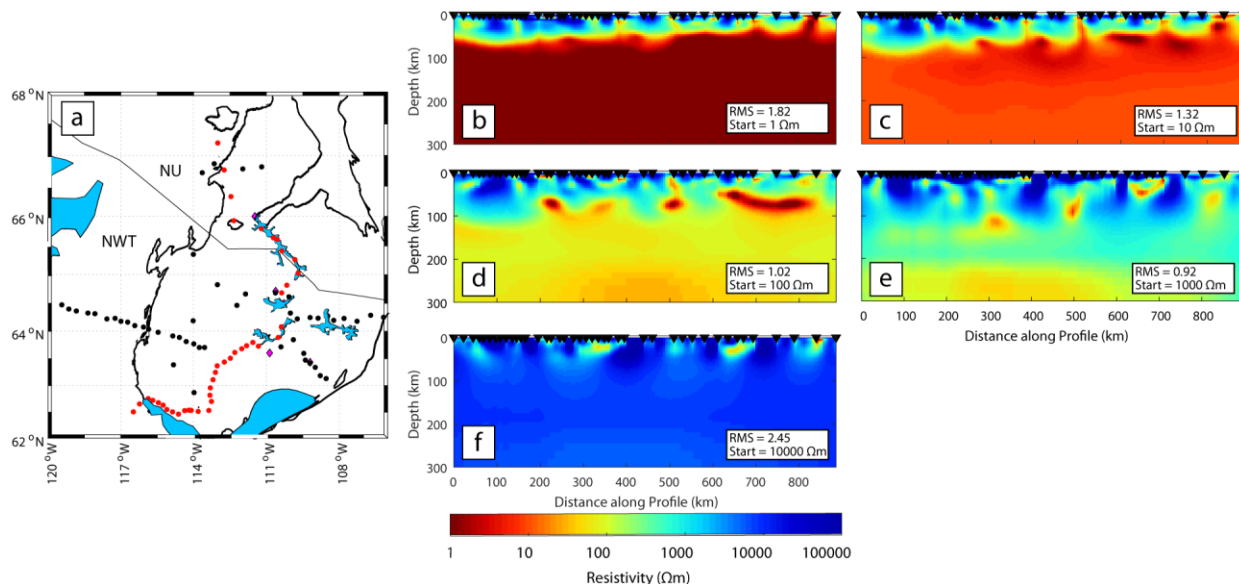


Figure 7.10: Model depth slices produced by varying the starting model used in the inversion. Stations along the depth slices are highlighted in red on the base map. Resistivity models are shown that were produced using starting models of (a) 1 Ωm , (b) 10 Ωm , (c) 100 Ωm , (d) 1000 Ωm and 10000 Ωm . The preferred model is used a starting model of 1000 Ωm and is shown in (d). NU = Nunavut. NWT = Northwest Territories.

7.5.2.1 Investigating the 100 Ωm and 1000 Ωm Starting Models with a Simple Three-Layer Synthetic

In Section 7.5.2 , it was not clear whether a 100 Ωm or a 1000 Ωm starting model produced the most reliable resistivity model. To test which starting model is better, data were created by calculating a forward response for a simple three-layer resistivity model. The data were then inverted using 100 and 1000 Ωm starting models and the results were compared. The starting model which is able to most closely reproduce the simple three-layer model will be considered the best starting model. The three-layer model was constructed as follows:

- (1) A 90 km thick layer of 10000 Ωm to represent the resistive crust and uppermost mantle.
- (2) A 300 Ωm layer extending from 90 km to 220 km to represent the moderately resistive sub-continental lithospheric mantle
- (3) A halfspace of 50 Ωm below 220 km to represent C3

These resistivity values were chosen as approximations of resistivities found in the Slave craton in previous magnetotelluric studies (Jones et al., 2001a; Jones et al., 2003; Spratt et al., 2009) and with the exception of the local regions with the CSMC are largely representative of the resistivities found in the cratonic lithosphere of the Slave craton. Synthetic MT data were calculated for periods of 1 - 10000s, and 5% Gaussian noise was added to the data to simulate a real data set. This synthetic test was performed using the actual distribution of MT stations. The 100 Ωm starting model converged to an overall r.m.s. misfit of 2.01 and the 1000 Ωm starting model converged to an overall r.m.s. misfit of 1.18. Evidently, the 1000 Ωm is able to compensate for the higher resistivities in the Slave craton better than a 100 Ωm starting model. In addition, using a 1000 Ωm starting model produces a resistivity model with clear layering (Figure 7.11d) with the exception of a handful of outlier curves, however, these are over one standard deviation outside of the predicted resistivity values (Figure 7.11c). In contrast, the 100 Ωm starting model did not recover the three layers effectively and produces a resistivity model where there is more scatter in the resistivity curves (Figure 7.11a) and taking the average resistivity predicts a resistivity that is over an order of magnitude less than the true resistivity of layer 2 (Figure 7.11b). Based upon these results the 1000 Ωm starting model is more reliable than the 100 Ωm starting model. This is likely due to the 100 Ωm starting model being too far from the above average resistivities found in the Slave craton.

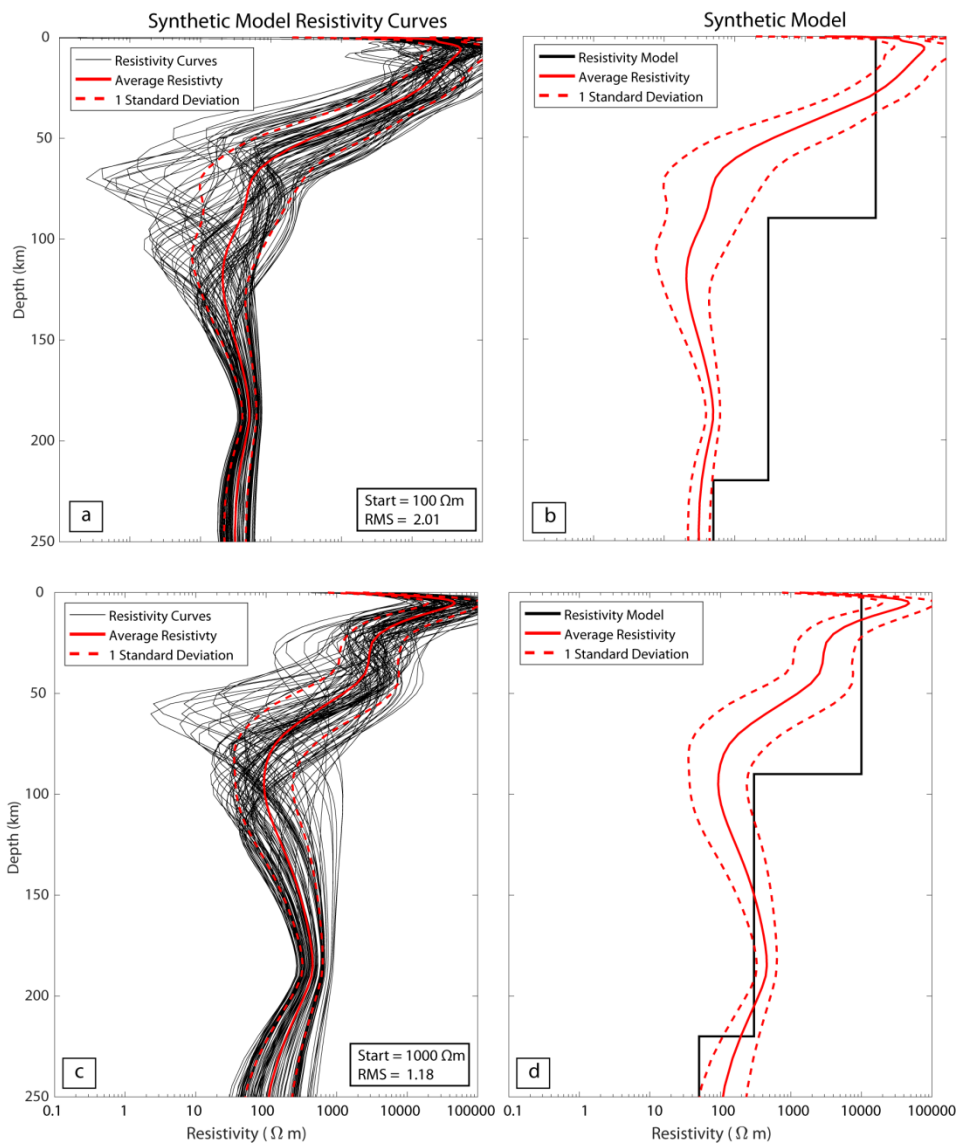


Figure 7.11: (a) Resistivity depth curves for each magnetotelluric station obtained from inverting the MT data produced from the three-layer synthetic with a 100 Ωm starting model. Each depth curve plotted in black corresponds to a station in the model. The solid red line is the average resistivity between all stations and the red dotted line corresponds to one standard deviation above or below the average resistivity. (b) The true synthetic three-layer model (solid black line) compared with the average resistivity obtained when inverting with a 100 Ωm starting model (red line) plus or minus one standard deviation (red dashed line). (c) Resistivity depth curves for each magnetotelluric station obtained from inverting the MT data produced from the three-layer synthetic with a 1000 Ωm starting model. Each depth curve plotted in black corresponds to a station in the model. The solid red line is the average resistivity between all stations and the red dotted line corresponds to 1 standard deviation above or below the average resistivity. (d) The true synthetic three-layer model (solid black line) compared with the average resistivity obtained when inverting with a 1000 Ωm starting model (red line) plus or minus one standard deviation (red dashed line).

7.5.3 Effect of Varying the Covariance Parameter

As with the 2-D inversions described in Section 6.6.1, a 3-D MT inversion searches for the spatially smoothest resistivity model that can fit the MT data to a specified statistical tolerance. Depending upon the degree of smoothing, a range of models can be obtained, which for the ModEM algorithm (Kelbert et al., 2014) is controlled by the covariance parameter. The covariance parameter in ModEM controls the degree of spatial smoothing applied to the resistivity model in the x, y and z direction. In the ModEM inversion package (Kelbert et al., 2014), the covariance parameter is in the range 0 to 1, but for practical purposes it is only varied between 0.1 and 0.9. The covariance parameter is analogous to the tau parameter in the 2-D inversion that was discussed in Section 6.6.1. A higher covariance results in a spatially smoother model while a lower covariance results in a spatially rougher model. Thus, an ideal 3-D inversion uses a covariance parameter that produces a model that fits the measured data, but does not over-smooth the model. 3-D inversions are much more computationally intensive than 2-D inversions, which means that it is often not feasible to test every covariance parameter and generate an L-curve. Hence, representative covariance parameters were tested for values of 0.1, 0.3, 0.4, 0.5, 0.6 and 0.9 rather than testing values evenly by 0.05 or 0.1 intervals. The resulting resistivity models are shown in Figure 7.5 and Figure 7.13. A covariance parameter of 0.3 was found to produce the best resistivity model as it does not smear the resistivity model significantly as seen for values of 0.6 and 0.9, but does not leave the model too rough as seen with a covariance of 0.1.

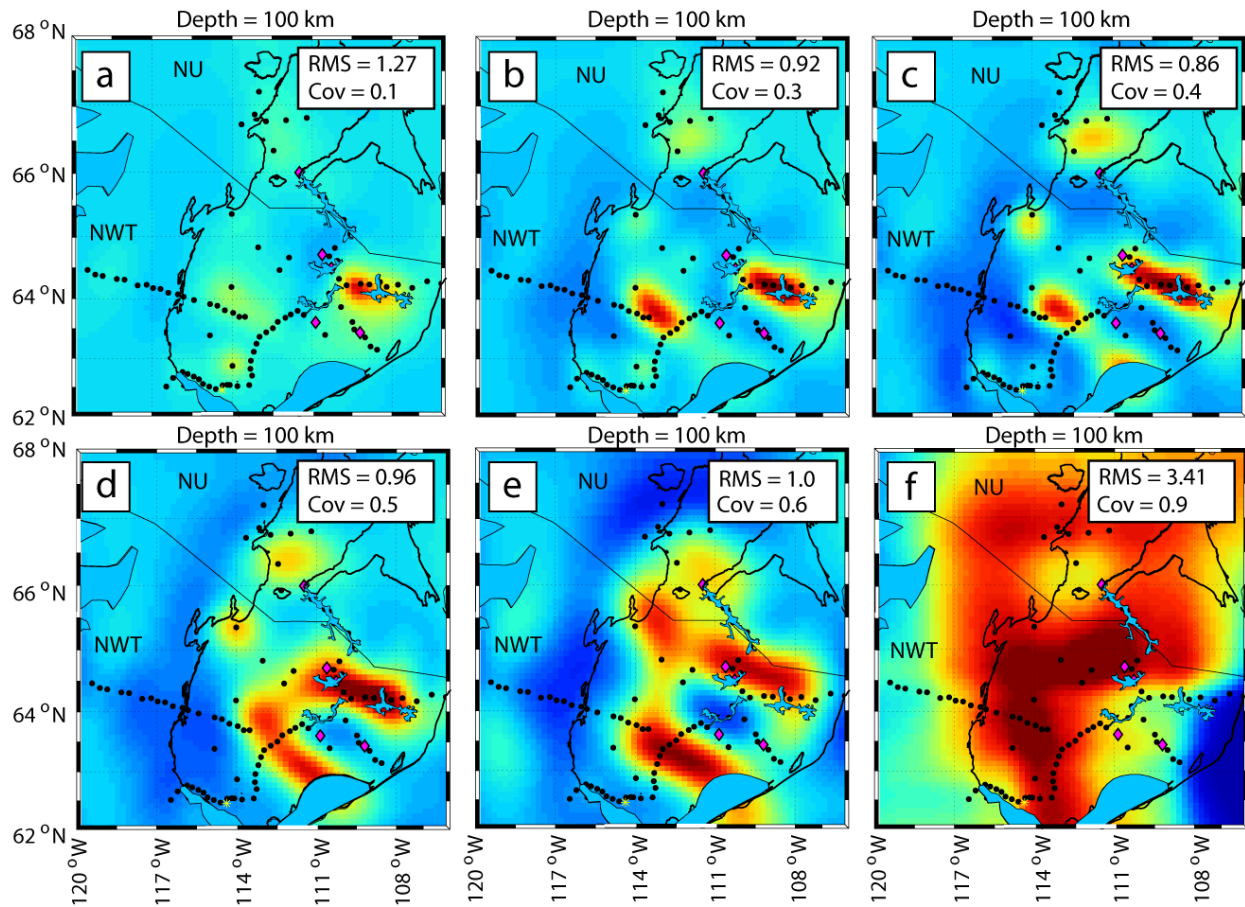


Figure 7.12: Horizontal slices of inversion models produced by varying the covariance parameter for inverting the magnetotelluric data. Horizontal model slices at 100 km depth produced using a covariance parameter of (a) 0.1, (b) 0.3, (c) 0.4, (d) 0.5 and (e) 0.6 and (f) 0.9. The preferred model uses a covariance of 0.3 and is shown in (b).

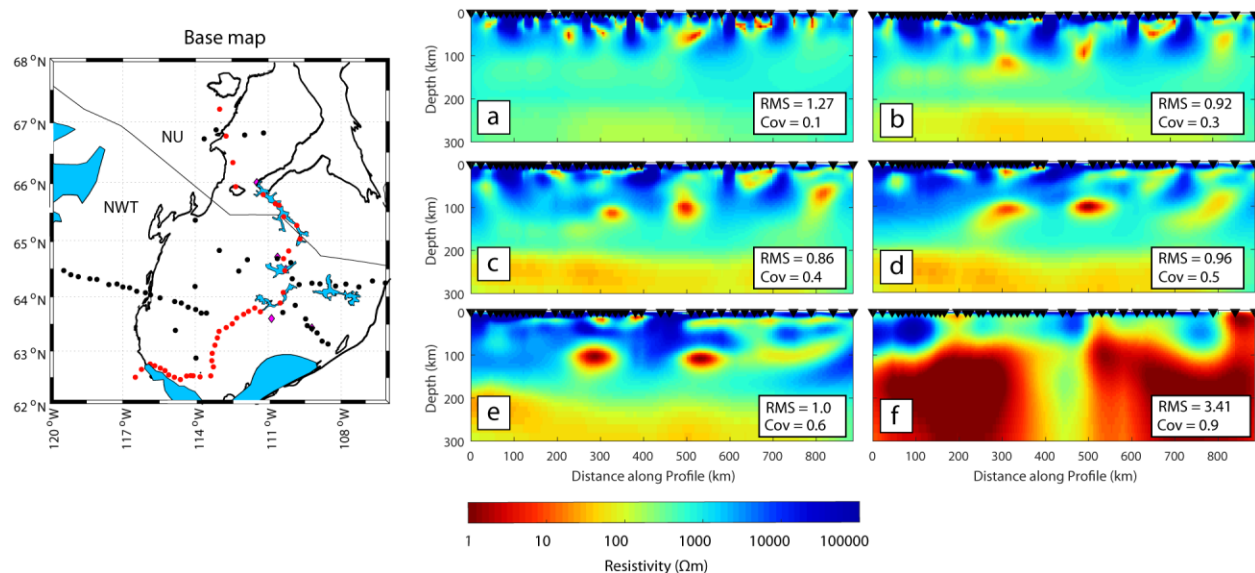


Figure 7.13: Model depth slices produced by varying the covariance parameter for the preferred resistivity model. Stations along the depth slices are highlighted in red on the base map. Resistivity models are shown that were produced using a covariance parameter of (a) 0.1, (b) 0.3, (c) 0.4, (d) 0.5, (e) 0.6, and (f) 0.9. The preferred model uses a covariance parameter of 0.3 and is shown in (d). NU = Nunavut. NWT = Northwest Territories.

7.6 Investigating the Preferred Resistivity Model (s92p21r8) Using Sensitivity Tests

In the following section the robustness of the preferred resistivity model (s92p21r8) (Figure 7.5 and Figure 7.6) and the major features will be investigated using two types of tests. The first set of sensitivity tests will use forward modelling to examine the effect of modifying C1, C2, C3 and C4 on the data fit to determine if these features are required by the measured data. The second set of tests will invert synthetic data generated for a specified resistivity models. This will give a better understanding of the resolution of the preferred resistivity model (s92p21r8) and the inversion's ability to recover features with similar geometries to as those in the preferred resistivity model (s92p21r8). These tests are discussed in Section 7.6.1 and Section 7.6.2

7.6.1 Forward Modelling

In this section, the resolution of model features C1, C2, C3 and C4 are investigated by comparing data fits between a modified resistivity model and the preferred resistivity model

(s92p21r8). The data fits are compared to determine if the features removed are robust i.e. required by the data, which is an important step for ensuring an accurate interpretation. Two methods are used to determine if there is a significant difference between the response of the preferred and modified resistivity models: (1) the Kolmogorov - Smirnov (KS) test and (2) a comparison of the data fit and r.m.s. misfit of individual stations.

The KS test compares the data distribution of a reference data set (i.e. the data response of the preferred resistivity model (s92p21r8)) and an empirical data set (i.e. the data response of the modified resistivity model) to determine whether there is a difference between the distributions for a given significance level. The chosen significance level is $p < 0.05$, which is arbitrary, however, this is generally considered a standard significance level in statistics. Thus, it is assumed in each KS test that $p < 0.05$ is statistically significant while $p \geq 0.05$ is considered statistically insignificant suggesting the two compared models are not distinguishable from each other. The second method for determining the robustness of model features examines the effect of modifying the model on (1) the r.m.s. misfit on a per site basis and (2) the forward data responses (e.g., Delucia et al., 2019). Looking at the change in r.m.s. misfit for individual sites after modifying the model provides more information than the overall r.m.s. misfit for the entire model. The overall r.m.s misfit averages the r.m.s. misfit for each station, which produces one number that represents the overall fit of the model, but this does not capture how the r.m.s. misfit changes locally in the region of the model, which has been modified. If the r.m.s. misfit increases significantly for sites in the region where the model was modified it suggests that the feature is required by the data. Conversely, if the r.m.s. misfit for the sites in the region where the model was modified does not change significantly it suggests that the feature is not required by the data. However, there is no level of significance to determine how much the r.m.s. misfit must change to be considered significant, which is a drawback compared to the more rigorous KS test discussed previously. Thus, in addition to increasing the r.m.s. misfit it is suggested that an additional criteria be met, which is that the forward data response of the modified model must also exceed the error bars of the MT data to be considered a significant change (Lee et al., in press, 2019).

7.6.1.1 Resolution Test of the C1 Conduit Structures

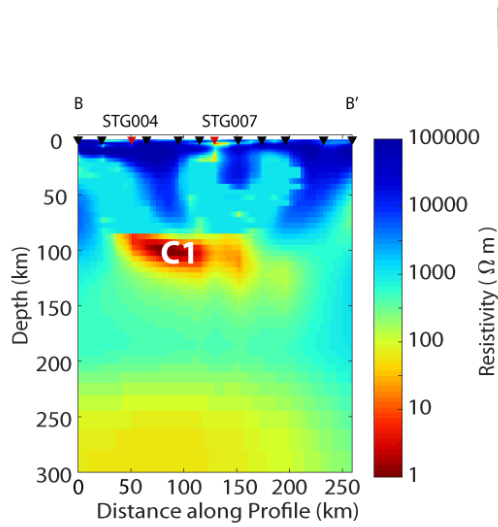
Three conduit structures branch from the conductor C1 in Figure 7.5(b). Similar features are not present elsewhere in the model and it remains unclear whether these structures are well

resolved. The robustness of the conduits are tested by changing their resistivity to 1000 Ωm to match the starting model resistivity and then computing the forward response of the modified resistivity model.

Figure 7.14 shows the modified resistivity model (Figure 7.14a) and the effect of modifying the model through (1) data fits for the preferred and modified solution (Figure 7.14b), (2) r.m.s. misfits of individual stations (Figure 7.14(c,d) and their respective r.m.s. misfit ratios (Figure 7.14f) and (3) the p-values generated with a KS test (Figure 7.14e) as described in Section 7.6.1. Example data fits are shown for stations STG004 and STG007 (Figure 7.14b), which worsen appreciably in the modified solution compared to the preferred solution as the apparent resistivity is overestimated and the phase is underestimated, particularly for the XY data. Furthermore, the apparent resistivity for the modified solution exceeds the error bars and the phase curves are on the lower end of the error bars. The worsening data fit is reflected in the r.m.s. misfit ratios for individual stations, which are on the order of 1.5 - 3 for stations overlying the conduits on profile A (Figure 7.14f). It should also be noted that the overall r.m.s. misfit of the model increases from 0.923 to 1.104 between models and individual stations in the modified solution also display substantially worse r.m.s. misfits when compared to the preferred model (Figure 7.14(c,d)).

The KS test returns a p-value of 0.0078 for the data set, which is below the threshold of 0.05 and thus is a statistically significant (Figure 7.14e). In addition, ten individual stations returned statistically significant p-values all of which were near the conduits (Figure 7.14e). It is concluded that the conduits are a robust feature in the preferred resistivity model (s92p21r8) as the resolution tests for the data revealed that removing these features results in (1) a worse data fit and (2) a statistically different data distribution under a for a $p < 0.05$ significance level.

a



b

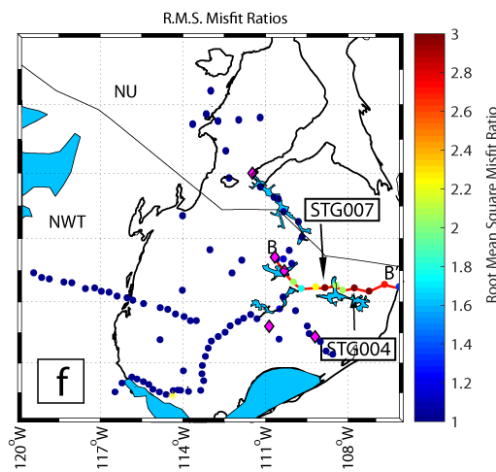
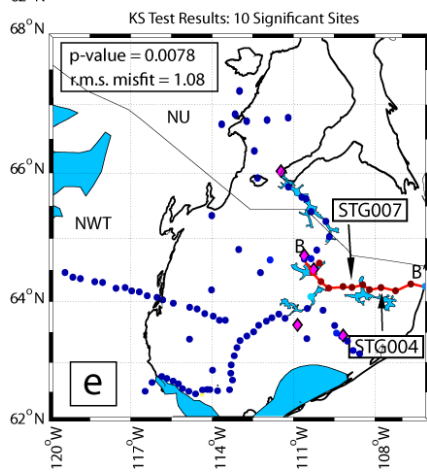
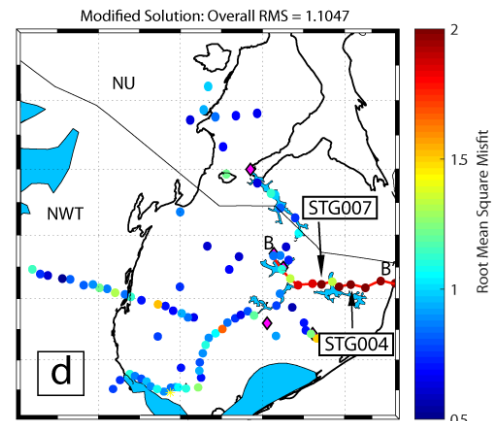
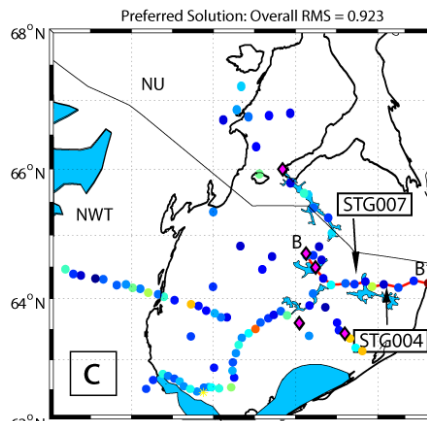
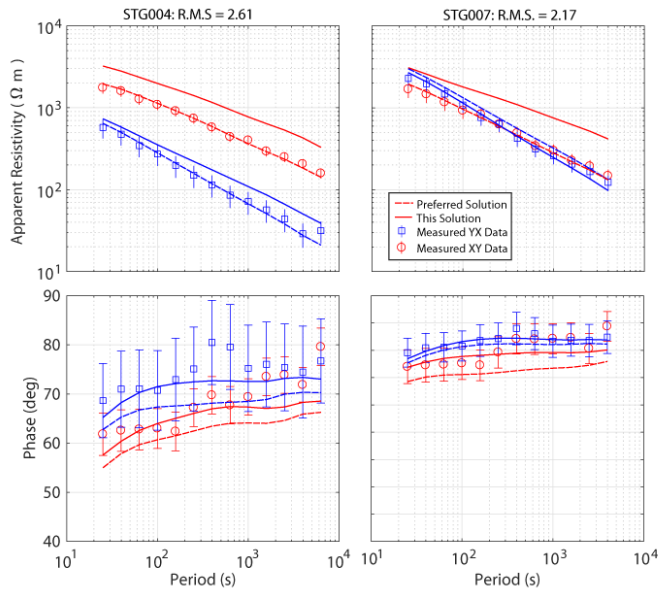


Figure 7.14: A resolution test to investigate conductor C1 (a) Profile B from Figure 7.5, which has been modified to replace the conduits that branch from C1 with a resistivity of $1000 \Omega\text{m}$. (b) Apparent resistivity and phase curves for the stations STG004 and STG007 are shown as examples of how the data fits change between the modified and preferred solutions. The sites STG004 and STG007 are indicated as red triangles in (a) and are labelled in map view in (c-f). Removing the conduits causes an overestimation of the apparent resistivity and an underestimation of the phase in the modified solution. (c) The r.m.s. misfit of the preferred solution shown as coloured circles. (d) The r.m.s. misfit of the modified solution shown as coloured circles. (e) P-values returned from the KS test shown as coloured circles comparing the preferred model and a modified model that removed the conduit structures from C1. The KS test returns a p-value of 0.0078 where a p-value less than 0.05 is considered statistically significant suggesting that the conduits are robust. (f) The r.m.s. misfit ratio between the modified solution and the preferred solution as coloured circles. A ratio greater than 1.0 indicates that the r.m.s. misfit has increased in the modified solution shown in (d) relative to the preferred solution shown in (c). Notably, the r.m.s. misfit ratio increases at all sites along Profile B further suggesting that the conduits are required to fit the data. These observations are taken as evidence that the conduits are robust structures in the model and are required by the data.

7.6.1.2 Resolution Test of C2

C2 is an upper mantle conductor on profile D and profile E in Figure 7.5. The resolution of this conductor requires investigation for two reasons: (1) it was not observed on profile D in previous magnetotelluric studies (Spratt et al., 2009) and (2) it is primarily constrained by MT stations on its edges leaving much of the conductor's extent to interpolation by the inversion. The resolution of C2 was tested by changing its resistivity to 1000 Ωm to match the starting model resistivity and then computing the forward response of the modified resistivity model.

Figure 7.15 shows the modified resistivity model (Figure 7.15a) and the effect of modifying the model through (1) data fits for the preferred and modified solution (Figure 7.15b), (2) r.m.s. misfits of individual stations (Figure 7.15 (c,d)) and their respective r.m.s. misfit ratios (Figure 7.15f) and (3) the p-values generated with a KS test (Figure 7.15e) as described in Section 7.6.1. Example data fits are shown for stations Snare and s2b002mg (Figure 7.15b), which change slightly in the modified solution compared to the preferred solution, however, the data responses for the modified solution remain within the error bars suggesting the data fit was acceptable. There was also not a significant change in r.m.s. misfit for stations near C2, as values increased from $\sim < 1$ to values in the range of 1 - 1.2 and the overall r.m.s. misfit increased to 0.923 to 0.955 (Figure 7.15(c,d)). These increases in r.m.s. misfit are still considered acceptable values for the modified solution, albeit, an acceptable r.m.s. misfit is arbitrary. The r.m.s. misfit ratios for sites near C2 were typically in the range of 1.1 - 1.3 showing a small increase in r.m.s. misfit with the exception of a few stations that had r.m.s. misfit ratios of as much as 1.5, but these were outliers relative to the majority of stations.

The KS test returns a p - value of 0.689 for the data set, which is above the threshold of 0.05 and thus is statistically insignificant (Figure 7.15e). However, one station in the data set returned a statistically significant p - value. The results of this resolution test seem inconclusive as the r.m.s. misfit increases for the modified solution, however, the data fit still remains in an acceptable range. The KS test returns a statistically insignificant p - value of 0.689 for the model and shows one station with a statistically significant change from removing the conductor. Therefore, C2 does not appear to be a robust feature in the data, however, there is also not enough evidence to suggest that C2 is entirely an artefact of the inversion. (2009)

Chapter 7 : 3-D Inversion of MT Data from the Slave craton

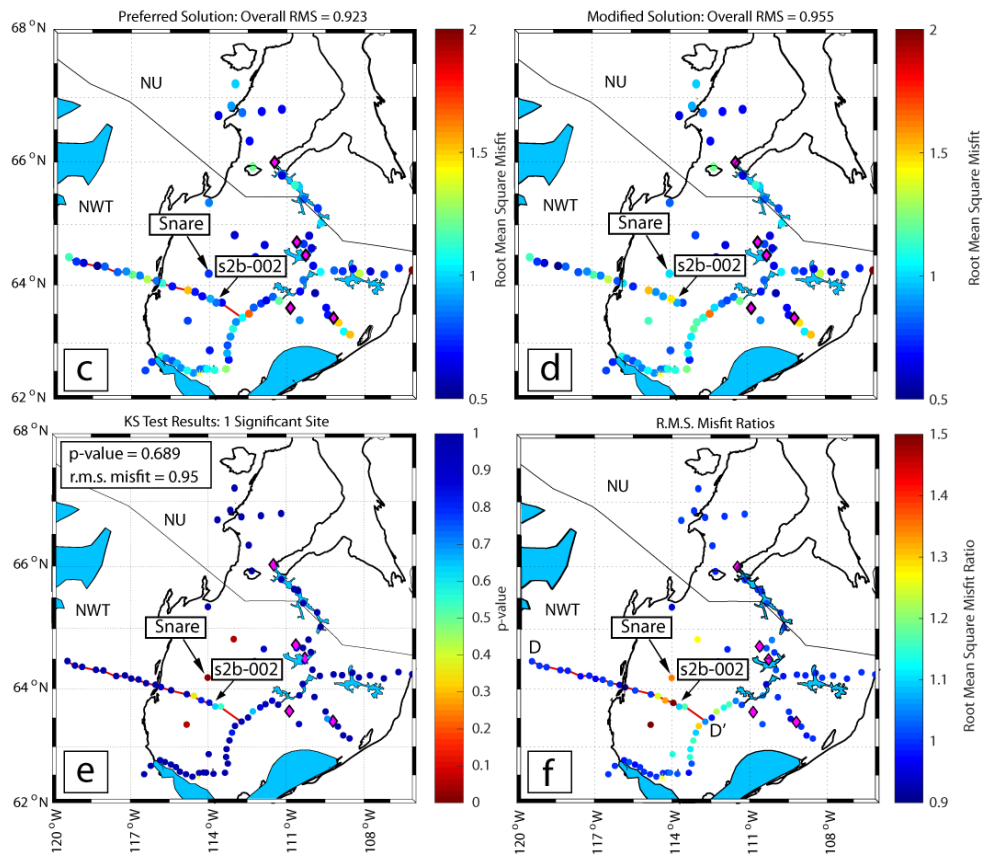
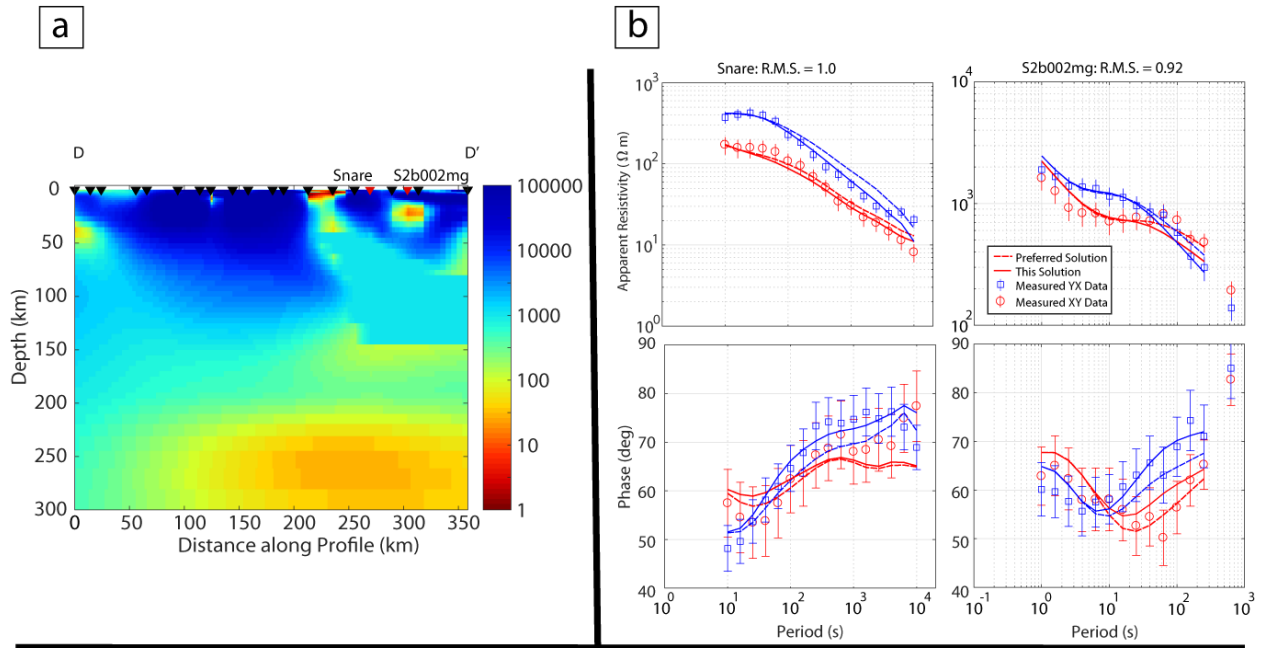


Figure 7.15: A resolution test to investigate conductor C2 (a) Profile D from Figure 7.5, which has been modified to replace C2 with a resistivity of 1000 Ωm . (b) Apparent resistivity and phase curves for the stations Snare and s2b-002 are shown as examples of how the data fits change between the modified and preferred solutions. The sites s2b002mg and Snare are indicated as red triangles in (a), but Snare has been projected onto the profile. Snare and s2b002 are labelled in map view in (c-f). (c) The r.m.s. misfit for each site of the preferred solution shown as coloured circles. (d) The r.m.s. misfit for each site of the modified solution shown as coloured circles. (e) P-values returned from the KS test shown as coloured circles comparing the preferred model and a modified model, which removed C2. The KS test returns a p-value of 0.689 where a p-value less than 0.05 is considered statistically significant suggesting that C2 may not be robust. (f) The r.m.s. misfit ratio between the modified solution and the preferred solution as coloured circles. A ratio greater than 1.0 indicates that the r.m.s. misfit has increased in the modified solution shown in (d) relative to the preferred solution shown in (c). Removing C2 does not appear to cause the data fits to become significantly worse in s2b-002 and Snare as the modified solutions generally remain within the error bars. The r.m.s. misfit ratio in (d) increases at most sites near Profile D, however, only by a factor of about 10%. These observations are taken as evidence that C2 may not be a robust feature in the model.

7.6.1.3 Resolution Test of C3

There is an obvious decrease in resistivity from 500 - 1000 Ωm to 50 - 100 Ωm at depths of 200 km along every profile in the preferred model (Figure 7.5). This interface appears uniformly across the entirety of the preferred resistivity model (s92p21r8) even in regions with a sparse station distribution. To determine if C3 is a required feature across the entirety of the model or is simply an interpolated feature, the resistivity of the C3 was changed to 1000 Ωm to match the starting model resistivity and then computing the forward response of the modified resistivity model.

Figure 7.16 shows the modified resistivity model (Figure 7.16a) and the effect of modifying the model through (1) data fits for the preferred and modified solution (Figure 7.16b), (2) r.m.s. misfits of individual stations (Figure 7.16 (c,d)) and their respective r.m.s. misfit ratios (Figure 7.16f) and (3) the p-values generated with a KS test (Figure 7.16e) as described in Section 7.6.1. Example data fits are shown for stations STG014 and prov (Figure 7.16b), which show significant variation at long periods (> 100 s) in the modified solution compared to the preferred solution. The modified forward response was unable to produce the low apparent resistivities and high phases in the data at periods greater than 100 s data far exceeds the error bars in the apparent resistivity and phase suggesting C3 is a robust feature (Figure 7.16b). This result also suggests that only the MT stations that have very long period data (greater than at least 100 s) are constraining the depth to C3, which is not a surprising result as this is the deepest resolved feature in the model. The r.m.s. misfits also show the greatest change for long period stations as the r.m.s. misfit ratio increases to values of at least 2.0 for stations with the longest periods in the data set (> 1000 s) (i.e. the lake bottom and float plane station groups labelled in Figure 5.1) whereas the rest of the data set was relatively unchanged with r.m.s. misfit ratios not exceeding values in the range 1.3 - 1.5 (Figure 7.16f). The overall r.m.s. misfit for the modified model also increased to 1.54 from 0.92 for the preferred model, which can be considered a significant increase. (Figure 7.16 (c,d)).

The KS test returns a p - value of 1.43×10^{-5} for the data set which, is below the threshold of 0.05 and thus is a statistically significant (Figure 7.16e). Additionally, seven individual stations returned statistically significant p-values all of which were lake bottom stations with periods up to 10000 s. It can be concluded that C3 is a robust feature in the preferred resistivity model (s92p21r8) as the resolution tests for the data revealed that removing C3 results in (1)

worse data fits, particularly at periods greater than 100 s and (2) a statistically different data distribution for a $p < 0.05$ significance level. Another notable result from this resolution test is that C3 is mostly constrained by the stations in the data set with the longest periods, but these stations are evenly scattered across the model suggesting C3 is well constrained spatially.

Chapter 7 : 3-D Inversion of MT Data from the Slave craton

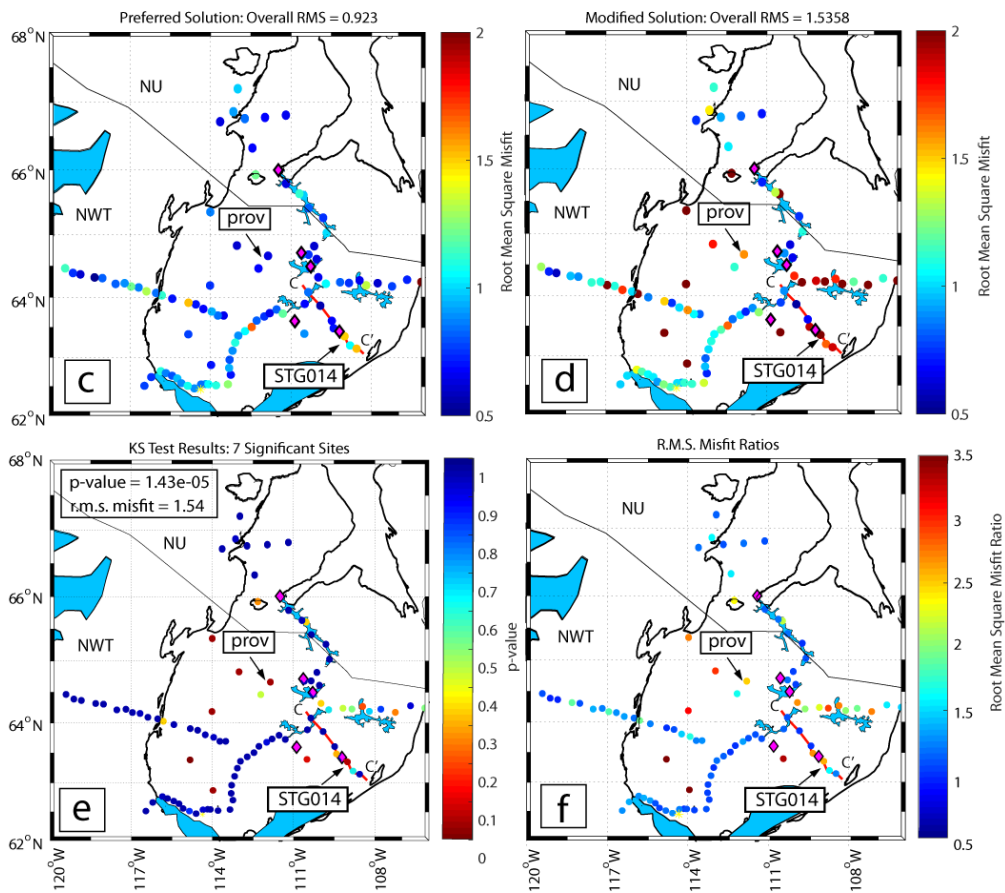
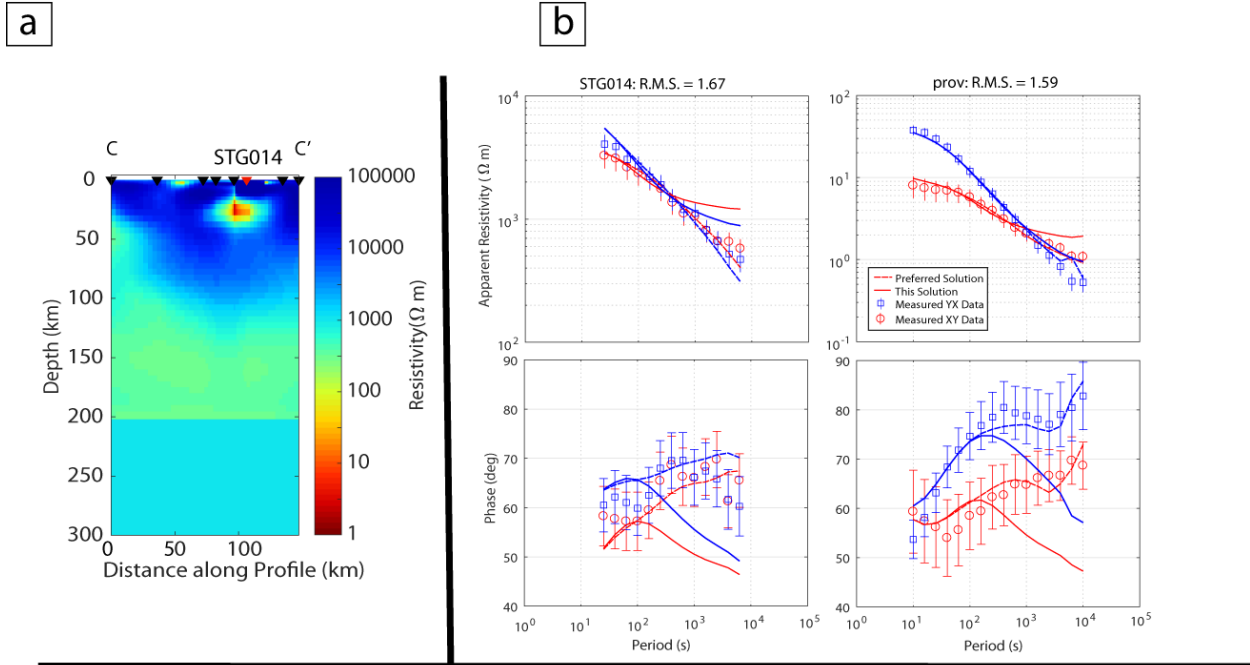


Figure 7.16: A resolution test to investigate conductor C3 (a) Profile C from Figure 7.5, which has been modified to replace C3 with a resistivity of $1000 \Omega\text{m}$. (b) Apparent resistivity and phase curves for the stations STG014 and prov are shown as examples of how the data fits change between the modified and preferred solutions. The site STG014 is indicated as a red triangle in (a) and prov is not located on profile C and thus is not shown. STG014 and STG007 are labelled in map view in (c-f). (c) The r.m.s. misfit for each site of the preferred solution shown as coloured circles. (d) The r.m.s. misfit for each site of the modified solution shown as coloured circles. (e) P-values returned from the KS test shown as coloured circles comparing the preferred model and a modified model, which removed C3. The KS test returns a p-value of $1.43\text{E-}05$ where a p-value less than 0.05 is considered statistically significant suggesting that C3 is robust. (f) The r.m.s. misfit ratio between the modified solution and the preferred solution as coloured circles. A ratio greater than 1.0 indicates that the r.m.s. misfit has increased in the modified solution shown in (d) relative to the preferred solution shown in (c). Removing C3 worsens the data fit appreciably, but seems to only affect the lake bottom and STG stations, which have the longest periods in the data set. This is taken as evidence that the C3 is a robust feature, but is likely only being constrained by a subgroup of data with the longest periods in the data set.

7.6.1.4 Resolution Test of C4

There is an obvious decrease in resistivity from 500 - 1000 Ωm to 50 - 100 Ωm at depths of 50 - 80 km north of Jericho on profile E in the preferred model (Figure 7.5). However, the station distribution is sparse in the north suggesting it should be investigated if C4 is a required feature by the data. To determine if C4 is a required feature the resistivity of the C4 was changed to 1000 Ωm to match the starting model resistivity and then the forward response was calculated for the modified resistivity model.

Figure 7.17 shows the modified resistivity model (Figure 7.17a) and the effect of modifying the model through (1) data fits for the preferred and modified solution Figure 7.17b), (2) r.m.s. misfits of individual stations (Figure 7.17 (c,d)) and their respective r.m.s. misfit ratios (Figure 7.17f) and (3) the p-values generated with a KS test (Figure 7.17e) as described in Section 7.6.1. Example data fits are shown for stations Ash-004 and Ash-006 (Figure 7.17b), which show minor variations at periods greater than 10 s in the modified solution compared to the preferred solution, but the data fit is still acceptable as the apparent resistivity and phases produced in the modified forward are within the data's error bars (Figure 7.17b). Thus, the changes in the data fit suggest that C4 is not a robust feature. The r.m.s. misfit ratio increases to values of 1.1 - 1.4 for northern stations overlying C4, but these increases can be taken as insignificant as the overall r.m.s misfit for the modified model only increases from 0.923 to 0.932, which can be considered negligible.

The KS test returns a p - value of 1.0 for the data set which is above the threshold of 0.05 and thus is a statistically insignificant (Figure 7.17e). There were also no individual stations returned with statistically significant p-values. Therefore, it can be concluded that C4 is not a robust feature in the preferred resistivity model (s92p21r8) as the resolution tests for the data revealed that removing C4 (1) does not significantly affect the data fit, and (2) does not produce a statistically different data distribution for a $p < 0.05$ significance level

Chapter 7 : 3-D Inversion of MT Data from the Slave craton

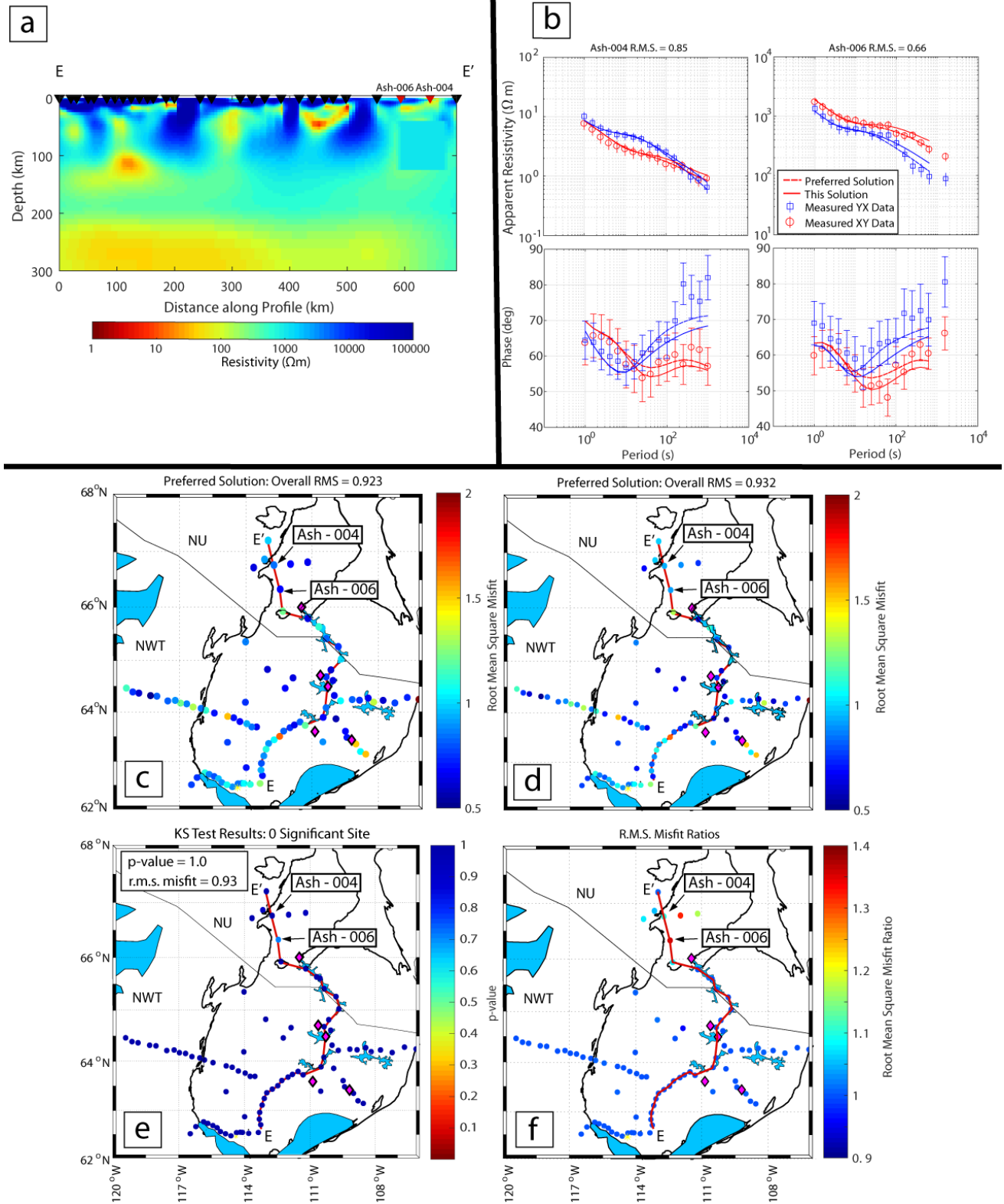


Figure 7.17: A resolution test to investigate conductor C4 (a) Profile E from Figure 7.5, which has been modified to replace C4 with a resistivity of 1000 Ωm . (b) Apparent resistivity and phase curves for the stations Ash-004 and Ash-006 are shown as examples of how the data fits change between the modified and preferred solutions. The sites Ash-004 and Ash-006 are indicated as red triangles in (a) and are labelled in map view in (c-f). (c) The r.m.s. misfit for each site of the preferred solution shown as coloured circles. (d) The r.m.s. misfit for each site of the modified solution shown as coloured circles. (e) P-values returned from the KS test shown as coloured circles comparing the preferred model and a modified model, which removed C4. The KS test returns a p-value of 1.0 where a p-value less than 0.05 is considered statistically significant suggesting that C4 is not robust. (f) The r.m.s. misfit ratio between the modified solution and the preferred solution as coloured circles. A ratio greater than 1.0 indicates that the r.m.s. misfit has increased in the modified solution shown in (d) relative to the preferred solution shown in (c). Removing C4 does not appear to cause the data fits to become significantly worse in s2b-002 and Snare as the modified solutions generally remain within the error bars. This is taken as evidence that the C4 is not a robust feature.

7.6.2 Synthetic Inversion tests

In the next set of tests, a synthetic inversion approach is used. Synthetic MT models were generated and then synthetic MT data were calculated for the period range 1 - 10000 s, which matches the period range inverted for the measured data. To simulate real data, 5% Gaussian noise was added to the synthetic MT data. The data were then inverted using (a) the actual, non-uniform station distribution and (b) an ideal uniform station distribution that added MT sites approximately every 50 km throughout the Slave craton.

7.6.2.1 Resolution Test of the Geometry of C1

The conductor C1 in the preferred 3-D resistivity model in Figure 7.5(b) appears to be similar to the Central Slave Mantle Conductor (CSMC), which was found in the central Slave craton by Jones et al. (2003) and thus is likely the same feature. However, C1 differs from that in previous publications in that it is centred beneath Aylmer Lake rather than Lac de Gras and is smaller spatially than found by Jones et al. (2003). The ability of the inversion to recover a conductor with similar geometry to the CSMC proposed by Jones et al. (2003) was tested to determine if the discrepancy could be a result of the irregular station spacing. A conductor was placed at 80 - 120 km depth with approximately the same spatial extent as proposed by Jones et al. (2003) to determine if such a conductor would be resolved with the current station distribution. Resistivity values of 1 and 10 Ωm were tested and compared to the actual station spacing and a hypothetical station distribution that added synthetic stations every ~ 50 km to create a more regular grid (Figure 7.18). The synthetic CSMC was recovered well with both the

current station distribution and the synthetic station distribution, which suggests that the current station spacing would resolve the CSMC as found in previous 2-D modelling. This result is not surprising since the majority of the synthetic CSMC coincides with regions of the model with the densest station spacing and as such the model should be well constrained in these areas. The edges of the conductor were imaged more clearly with the proposed station distribution, but the improvement was negligible and does not suggest that collecting these data would improve the resolution significantly for imaging a conductor of this geometry in the model. Therefore, feature C1 imaged in this study is likely not as large as the CSMC proposed by Jones et al. (2003). The modelling exercise in this chapter has proven that the inversion would be able to recover such a conductor if it was present.

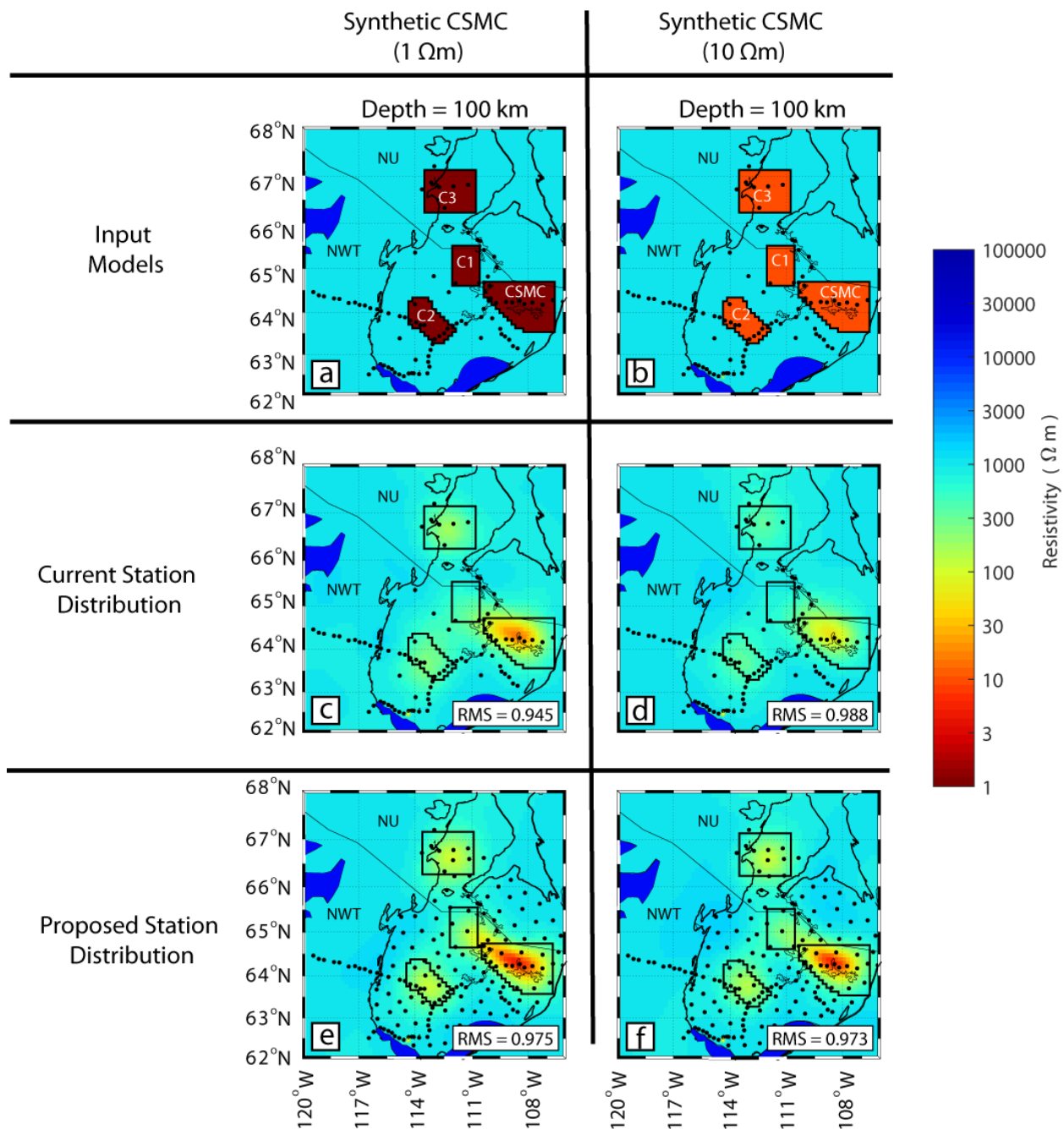


Figure 7.18: Synthetic test recovering a mantle conductor with the same spatial extent as the CSMC proposed by Jones et al. (2003). A black line in each panel outlines the extent of the input model. The thickness of the conductor is 40 km at depths of 80 - 120 km. The panels show (a) the 1 Ωm input model, (b) the 10 Ωm input model, (c) the recovered model for the 1 Ωm input model with the current station distribution, (d) the recovered model for the 10 Ωm input model with the current station distribution, (e) the recovered model for the 1 Ωm input model with the proposed station distribution and (f) the recovered model for the 10 Ωm input model with the proposed station distribution.

7.6.2.2 Investigation of the Depth to C3

The resistivity in the preferred model decreases to 50 - 100 Ωm at depths greater than 200 km reaching a minimum at ~ 250 km, however, the true depth to the LAB is ambiguous as the transition in resistivity occurs over tens of kilometres. Comeau et al. (2016) found that a sharp halfspace resistivity contrast will be imaged as a smooth resistivity gradient in the inversion model and concluded that the true depth to the top of a conductor would be imaged as the inflection point of the resistivity depth curves rather than the minimum resistivity. The procedure of Comeau et al. (2016) is used to investigate the depth of the LAB by inverting for a simple two-layer model which was constructed as follows:

- (1) A 220 km thick layer of 1000 Ωm to represent the resistive lithospheric mantle.
- (2) A halfspace of 100 Ωm below the resistive mantle to represent C3

Synthetic MT data were calculated for the period range 1 - 10000s, which matches the periods inverted to produce the preferred model. 5% Gaussian noise was added to the synthetic MT data. The station distribution matched the distribution in the preferred resistivity model (s92p21r8) and the r.m.s. misfit converged to a value of 0.97 after 132 iterations. The results of this test show that when recovering a conductive halfspace below a resistor, the top of the conductor coincides with the inflection point of the resistivity contours (Figure 7.19b), which is in agreement with the conclusions of Comeau et al. (2016). Therefore, the depth to C3 is taken as 210 ± 10 km, which corresponds to the inflection point of the resistivity depth curves for the preferred resistivity model (s92p21r8) (Figure 7.19a). Secondly, this test shows there is significant scatter in the recovered resistivity values, which proves that the difference in recovered resistivity between the north and south Slave craton is more likely an artefact of the station distribution rather than an actual change in the resistivity structure.

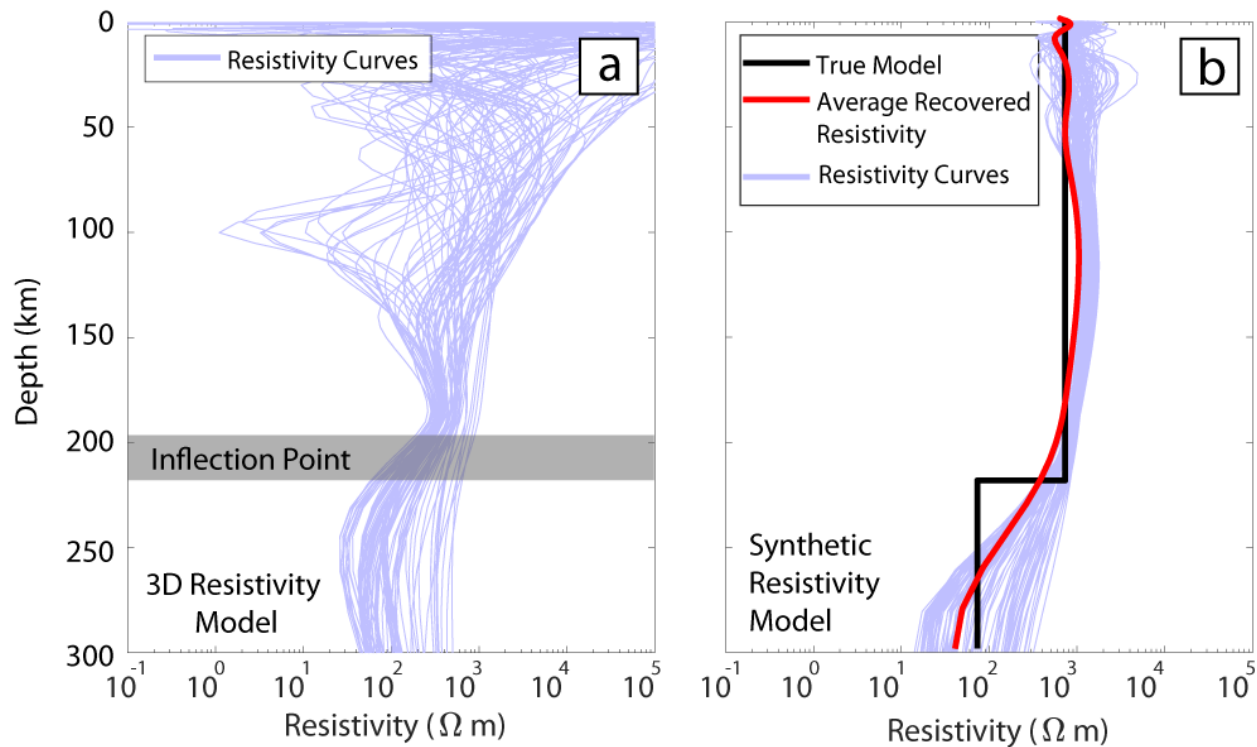


Figure 7.19: (a) Resistivity depth curves for each magnetotelluric station in the preferred 3-D resistivity model. The depth to the top of the conductor is given by the inflection point of the resistivity depth curve in agreement with Comeau et al. (2016). (b) Results from a synthetic inversion showing the change in resistivity character when encountering a conductive halfspace. The average resistivity is given for all MT stations in the model (red line) compared to the true two layer model (black line). All recovered resistivity curves in the synthetic model are shown as light blue lines. The top of the halfspace is defined by the inflection point.

7.7 Other Inversions

As mentioned in Section 7.3, the preferred resistivity model (s92p21r8) was the result of a long process of trial and error. This section gives a brief overview of the inversions that were completed early in this project to show the progression towards the final resistivity model described in Section 7.3. This includes earlier inversions that were investigated and a comparison between the ModEM and WSINV3DMT inversion algorithms to ensure the model obtained with the ModEM inversion algorithm is robust.

7.7.1 Initial Inversions

The initial inversions that were run for the data set included MT stations on the Slave craton as well as stations located to the south of the Slave craton. However, only every other station was used because of the memory constraints required for the large model size, which reduced the MT data density that could be used in the inversion. A coarse vertical mesh was also

used, which geometrically increased in thickness by a factor of 1.2 to compensate for the large model size. It was found that reducing the spatial density of MT data in the Slave craton reduced the resolution of the model too much to justify keeping the data to the south of the Slave craton. Thus, in all later inversion models the MT data to the south were not included, which allowed for all data on the Slave craton to be utilized and for a finer mesh to be used for the inversions. The mesh parameters are listed in Table 7.1 for comparison with the mesh used in the preferred model. Figures showing the inversion models for the initial inversions and control parameters investigated are in the Appendix.

7.7.2 Focussed Inversions

Inversions completed after the initial inversions yielded significantly better results as they were higher resolution due to using (1) a denser grid of MT stations and (2) a finer vertical mesh. Specifically, the vertical mesh had a constant thickness of 5 km for the depth range 30 - 155 km, which increased resolution in the upper mantle. However, these inversion models showed that there were potentially conductors at depths greater than 155 km, which were still not well resolved with this mesh. For this reason, the final resistivity models used a mesh with a vertical thickness of 5 km in the depth range 27 - 220 km. The mesh description is shown in Table 7.1 for comparison with the other inversion meshes. Figures showing the inversion models for the focussed inversions and the parameters investigated can be found in the Appendix.

7.7.3 Comparing the ModEM and WSINV3DMT Inversion Algorithms for a Data Subset

A subset of the magnetotelluric data from the Slave craton was inverted using the ModEM and the WSINV3DMT inversion algorithm to determine if the two inversion algorithms produce consistent models. The entire MT data set would have been used for comparison, however, the WSINV3DMT algorithm was found to unexpectedly stall during inversions leading to difficulties in producing larger models. Therefore, only a subset of the data were investigated, but this does not hinder the ability to compare the two inversion algorithms. If the inversion algorithms produce similar models from the same subset, then the preferred resistivity model (s92p21r8) using ModEM can be considered a robust model. The inversions were run using the same set of parameters as in the preferred model and starting models of 100 Ωm and 1000 Ωm . A description of the mesh used is listed in Table 7.1.

7.7.4 Comparison of the ModEM and WSINV3DMT Inversion Algorithm

The resistivity models are remarkably similar between the ModEM (Kelbert et al., 2014) and WSINV3DMT (Siripunvaraporn et al., 2005) inversion algorithms. The spatial extent of conductors are almost identical to between the two algorithms (Figure 7.20 and Figure 7.23) and in cross section the resistivity models show similar crustal and mantle structures (Figure 7.21 and Figure 7.22). The main difference between the algorithms is that the resistivity of the CSMC in models obtained with ModEM seems to be more strongly influenced by the starting model than in the WSINV3DMT models. The resistivity of the conductors in the WSINV3DMT model appears to be $\sim 10 \Omega\text{m}$ for both starting models while the resistivity of the conductors in the ModEM models are $1 \Omega\text{m}$ and $10 \Omega\text{m}$ for the $100 \Omega\text{m}$ and $1000 \Omega\text{m}$ starting models respectively. However, the resistivity structure remains similar between both algorithms when using the same starting model suggesting that the ModEM algorithm is robust. Therefore, it was concluded that the ModEM algorithm will not produce significantly different results from other inversion algorithms and can be trusted for interpretation.

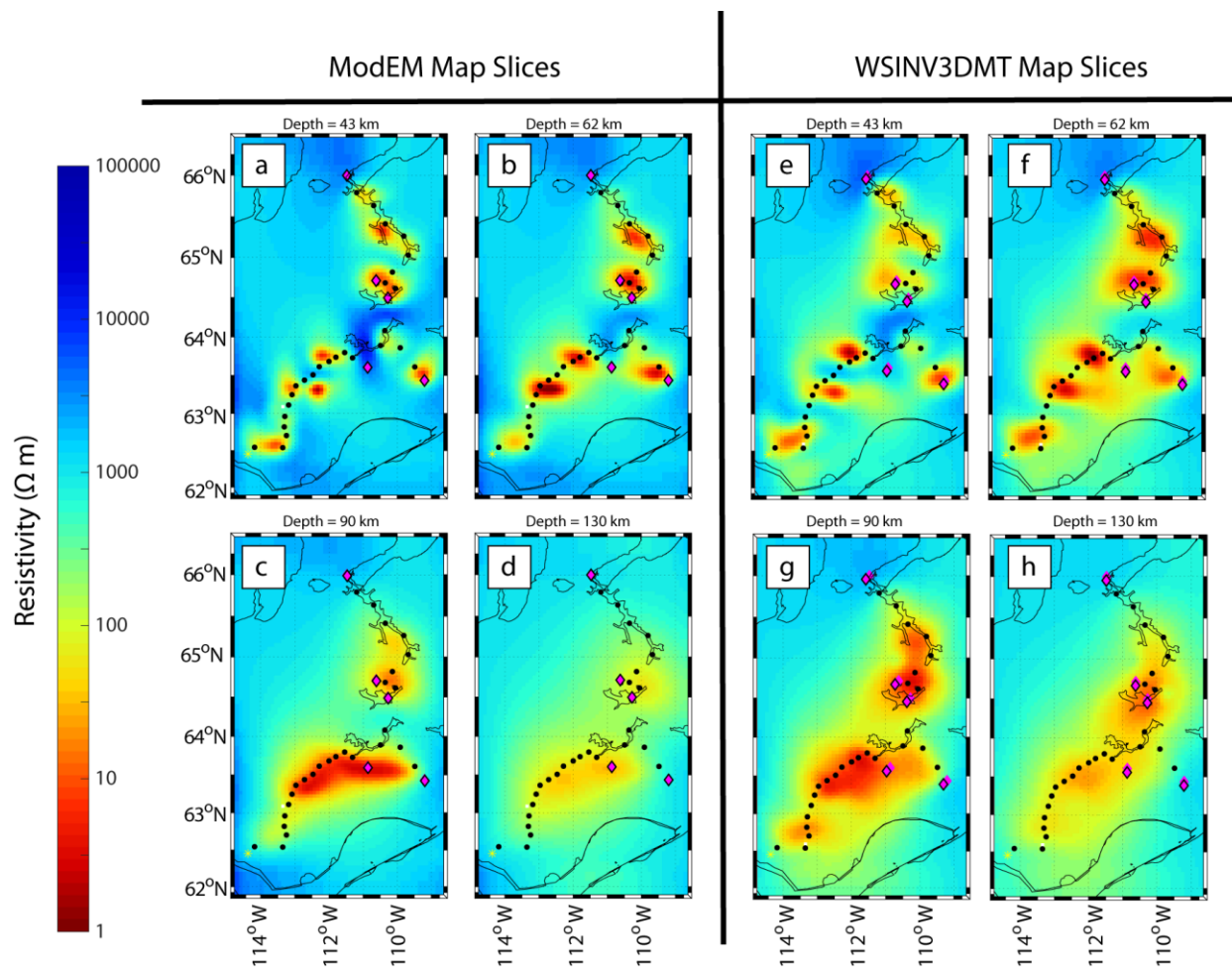


Figure 7.20: Map slices comparing models obtained from the WSINV3DMT and ModEM inversion algorithms for a subset of the Slave magnetotelluric data at depths of (a,e) 43 km, (b,f) 62 km, (c,g) 90 km and (d,h) 130 km. The starting model was $1000 \Omega m$ and similar features are visible at each depth between the WSINV3DMT and ModEM models. The overall r.m.s. misfit for the WSINV3DMT and ModEM inversions are 1.02 and 1.67, respectively.

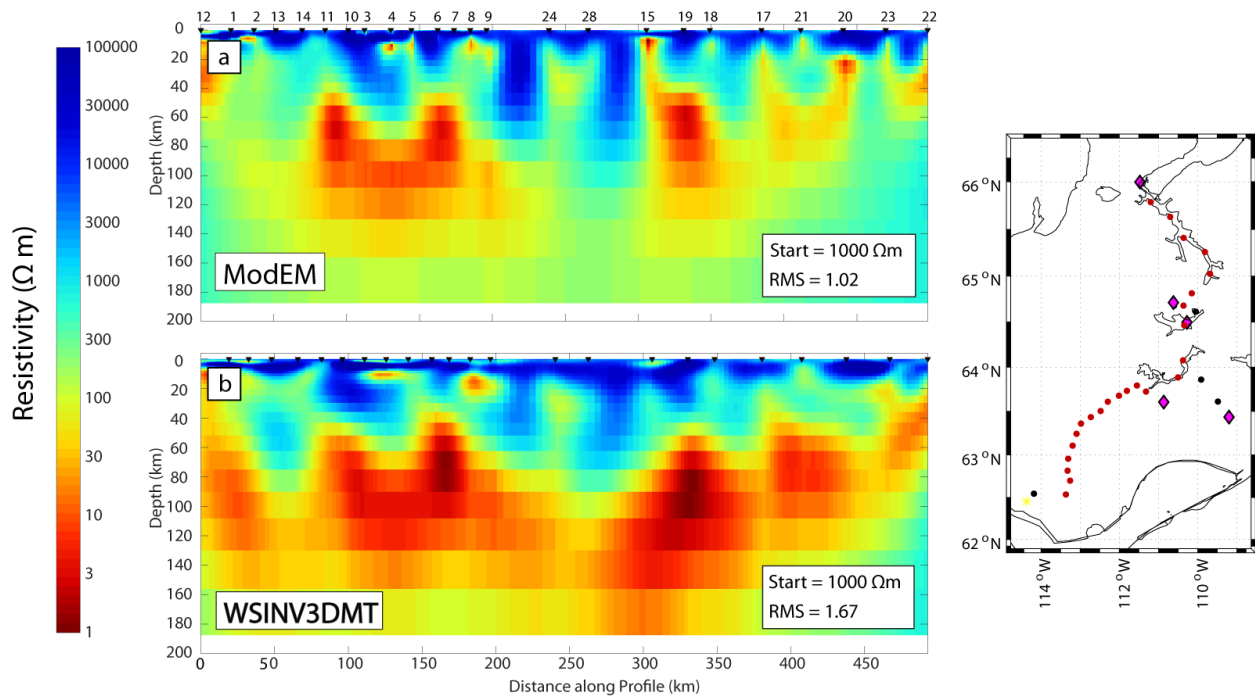


Figure 7.21: Comparison of depth slices for the models obtained with the WSINV3DMT and ModEM inversion algorithms for a subset of the Slave magnetotelluric data. Depth slices were extracted beneath the magnetotelluric sites, which are indicated as red dots on the base map. The starting model was 1000 Ωm and similar features are visible at each depth in both the WSINV3DMT and ModEM models. The r.m.s. misfit for the WSINV3DMT and ModEM inversions are 1.02 and 1.67 respectively.

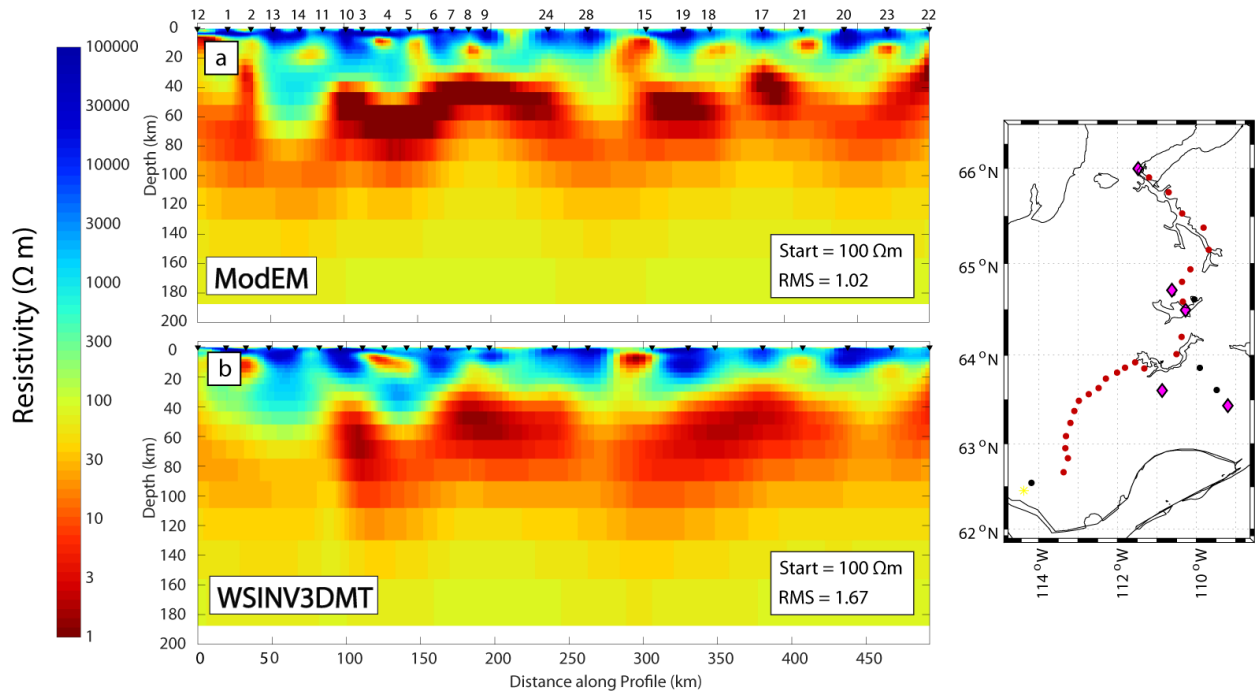


Figure 7.22: Comparison of depth slices for the WSINV3DMT and ModEM inversion algorithms for a subset of the Slave magnetotelluric data. Depth slices are extracted beneath the magnetotelluric sites, which are indicated as red dots on the base map. The starting model was 100 $\Omega\text{ m}$ and similar features are visible at each depth between the WSINV3DMT and ModEM models. The r.m.s. misfit for the WSINV3DMT and ModEM inversions are 1.02 and 1.67 respectively.

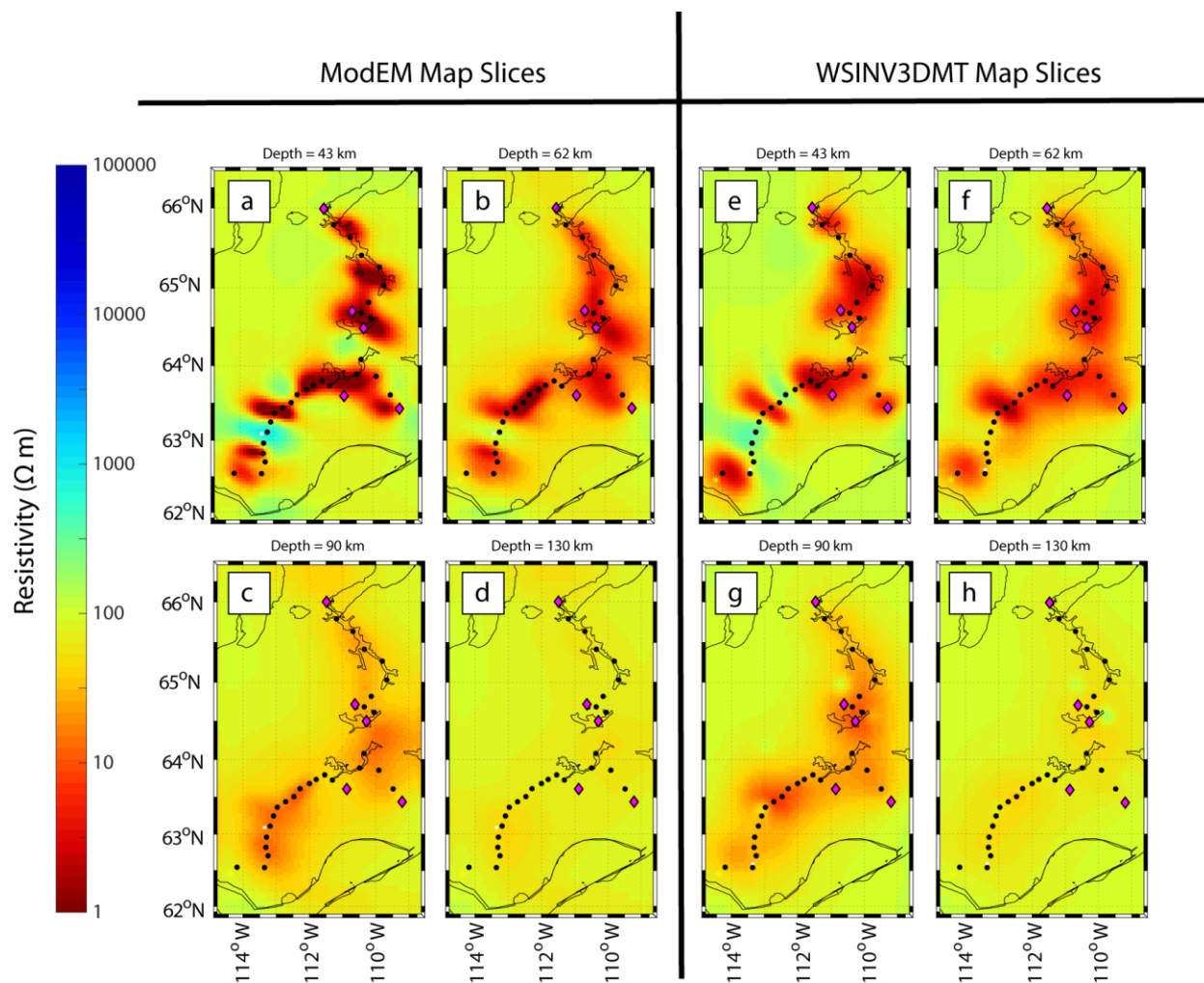


Figure 7.23: Map slices comparing the WSINV3DMT and ModEM inversion algorithms for a subset of the Slave magnetotelluric data for depths of (a,e) 43 km, (b,f) 62 km, (c,g) 90 km and (d,h) 130 km. The starting model was 1000 Ωm and similar features are visible at each depth between the WSINV3DMT and ModEM models. The r.m.s. misfit for the WSINV3DMT and ModEM inversions are 1.02 and 1.67 respectively.

7.8 Model Discussion

7.8.1 Crustal Structure (Depth of 0 - 40 km)

Southwestern Slave craton (Profile A, Figure 7.5)

The four stations at the western most end of Profile A (sno-101 - sno-104) show a 3 km thick moderately conductive layer (300 Ωm), which is likely an expression of the Phanerozoic sedimentary rocks of the Fort Simpson Sedimentary Basin to the south of the Slave craton. The remainder of profile A is located on the Slave craton where the crust is highly resistive ($> 10000 \Omega\text{m}$) characteristic of crystalline metamorphic rocks of the crust. The only exception is the

crustal conductor C5 located east of Yellowknife that has a resistivity of $\sim 100 \Omega\text{m}$. This feature (C5) was previously identified by Jones et al. (2003) and is suggested to be caused by mineralization along the Yellowknife fault (Jones and Garcia, 2006). The electric Moho is also visible on the eastern end of the profile as a transition from the highly resistive crust ($> 10000 \Omega\text{m}$) to a moderately resistive mantle ($1000 - 10000 \Omega\text{m}$), which was first observed on this profile by Jones and Ferguson (2001). A change in resistivity at the same depth as the seismically defined Moho cannot typically be observed in a resistivity model due to the presence of conducting phases in the lower crust which prevent detecting the subtle variation in electrical properties, however, the Slave craton's resistive lower crust permits imaging of this boundary (see Jones and Ferguson (2001) for a discussion of the electric Moho in the Slave craton).

East Central Slave craton (Profile B, Figure 7.5)

Profile B exhibits a highly resistive crust ($> 10000 \Omega\text{m}$), which is penetrated by three conduit-like structures with resistivities of $\sim 100 \Omega\text{m}$. These structures are particularly interesting as the westernmost conduit appears to extend beneath Lac de Gras and is close to the Ekati and Diavik diamond mines. These features were not resolved in previous 2-D modelling (Jones et al., 2003). Sensitivity tests in Section 7.6.1.1 showed that these structures were robust features in the model.

Southeastern Slave craton (Profile C, Figure 7.5)

Profile C shows a highly resistive crust ($> 10000 \Omega\text{m}$) with the exception of the lower crustal conductor C6 beneath Gacho Kue of unknown origin. It is possible that this is related to sulphide mineralization or graphite, but this remains speculative. A similar conductor was imaged in this location by Jones et al. (2003), but no interpretation was suggested.

Wopmay Orogen to the Western Slave craton (Profile D, Figure 7.5)

The five westernmost stations of Profile D overlie a thin moderately conductive ($\sim 300 \Omega\text{m}$) layer, which extends from site s2b-015 to the westernmost site s2b-020. This layer is likely the Phanerozoic sedimentary cover, which is present west of the Slave craton as previously interpreted by Spratt et al. (2009). The crustal anomaly C9 is also present between sites s2b-008 and s2b-005 and appears to extend and connect with the upper mantle conductor, C2. In previous

studies, a 2-D inversion of these stations imaged two separate crustal conductors (Spratt et al., 2009) whereas C9 is imaged as a single crustal conductor in Figure 7.5(d). The preferred resistivity model (s92p21r8) likely does not resolve the true geometry of near surface conductors as effectively as previous 2-D studies because frequencies > 1 Hz were not inverted and the horizontal size of the model cells are 10 km which is too large to resolve fine near surface details. Therefore, the geometry of the C9 is more than likely two distinct crustal conductors, which have been merged due to poor resolution near the surface in the preferred resistivity model (s92p21r8) Figure 7.5(d). Spratt et al. (2009) found the first conductor beneath site s2b-008 was quite shallow (~ 2 km) and was interpreted to be a localized deposit of interconnected sulphides. The second conductor was located between sites s2b-006 and s2b-007 and displayed a dipping geometry to depths of at least 30 km, which was ascribed to mineralization along the West-Bay Indin Fault Zone as the two features are spatially coincident. The preferred resistivity model (s92p21r8) shows a similar dipping conductor, however, it extends to mantle depths (100 km) and connects with C2. However, it is unclear whether this dipping conductor is an artefact of the resistivity model as when this feature and C2 were removed in the sensitivity tests in Section 7.6.1.2, it was found that it did not affect the data fit appreciably. This suggests that the dipping conductor may not be required by the data or at least the dip may not be required to extend to more than the 30 km depth found by Spratt et al. (2009). Finally, the preferred resistivity model (s92p21r8) reveals a moderately conductive crustal anomaly labelled as C7 (10 - 100 Ωm) in the lower crust on the eastern end of the profile, which coincides with a similar anomaly of ~ 500 Ωm found by Spratt et al. (2009). It was suggested that this anomaly may be a contact between crystalline plutonic rocks in the crust of the Slave craton and mafic lower crustal rocks (Spratt et al., 2009).

Central Slave craton (Profile E, Figure 7.5)

A distinct lower crustal conductor labelled as C8 with resistivity around 10 Ωm is present on profile E. C8 is located between the Ekati and Jericho mines and lies primarily beneath Contwoyto Lake. A similar lower crustal conductor was visible in the 2-D resistivity model along the same profile by Jones et al. (2003), however, the model cell discretization now more clearly resolves its geometry. The origin of this conductor is unclear and it was not interpreted by Jones et al. (2003) but could be again be due to graphite or sulphide mineralization. The electric

Moho is visible on the profile as a transition from a highly resistive crust ($> 10000 \Omega\text{m}$) to a moderately resistive upper mantle ($1000 - 10000 \Omega\text{m}$).

7.8.2 Upper Mantle Structure (Depth of 40 - 200 km)

Southern Slave craton (Profile A, Figure 7.5a)

The upper mantle is highly resistive east of sno-104 ($> 10000 \Omega\text{m}$) and moderately resistive west of this point ($100 - 1000 \Omega\text{m}$). This abrupt change in resistivity likely marks the edge of the cratonic root of the Slave craton. This profile compares remarkably well with the previously published 2-D resistivity model (Jones et al., 2003), which found a similar quasi 1D layered lithosphere in this region.

East Central Slave craton (Profile B, Figure 7.5b)

The conductor C1 is on Profile B as a prominent upper mantle conductor with resistivity $1-10 \Omega\text{m}$ at a depth of around 100 km. C1 is interpreted to be the Central Slave Mantle Conductor (CSMC) as first described by Jones et al. (2001a). In map view the CSMC is centred beneath Aylmer Lake and extends as far west as Lac de Gras (Figure 7.6d). The extent of the CSMC in the model is in good agreement with the 3-D MT model published by Snyder et al. (2014). The internal resistivity is similar to that obtained by 2-D inversion and which suggested a maximum resistivity of $30 \Omega\text{m}$ (Jones et al., 2003). However, the spatial extent of the CSMC is likely not as large as that suggested by Jones et al. (2003) from 2-D results. This is supported by the resolution tests in Section 7.6.2.1, which showed that a conductor of a similar size to that proposed by Jones et al. (2003) could be recovered satisfactorily using the same inversion parameters as the preferred resistivity model (s92p21r8). Furthermore, phase tensors showed that data at stations to the east and south of Lac de Gras are 3-D in nature and thus a 2-D inversion would not be able to accurately model the resistivity these regions as 2-D inversions cannot compensate for off profile effects or galvanic distortion. Beneath the CSMC the mantle is moderately resistive ($300 - 1000 \Omega\text{m}$), which is similar to the mantle at these depths ($> 100 \text{ km}$) along other profiles in the Slave craton.

Southeastern Slave craton (Profile C, Figure 7.5c)

The upper mantle beneath the south eastern Slave craton (Profile C, Figure 4) is homogeneous and quite resistive (1000 - 10000 Ωm) before transitioning to a moderately resistive upper mantle (300 - 1000 Ωm) at depths greater than 100 km. The resistivity structure of the mantle beneath Profile C compares well with the 2-D inversion model from Jones et al. (2003) for the same profile.

Wopmay Orogen to the Western Slave craton (Profile D, Figure 7.5d)

At depths of $\sim 50 - 100$ km there is a transition from high resistivities (> 10000 Ωm) east of the mapped surface expression of the Great Bear magmatic zone (GBMZ) to resistivities on the order of ~ 1000 Ωm west of the GBMZ. This decrease in resistivity was previously observed by Spratt et al. (2009) and was interpreted to be the western edge of the cratonic root of the Slave craton. Spratt et al. (2009) interpreted the decrease in resistivity observed west of the cratonic roots to be a result of a mantle shear zone between the Slave craton and the Wopmay Orogen. The shear zone may have reduced the size of the olivine grains compared to the mantle of the Slave craton and consequently decreased the resistivity.

On the eastern end of the profile (east of station s2b-004) there is an upper mantle conductor, which is denoted as C2 at a depth of ~ 100 km with an internal resistivity of ~ 10 Ωm . Sensitivity testing in Section 7.6.1.2 revealed that removing C2 from the preferred resistivity model (s92p21r8) does not have a large effect on the data fit suggesting that C2 may not be a robust feature. It is possible that C2 is a real feature as removing C2 did have some effect on the data fit, but the effect does not reach the level of significance required to conclude it is a required feature. This may be a result of all stations constraining the conductor being located on its edge (Figure 7.6d), which leaves much of the conductor's extent to interpolation by the inversion. Snyder et al. (2014) also imaged an upper mantle conductor in the same region, however, they did not perform a sensitivity test on this feature. Spratt et al. (2009) did not image an upper mantle conductor similar to C2 on Profile D, but penetration depth calculations for the MT signal revealed low resolution at depths greater than 100 km on the eastern end of the profile suggesting that a conductor may not have been resolvable under the 2-D analysis. Phase tensors (Figure 6.2) lend support to this hypothesis as data east of the S2B profile coinciding with C2 becomes highly 3-D ($\beta > 3^\circ$) at periods greater than 30 s, which cannot be modelled in 2-D.

Central Slave craton (Profile E, Figure 7.5)

The upper mantle structure beneath profile E displays more heterogeneity than on the other profiles as multiple upper mantle conductors were imaged. C1, C2, and C4 intersect profile E and are labelled on Figure 7.5(e). C4 is located in the most northern segment of the profile (~ 100 km north of Jericho beneath stations Ash-006 - Ash-002) and is moderately resistive (~ 100 Ωm) at depths of 70 km. Snyder et al. (2014) also imaged an upper mantle conductor in this region with a resistivity of 100 Ωm at a depth of 80 km. Resolution tests in Section 7.6.1.4 revealed that C4 was not required by the data, but it is still noteworthy that the surrounding mantle is about an order of magnitude less resistive than the mantle at similar depths to the south. Progressing south the mantle becomes highly resistive (> 10000 Ωm) at depths of up to 100 km with the exception of the edges of C1 and C2, but these conductors have already been discussed for Profiles B and D. At depths between 100 and 200 km the same moderate resistivities (300 - 1000 Ωm) are seen at the same depths as in the other regions of the Slave craton.

7.8.3 Deep Mantle Structure (Depths greater than 200 km, Figure 7.5)

At depths greater than 200 km the conductor C3 is the only notable feature in the model in Figure 7.5(a-e). Feature C3 is defined as an obvious decrease in resistivity from values in the range 300 - 1000 Ωm to the range 50 - 100 Ωm beginning at a depth of ~210 km on all profiles and reaches its minimum resistivity at a depth of 250 km. This decrease in resistivity occurs uniformly at depth and extends across the entirety of the Slave craton. Sensitivity tests investigated the effect of removing C3 on the data fit in the preferred resistivity model (s92p21r8) in Section 7.6.1.3 and found that C3 is a required feature as long period data were not fit well without the conductor. Further sensitivity tests in Section 7.6.2.2 investigated the depth of C3 and concluded that the depth to the top of the conductor is 210 ± 10 km, which corresponds to the inflection point of resistivity depth curves in the preferred model. This depth corresponds well with the depth to the base of the lithosphere reported by previous magnetotelluric studies (Jones et al., 2003; Spratt et al., 2009) suggesting that C3 is likely the asthenosphere. The depth to the lithosphere-asthenosphere boundary will be discussed further in the following chapter.

7.9 Conclusions

The magnetotelluric data presented in earlier chapters were inverted using the ModEM inversion algorithm to produce a 3-D resistivity model of the lithosphere in the Slave craton and the data were fit to a satisfactory level with an overall r.m.s. misfit of 0.92. The resistivity model shows four prominent upper mantle conductors, which were labelled as C1, C2, C3 and C4. It was found that C1 and C3 are robust features and C4 is not a robust feature. C2 was also investigated with synthetic inversions and was not found to be a clearly robust feature, however, there is also not enough evidence to definitely categorize C2 as an artefact.

C1 is interpreted to be the CSMC that was first described by Jones et al. (2001a). C1 is not as spatially extensive as the CSMC reported in previous studies. However, synthetic inversions found that a conductor with the geometry proposed by Jones et al. (2003) would be resolvable with the current station distribution. C3 is interpreted to be the asthenosphere with a depth of 210 ± 10 km with the depth chosen as the inflection point of the decrease in resistivity at C3. Feature C2 and C4 have not been interpreted as they are not robust features in the model. A subset of the MT data were inverted using both the WSINV3DMT and ModEM algorithms and it was found that the models were similar suggesting the ModEM model is robust. Determining the origin of the CSMC described in this chapter will be the focus of the interpretation in Chapter 8. Water content estimates in the mantle and the estimate of the LAB depth will also be discussed in Chapter 8.

Chapter 8 : Interpretation

8.1 Introduction

In the previous chapter, the preferred 3-D resistivity model was presented for the Slave craton and the robustness of the model was investigated. This chapter focuses on the interpretation of the preferred resistivity model (s92p21r8) presented in Figures 7.5 and 7.6. The analysis begins with a discussion of the thickness of the lithosphere, as determined from the 3-D resistivity model. The depth obtained from the model will be compared to previously published results from magnetotelluric exploration, seismic studies and xenolith analyses. Following this, petrologic data, laboratory experiments and teleseismic data are combined with the preferred resistivity model (s92p21r8) to determine the most likely explanation of the high conductivity for the Central Slave Mantle Conductor (CSMC). The relationship between the resistivity structure of the mantle in the Slave craton and distribution of diamonds is then discussed including a discussion of the relationship between upper mantle conductors and diamondiferous kimberlites. Finally, the chapter concludes with a discussion of the estimated water content in the upper mantle and a comparison of the 3-D resistivity model with published teleseismic studies.

8.2 Lithospheric Thickness

The lithosphere-asthenosphere boundary (LAB) is a first-order boundary that separates the rigid outer shell of the Earth from the underlying, weaker asthenosphere. Xenoliths, electrical resistivity and seismic velocities can provide indirect information about the change in properties that occurs at the LAB and can be used to estimate the depth of this interface (e.g., Eaton et al., 2009). Xenolith studies provide a snapshot of the depth to the LAB at the time of kimberlite emplacement, which can differ from seismic and magnetotelluric studies that image the present day asthenosphere depth.

Xenolith studies have been completed in each of the four domains of the Slave craton (i.e. the southwest, southeast, central and north regions of the Slave craton as outlined in Figure 2.2). In the northwest Slave craton, xenoliths from the Jericho pipe estimate the LAB to be at a depth of 190 km (Kopylova and Russell, 2000). In the southeast the depth of the LAB is 220 - 250 km (Kopylova and Caro, 2004) while in the southwest Slave craton the minimum depth is 160 - 190 km (Carbno and Canil, 2002). Finally, the thickness of the lithosphere beneath the central Slave craton was found to be at least 200 km (Pearson et al., 1999; Griffin et al., 1999).

There have been two previous MT studies that estimated the depth to the LAB prior to this study. Jones et al. (2003) estimated the depth to the LAB to be ~ 260 km using a 1-D resistivity model that averaged all available MT data in the Slave craton. However, it was argued that this depth may not be representative beneath the central Slave craton due to the majority of the stations being concentrated in the southern portion of the craton aliasing the depth estimate (Jones et al., 2003). In order to find a representative lithospheric thickness beneath the central Slave craton, Jones et al. (2003) used long period MT data obtained from a lake bottom MT station beneath Lac de Gras and found that the depth of the LAB was ~ 200 km by fitting a 1-D resistivity model to the MT data. A depth estimate for the LAB in the western Slave craton was obtained from a 2-D MT resistivity model of the transition from the Wopmay orogen to the western Slave craton (see Section 5.3.1 for a review of this model) (Spratt et al., 2009). In the resistivity model the LAB was imaged at a depth of ~ 210 km beneath the Slave craton, with the depth shallowing to ~ 150 km at the transition to the Wopmay orogen. Finally, this MT study imaged the LAB to occur at depths of $\sim 210 \pm 10$ km where the error bars are assigned based upon synthetic results discussed in Section 7.5.3. The decrease in resistivity to 50 - 100 Ωm at the LAB occurred very uniformly across all regions in the preferred resistivity model (Figure 7.8) and thus the estimate of 210 ± 10 km can be taken as representative for the entire Slave craton.

There were two seismic studies in the Slave craton that have investigated the depth of the LAB. Chen et al. (2007) produced a 1-D velocity model of the Slave craton using Rayleigh phase and amplitude data and found a low velocity gradient at with its centre at ~ 220 km depth, which was interpreted as the LAB. However, the velocity model was not well resolved at depths greater than 200 km and for this reason the depth to asthenosphere was taken to be $\sim 220 \pm 65$ km. Banks et al. (2000) completed the first body-wave tomography model of the Slave craton and interpreted a decrease in velocity of $\sim 0.5\%$ as the transition to the LAB. The boundary showed some variation across the Slave craton and thus was taken to be a value of 250 ± 50 km. Esteve et al. (2019) recently published an updated tomographic model of the Slave craton, but did not find any evidence of a decrease in velocity that would be expected at the LAB. As such the only tomographic estimate available is from Banks et al. (2000).

The previously published magnetotelluric models all predict an LAB depth in the range of 200 - 220 km with the exception of the 260 km depth estimate from Jones et al. (2003).

However, the latter estimate is likely not as accurate compared to other MT studies as it was derived from a 1-D model derived from MT data averaged over all sites in the Slave craton. An estimate of 200 - 220 km derived from MT models also lies within the error bars of the depth estimate from seismic studies, which have much less constrained estimates of the LAB due to low resolution in the respective studies. In comparison, there is much more variation in LAB depth estimates derived from xenolith studies, which have estimates that range from as shallow as 160 km to as deep as 250 km. The depth estimate from the proposed resistivity model does not find that the LAB depth changes across the craton as observed in xenoliths, but the xenoliths depth estimates have large time gaps between them where the depth of the LAB could change due to convective instabilities (Conrad, 2000; Morency et al., 2002). The Lac de Gras kimberlite cluster in the central Slave craton is the youngest group of kimberlites, which are dated to the Eocene (45 - 75 Ma) (Heaman et al., 2003). Thus, the minimum depth estimate of ~200 km from xenoliths in the central Slave craton is likely the best representation of the modern lithospheric structure and is the best depth to use for comparison with present day magnetotelluric and studies. Therefore, the depth estimate for the LAB of 210 ± 10 km found in this study is well within the range of previous geophysical studies and is in agreement with the most recently erupted xenoliths from the youngest kimberlites (45 - 75 Ma). A comparison of all depth estimates to LAB including this study is given in Figure 8.1 and the respective location of the study.

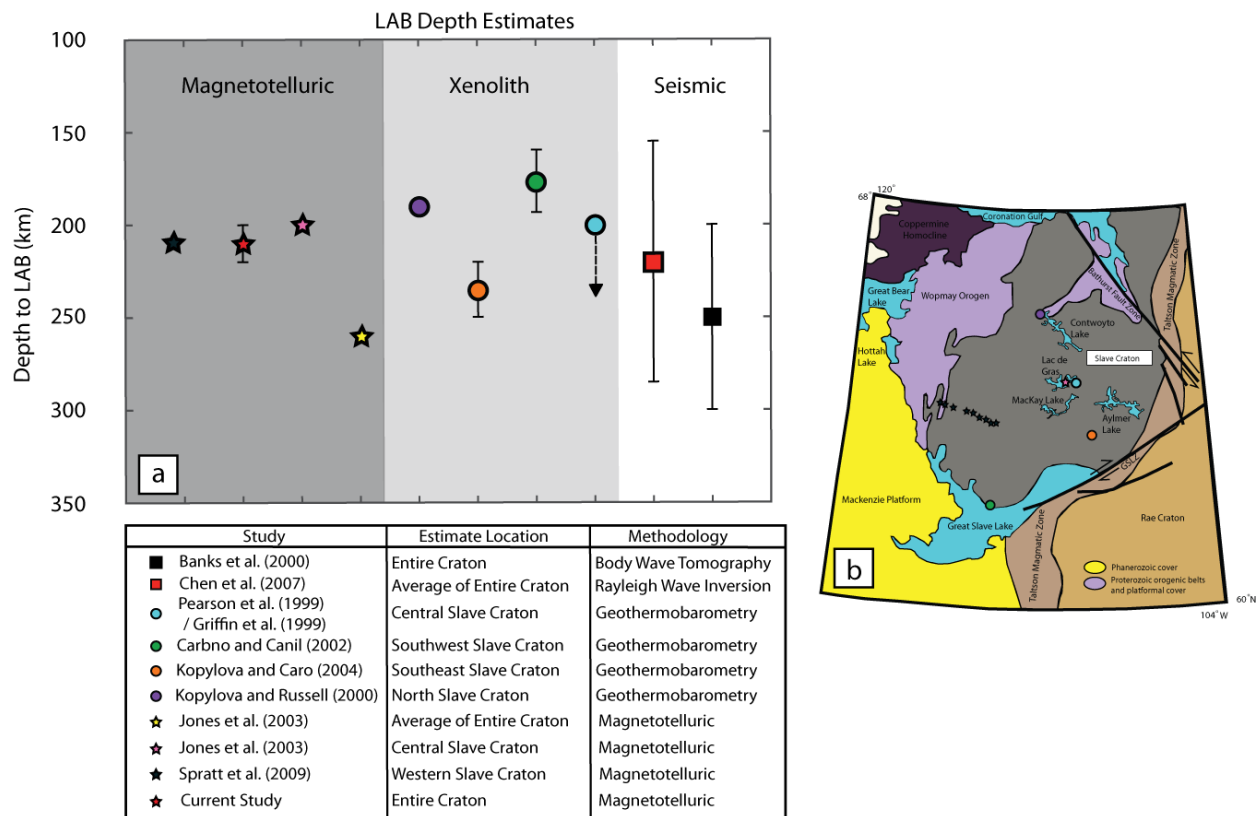


Figure 8.1: (a) A summary of depth estimates for the lithosphere-asthenosphere boundary (LAB) from various studies as described in text. The light blue circle with an arrow pointing downwards indicates that the depth is a minimum estimate. The depth estimate obtained from this study is indicated by a red star. (b) The locations of the studies with a specific location listed in (a) on the base map. Studies that are 1-D estimates or estimates for the whole Slave craton are not included on the base map. See text for further details of each study.

8.3 Conduction Mechanisms for the Central Slave Mantle Conductor

The 3-D resistivity model of the Slave craton presented in Figures 7.8 and 7.9 provides the most robust image of the Slave lithosphere to date, but the physical mechanism for the high conductivity of the Central Slave Mantle Conductor and the conduit structures remain unclear. In this section, five possible conduction mechanisms are systematically considered that could significantly elevate the conductivity of the mantle. These conduction mechanisms can be summarized as follows: (1) graphite films, (2) sulphides, (3) nominally anhydrous minerals (clinopyroxene, orthopyroxene, garnet and olivine), (4) the hydrous minerals amphibole and phlogopite and (5) a combination of hydrous carbonatite melt or saline mantle brines. The following section of the thesis will consider if (a) these explanations can produce the observed

conductivity anomaly and (b) if it is reasonable to expect such a conduction mechanism could occur in cratonic lithosphere.

8.3.1 Option 1: Graphite

Graphite has long been considered a possible candidate for anomalously low resistivity in the mantle as it is orders of magnitude less resistive than common mantle minerals (olivine, orthopyroxene, clinopyroxene and garnet) (e.g., Duba and Shankland, 1982). Graphite has also been observed as an accessory mineral in xenoliths from cratonic lithosphere around the world providing evidence for its presence in the mantle (Pearson et al., 1994). In addition, interconnected graphite films have produced low resistivities in the lower crust (e.g., Frost et al., 1989) and thus it is possible that the same effect could occur in the upper mantle. As a result of these observations, some authors have suggested that graphite could be the cause of the low resistivity of the CSMC (Jones et al., 2001a; Jones et al., 2003; Chen et al., 2009; Selway, 2014). The resistivity of graphite is dependent upon the volume present and its depositional geometry. Thus sufficient quantities of graphite must be present to be interconnected and produce the low resistivities observed in the CSMC. This section discusses arguments for and against the existence of interconnected graphite films in the mantle to determine if graphite is a viable conduction mechanism for the CSMC as suggested in the past.

8.3.1.1 Evidence in Favour of Graphite

There is evidence that supports the hypothesis that graphite could be conductive in the upper mantle and be the cause of the low resistivity of the CSMC. Resistivity modelling suggests that just 0.01 wt% (or equivalently, 100 ppm) graphite would result in a bulk resistivity of $\sim 10 \Omega\text{m}$ (Duba and Shankland, 1982; Mathez, 1987). The concentration of carbon in the mantle is expected to be between 16 and 500 ppm (Deines, 2002) suggesting there could be on average enough carbon available in the mantle to produce an observable conductivity anomaly. Furthermore, laboratory experiments conducted by Wang et al. (2013) also showed that at upper mantle conditions ~ 1 wt% graphite in olivine aggregates would decrease mantle resistivity to values as low as $0.01 \Omega\text{m}$ in reducing environments. Therefore, it is possible to achieve a resistivity on the order of 1 - $10 \Omega\text{m}$ under the correct conditions.

8.3.1.2 Evidence Against Graphite

However, there are also arguments against graphite as the cause of the low resistivity of the CSMC. Xenoliths from the Diavik diamond mine reveal that the mantle in the central Slave craton is highly oxidizing (one log unit above the fayalite-magnetite-quartz (FMQ) oxygen fugacity buffer), which renders graphite unstable at depths less than ~135 km (Creighton et al., 2010) as graphite requires reducing conditions 1.5 - 2.5 log units below the FMQ to be stable (Stagno and Frost, 2010). In this oxidizing environment graphite would be converted to carbonate minerals (Stagno and Frost, 2010) and thus not be conductive. Additionally, multiple laboratory experiments completed over the last decade differ from the results of Wang et al. (2013) in that they suggest that graphite films may do not remain interconnected under upper mantle conditions. For example, Watson et al. (2010) found that trace amounts of grain boundary graphite in olivine aggregates (0.1 wt %) do not decrease resistivity appreciably under upper mantle conditions. Similarly, Zhang and Yoshino (2017) investigated the electrical conductivity of 0.8 vol % graphite in olivine aggregates under upper mantle conditions and found the resistivity of graphite-bearing olivine does not differ considerably from olivine itself suggesting the graphite films became disconnected. Zhang and Yoshino (2017) suggested this apparent discrepancy in laboratory experiments on graphite may be a consequence of Wang et al. (2013) not using representative concentrations of carbon in the mantle, which is expected to be between 16 and 500 ppm (Deines, 2002). These concentrations are far below the ~1 wt% (10000 ppm) graphite used by Wang et al. (2013). Thus, the results of Wang et al. (2013) are likely unrepresentative of natural mantle conditions and should be used with caution.

8.3.1.3 Summary of Graphite as a Conduction Mechanism

In summary, in considering all the arguments, graphite does not appear to be a likely candidate for the low resistivity of the CSMC. Arguments supporting that graphite would be conductive in as little as 100 ppm concentrations (Duba and Shankland, 1982; Mathez, 1987) did not consider that graphite films could be disconnected under the pressures and temperatures in the upper mantle or assumed unreasonable concentrations of carbon (Wang et al., 2013). Laboratory experiments that measured the resistivity of graphite-bearing olivine using carbon concentrations expected in the mantle have proven that graphite films will become disconnected in the upper mantle and thus will not decrease resistivity (Zhang and Yoshino, 2017; Watson et al., 2010). In addition to the laboratory experiments, the oxidation state of the upper mantle

beneath the central Slave craton inferred from xenoliths would not allow graphite to be stable. Therefore, graphite is rejected as a conduction mechanism as it would be neither stable nor decrease the resistivity if it were present.

8.3.2 Option 2: Sulphide Minerals

Sulphide minerals (e.g., pyrite, chalcopyrite or bornite) are highly conductive. Even when present in relatively low concentrations, they can greatly increase the bulk conductivity of a rock when interconnected and have been suggested as a cause of anomalously high conductivity in cratonic regions (e.g., Jones et al., 2005) or crustal-scale faults (e.g., Jones et al., 2001a; Jones and Garcia, 2006; Spratt et al., 2009). Thus, if sulphides are present in the mantle and interconnected they would certainly produce an observable mantle conductor such as the CSMC.

8.3.2.1 Evidence in Favour of Sulphide Minerals

An argument could be made for sulphides as Evans et al. (2011) suggested that the Bushveld upper mantle conductor in the Kaapvaal Craton originated from a network of interconnected sulphides and garnets. The CSMC could share a similar origin, however, this mechanism remains hypothetical as there have been no laboratory experiments to date that support this model. Massive sulphides such as those present in porphyry copper deposits can also have resistivity as low as 1 Ωm with sulphide concentrations of 20 wt% (Nelson and Van Voorhis, 1983), but such sulphides are local features and would not be expected to extend over large regions (Selway, 2014). Sulphides in the form of grain boundary films could provide a more reasonable means to produce large-scale mantle features than massive sulphides that are found in the upper and lower crust as argued by Selway (2014). There is only one experiment to date that has measured the electrical behaviour of grain boundary sulphides under upper mantle conditions and this experiment showed 1.4 wt% grain boundary sulphides in olivine decreased resistivity by between one and two orders of magnitude (Watson et al., 2010). It should also be noted that the sulphides in this experiment were not well connected in the samples and the majority of the sulphides occurred as isolated blebs on the edges of the grain boundaries.

8.3.2.2 Evidence Against Sulphides

Sulphides are known to be conductive, but they are (1) not volumetrically abundant in the Earth (e.g., Ducea and Park, 2000) and (2) are only stable in the uppermost portions of the mantle (Sack and Ebel, 2006). Additionally, experiments on grain boundary sulphides (Watson

et al., 2010), the most likely sulphide mechanism in the mantle, could only achieve resistivities of $\sim 1000 \Omega\text{m}$ under the expected temperature of $\sim 775 \text{ }^\circ\text{C}$ in the CSMC (Mathers, 2012). A resistivity of $\sim 1000 \Omega\text{m}$ is at least two orders of magnitude too resistive to produce the 1 - 10 Ωm observed in the CSMC. Molten sulphides have also been proposed to occur in the deep continental lithosphere (Helfrich et al., 2011; Zhang et al., 2018), but the geotherm (Mathers, 2012) does not predict high enough temperatures at depths of 100 km to allow for such a mechanism.

8.3.2.3 Summary of Sulphide Minerals as a Conduction Mechanism

In summary, when considering all of the arguments, it is difficult to rule out grain boundary sulphides in the mantle, but there is not strong evidence to support this hypothesis either. The electrical resistivity of the grain boundary sulphides in the mantle measured by Watson et al. (2010) would not be able to produce the low resistivity of the CSMC (1 - 10 Ωm), but this experiment was performed on olivine samples that did not have well connected sulphides in the grain boundaries. If sulphides occurred in sufficient quantities in the mantle to be well connected, then it would be more conductive than sulphides that were isolated at the edges or corners of grain boundaries. The existence of interconnected sulphides in the mantle remains speculative, but a similar mechanism was suggested by Evans et al. (2011) in the Kaapvaal craton to explain the cause of the low resistivity observed in the Bushveld complex. Further experimental work is needed to determine if (1) interconnected sulphides can exist in the upper mantle and (2) what the electrical resistivity of these interconnected sulphides are under upper mantle conditions before this conduction mechanism can be accepted or rejected.

8.3.3 Option 3: Hydrogen Diffusion in Nominally Anhydrous Minerals

The mantle comprises primarily nominally anhydrous minerals (NAMs), which include olivine, clinopyroxene, orthopyroxene and garnet. The resistivity of these minerals is known to be very high ($> 100,000 \Omega\text{m}$) in the upper mantle without dissolved water present (e.g., Selway, 2014). When referring to dissolved water it is understood that water is not a fluid in the mantle, but is actually dissociated into hydroxyl (OH^-) and H^+ ions within the crystal lattice of mantle minerals. The resistivity of dry NAMs is unable to account for the low resistivity of the CSMC (1 - 10 Ωm), which has been rigorously investigated in the Slave craton from (1) direct resistivity measurements on xenoliths in the central Slave (Bagdassarov et al., 2007) and (2) from

resistivities predicted from mineral physics experiments for the central Slave craton's upper mantle (Jones et al., 2009a). However, the resistivity of NAMs drastically decreases if there is dissolved hydrogen in the crystal lattice (e.g., Karato, 1990). Thus, if water (i.e. a source of hydrogen) is introduced into the lithosphere, it could decrease the resistivity sufficiently to produce the low resistivity of the CSMC.

8.3.3.1 Evidence Against Hydrogen Diffusion in Nominally Anhydrous Minerals

There are a number of arguments against dissolved water in NAMs as the cause of the low resistivity of the CSMC. First there, there is no evidence of water in xenoliths recovered in the central Slave craton (Aulbach, 2011). Furthermore, the upper mantle in the depth range 95 - 160 km beneath the central Slave craton comprises ultradepleted hazburgite (Griffin et al., 1999), which would not be expected to be hydrated as by definition it should be depleted of incompatible elements and water (Selway, 2014). In general, in the depth range of 100 - 150 km cratons are not expected to be hydrous (Dixon et al., 2004) and thus it would be uncharacteristic for the cratonic lithosphere beneath the central Slave craton to be hydrous. Similarly, Grant et al. (2007) found that dissolved water is only present in small quantities at these depths with the upper bound of water concentration in the upper mantle expected to be no more than 55 ppm in olivine, 400 ppm in clinopyroxene, 200 ppm in orthopyroxene and 20 ppm in garnet based upon data from various upper mantle tectonic settings.

8.3.3.2 Evidence in Favour of Hydrogen Diffusion in Nominally Anhydrous Minerals

However, there are also arguments that could support dissolved water in NAMs as the cause of the low resistivity of the CSMC. Only small volume fractions of dissolved water have been shown to decrease the resistivities of NAMs by orders of magnitude (e.g., Karato, 1990). It can also be argued that the water concentration observed in xenoliths represent a lower bound because water can escape when xenoliths are exhumed and equilibrate at the surface (e.g., Peslier et al., 2006). Therefore, it is possible that the xenoliths underestimate the water content in the mantle. The Tanzania Craton was observed to have water contents as high as 0.01 wt% (100 ppm) at depths of ~ 90 km, which was suggested to have been emplaced as a result of kimberlite magmatism in the Jurassic to Cretaceous periods (Selway et al., 2014). Kimberlite magmatism has occurred as recently as the Eocene in the Slave craton (Heaman et al., 2003) and thus it is possible that the coincidence of CSMC with the Lac de Gras kimberlites is related to a similar

process as in Tanzania that rehydrated the Slave craton lithosphere. Therefore, although the mantle is expected to be dry as argued in Section 8.3.3.1 (Dixon et al., 2004), there are case studies to suggest that cratonic lithosphere can be wet under some circumstances. As such, it is worthwhile to calculate if it is possible for the low resistivity of the CSMC to be caused by dissolved water in NAMs. The methodology of Rippe et al. (2013) was used to estimate the water content required to produce the resistivity of the CSMC.

The water content values were calculated using the methodology of Rippe et al. (2013), which compares the maximum possible solubility of olivine (calibrated from Lizarralde et al., 1995 and Bell et al., 2003) with the water content required to produce the observed resistivities based upon laboratory experiments (Wang et al., 2006; Yoshino et al., 2009; Karato, 1990) to determine if the predicted water contents are possible. The methodology of Rippe et al. (2013) also takes into account that the water reduces the melting temperature of olivine and calculates the minimum amount of water required to induce hydrous melting at the expected mantle temperatures and compares this value with the predicted water content to determine if hydrous melting is required. Station STG008 is chosen as a representative station for calculating the water content of the CMSC and the results are shown in Figure 8.2. The water content required to produce the resistivity of the CSMC is greater than 0.3 wt% or 3000 ppm, which far exceeds the solubility limit. Therefore dissolved water cannot be the cause of the low resistivity in the CSMC. This resistivity would require between 0.4 and 0.5% volume percent hydrous basaltic melt depending upon which model is used between Wang et al. (2006), Yoshino et al. (2009) and Karato (1990). Water induced melting in shallow cratonic lithosphere is also likely unrealistic due to the cold geotherms (Selway, 2014). One could also appeal to hydrous orthopyroxene (Dai and Karato, 2009b), hydrous clinopyroxene (Dai and Karato, 2009b) and hydrous garnet (Dai and Karato, 2009a), but olivine comprises the majority of the mantle composition in the Slave craton (71% olivine, 21% orthopyroxene, 3% clinopyroxene and 5% garnet (Kopylova and Russell, 2000)) and the effects of these additional minerals would not be expected to change the conclusion drawn from Figure 8.2.

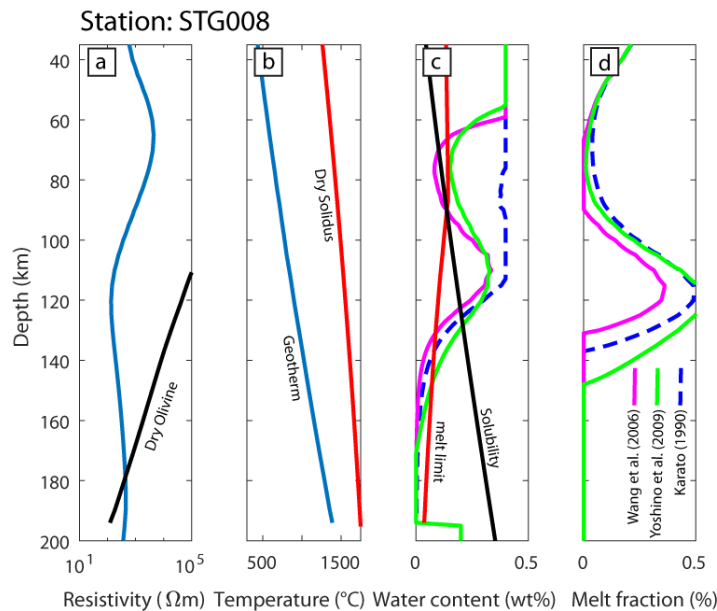


Figure 8.2: Estimated water content from electrical resistivity for STG008 overlying the CSMC in the Slave craton using the methodology of Rippe et al. (2013). The panels from left to right are: (a) the electrical resistivity profile (blue line) and the electrical resistivity of dry olivine from the SEO3 model (black line) (Constable, 2006). (b) The geotherm predicted for the Slave craton (Mathers, 2012) (blue line) and the solidus of dry peridotite (red line). (c) The Water content predicted by Wang et al. (2006) (pink line), Yoshino et al. (2009) (green line) and Karato (1990) (blue dashed line). Water solubility limit (black line) (Lizarralde et al., 1995; Bell et al., 2003). Water content required for hydrous melt (red line). (d) Predicted melt fractions using resistivity relationships of Wang et al. (2006) (pink line), Yoshino et al. (2006) (green line) and Karato (1990) (blue dashed line).

8.3.3.3 Summary of Hydrogen Diffusion in NAMs

In summary, it does not seem likely that water or rather dissolved hydrogen or hydroxyl groups are responsible for the low resistivity of the CSMC. There is no evidence for water in xenoliths and even if it is assumed that the xenoliths are unrepresentative of the hydration of the mantle, the 1 - 10 Ωm resistivity of the CSMC cannot be produced without exceeding the solubility limit at depth. Therefore, the electrical properties of the CSMC cannot be explained by hydrogen diffusion in NAMs.

8.3.4 Option 4: Hydrous Minerals (Amphibole and Phlogopite)

Recent laboratory experiments have found phlogopite (Li et al., 2016; Li et al., 2017) and amphibole (Wang et al., 2012; Hu et al., 2018) to have a conductivity that is orders of magnitude greater than that of the NAMs, discussed in Section 8.3.3. Thus, if sufficiently interconnected, accumulations of phlogopite or amphibole could produce anomalously high conductivity in the

mantle. Phlogopite has also in the past been suggested to increase conductivity in the upper mantle (e.g., Boerner et al., 1999) and more recently amphibole has also been considered as a mechanism for increasing conductivity in the mantle (Selway, 2018). However, amphibole is only stable to pressures of ~ 3 GPa (~ 90 km) and thus is not stable at the depth of the CSMC (~ 100 km) (Frost, 2006). In comparison, phlogopite is stable to much higher pressures and temperatures (Frost, 2006) and would be stable at depths greater than 100 km. Therefore, this section will focus on phlogopite rather than amphibole, as it can be electrically conductive and stable at depths greater than 100 km. It should also be noted that hydrous minerals were previously rejected as a conduction mechanism for the CSMC (Jones et al., 2003; Jones et al., 2001a). In the following section arguments against phlogopite are discussed first and then counter arguments are proposed that provide support for phlogopite in the upper mantle. It is argued that phlogopite should be re-examined as a cause for the high conductivity of the CSMC because (1) laboratory experiments, which were not available two decades ago show that phlogopite is conductive under upper mantle conditions, (2) hydrous minerals and specifically phlogopite may be more common than observed in xenoliths and (3) hydrous minerals are proposed to cause mid-lithosphere discontinuities (MLD) and a MLD is spatially coincident with the CSMC (Chen et al., 2009). Finally, this section concludes with modelling the resistivity of a phlogopite rich layer in the upper mantle of the central Slave craton using the new laboratory results (Li et al., 2016; Li et al., 2017) to determine if such a layer could produce the observed 1 - 10 Ωm resistivity in the CSMC.

8.3.4.1 Evidence Against Phlogopite

There are a number of arguments against phlogopite playing a major role in increasing mantle conductivity in the CSMC. Jones et al. (2001a) and Jones et al. (2003) argued that phlogopite was not responsible for the high conductivity of the CSMC as it was not commonly observed in xenoliths in the Slave craton and when observed is not interconnected. Xenolith studies in the central Slave craton found rare observations of phlogopite volume fractions of up to 50% at Diavik (Aulbach, 2007) and phlogopite has also been observed in xenoliths from the Ekati property (Creaser et al., 2004) and southwest of the Jericho mine at the MuskoX kimberlite (Newton et al., 2015). Therefore, there is evidence for xenoliths rich in phlogopite with sufficient volume fractions for it to be interconnected, however, these observations are still rare suggesting that phlogopite may not be abundant in the lithosphere of the Slave Craton.

A second argument against phlogopite is that some authors have found that large volumes of hydrous minerals could lead to density instabilities over billions of years and would not be expected to survive over such time periods. This could be problematic considering that most previous interpretations of the CSMC have ascribed an Archean age (Chen et al., 2009; Davis et al., 2003; Jones et al., 2003) with the exception of Selway (2014) who suggested an Eocene age for the CSMC. Still, other authors argue the opposite and suggest that hydrous minerals such as phlogopite may be a requirement for the stability of cratons (Eeken et al., 2018). As such the longevity of hydrous minerals seems to be controversial and this analysis will continue assuming that hydrous minerals in the upper mantle are either (1) stable over long time periods (billions of years) or (2) were deposited recently enough to have survived until present day.

8.3.4.2 Evidence in Favour of Phlogopite

In Section 8.3.4.1 it was argued that phlogopite observations are rare, however, some authors have argued that hydrous minerals in general may be more common in the mantle than observed because they may be prone to (1) preferential disruption when exhumed (e.g., Giuliani et al., 2016) or (2) under sampling due to researchers being focussed on determining ages of cratonic formation, which is best done in rocks free of metasomatic minerals (Aulbach et al., 2017a). This implies that regions with xenoliths that find phlogopite to be rare or non-existent might be unrepresentative of the true composition of the upper mantle and that it is reasonable to suggest that hydrous minerals are more common than observed (see Aulbach et al., 2017a for an excellent review of this topic).

The main argument in favour of phlogopite as the cause of low resistivity of the CSMC is that a seismic mid-lithosphere discontinuity (MLD) is observed to be coincident with the CSMC (Chen et al., 2009) suggesting a common cause for the two geophysical responses. MLDs are a widely observed feature in cratonic lithosphere in the depth range of 80 – 100 km. One of the leading hypotheses for their origin is accumulations of hydrous minerals such as amphibole and phlogopite or carbonates, as these minerals reduce shear wave velocities relative to mantle peridotite (Selway et al., 2015; Rader et al., 2015; Aulbach et al., 2017a; Kovács et al., 2017; Eeken et al., 2018; Saha et al., 2018), (See Karato et al., 2015 for an excellent summary of all MLD mechanisms). In this model for MLDs volatile-rich melts generated in the mantle migrate upwards and crystallize hydrous minerals or carbonates at MLD depths after intersecting their solidus. Laboratory experiments also support this frozen-melt model as it has been found that

volatile-rich melts freeze in the depth range of 90 – 140 km depending upon the geotherm and saturation of CO₂ and water, which coincides with the depths of most MLDs worldwide (Dasgupta, 2018). Chen et al. (2009) suggested that the MLD in the central Slave craton was an expression of an ancient metasomatic alteration front that deposited as much as 50% phlogopite, which could produce the observed MLD and shear wave velocity reductions of 9 - 21%. It was further suggested that the CSMC and MLD may share an origin due to their spatial overlap, which seems possible as phlogopite is now known to be conductive (Li et al., 2016; Li et al., 2017). Additionally, joint modelling of teleseismic data (Chen et al., 2007; Chen et al., 2009) and magnetotelluric data (Jones et al., 2001a; Jones et al., 2003) from the Slave craton show that regions of low resistivity correlate spatially with a layer of reduced shear wave velocities (Moorkamp et al., 2007; Moorkamp et al., 2010), which lends further support to a common mechanism causing the anomalous resistivity and seismic velocity. Teleseismic sites showing reduced shear wave velocities from the studies of Moorkamp et al. (2007) and Moorkamp et al. (2010) and Chen et al. (2009) are plotted on the 100 km depth slice in Figure 7.9, which highlights the apparent spatial correlation between the CSMC and reduced shear wave velocities. Therefore, the coincidence of the CSMC and MLD could potentially be explained by a phlogopite-rich layer in the upper mantle of the central Slave craton. An example of a recently deposited phlogopite-rich layer has also been observed in southwest Greenland where xenoliths show a phlogopite-rich layer at depths of 90 – 110 km in the mantle (Aulbach et al., 2017b). Aulbach et al. (2017b) interpreted the phlogopite-rich layer to be an expression of volatile rich melt metasomatism that was a precursory event to the emplacement of Mesozoic kimberlites in the area. There has been kimberlite magmatism as recently as the Eocene in the Slave craton (Heaman et al., 2003) and thus it is possible that a phlogopite-rich layer was deposited under similar circumstances as in southwest Greenland. The next step is to determine if the resistivity of a phlogopite-rich layer can produce a resistivity of 1 - 10 Ωm in the CSMC.

8.3.4.3 Modelling the Conductivity of Phlogopite Bearing Peridotite

The composition of the Slave craton's upper mantle is well understood from xenolith samples and is primarily composed of olivine, orthopyroxene, clinopyroxene and garnet (Kopylova and Russell, 2000). The conductivity of these minerals will be modelled using the same conductivity relationships from Jones et al. (2009a). The bulk conductivity of a mixture of

olivine, orthopyroxene, clinopyroxene, garnet and phlogopite can be modelled using a multiphase Archie's Law (Glover, 2010), which is given as

$$\sigma_{\text{bulk}} = \sum_{i=1}^N \sigma_i \phi_i^{m_i}$$

where N is the number of phases, ϕ is the volume percent of the phase, m is a coefficient bound by $1 \leq m \leq 2$ representing the degree of interconnection in the material and σ is the conductivity of the phase. A value of $m = 1$ represents a parallel circuit while a value of $m = 2$ represents phlogopite deposited as isolated conductors within the rock. Phlogopite has been theorized to develop vein-like structures in the lithospheric mantle (Foley, 1992) which would support a well-connected model, however, it is also possible that it is deposited as disconnected lenses in the rock modelling a series circuit. Thus, values of m of 1, 1.5 and 2 are modelled for phlogopite-bearing peridotite to test the effect of different possible depositional geometries (Figure 8.4). A maximum volume fraction of up to 50% was modelled, which corresponds to the highest volume fraction observed in xenoliths in the Slave craton (Aulbach et al., 2007) and the highest volume fraction suggested by Chen et al. (2009) to explain the observed MLD in the central Slave craton. The temperature at 100 km depth is estimated to be $775 \pm 50^\circ\text{C}$ (Mathers, 2012) and phlogopite conductivity modelling for this temperature reveals that it is not possible to achieve the $1 \Omega\text{m}$ observed in the CSMC, but it is possible to reach the upper limit of $10 \Omega\text{m}$ (Figure 8.4). The phlogopite volume fraction required to reach $10 \Omega\text{m}$ at $775 \pm 50^\circ\text{C}$ is 25% for well connected, 37% for partially connected and 50% for a disconnected geometry (Figure 8.1). It is worth mentioning that a well-connected model is idealistic for two reasons: (1) a parallel circuit (i.e. $m = 1$) would be the ideal phlogopite configuration for enhanced electrical conductivity and (2) volume fractions over 20% do not seem likely to occur over large regions. Therefore, the well-connected model is an overly optimistic scenario, which is still only able to reach the upper bound resistivity of $10 \Omega\text{m}$ for the CSMC. It should also be noted that a minimum of 20% phlogopite would be required to produce the lower bound of a 9% reduction in shear wave velocity observed for the MLD in the central Slave craton (Rader et al., 2015), which is a higher volume fraction than is expected in most frozen-melt models (2 - 15% phlogopite, Aulbach et al., 2017a).

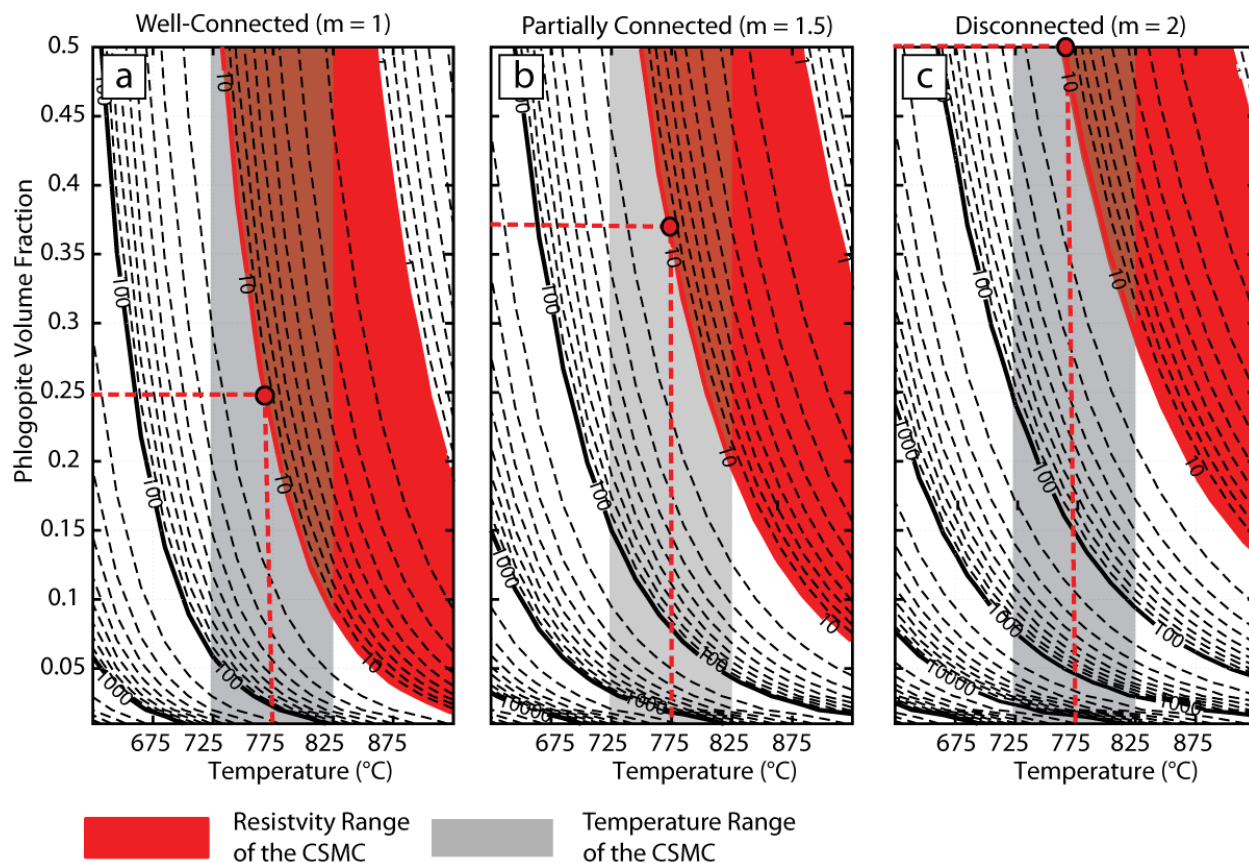


Figure 8.3: Resistivity contours calculated using the Modified Archie's Law (Glover, 2010) plotting phlogopite volume fraction against temperature (K). Each panel models a different depositional geometry including (a) well-connected ($m = 1$), (b) partially connected ($m = 1.5$) and (c) disconnected ($m = 2$). This model is used to constrain the phlogopite volume fraction required to produce the observed resistivities in the CSMC under different depositional geometries. Red lines are the upper and lower resistivity bound of the CSMC. The temperature range is defined from the geotherm of Mathers (2012).

8.3.4.4 Summary of Hydrrous Minerals as a Conduction Mechanism

Amphibole is unstable at a depth of 100 km and thus cannot be the cause of the low resistivity of the CSMC or the MLD. Phlogopite on the other hand is stable and there are some rare observations of xenoliths with phlogopite fractions as high as 50% in the central Slave craton. Phlogopite is also conductive and has been proposed as a cause for MLDs in cratonic lithosphere and there is a MLD observed in the central Slave craton. A minimum of 20% phlogopite is required to produce the velocity reductions observed for the MLD in the central Slave craton and a minimum of 25% phlogopite is required to achieve a resistivity of 10 Ωm

assuming a parallel circuit model, which is highly optimistic. Therefore, phlogopite can possibly reproduce either the CSMC or MLD under an ideal depositional geometry and high volume fraction. Thus, phlogopite is a possible explanation for the low resistivity observed in the CSMC, but it requires highly optimistic geometries and volume fractions.

8.3.5 Option 5: High-Density Fluids

High-density fluids have long been observed as inclusions in fibrous diamonds (Navon et al., 1988; Schrauder and Navon, 1994) and can be broadly categorized as either carbonatitic, silicic or saline (brines) (Izraeli et al., 2001; Frezzotti and Touret, 2014). Some authors have recently proposed that low electrical resistivity and seismic velocities observed in the upper mantle of the central Slave craton could be reconciled by accumulations of HDFs such as hydrous carbonatite melts (Yoshino et al., 2018) or saline brines (Aulbach, 2018). Silicic melts in the Slave upper mantle seem unlikely due to their high solidus temperature (Hirschmann, 2000), but if brines or carbonatitic fluids stalled at mid-lithosphere depths, it would produce a coincident MLD and upper mantle conductor, which is observed in the central Slave craton. Laboratory experiments were also recently completed to evaluate the conductivity behaviour of NaCl brines (Guo and Keppler, 2019) and hydrous carbonatite melts (Yoshino et al., 2018) under high temperature and pressure conditions characteristic of the upper mantle. These hypotheses are considered in more detail in the following section.

8.3.5.1 Carbonate-Rich Melts

Low-velocity zones in the upper mantle have long been associated with high conductivity, which was speculated to be caused by small fractions of partial melt (Oldenburg, 1981; Shankland et al., 1981). Still, melts in cratonic lithosphere have generally been rejected on the premise of the cool geotherms associated with cratons (Selway, 2014; Selway et al., 2015), but in the past carbonate-rich melts could not be thoroughly considered due to limited laboratory experiments investigating their conductivity. Carbonatite melt is orders of magnitude more conductive than silicate melts (Gaillard et al., 2008; Yoshino et al., 2012; Yoshino et al., 2018) and form low dihedral angles with the host rock in the range $20 - 30^\circ$, leading to interconnected melts at volumes as small as 0.05 wt% (Minarik and Watson, 1995). In general, the bulk conductivity of melts are controlled primarily by the degree of connectivity and melt fraction (Waff, 1974) and thus the properties of carbonatite melts allow small melt fractions to increase

the conductivity appreciably in the mantle (e.g., Pinto et al., 2010). Certainly, laboratory experiments show that anhydrous carbonatite melt is below its solidus at 100 km depth ($\sim 775^{\circ}\text{C}$) (e.g., Gaillard et al., 2008; Yoshino et al., 2018) in the Slave craton's upper mantle and thus cannot produce the 1 - 10 Ωm observed in the CSMC. However, recent laboratory experiments show that adding 3 wt% dissolved water to carbonatite melts reduces the eutectic temperature to 675 - 700 $^{\circ}\text{C}$, which enables such melts to be interconnected and above their solidus at depths greater than 80 km (Yoshino et al., 2018). Conductivity modelling of hydrous carbonatite melts in peridotite by Yoshino et al. (2018) showed that between 1 and 10% melt could produce a resistivity of 10 Ωm at 80 and 120 km respectively in the Slave craton (Figure 8.4). Therefore, it is possible that hydrous carbonatite melts have infiltrated the upper mantle of the Slave craton and caused the CSMC. Indeed, it is well known that carbonate rich melt has episodically penetrated the upper mantle as recently as the Eocene as is evident from kimberlite magmatism (Heaman et al., 2003).

8.3.5.1.1 Evidence in Favour of Hydrous Carbonate-Rich Melts

A consequence of a stalled layer of partial melt is that it would reduce shear wave velocities appreciably and would create an observable mid-lithosphere discontinuity (MLD) in the lithosphere (e.g., Thybo and Perchuc, 1997; Thybo, 2006). There are seismic data that support the hypothesis of stalled melts as the cause for the CSMC as a MLD with shear wave velocity reductions of 9 - 21% has been observed in the central Slave craton (Chen et al., 2009). There are few studies quantifying the effect of seismic velocities as a function of melt fraction in the mantle, but one available study predicts melt fractions in the range of 1-2% would result in an 8-22% reduction in shear wave velocities (Hammond and Humphreys, 2000). These velocity reductions are in good agreement with the observations of Chen et al. (2009) of 9 - 21%. Chen et al. (2009) also determined that less than 3% partial melt of basaltic composition could cause the observed velocity reductions in the MLD, however, they argued that this was an unreasonable explanation as such a melt would freeze over time scales of millions of years. However, the solidus for hydrous carbonatite melt is less than the expected temperature at 100 km depth of $\sim 775^{\circ}\text{C}$ suggesting a melt of this composition would not freeze. Esteve et al. (2019) also published a body wave tomography model for the Slave craton, but did not detect a low velocity zone coincident with the MLD. However, it was noted that the resolution of the tomography model would be too low to detect this MLD (Esteve et al., 2019).

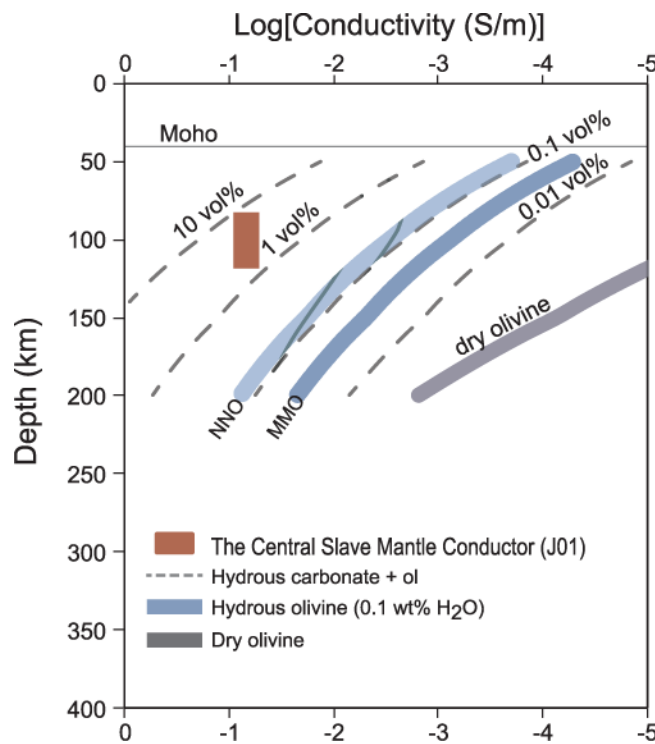


Figure 8.4: Grey dashed lines are isocontours of the conductivity of different volume fractions of an olivine - hydrous carbonatite melt mixture for melt fractions between 0.01 vol% and 10 vol%. For comparison, the conductivity of dry olivine and 0.1 wt% hydrous olivine under different oxygen buffers (NNO = NiNiO: Yoshino et al., 2006 and MMO = MoMoO₂: Yoshino et al., 2009) are plotted as thick grey and blue lines respectively. The red are represents the conductivity of the Central Slave Mantle Conductor from Jones et al. (2001a). (Modified from Yoshino et al., 2018).

8.3.5.1.2 Evidence Against Hydrous Carbonate-Rich Melts

However, there is an argument against carbonatite melts as a cause for the CSMC as it is uncertain if these melts would remain in the upper mantle over geologic timescales. Carbonatite melts are highly reactive and upon contact with peridotite will rapidly react to form wehrlite (Dalton and Wood, 1993), which poses a problem for their longevity in the lithosphere. This does not necessarily rule out their existence in the lithosphere of the Slave craton, but it does suggest that these melts must have migrated to the shallow lithosphere recently otherwise they would rapidly be replaced with wehrlites.

8.3.5.1.3 Summary of Hydrous Carbonate-Rich Melts as a Conduction Mechanism

Evidence supporting hydrous carbonatite melts includes that these melts are above their solidus at depths of 100 km in the Slave craton and can achieve a resistivity of 10 Ω m. Additionally, stalled melt in the lithosphere would lead to a coincident MLD, which is observed

in the central Slave Craton. However, carbonatites are highly reactive with peridotite suggesting they may not be stable over geologic time periods. In summary when considering the arguments for and against hydrous carbonatite melts it seems that it is possible that the cause of the CSMC is related to hydrous carbonatite melts, but it would likely have to be from a very recent event to be observed today.

8.3.5.2 Brines

Saline brines are a second class of HDFs that were recently proposed as an alternative explanation to melts for the anomalous upper mantle conductivity and seismic velocities (Aulbach, 2018). Brines are typically invoked to explain crustal-scale anomalies (e.g., Ogawa et al., 2014; Boonchaisuk et al., 2014). However, highly saline fluids have been reported as inclusions alongside carbonate-rich melts in fibrous diamonds from the upper mantle and are stable in the upper 100 km of the lithosphere (Izraeli et al., 2001; Frezzotti and Touret, 2014). There have also been direct observations of these fluids in fibrous diamonds in the central Slave craton from the Ekati and Diavik mines (Klein-BenDavid et al., 2004; Klein-BenDavid et al., 2007; Klein-BenDavid et al., 2014; Weiss, et al., 2015), which are spatially correlated with the CSMC. Considering that brines are highly conductive and have been observed as inclusions in the lithosphere in the central Slave craton, it is possible that the origin of the CSMC is related to the presence of interconnected brines as suggested by Aulbach (2018).

8.3.5.2.1 Evidence in Favour of Brines

The first argument in favour of brines is that if interconnected, it would only require small volume fractions to produce the 1- 10 Ωm resistivity observed in the CSMC. Laboratory experiments by Guo and Keppler (2019) found that 5 wt% NaCl brine at 3 GPa and 775 °C would have a resistivity of $\sim 0.01 \Omega\text{m}$ and thus only a small volume fraction of (< 1%) of saline brines would be required to achieve the resistivity of 1 - 10 Ωm (or equivalently 1 - 0.1 S/m) observed in the CSMC. The resistivity of interconnected brines was modelled using the Hashin Shtrickman upper bound (Hashin and Shtrickman, 1963) for volume fractions between 1 and 0.01 and NaCl concentrations between 5.5 wt% and 0.55 wt% (or equivalently a molarity of 1M or 0.1M) (Figure 8.5). Concentrations of NaCl as high as 50 % have also been observed (Frezzotti and Touret, 2014), but even at lower concentrations small volume fractions would be sufficient to produce the CSMC resistivity of 1 - 10 Ωm .

A second argument in favour of brines is that Förster et al. (2019) who showed that saline fluids similar to those observed in the central Slave craton can be produced from subducting sediments and will migrate upwards towards MLD depths when released into the lithosphere. A MLD is observed in the central Slave craton with shear wave velocity reductions on the order of 9 - 21% (Chen et al., 2009) and thus it is possible that brines produced this MLD. There are no studies on the effect of saline fluids in the mantle on seismic velocities, but being a fluid they may affect shear wave velocities similar to melts. Thus, applying the same argument as for hydrous carbonatite melts in Section 8.3.5.1 it would be expected that only a small volume fraction of brines would be required to produce between the reduction in shear wave velocities observed by Chen et al. (2009). Therefore, brines could produce a MLD in addition to the observed low resistivity of the CSMC.

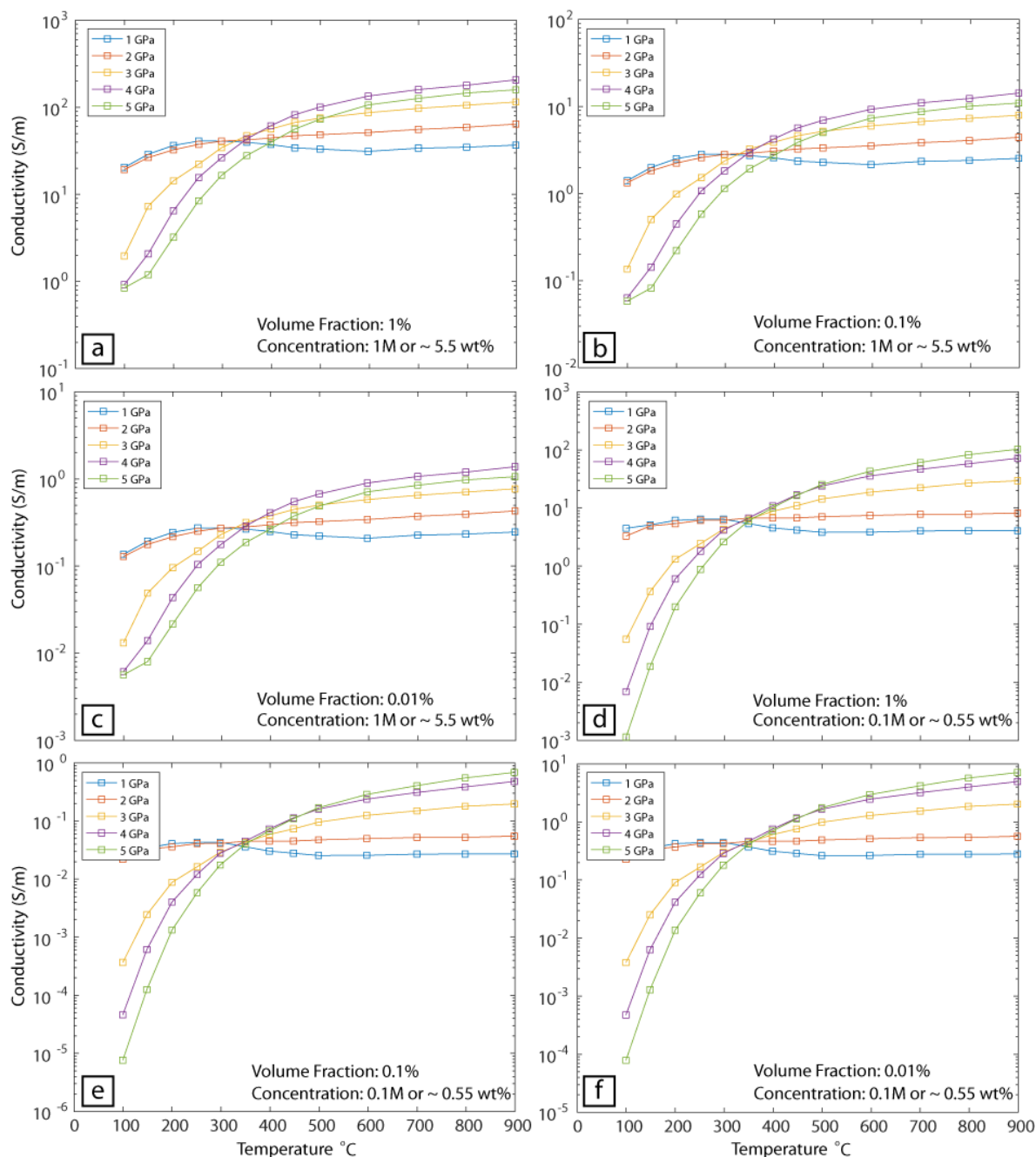


Figure 8.5: The conductivity of interconnected brines in olivine modelled using the upper Hashin Shtrickman bound (Hashin and Shtrickman, 1963). The conductivity of the brines used the conductivity relationship from Guo and Keppler (2019). The conductivity of interconnected brines are shown for volume fractions of 1, 0.1 and 0.01 and concentrations of 1M and 0.1M or equivalently 5.5wt% and 0.55 wt%. The panels show the conductivity as a function of temperature and pressure for (a) 1% volume fraction and 5.5 w% brine, (b) 0.1 wt% volume fraction and 5.5 wt% brine, (c) 0.01 wt% and 5.5 wt% brine, (d) 1% volume fraction and 0.55 wt% brine, (e) 0.1% volume fraction and 0.55 wt% brine and (f) 0.01% volume fraction and 0.55 wt% brine.

8.3.5.2.2 Evidence Against Brines

An argument against saline brines is that similar to carbonatite melts, saline fluids are highly reactive and below MLD depths will react to form alkali chlorides when interacting with peridotite (Förster et al., 2019). Therefore, it remains uncertain if saline fluids percolating through the mantle would be fully consumed in a reaction to produce alkali chlorides or if it is possible for a fraction of the saline fluids to remain preserved in the lithosphere. However, there are few petrological constraints currently available to quantify the behaviour of brines under mantle conditions making it difficult to conclude if brines would be stable over long time periods or at all. Thus, brines suffer from the same uncertainty as carbonatite melts in that they may be consumed in a reaction with the surrounding peridotite in the lithosphere.

8.3.5.2.3 Summary of Brines as a Conduction Mechanism

After this analysis, brines remain as a possible conduction mechanism for the CSMC. First, brines are able to achieve the bulk resistivity of 1 - 10 Ωm observed in the CSMC assuming they are interconnected in the upper mantle. Secondly, there is direct evidence of brines as inclusions from fibrous diamonds erupted from the most recent kimberlites (45 - 75 Ma) in the central Slave craton at Ekati and Diavik. Finally, low volume fractions of brines may be able to produce a MLD with the shear wave velocity reductions as observed by Chen et al. (2009). The main uncertainty for this hypothesis is whether brines will be fully consumed in a reaction with peridotite. Further petrological constraints are likely needed to be certain that brines are stable in the lithosphere, however, considering that interconnected brines can simultaneously explain the seismic and electrical anomalies, it remains one of the best candidates for the cause of the CSMC.

8.4 Cause of the CSMC

Based upon evidence described in Section 8.3.4, either saline brines or hydrous carbonate melts (or some combination of both fluids) are a good candidate to explain the coincidence of the MLD and CSMC in the central Slave craton, but the nature of the process which led to their emplacement must still be answered. The HDFs in the fibrous diamonds from the Ekati and Diavik mines have short mantle residency times (< 200 Mya) suggesting they were emplaced by a relatively recent tectonic event (Weiss et al., 2015). Weiss et al. (2015) noted that subduction zones were commonplace in western North America during the Mesozoic which is similar to the

age of the HDFs observed at the Ekati and Diavik mines. As such, it was suggested that slab-derived fluids infiltrated the overlying lithosphere when a Mesozoic slab subducted beneath the Slave craton (Weiss et al., 2015). It is possible that a fraction of these fluids ascended through the overlying lithosphere before stalling at mid-lithosphere depths leading to the formation of both the CSMC and MLD observed in the central Slave craton (Figure 8.2). Thus, it is suggested that the CSMC and MLD are at most early Mesozoic in age and their origin is a consequence of subduction-derived fluids rather than being tied to ancient cratonic assembly as proposed by many previous authors (Jones et al., 2003; Davis et al., 2003; Chen et al., 2009). This also removes any causality between the ancient ultradepleted hazburgitic layer and the CSMC which is difficult to reconcile as an ultradepleted layer should be depleted of conductive constituents (H₂O, Al, Fe...) (see Selway, (2014) for a discussion on this topic). The spatial correlation between the CSMC and the Lac de Gras kimberlite field may then be a result of kimberlite magmas following zones of weakness in the lithosphere as a result of the metasomatism caused by the slab-derived fluids. This phenomena has been observed worldwide, since kimberlite provinces tend to overly anomalous zones of the lithosphere, which have been metasomatically enriched (Klein BenDavid, 2009; Artemieva, 2009). The majority of kimberlites also overly a steep gradient in effective elastic thickness suggesting that the Lac de Gras kimberlites overlie a weak zone in the lithosphere (Poudjom Djomani et al., 2005a). Overall, stalled HDFs in the lithosphere provide a satisfactory explanation for the observed seismic and electrical anomalies, but a major uncertainty which is unresolved in this model is the reactivity of HDFs with the surrounding peridotite in the lithosphere. For this reason, further petrological constraints are needed in regards to the reactivity of HDFs in the lithosphere before this model can be accepted entirely.

Lastly, the conduits which branch from the CSMC and penetrate the lower crust could be kimberlite melt pathways which metasomatized the wall rock decreasing the resistivity. It is particularly interesting that one of the conduits extends beneath Lac de Gras coinciding with the Ekati and Diavik diamond mines, however, this interpretation is difficult to reconcile as the origin of the CSMC may not be directly related to the kimberlite magmatism in the central Slave craton. The saline fluids discussed in Section 8.3.5.2.1 also have low resistivity (< 100 Ω m or 0.01 S/m) at shallow depths and thus their origin could be tied to the same processes as the CSMC. Jones et al. (2003) found evidence for conductive vertical crustal sheets in their

preliminary 3-D resistivity model for the furthest east stations (east of $\sim 106^\circ\text{W}$), which were attributed to sulphides or graphite along Bathurst fault zone, but the conduits visible along Profile B are too far west to be related to the Bathurst fault zone. Further high resolution geophysical data may be required before the origin of these enigmatic features can be determined.

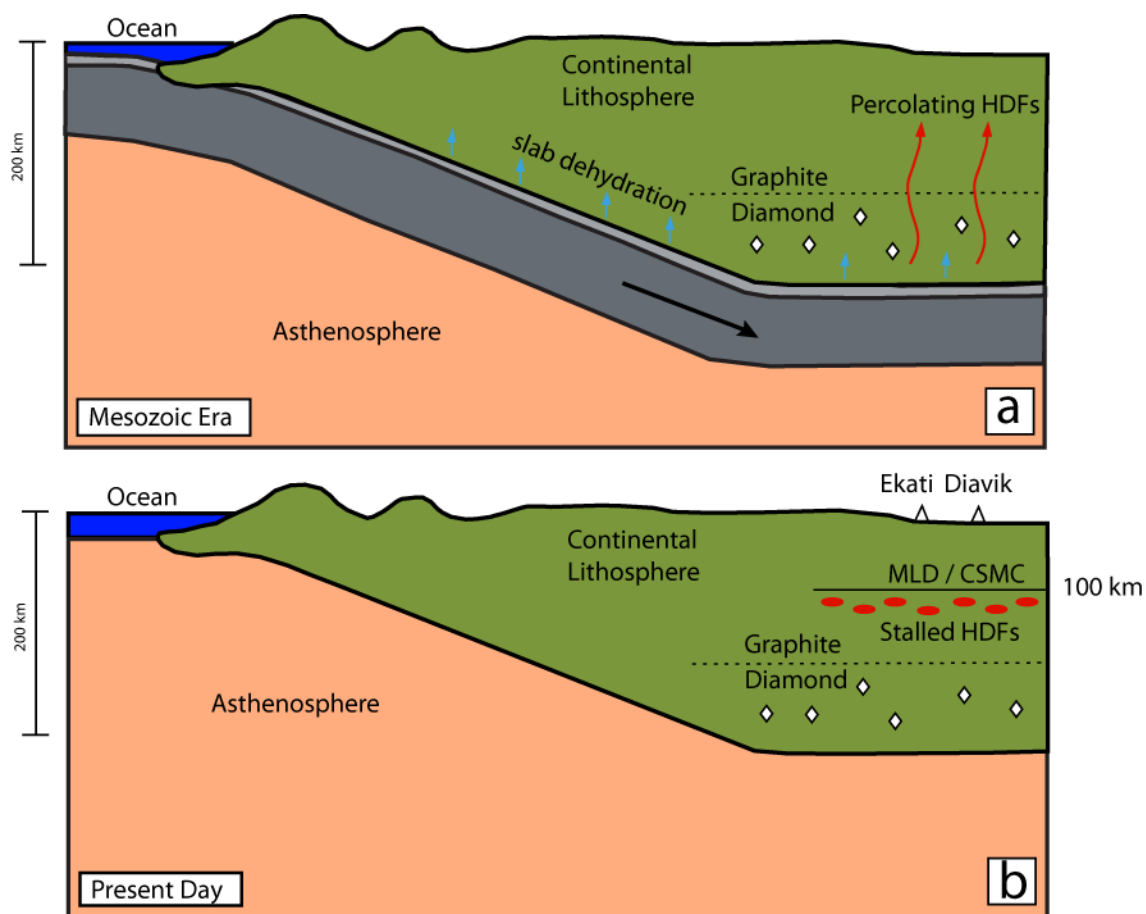


Figure 8.6: The suggested relationship between Mesozoic subduction events and the CSMC and MLD located in the central Slave craton. (a) A slab subducts at a low angle beneath the Slave craton during the Mesozoic and releases high density fluids that percolate upwards through the lithosphere stalling at mid-lithosphere depths. (b) The high density fluids remain trapped beneath the Slave craton simultaneously producing a MLD and the CSMC. (Adapted from Weiss et al., 2015).

8.5 Upper Mantle Conductors and Diamondiferous Kimberlites

Considering that the CSMC may have altered the lithosphere creating a preferential pathway for kimberlite magmatism in the Slave craton, it is informative to revisit if a genetic relationship exists between diamondiferous kimberlites and upper mantle conductors as proposed by previous authors (Jones and Craven, 2004; Jones et al., 2005). The relationship between mantle resistivity structure and diamondiferous kimberlites is now discussed in well-studied cratons globally to determine if there is a correlation outside of the Slave craton.

Jones et al. (2005) observed an upper mantle conductor with similar characteristics to the CSMC beneath the Sask Craton, but the MT profile lies 100 km from the Fort a la Corne kimberlite field making it difficult to directly correlate these features. Furthermore, the deep conductor is not well-resolved as it is beneath the North American Central Plains Anomaly, which is a highly conductive crustal conductor that potentially masks the signature of deeper conductors (Jones et al., 2005). In Alberta, the Buffalo Head Hills kimberlite field is more diamondiferous than the Birch Mountain kimberlite field, but the Buffalo Head Hills kimberlite field is underlain by a thick resistive depleted lithosphere while the Birch Mountain kimberlite field is underlain by an upper mantle conductor (Wang, 2019). This result suggests that diamondiferous kimberlite fields may be unrelated to the existence of upper mantle conductors, however, this does not rule out a possible relationship between kimberlite magmatism and upper mantle conductors. The Kaapvaal Craton has a prominent upper mantle conductor in the Bushveld complex, but this conductor was suggested to be correlated with a subduction event, which created an interconnected series of garnets and sulphides and is seemingly unrelated to kimberlite emplacement (Evans et al., 2011). The Gawler Craton also has an upper mantle conductor, which has been suggested to be a result of a plume enrichment of the mantle with iron and hydrogen, but has also not been correlated with kimberlite magmatism (Thiel and Heinson, 2013). With these case studies in mind, it appears that a genetic relationship between upper mantle conductors and diamondiferous kimberlites does not hold true universally. There may be a relationship in the Slave craton, but this appears to be the exception rather than the norm suggesting that caution should be taken when correlating mantle conductivity with diamondiferous kimberlites.

8.6 Comparison to Previous Teleseismic Studies

Bostock (1998) imaged seismic velocity discontinuities in crust and mantle in the southern Slave craton using P to S conversions otherwise known as the P-receiver function (PRF). Bostock (1998) found three prominent seismic discontinuities denoted as H, X and L. The H discontinuity was very sharp occurring over a thickness of no more than 100 m at a depth of 70 - 80 km and had strong localized anisotropy ($\pm 5\%$). The discontinuity was interpreted to be Archean oceanic crust, which was obducted below an existing proto-continent. The X discontinuity exhibited more complexity and was composed of multiple layers with thicknesses of 5 - 10 km between the depths of 120 - 150 km. The H and X discontinuities were interpreted to be related to shallow angle subduction processes. It was suggested H is oceanic crust, which marks the top of an oceanic plate and X marks the top of a second oceanic plate that was juxtaposed in a subsequent subduction process. The L discontinuity dips from a depth of 170 km on the west end of the profile to a depth of 230 km on the east end of the profile over a lateral distance of ~ 120 km. The L discontinuity was suggested to be an extension of a shallower interface observed ~ 300 km west by Cook et al. (1999) using reflection seismic. The interpreted reflection seismic section (Cook et al., 1999) and the seismic section produced using PRFs by Bostock (1998) are compared with profile A from the preferred resistivity model (s92p21r8) (Figure 7.5a). There does not appear to be any direct correlations between the H, X and L discontinuities observed by Bostock (1998). This is not necessarily surprising as MT is sensitive to conducting phases whereas PRFs are sensitive to changes in fabric orientation of mantle minerals. If the composition is similar between the hypothetical subducted oceanic plates of H and X, but the fabric is different from varied localized strain within the plates, then it would be expected that the electrical resistivity would be unaffected. Therefore, the magnetotelluric model does not dispute shallow angle subduction proposed by Bostock (1998), but it does suggest that no conducting phases were introduced by these subduction events.

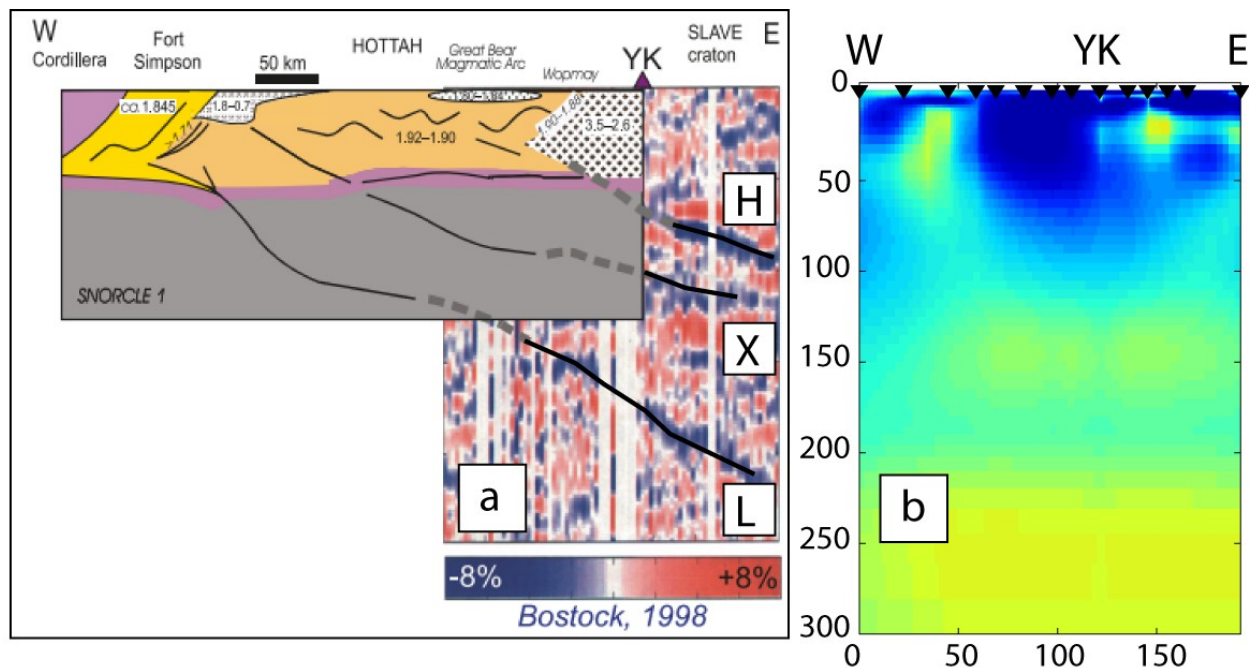


Figure 8.7: (a) Interpreted seismic reflection section from Cook et al. (1997) combined with the seismic model produced with PRFs by Bostock (1998) beneath the southern Slave craton. The seismic discontinuities H, X and L are labelled on the seismic section and are described in text. (b) The preferred electrical resistivity model for Profile A from Figure 7.5. There is no clear correlation between the H, X and L seismic discontinuities and the electrical resistivity for Profile A. YK = Yellowknife. The vertical scale on the seismic model in (a) is the same vertical scale as the vertical scale in (b). (Modified from Snyder and Grütter, 2010)

8.7 Comparison to Body Wave Tomography Studies

Esteve et al. (2019) produced P- and S-wave tomography models of the Slave craton. The P- and S-wave velocity models imaged to depths of over 400 km, but comparisons with the preferred magnetotelluric model will only be made for features in the depth range of 100 - 220 km. This depth range was chosen as the tomography model did not resolve crustal features while the magnetotelluric model was unable to image depths greater than 250 km due to the conductive asthenosphere (C3 from Chapter 7) masking deeper features. The P-wave and S-wave velocity models are shown at depths of 100, 160 and 220 km for direct comparison with the preferred magnetotelluric model in Figure 8.8 (tomography slices at these depths were obtained from Esteve via personal communication). Unfortunately, the velocity model slices cover a much larger area spatially than the MT model, which makes it more difficult to compare the models. To make it easier to compare the models the extent of the MT model as a red box is overlain on the tomography slices and the locations of the teleseismic stations from the POLARIS array are

plotted on the MT depth slices to provide a point of reference when referring between the MT and velocity models (Figure 8.5).

Esteve et al. (2019) found an alternating pattern of fast and slow velocities in the P-wave model going from east to west across the central Slave craton. Relatively fast P-wave velocities were observed ($\delta V_p = \sim 0.8\%$) on the eastern side of the Slave craton between depths of 150 - 250 km. Directly beneath the region surrounding Lac de Gras there is a relatively slow P-wave anomaly ($\delta V_p = \sim 0.7\%$). In comparison, the S-wave model shows relatively fast velocities on the eastern side of the Slave craton ($\delta V_s = \sim 0.3\%$), but not quite as fast as for the P-wave model. The S-wave model did not display the alternating fast and slow velocities from east to west were also not as clear as in the P-wave model. At a 100 km depth the P-wave model shows an alternating pattern of fast and slow velocities going from south to north in the central Slave craton. The S-wave model differs from the P-wave model at a depth of 100 km in that it shows the central Slave craton as entirely relatively fast velocities. Lastly, Esteve et al. (2019) did not find any evidence for a sharp lithosphere asthenosphere boundary (LAB) in their model, but this was suggested to be due to low sensitivity of vertically-propagating body waves to horizontal boundaries (i.e. the LAB) and vertical smearing.

When comparing the velocities observed by Esteve et al. (2019) with the preferred MT model, there are some interesting correlations between the models. The CSMC is at a depth of 100 km in the preferred MT model and is co-located with relatively fast P-and S-wave velocities. C2 is also at a depth of 100 km and is co-located with relatively slow P-and S-wave velocities. Low velocities are often associated with low resistivity, which is observed for C2, however, it is difficult to explain the high velocities that are co-located with the CSMC. In Section 8.3 it was suggested that the source of the high conductivity in the CSMC is related to stalled HDFs, but the fast S-wave velocities from the tomography model are incompatible with this interpretation as fluids should reduce the S-wave velocity. However, Esteve et al. (2019) also found that they were unable to resolve the MLD observed by Chen et al. (2009), which corresponded to a large reduction in the S-wave velocity in the central Slave craton. Seismic tomography has better lateral resolution than vertical resolution due to body waves travelling nearly vertically (Esteve, pers comm) and thus it is possible that this discrepancy between tomography, receiver functions and MT models is a result of the CSMC being too fine scale to be imaged with tomography. A conduction mechanism which wouldn't be expected to affect seismic velocity would be graphite,

but this conduction mechanism does not seem likely for the CSMC as reviewed in Section 8.3.1. It should also be noted that there are very few teleseismic stations coincident with the CSMC, which would also reduce resolution. On the other hand, C2 is co-located with relatively slow velocities, which would be consistent with fluids. However, C2 was not found to be a robust feature in the model and thus caution should be taken before drawing conclusions from this correlation. Finally, Esteve et al. (2019) suggested the relatively slow velocities at 150 - 250 km beneath the region surrounding Lac de Gras were suggested to be trapped regions of fertile mantle, which were metasomatized resulting in relatively slower velocities compared to other regions in the Slave craton. The MT model does not appear to show any correlation with the slow velocities beneath the region surrounding Lac de Gras. This is not necessarily surprising as the resistivity of fertile mantle and depleted mantle vary by less than half an order of magnitude (see Selway, 2018, Section 5.2.2).

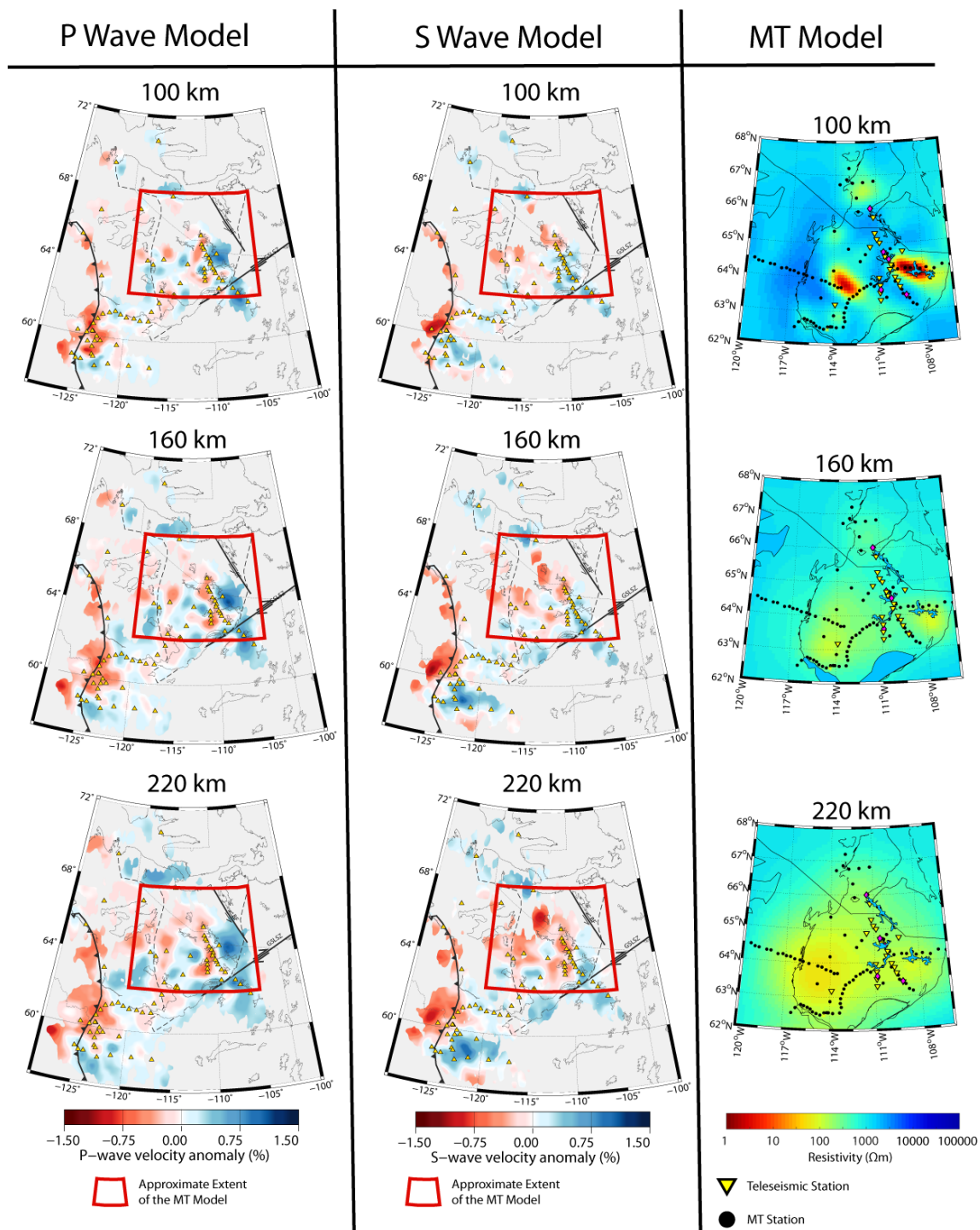


Figure 8.8: P and S wave model depth slices and MT model depth slices for 100 km, 160 km and 220 km. Yellow triangles are the teleseismic station locations. Thick black lines are the Great Slave Lake Shear Zone (NE SW trending) and the Bathurst fault (NW SE trending). Red colours are slower than average velocities and blue colours are faster than average velocities.

8.8 Estimating Mantle Water Content in the Slave Craton

Understanding the distribution of water in the mantle is important as it controls many physical and chemical properties of minerals in the mantle including their electrical resistivity. It should be noted that water is not a fluid in the mantle, but is actually dissociated into hydroxyl (OH⁻) or equivalently H⁺ within the crystal lattice of mantle minerals. Extensive work has been done to understand the relationship between water content and electrical resistivity of olivine (Wang et al., 2006; Yoshino et al., 2009; Karato, 1990) allowing for water content estimations to be derived from electrical resistivity measurements assuming the geotherm is known. Unfortunately, the resistivities predicted from these laboratory experiments are not in agreement and lack a consensus on the correct resistivity relationship. Thus, it is necessary to compare the water contents predicted from each experiment (e.g., Jones et al., 2012). In this section the resistivity relationships for hydrous olivine from Wang et al. (2006), Yoshino et al. (2009) and Karato (1990) were compared and used to investigate the water content predicted for the electrical resistivity obtained from the preferred resistivity model (s92p21r8). The water content values were calculated using the methodology of Rippe et al. (2013), which compares the maximum possible solubility of olivine (calibrated from Lizarralde et al., 1995 and Bell et al., 2003) with the water content required to produce the observed resistivities based upon the laboratory experiments (Wang et al., 2006; Yoshino et al., 2009; Karato, 1990) to determine if the predicted water contents are possible. The methodology of Rippe et al. (2013) also takes into account that water reduces the melting temperature of olivine and calculates the minimum amount of water required to induce hydrous melting at the expected mantle temperatures and compares this value with the predicted water content to determine if hydrous melting is required. Basaltic melt would not typically be expected in cratonic lithosphere due to the cold geotherms (e.g., Selway, 2014), however, the hydrous melting calculations will still be included for completeness.

8.9 Water-Content Estimations for Representative Sites

The code written by Rippe et al. (2013) was applied to three representative magnetotelluric stations in the Slave craton to predict water content in the mantle. The stations chosen are s99-018a near Lac de Gras, Sno-108 in the south western Slave craton and s99-028a near Jericho in the north Slave craton. The water contents predicted for the resistivity profiles at each of these

stations is shown in Figure 8.9 and the predicted water contents will be described in detail in the following section.

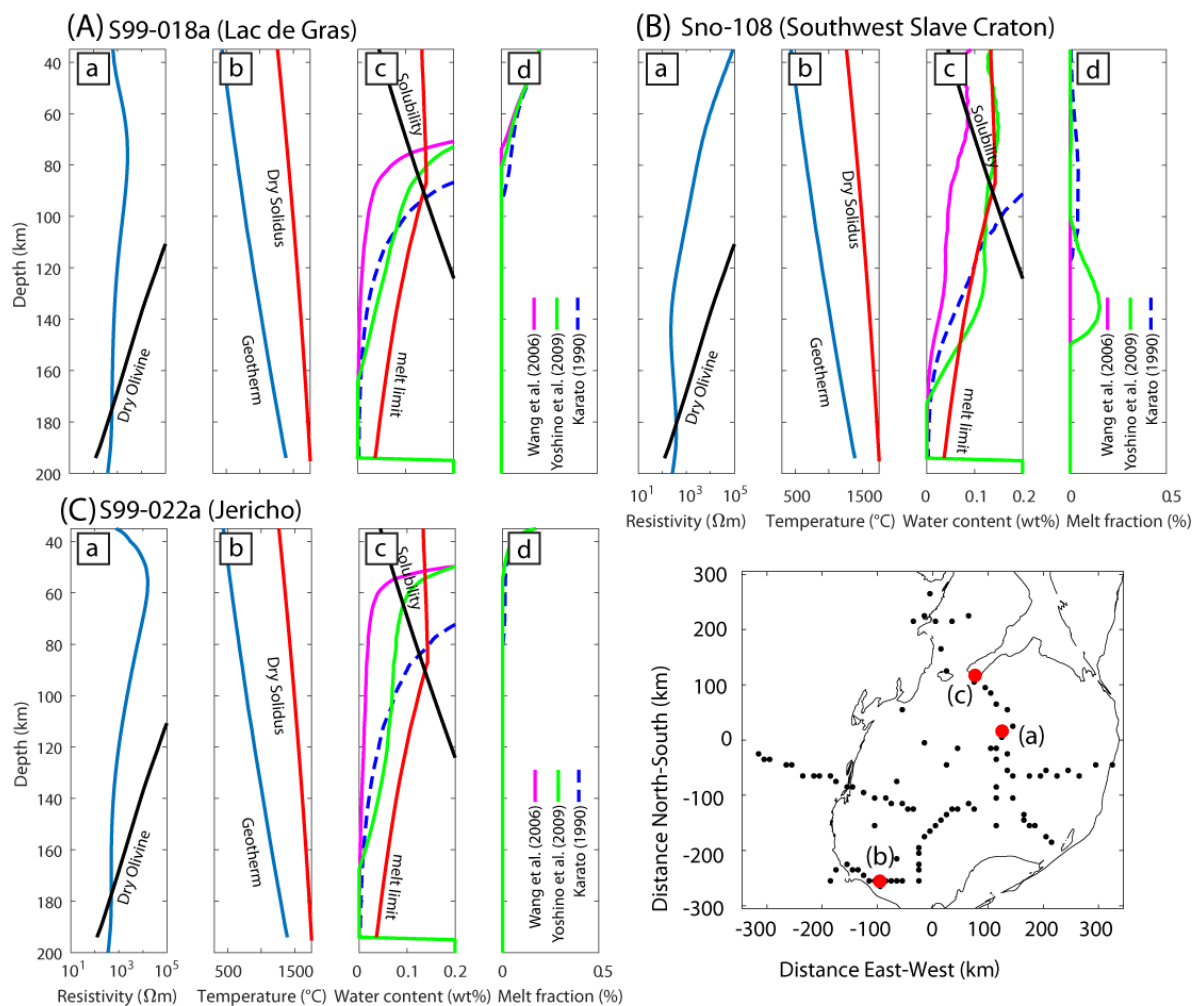


Figure 8.9: Estimated water content from electrical resistivity for example three stations in the Slave craton using the methodology of Rippe et al. (2013). (A) S99-018a near Lac de Gras, (B) Sno-108 in the south western Slave craton and (C) S99-022a near the Jericho diamond mine. The locations of these MT stations are labelled as red dots on the base map. The panels from left to right are: (a) the electrical resistivity profile (blue line) and the electrical resistivity of dry olivine from the SEO3 model (black line) (Constable, 2006). (b) The geotherm predicted for the Slave craton (blue line) and the solidus of dry peridotite (red line). (c) The Water content predicted by Wang et al. (2006) (pink line), Yoshino et al. (2009) (green line) and Karato (1990) (blue dashed line). Water solubility limit (black line) (Lizarralde et al., 1995; Bell et al., 2003). Water content required for hydrous melt (red line). (d) Predicted melt fractions using resistivity relationships of Wang et al. (2006) (pink line), Yoshino et al. (2006) (green line) and Karato (1990) (blue dashed line).

8.9.1 Station S99-018a (Figure 8.9a)

Station S99-018a is located to the north of Lac de Gras in the central Slave craton. The electrical resistivity is lower than that for dry olivine for depths less than 170 km suggesting the presence of an additional conducting phase. The solubility limit is exceeded at depths less than 75 km for the Wang et al. (2006) model, 85 km for the Yoshino et al. (2009) model and 95 km for Karato (1990) model. The Wang et al. (2006) model predicts 0.11 wt% water at 75 km depth, which decreases to ~ 0 wt% water at a depth of 170 km. In comparison, the Yoshino et al. (2009) model predicts as much as 0.13 wt% water at 85 km and decreases to ~0 wt% water at 170 km depth. The Karato et al. (1990) model predicts the highest water content of 0.142 wt% water at 95 km depth, which decreases to ~0 wt% water at 170 km depth. Basaltic melt is not required by any of the three models.

8.9.2 Station Sno-108 (Figure 8.9b)

Station Sno-108 is located in the southwestern region of the Slave craton. The electrical resistivity at depths greater than 100 km does not vary significantly and stays between 500 - 1000 Ωm , which is at least two orders of magnitude less resistive than that predicted for dry olivine (Figure 8.9(b)) suggesting the presence of an additional conducting phase. There is significant variation in the predicted water contents depending upon the chosen model. The solubility limit is exceeded at depths less than 60 km for the Wang et al. (2006) model, 85 km for the Yoshino et al. (2009) model and 100 km for Karato (1990) model. The Wang et al. (2006) model predicts the lowest water content with 0.1 wt% at 60 km, which decreases to ~0 wt% water at a depth of 170 km. In comparison, the Yoshino et al. (2009) model predicts as much as 0.13 wt% water at 85 km and decreases to 0 wt% water at a depth of 170 km. The Karato et al. (1990) model predicts the highest water content of 0.16 wt% water at a depth of 100 km, which decreases to zero water content at a depth of 170 km. The resistivity model of Yoshino et al. (2009) requires 0.1 wt% basaltic melt at a depth of 110 - 150 km, but this would be uncharacteristic of cold cratonic lithosphere and it is more likely that there is no melt as predicted by the Wang et al. (2006) and the Karato (1990) models.

8.9.3 Station S99-022a (Figure 8.9c)

Station S99-022a is located in the northern Slave craton near the Jericho diamond mine. The electrical resistivity for depths less than 170 km is less than dry olivine suggesting the presence

of an additional conducting phase. The solubility limit is exceeded at depths less than 55 km for the Wang et al. (2006) model, 65 km for the Yoshino et al. (2009) model and 85 km for the Karato (1990) model. The Wang et al. (2006) model predicts 0.075 wt% water at 55 km depth, which decreases to ~ 0 wt% water by 170 km depth. In comparison, the Yoshino et al. (2009) predicts as much as 0.095 wt% water at 65 km and decreases to ~ 0 wt% water at 170 km depth. The Karato et al. (1990) model predicts the highest water content of 0.13 wt% water at 95 km depth, which decreases to zero water content at 170 km depth. Basaltic melt is not required by any of the three models.

8.9.4 Water Concentration Estimates at 100 and 150 km Depth

Water contents were calculated for every station at depths of 100 km (Figure 8.10) and 150 km (Figure 8.11) to investigate the water distribution in the model. The water content estimates were found to be greater than 0.1 wt% water (1000 ppm) for the majority of the preferred resistivity model (s92p21r8) at 100 km depth regardless of which model was used to estimate water content. Such high water contents are not characteristic of cratonic lithosphere, which is expected to be relatively dry at these depths (Dixon et al., 2004). For comparison, water content in olivine measured in xenoliths from the Kaapvaal Craton were found to contain less than 0.01 wt% or 100 ppm at a depth of around 100 km.

At 150 km depth the water content estimates are reduced compared to the water content estimated at 100 km depth, but there is significant variation depending upon the model used. Water content estimations that are co-located with C2 and the CSMC are very high (0.02 wt% - 0.1 wt% or 200 - 1000 ppm). In regions that are not beneath an upper mantle conductor water contents are predicted to be 0.001 - 0.015 wt% water (10 - 150 ppm) for the Wang et al. (2006) model, 0.01 - 0.025 wt% water (100 - 250 ppm) for the Karato (1990) model and 0.02 - 0.055 wt% water (200 - 550 ppm) for the Yoshino et al. (2009) model. The significance of these results is discussed in the following section.

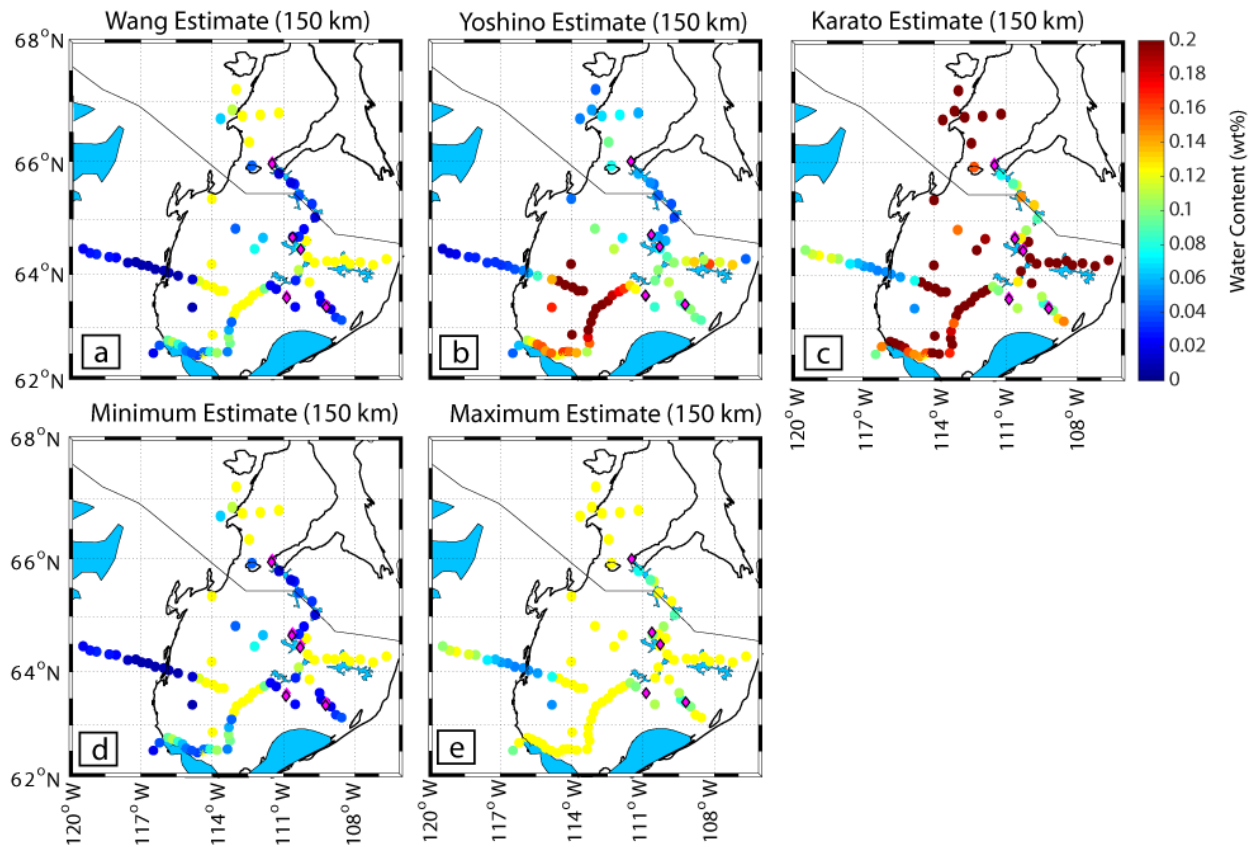


Figure 8.10 Water content estimations at a depth of 100 km depth for each site using the methodology of Rippe et al. (2013). The water content estimates are represented as coloured circles for (a) the Wang et al. (2006) model, (b) the Yoshino et al. (2009) model, (c) the Karato (1990) model, (d) the minimum water content estimated of the three aforementioned models and (e) the maximum water content estimated without exceeding the solubility (Lizarralde et al., 1995; Bell et al., 2003) from the three models.

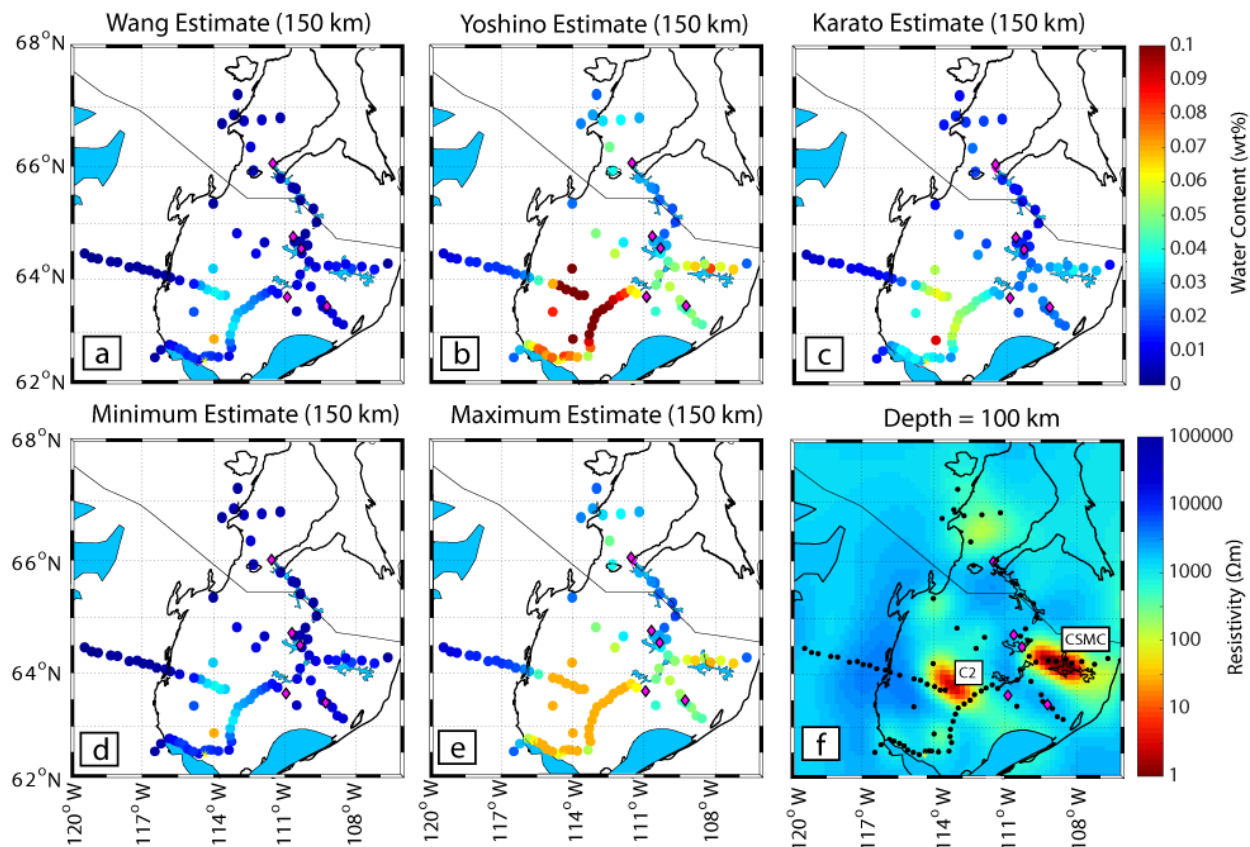


Figure 8.11 Water content estimates at a depth of 150 km depth for each site using the methodology of Rippe et al. (2013). The water content estimates are represented as coloured circles for (a) the Wang et al. (2006) model, (b) The Yoshino et al. (2009) model, (c) the Karato (1990) model, (d) the minimum water content estimated of the three aforementioned models and (e) the maximum water content estimated without exceeding the solubility (Lizarralde et al., 1995; Bell et al., 2003) from the three models. (f) Horizontal depth slice at 100 km to show the correlation between upper mantle conductors and above average water content estimates. Notably water contents estimated beneath the upper mantle conductors C2 and the CSMC predict much higher water contents than water content predicted beneath resistive mantle.

8.9.5 Discussion of Water Estimates

The water content estimates from the three representative profiles suggest very high water estimates (> 0.1 wt% water or 1000 ppm) for the upper 100 km, which appears to be true for the entire model (Figure 8.10). However, these estimates are likely not accurate due to the attenuating effect of lower crustal conductors. Inversion models search for a smooth solution and thus the resistivity recovered below a conductor may not be reflective of the true resistivity, which is demonstrated in Figure 8.7 from Jones (1999). In this theoretical model a lower crustal conductor is at 40 km (thick black line in Figure 8.7c), but the smooth inversion model (smooth light grey line in Figure 8.7c) does not recover a resistivity that corresponds to the true resistivity

until a depth of ~ 100 km (Figure 8.7c). Therefore, to extract meaningful water estimates in the Slave craton a depth range must be chosen, which does not have a downward biased resistivity due to an overlying conductor otherwise the water content will be incorrectly estimated. The same argument can be applied to estimating water content in the mantle beneath an upper mantle conductor such as the CSMC and thus one must be cautious of estimating water content beneath any conductive feature. Therefore, the high water contents predicted at depths less than 100 km depth are not reliable as the smoothing effect applied to the resistivity model beneath the lower crustal conductors has likely resulted in downward biased resistivities (see Figure 8.12c) and consequently an upward biased water content.

The water contents estimated at 150 km depth appear to be more reasonable with the exception of regions that are beneath C2 and the CSMC, which yield water contents of 0.02 wt% - 0.1 wt% or 200 - 1000 ppm. These high water contents are likely not reliable due to the effect of the overlying upper mantle conductor. The Yoshino et al. (2009) model predicts the highest water content of 0.02 - 0.055 wt% (200 - 550 ppm) while the Wang et al. (2006) and Karato (1990) models predict 0.001 - 0.015 wt% (10 - 150 ppm) and 0.01 - 0.025 wt% (100 - 250 ppm) respectively. The water contents predicted by the Wang et al. (2006) model and Karato (1990) model appear to be the most reasonable and are more in line with water contents observed in other cratons (e.g., Peslier et al., 2010). The Yoshino et al. (2009) model appears to be an outlier and predicts much higher than average water contents and may not be a good estimate. A corrigendum was also released for the Yoshino et al. (2009) study showing that the resistivities predicted for hydrous olivine were off by an order of magnitude (Yoshino et al., 2014). Therefore the studies of Wang et al. (2006) and Karato (1990) may be more trustworthy for predicting water content.

The last significant finding from this assessment is that the mantle at depths greater than 170 km is predicted to be dry. Peslier et al. (2010) found a similar water content distribution in the Kaapvaal Craton in that the mantle was hydrous at pressures less than 6 GPa (~ 180 km depth) and dry at pressures greater than 6 GPa. The dry layer at the base of the lithosphere was suggested to be important for long term craton survival as the dry lithosphere would be viscous and therefore retard the removal by the underlying convecting asthenosphere. It is possible that the survival of the Slave craton is linked to a dry layer at the base of its lithosphere, which is rheologically strong and prevents the cratonic root from being eroded by the convecting mantle.

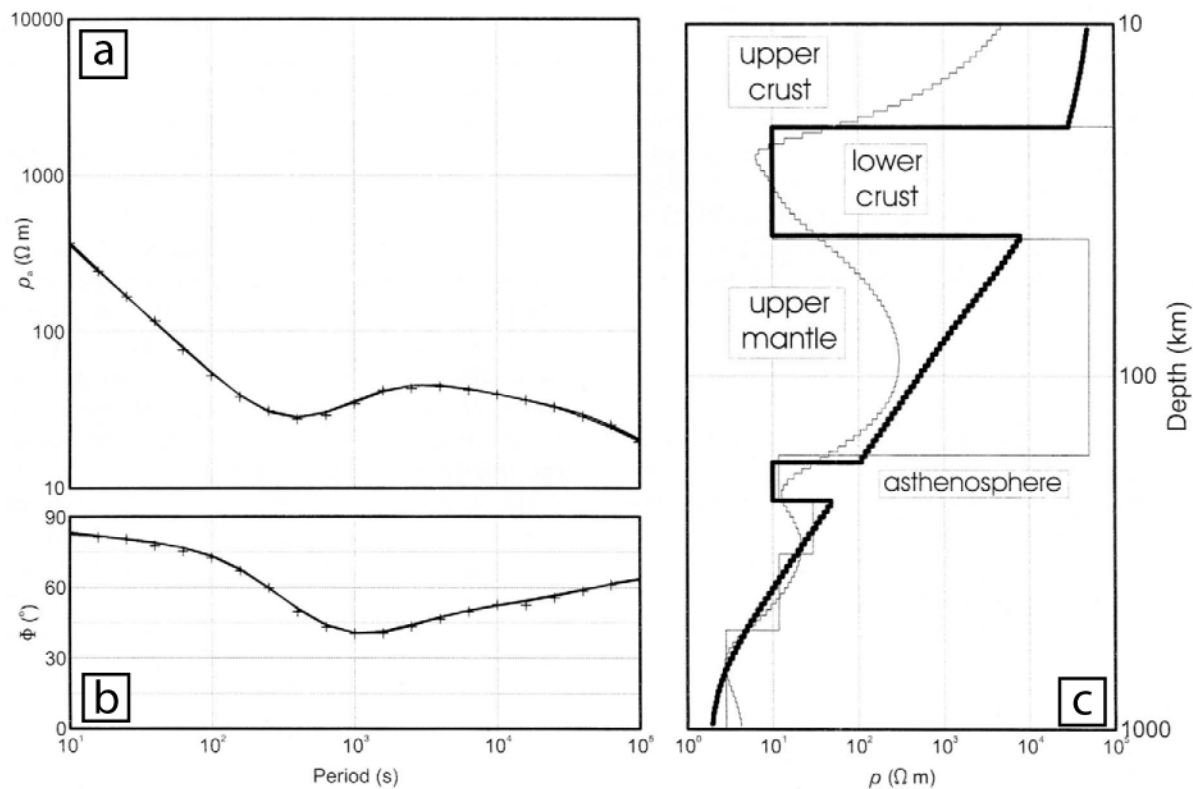


Figure 8.12 (a) Apparent resistivity data generated from a theoretical model containing a lower crustal conductor and the asthenosphere. (b) Phase data generated from a theoretical model containing a lower crustal conductor and the asthenosphere. (c) A theoretical model containing a lower crustal conductor and the asthenosphere (thick black line) and the inversion models recovered using a smooth model (smooth light grey line) and a sharp 7-layer inversion (sharp light grey line). (From Jones, 1999).

8.10 Conclusions

The 3-D resistivity model derived for the Slave craton has given a new insight into the structure of this region. The major results are as follows:

- (1) The lithospheric thickness of the Slave craton is 210 ± 10 km, which is in agreement with xenolith estimates from the most recently erupted kimberlites (45 - 75 Ma). Discrepancies in depth estimates from older kimberlite fields may be due to convective instabilities that can vary the thickness of cratonic roots varying over time.
- (2) There does not appear to be a genetic relationship between upper mantle conductors and diamondiferous kimberlites based upon case studies of the lithosphere below kimberlite fields worldwide. This study suggests that there may be a correlation between kimberlite

magmatism and upper mantle conductivity, but further data are needed to verify this hypothesis.

- (3) Petrologic data, laboratory experiments and teleseismic data were combined to constrain the conduction mechanism responsible for the high conductivity of the CSMC. The conduction mechanisms considered were (1) graphite, (2) sulphides, (3) nominally anhydrous minerals (clinopyroxene, orthopyroxene, garnet and olivine), (4) the hydrous minerals amphibole and phlogopite and (5) hydrous carbonatite melt or saline mantle brines. The only conduction mechanism considered that can simultaneously produce the observed reduction in shear wave velocities and resistivity in the central Slave craton are HDFs such as saline brines or hydrous carbonatite melts.
- (4) The main concern with this hypothesis is that saline brines and hydrous carbonatite melts are known to react with peridotite to form alkali chlorides and wehrlite respectively upon contact, which raises questions regarding how such fluids could remain stable until the present day. However, the geophysical evidence presented provides strong evidence of a fluid in the lithosphere and thus further petrological and laboratory experiments are likely required before a solution to this discrepancy can be found.
- (5) HDFs trapped in fibrous diamonds from Ekati and Diavik in the central Slave craton point towards a subduction origin for the fluids and the short residency time of the diamonds (< 200 Mya) suggests the fluids originated from a Mesozoic subduction event. It is possible that the fluids released from this subduction event metasomatized the lithosphere and weakened it allowing for kimberlites to preferentially penetrate the region, however, further geophysical studies are needed to verify this correlation.

Chapter 9 : Conclusions

9.1 Introduction

The Slave craton is a 400 x 600 km Archean block in Northwest Canada that contains many of the country's diamond mines. In this thesis the electrical resistivity structure of the Slave craton lithosphere was mapped using magnetotellurics for the purpose of better understanding lithospheric structure, which may improve regional diamond targeting as diamonds are formed in cratonic lithosphere. All available legacy magnetotelluric data in the Slave craton were used to construct the highest resolution 3-D resistivity model of the lithosphere to date. This contribution improved upon earlier studies which either used 2-D modelling, or used 3-D modelling that did not utilize all the available data and did not invert the full impedance tensor. The major findings from the present study are as follows:

9.2 Water Content in the Upper Mantle

The Slave craton in the depth range 100 - 170 km has a lower resistivity than expected for a dry mantle, which suggests that it may be hydrous to some degree. The water content for the Slave craton was interpreted using resistivity relationships derived for hydrous olivine and it was found that the mantle required water contents on the order of 10 - 150 ppm in the depth range 100 -170 km. Below these depths the lithosphere appears to be dry (< 5 ppm). The dry base of the lithosphere may act as a resistant boundary preventing the cratonic root from being eroded by the underlying asthenosphere.

9.3 Cause of the Central Slave Mantle Conductor (CSMC)

Early magnetotelluric studies of the Slave craton proposed that the low resistivity of the Central Slave Mantle Conductor (C1 from Chapter 7) was caused by graphite films deposited during the construction of the Slave craton. However, graphite films are likely not stable at these depths based upon results from recent laboratory experiments. In this study the Central Slave Mantle Conductor was interpreted as a layer of high density saline fluids that were emplaced from a Mesozoic subduction event (Weiss et al., 2015). Evidence supporting this interpretation includes saline fluids observed as inclusions from diamonds in the central Slave craton and a coincident mid-lithosphere discontinuity with reduced shear wave velocity relative to the surrounding mantle. It is further suggested that the spatial correlation between the low resistivity layer and the Lac de Gras kimberlite field could be the result of kimberlite magmas following zones of

weakness in the lithosphere as a result of the metasomatism caused by the slab-derived fluids. It should be noted that this interpretation is not without objections as fluids are positively buoyant and potentially highly reactive with the surrounding lithosphere and thus it may be difficult for fluids to remain over long time periods. Phlogopite and sulphides still remain possible candidates for the cause of the low resistivity of the CSMC, but these interpretations also have limitations as large quantities of phlogopite would be required ($> 20\%$) which is not well supported by xenoliths and interconnected sulphides in the mantle remain hypothetical and do not have sufficient laboratory experiments to characterize their electrical properties in the mantle.

9.4 Relationship Between Upper Mantle Conductors and Diamondiferous Kimberlites

In the past, some authors asserted that kimberlites in the central Slave craton were diamondiferous because there was an abundant source of carbon within the diamond stability field, which was conducive to diamond formation (Jones and Craven, 2004). Jones et al. (2005) further speculated that upper mantle conductors may be genetically related to the formation of diamondiferous kimberlites in cratonic lithosphere. However, recent laboratory experiments have found that graphite films do not remain interconnected in the upper mantle and thus will not lower the resistivity. Therefore, it is not possible to correlate regions of low resistivity to being more carbon rich and more prospective for diamond exploration. Analyzing the resistivity structure of prominent cratons in the world further suggests that there may not be a genetic relationship between upper mantle conductors below kimberlite fields and diamondiferous kimberlites. A relationship may exist between the Central Slave Mantle Conductor and the kimberlites in the central Slave craton, but this appears to be an exception and further work is needed to prove this hypothesis.

9.5 The Lithosphere-Asthenosphere Boundary

The lithosphere asthenosphere boundary (LAB) is a first-order boundary that separates the rigid outer shell of the Earth from the underlying, weaker asthenosphere. The depth estimate obtained from the preferred resistivity model (s92p21r8) for the LAB was 210 ± 10 km, which was marked by a transition from a resistivity of 300 - 1000 Ωm to 50 - 100 Ωm . The depth to the LAB corresponded to the inflection point of the resistivity depth curves, which was proven using a simple two layer synthetic model. A depth of 210 ± 10 km was found to be well within range previous geophysical studies and is in agreement with the most recently erupted xenoliths from

the youngest kimberlites (45 - 75 Ma). Discrepancies in depth estimates from older kimberlite fields may be due to convective instabilities that can vary the thickness of cratonic roots over time.

9.6 Future Work

The 3-D resistivity model for the Slave craton is the most robust model to date of the lithosphere, but there are still large gaps in the data set which hamper the interpretation of the CSMC and other mantle features. Our understanding of the resistivity structure of the Slave craton could be improved through the following suggestions:

1. The 3-D inversion model could be improved by collecting a grid of long period MT data over the central Slave craton. Currently, there is very sparse data west of Lac de Gras and the CSMC is constrained primarily by just one EW profile. A dense grid of MT data could provide better constraints on the spatial extent of the CSMC and its geometry. This is particularly interesting as it would reveal if the CSMC fully overlaps with the MLD described by Chen et al. (2009) as with the current array of MT stations it is unclear if the CSMC extends further west.
2. The conduit structures that penetrate the lower crust beneath Aylmer Lake and Lac de Gras are not constrained away from the EW profile. Collecting a grid of broadband MT data over this region would help constrain the origin and geometry of these structures. Understanding the structure of these features may help determine if the conduits are related to kimberlite magmatism or possibly a different process.
3. The MLD and CSMC are coincident beneath Lac de Gras, but it is not clear if the MLD extends beneath Aylmer Lake where the CSMC is centred. A NS profile using shear wave receiver functions (SRF) would be valuable over Aylmer Lake to confirm if the MLD extends to where the CSMC is observed in the resistivity model.
4. The change in data fit caused by removing C2 was investigated using (1) the KS test and (2) a direct comparison between data fits. The results found that C2 is not a robust feature, however, there was not strong enough evidence to prove that C2 is entirely an

artefact. Collecting a dense grid of long period MT data over C2 could further constrain the resistivity structure to verify if C2 is a real feature. Furthermore, if C2 is a real feature, additional data would better constrain its structure and possibly its origin.

References

- Archie, G. E., 1942, The electrical resistivity log as an aid in determining some reservoir characteristics: Transactions of the American Institute of Mechanical Engineers, 146, 54–67.
- Artemieva, I. M. (2009). The continental lithosphere: reconciling thermal, seismic, and petrologic data. *Lithos*, 109(1-2), 23-46.
- Aulbach, S. (2018). Cratonic Lithosphere Discontinuities: Dynamics of Small-Volume Melting, Metacratonization, and a Possible Role for Brines. *Lithospheric Discontinuities*, 177-203.
- Aulbach, S., Massuyeau, M., & Gaillard, F. (2017a). Origins of cratonic mantle discontinuities: A view from petrology, geochemistry and thermodynamic models. *Lithos*, 268, 364-382.
- Aulbach, S., Pearson, N. J., O'reilly, S. Y., & Doyle, B. J. (2007). Origins of xenolithic eclogites and pyroxenites from the Central Slave Craton, Canada. *Journal of Petrology*, 48(10), 1843-1873.
- Aulbach, S., Stachel, T., Heaman, L. M., & Carlson, J. A. (2011). Microxenoliths from the Slave craton: Archives of diamond formation along fluid conduits. *Lithos*, 126(3), 419-434.
- Aulbach, S., Sun, J., Tappe, S., Höfer, H. E., & Gerdes, A. (2017b). Volatile-rich metasomatism in the Cratonic Mantle beneath SW Greenland: link to Kimberlites and Mid-lithospheric discontinuities. *Journal of Petrology*, 58(12), 2311-2338.
- Bagdassarov, N. S., Kopylova, M. G., & Eichert, S. (2007). Laboratory derived constraints on electrical conductivity beneath Slave craton. *Physics of the Earth and Planetary Interiors*, 161(1-2), 126-133.
- Bank, C. G., Bostock, M. G., Ellis, R. M., & Cassidy, J. F. (2000). A reconnaissance teleseismic study of the upper mantle and transition zone beneath the Archean Slave craton in NW Canada. *Tectonophysics*, 319(3), 151-166.

References

- Bell, D. R., Rossman, G. R., Maldener, J., Endisch, D., & Rauch, F. (2003). Hydroxide in olivine: A quantitative determination of the absolute amount and calibration of the IR spectrum. *Journal of Geophysical Research: Solid Earth*, *108*(B2).
- Bleeker, W. (2003). The late Archean record: a puzzle in ca. 35 pieces. *Lithos*, *71*(2-4), 99-134.
- Bleeker, W., Ketchum, J. W., Jackson, V. A., & Villeneuve, M. E. (1999). The Central Slave Basement Complex, Part I: its structural topology and autochthonous cover. *Canadian Journal of Earth Sciences*, *36*(7), 1083-1110
- Bleeker, W., LeCheminant, A. N., Davis, W. J., Buchan, K. L., Ketchum, J. W., Sircoulon, J., ... & Ootes, L. (2007). *Transect across the southwestern Slave Craton: From Phanerozoic platform edge to the core of the Yellowknife supracrustal domain*. GAC-MAC Yellowknife 2007 Organizing Committee.
- Boerner, D. E., Kurtz, R. D., Craven, J. A., Ross, G. M., Jones, F. W., & Davis, W. J. (1999). Electrical conductivity in the Precambrian lithosphere of western Canada. *Science*, *283*(5402), 668-670.
- Booker, J. R. (2014). The magnetotelluric phase tensor: a critical review. *Surveys in Geophysics*, *35*(1), 7-40.
- Boonchaisuk, S., Noisagool, S., Amatyakul, P., Rung-Arunwan, T., Vachirastienchai, C., & Siripunvaraporn, W. (2017). 3-D magnetotelluric imaging of the Phayao Fault Zone, Northern Thailand: evidence for saline fluid in the source region of the 2014 Chiang Rai earthquake. *Journal of Asian Earth Sciences*, *147*, 210-221.
- Bostock, M. G. (1998). Mantle stratigraphy and evolution of the Slave province. *Journal of Geophysical Research: Solid Earth*, *103*(B9), 21183-21200.
- Bowring, S. A., & Williams, I. S. (1999). Priscoan (4.00–4.03 Ga) orthogneisses from northwestern Canada. *Contributions to Mineralogy and Petrology*, *134*(1), 3-16.
- Caldwell, T. G., Bibby, H. M., & Brown, C. (2004). The magnetotelluric phase tensor. *Geophysical Journal International*, *158*(2), 457-469.

References

- Carbno, G. B., & Canil, D. (2002). Mantle structure beneath the SW Slave craton, Canada: constraints from garnet geochemistry in the Drybones Bay kimberlite. *Journal of Petrology*, *43*(1), 129-142.
- Chakraborty, S. (2008). Diffusion in solid silicates: a tool to track timescales of processes comes of age. *Annu. Rev. Earth Planet. Sci.*, *36*, 153-190.
- Chave, A. D., & Jones, A. G. (Eds.). (2012). *The magnetotelluric method: Theory and practice*. Cambridge University Press.
- Chen, C. W., Rondenay, S., Evans, R. L., & Snyder, D. B. (2009). Geophysical detection of relict metasomatism from an Archean (~ 3.5 Ga) subduction zone. *science*, *326*(5956), 1089-1091.
- Chen, C. W., Rondenay, S., Weeraratne, D. S., & Snyder, D. B. (2007). New constraints on the upper mantle structure of the Slave craton from Rayleigh wave inversion. *Geophysical Research Letters*, *34*(10).
- Conrad, C. P. (2000). Convective instability of thickening mantle lithosphere. *Geophysical Journal International*, *143*(1), 52-70.
- Constable, S. (2006). SEO3: a new model of olivine electrical conductivity. *Geophysical Journal International*, *166*(1), 435-437.
- Cook, F. A., Van der Velden, A. J., & Hall, K. W. (1997). Upper mantle reflectors beneath the SNORCLE transect—Images of the base of the lithosphere. In *Slave-Northern Cordillera Lithospheric Evolution (SNORCLE) Transect and Cordilleran Tectonics Workshop Meeting: University of Calgary* (pp. 58-62).
- Cook, F. A., van der Velden, A. J., Hall, K. W., & Roberts, B. J. (1999). Frozen subduction in Canada's Northwest Territories: Lithoprobe deep lithospheric reflection profiling of the western Canadian Shield. *Tectonics*, *18*(1), 1-24.
- Creaser, R. A., Grütter, H., Carlson, J., & Crawford, B. (2004). Macrocrystal phlogopite Rb–Sr dates for the Ekati property kimberlites, Slave Province, Canada: evidence for multiple intrusive episodes in the Paleocene and Eocene. *Lithos*, *76*(1-4), 399-414.

References

- Creighton, S., Stachel, T., Eichenberg, D., & Luth, R. W. (2010). Oxidation state of the lithospheric mantle beneath Diavik diamond mine, central Slave craton, NWT, Canada. *Contributions to Mineralogy and Petrology*, 159(5), 645-657.
- Dai, L., & Karato, S. I. (2009a). Electrical conductivity of pyrope-rich garnet at high temperature and high pressure. *Physics of the Earth and Planetary Interiors*, 176(1-2), 83-88.
- Dai, L., & Karato, S. I. (2009b). Electrical conductivity of orthopyroxene: Implications for the water content of the asthenosphere. *Proceedings of the Japan Academy, Series B*, 85(10), 466-475.
- Dalton, J. A., & Wood, B. J. (1993). The compositions of primary carbonate melts and their evolution through wallrock reaction in the mantle. *Earth and Planetary Science Letters*, 119(4), 511-525.
- Dasgupta, R. (2018). Volatile-bearing partial melts beneath oceans and continents—Where, how much, and of what compositions?. *American Journal of Science*, 318(1), 141-165.
- Davis, W. J., Canil, D., MacKenzie, J. M., & Carbno, G. B. (2003). Petrology and U–Pb geochronology of lower crustal xenoliths and the development of a craton, Slave Province, Canada. *Lithos*, 71(2-4), 541-573.
- Day, H. W. (2012). A revised diamond-graphite transition curve. *American Mineralogist*, 97(1), 52-62.
- Deines, P. (2002). The carbon isotope geochemistry of mantle xenoliths. *Earth-Science Reviews*, 58(3-4), 247-278.
- DeLucia, M. S., Murphy, B. S., Marshak, S., & Egbert, G. D. (2019). The Missouri High-Conductivity Belt, revealed by magnetotelluric imaging: Evidence of a trans-lithospheric shear zone beneath the Ozark Plateau, Midcontinent USA?. *Tectonophysics*, 753, 111-123.
- Dixon, J. E., Dixon, T. H., Bell, D. R., & Malservisi, R. (2004). Lateral variation in upper mantle viscosity: role of water. *Earth and Planetary Science Letters*, 222(2), 451-467.

References

- Duba, A. G., & Shankland, T. J. (1982). Free carbon & electrical conductivity in the Earth's mantle. *Geophysical Research Letters*, 9(11), 1271-1274.
- Ducea, M. N., & Park, S. K. (2000). Enhanced mantle conductivity from sulfide minerals, southern Sierra Nevada, California. *Geophysical Research Letters*, 27(16), 2405-2408.
- Eaton, D. W., & Perry, H. C. (2013). Ephemeral isopycnicity of cratonic mantle keels. *Nature Geoscience*, 6(11), 967.
- Eaton, D. W., Darbyshire, F., Evans, R. L., Grütter, H., Jones, A. G., & Yuan, X. (2009). The elusive lithosphere–asthenosphere boundary (LAB) beneath cratons. *Lithos*, 109(1-2), 1-22.
- Eeken, T., Goes, S., Pedersen, H. A., Arndt, N. T., & Bouilhol, P. (2018). Seismic evidence for depth-dependent metasomatism in cratons. *Earth and Planetary Science Letters*, 491, 148-159.
- Ernst, R. E., Head, J. W., Parfitt, E., Grosfils, E., & Wilson, L. (1995). Giant radiating dyke swarms on Earth and Venus. *Earth-Science Reviews*, 39(1-2), 1-58.
- Esteve, C., Schaeffer, A. J., & Audet, P. (2019). Upper mantle structure underlying the diamondiferous Slave craton from teleseismic body-wave tomography. *Tectonophysics*.
- Evans, R. L., Jones, A. G., Garcia, X., Muller, M., Hamilton, M., Evans, S., ... & Hutchins, D. (2011). Electrical lithosphere beneath the Kaapvaal craton, southern Africa. *Journal of Geophysical Research: Solid Earth*, 116(B4).
- Ferguson, I. J., Craven, J. A., Kurtz, R. D., Boerner, D. E., Bailey, R. C., Wu, X., ... & Norton, M. (2005). Geoelectric response of Archean lithosphere in the western Superior Province, central Canada. *Physics of the Earth and Planetary Interiors*, 150(1-3), 123-143.
- Foley, S. (1992). Vein-plus-wall-rock melting mechanisms in the lithosphere and the origin of potassic alkaline magmas. *Lithos*, 28(3-6), 435-453.

References

- Förster, M. W., Foley, S. F., Marschall, H. R., Alard, O., & Buhre, S. (2019). Melting of sediments in the deep mantle produces saline fluid inclusions in diamonds. *Science Advances*, 5(5), eaau2620.
- Fournier, D., Kang, S., McMillan, M. S., & Oldenburg, D. W. (2017). Inversion of airborne geophysics over the DO-27/DO-18 kimberlites—Part 2: Electromagnetics. *Interpretation*, 5(3), T313-T325.
- Frezzotti, M. L., & Touret, J. L. (2014). CO₂, carbonate-rich melts, and brines in the mantle. *Geoscience Frontiers*, 5(5), 697-710.
- Frost, B. R., Fyfe, W. S., Tazaki, K., & Chan, T. (1989). Grain-boundary graphite in rocks and implications for high electrical conductivity in the lower crust. *Nature*, 340(6229), 134.
- Frost, D. J. (2006). The stability of hydrous mantle phases. *Reviews in Mineralogy and Geochemistry*, 62(1), 243-271.
- Gaillard, F., Malki, M., Iacono-Marziano, G., Pichavant, M., & Scaillet, B. (2008). Carbonatite melts and electrical conductivity in the asthenosphere. *Science*, 322(5906), 1363-1365.
- Giuliani, A., Phillips, D., Kamenetsky, V. S., & Goemann, K. (2016). Constraints on kimberlite ascent mechanisms revealed by phlogopite compositions in kimberlites and mantle xenoliths. *Lithos*, 240, 189-201.
- Glover, P. W. (2010). A generalized Archie's law for n phases. *Geophysics*, 75(6), E247-E265.
- Grant, K., Ingrin, J., Lorand, J. P., & Dumas, P. (2007). Water partitioning between mantle minerals from peridotite xenoliths. *Contributions to Mineralogy and Petrology*, 154(1), 15-34.
- Griffin, W. L., Doyle, B. J., Ryan, C. G., Pearson, N. J., Suzanne, Y. O. R., Davies, R., ... & Natapov, L. M. (1999). Layered mantle lithosphere in the Lac de Gras area, Slave craton: composition, structure and origin. *Journal of Petrology*, 40(5), 705-727.

References

- Groom, R. W., & Bailey, R. C. (1989). Decomposition of magnetotelluric impedance tensors in the presence of local three-dimensional galvanic distortion. *Journal of Geophysical Research: Solid Earth*, *94*(B2), 1913-1925.
- Grütter, H. S., Apter, D. B., & Kong, J. (1999). Crust–mantle coupling: evidence from mantle-derived xenocrystic garnets. In *Proceedings of the 7th International Kimberlite Conference*(Vol. 1, pp. 307-313). Red Roof Design Cape Town.
- Guo, H., & Keppler, H. (2019). Electrical Conductivity of NaCl-Bearing Aqueous Fluids to 900° C and 5 GPa. *Journal of Geophysical Research: Solid Earth*, *124*(2), 1397-1411.
- Hammond, W. C., & Humphreys, E. D. (2000). Upper mantle seismic wave velocity: Effects of realistic partial melt geometries. *Journal of Geophysical Research: Solid Earth*, *105*(B5), 10975-10986.
- Hashin, Z., & Shtrikman, S. (1963). A variational approach to the theory of the elastic behaviour of multiphase materials. *Journal of the Mechanics and Physics of Solids*, *11*(2), 127-140.
- Heaman, L. M., & Pearson, D. G. (2010). Nature and evolution of the Slave Province subcontinental lithospheric mantle. *Canadian Journal of Earth Sciences*, *47*(4), 369-388.
- Heaman, L. M., Kjarsgaard, B. A., & Creaser, R. A. (2003). The timing of kimberlite magmatism in North America: implications for global kimberlite genesis and diamond exploration. *Lithos*, *71*(2-4), 153-184.
- Helffrich, G., Kendall, J. M., Hammond, J. O., & Carroll, M. R. (2011). Sulfide melts and long-term low seismic wavespeeds in lithospheric and asthenospheric mantle. *Geophysical Research Letters*, *38*(11).
- Helmstaedt, H. H., & Gurney, J. J. (1995). Geotectonic controls of primary diamond deposits: implications for area selection. *Journal of Geochemical Exploration*, *53*(1-3), 125-144.
- Hirschmann, M. M. (2000). Mantle solidus: Experimental constraints and the effects of peridotite composition. *Geochemistry, Geophysics, Geosystems*, *1*(10).

References

- Hoffman, P. F., Bally, A. W., & Palmer, A. R. (1989). Precambrian geology and tectonic history of North America. *The geology of North America—an overview*, 447-512.
- Hou, G., Kusky, T. M., Wang, C., & Wang, Y. (2010). Mechanics of the giant radiating Mackenzie dyke swarm: a paleostress field modeling. *Journal of Geophysical Research: Solid Earth*, 115(B2).
- Hu, H., Dai, L., Li, H., Sun, W., & Li, B. (2018). Effect of dehydrogenation on the electrical conductivity of Fe-bearing amphibole: Implications for high conductivity anomalies in subduction zones and continental crust. *Earth and Planetary Science Letters*, 498, 27-37.
- Izraeli, E. S., Harris, J. W., & Navon, O. (2001). Brine inclusions in diamonds: a new upper mantle fluid. *Earth and Planetary Science Letters*, 187(3-4), 323-332.
- Jansen, J., & Witherly, K. (2004). The Tli Kwi Cho kimberlite complex, Northwest Territories, Canada: A geophysical case study. In *SEG Technical Program Expanded Abstracts 2004* (pp. 1147-1150). Society of Exploration Geophysicists.
- Jones, A. G. (1988). Static shift of magnetotelluric data and its removal in a sedimentary basin environment. *Geophysics*, 53(7), 967-978.
- Jones, A. G. (1999). Imaging the continental upper mantle using electromagnetic methods. In *Developments in Geotectonics* (Vol. 24, pp. 57-80). Elsevier.
- Jones, A. G., & Craven, J. A. (2004). Area selection for diamond exploration using deep-probing electromagnetic surveying. *Lithos*, 77(1-4), 765-782
- Jones, A. G., & Ferguson, I. J. (2001). The electric moho. *Nature*, 409(6818), 331.
- Jones, A. G., & Garcia, X. (2006). Electrical resistivity structure of the Yellowknife River Fault Zone and surrounding region. *Gold in the Yellowknife Greenstone Belt, Northwest Territories: Results of the EXTECH III Multidisciplinary Research Project*, 3, 126-141.
- Jones, A. G., Evans, R. L., & Eaton, D. W. (2009a). Velocity–conductivity relationships for mantle mineral assemblages in Archean cratonic lithosphere based on a review of laboratory data and Hashin–Shtrikman extremal bounds. *Lithos*, 109(1-2), 131-143.

References

- Jones, A. G., Evans, R. L., Muller, M. R., Hamilton, M. P., Miensoopust, M. P., Garcia, X., ... & Jelsma, H. (2009b). Area selection for diamonds using magnetotellurics: Examples from southern Africa. *Lithos*, *112*, 83-92.
- Jones, A. G., Ferguson, I. J., Chave, A. D., Evans, R. L., & McNeice, G. W. (2001a). Electric lithosphere of the Slave craton. *Geology*, *29*(5), 423-426.
- Jones, A. G., Ledo, J., & Ferguson, I. J. (2005). Electromagnetic images of the Trans-Hudson orogen: the North American Central Plains anomaly revealed. *Canadian Journal of Earth Sciences*, *42*(4), 457-478.
- Jones, A. G., Lezaeta, P., Ferguson, I. J., Chave, A. D., Evans, R. L., Garcia, X., & Spratt, J. (2003). The electrical structure of the Slave craton. *Lithos*, *71*(2-4), 505-527.
- Jones, A. G., Snyder, D., & Spratt, J. (2001b). *Magnetotelluric and teleseismic experiments as part of the Walmsley Lake project, Northwest Territories: experimental designs and preliminary results*. Natural Resources Canada, Geological Survey of Canada.
- Jordan, T. H. (1978). Composition and development of the continental tectosphere. *Nature*, *274*(5671), 544.
- Karato, S. I. (1990). The role of hydrogen in the electrical conductivity of the upper mantle. *Nature*, *347*(6290), 272.
- Karato, S. I., Olugboji, T., & Park, J. (2015). Mechanisms and geologic significance of the mid-lithosphere discontinuity in the continents. *Nature Geoscience*, *8*(7), 509.
- Keating, P., & Sailhac, P. (2004). Use of the analytic signal to identify magnetic anomalies due to kimberlite pipes. *Geophysics*, *69*(1), 180-190.
- Kelbert, A., Meqbel, N., Egbert, G. D., & Tandon, K. (2014). ModEM: A modular system for inversion of electromagnetic geophysical data. *Computers & Geosciences*, *66*, 40-53.
- Klein-BenDavid, O., Izraeli, E. S., Hauri, E., & Navon, O. (2004). Mantle fluid evolution—a tale of one diamond. *Lithos*, *77*(1-4), 243-253.

References

- Klein-BenDavid, O., Izraeli, E. S., Hauri, E., & Navon, O. (2007). Fluid inclusions in diamonds from the Diavik mine, Canada and the evolution of diamond-forming fluids. *Geochimica et Cosmochimica Acta*, *71*(3), 723-744.
- Klein-BenDavid, O., Logvinova, A. M., Schrauder, M., Spetius, Z. V., Weiss, Y., Hauri, E. H., ... & Navon, O. (2009). High-Mg carbonatitic microinclusions in some Yakutian diamonds—a new type of diamond-forming fluid. *Lithos*, *112*, 648-659.
- Klein-BenDavid, O., Pearson, D. G., Nowell, G. M., Ottley, C., McNeill, J. C., Logvinova, A., & Sobolev, N. V. (2014). The sources and time-integrated evolution of diamond-forming fluids—Trace elements and isotopic evidence. *Geochimica et Cosmochimica Acta*, *125*, 146-169.
- Kohlstedt, D. L., Keppler, H., & Rubie, D. C. (1996). Solubility of water in the α , β and γ phases of (Mg, Fe) 2SiO_4 . *Contributions to Mineralogy and Petrology*, *123*(4), 345-357.
- Kopylova, M. G., & Caro, G. (2004). Mantle xenoliths from the southeastern Slave craton: evidence for chemical zonation in a thick, cold lithosphere. *Journal of Petrology*, *45*(5), 1045-1067.
- Kopylova, M. G., & Russell, J. K. (2000). Chemical stratification of cratonic lithosphere: constraints from the Northern Slave craton, Canada. *Earth and Planetary Science Letters*, *181*(1), 71-87.
- Kopylova, M. G., Russell, J. K., & Cookenboo, H. (1999). Petrology of peridotite and pyroxenite xenoliths from the Jericho kimberlite: implications for the thermal state of the mantle beneath the Slave craton, northern Canada. *Journal of Petrology*, *40*(1), 79-104.
- Kopylova, M.G., 2002. The deep structures of the Slave Craton. Presented at ‘‘Diamond Short Course’’, held in Vancouver, Canada, B.C., 21 February.
- Kopylova, M.G., Russel, J.K., Cookenboo, H., 1997. Petrology of peridotite and pyroxenite xenoliths from Jericho Kimberlite; implications for the thermal state of the mantle beneath the Slave Craton, northern Canada. *J. Petrol.* *40*, 79–104.

References

- Kopylova, M.G., Russell, J.K., Cookenboo, H., 1998. Upper-subduction zone from non-linear teleseismic travel-time mantle stratigraphy of the Slave craton, Canada: insights inversion. PhD Thesis, University of Washington, Seattle, into a new kimberlite province. *Geology* 26 (4), 315–318.
- Kovács, I., Lenkey, L., Green, D. H., Fancsik, T., Falus, G., Kiss, J., ... & Viktor, Z. (2017). The role of pargasitic amphibole in the formation of major geophysical discontinuities in the shallow upper mantle. *Acta Geodaetica et Geophysica*, 52(2), 183-204.
- La Terra, E. F., & Menezes, P. T. (2012). Audiomagnetotelluric 3-D imaging of the Regis kimberlite pipe, Minas Gerais, Brazil. *Journal of Applied Geophysics*, 77, 30-38.
- LeCheminant, A. N., & Heaman, L. M. (1989). Mackenzie igneous events, Canada: Middle Proterozoic hotspot magmatism associated with ocean opening. *Earth and Planetary Science Letters*, 96(1-2), 38-48.
- Li, Y., Jiang, H., & Yang, X. (2017). Fluorine follows water: Effect on electrical conductivity of silicate minerals by experimental constraints from phlogopite. *Geochimica et Cosmochimica Acta*, 217, 16-27.
- Li, Y., Yang, X., Yu, J. H., & Cai, Y. F. (2016). Unusually high electrical conductivity of phlogopite: the possible role of fluorine and geophysical implications. *Contributions to Mineralogy and Petrology*, 171(4), 37.
- Lizarralde, D., Chave, A., Hirth, G., & Schultz, A. (1995). Northeastern Pacific mantle conductivity profile from long- period magnetotelluric sounding using Hawaii-to-California submarine cable data. *Journal of Geophysical Research: Solid Earth*, 100(B9), 17837-17854.
- Macnae, J. (1995). Applications of geophysics for the detection and exploration of kimberlites and lamproites. *Journal of Geochemical Exploration*, 53(1-3), 213-243.
- Macnae, J. C. (1979). Kimberlites and exploration geophysics. *Geophysics*, 44(8), 1395-1416.
- Mathers, K. (2012) A Xenolith-Based Lithospheric Transect of the Slave craton, N.W.T., Canada (Doctoral dissertation). Durham University, Durham, United Kingdom.

References

- Mathez, E. A. (1987). Carbonaceous matter in mantle xenoliths: Composition and relevance to the isotopes. *Geochimica et Cosmochimica Acta*, 51(9), 2339-2347.
- Maxwell, J. C., (1861). On physical lines of force. *Philosophical Magazine*.
- McNeice, G. W., & Jones, A. G. (2001). Multisite, multifrequency tensor decomposition of magnetotelluric data. *Geophysics*, 66(1), 158-173.
- Minarik, W. G., & Watson, E. B. (1995). Interconnectivity of carbonate melt at low melt fraction. *Earth and Planetary Science Letters*, 133(3-4), 423-437.
- Moorkamp, M., Jones, A. G., & Eaton, D. W. (2007). Joint inversion of teleseismic receiver functions and magnetotelluric data using a genetic algorithm: Are seismic velocities and electrical conductivities compatible?. *Geophysical Research Letters*, 34(16).
- Moorkamp, M., Jones, A. G., & Fishwick, S. (2010). Joint inversion of receiver functions, surface wave dispersion, and magnetotelluric data. *Journal of Geophysical Research: Solid Earth*, 115(B4).
- Morency, C., Doin, M. P., & Dumoulin, C. (2002). Convective destabilization of a thickened continental lithosphere. *Earth and Planetary Science Letters*, 202(2), 303-320.
- Navon, O., Hutcheon, I. D., Rossman, G. R., & Wasserburg, G. J. (1988). Mantle-derived fluids in diamond micro-inclusions. *Nature*, 335(6193), 784.
- Nelson, P. H., & Van Voorhis, G. D. (1983). Estimation of sulfide content from induced polarization data. *Geophysics*, 48(1), 62-75.
- Newton, D. E., Kopylova, M. G., Burgess, J., & Strand, P. (2015). Peridotite and pyroxenite xenoliths from the MuskoX kimberlite, northern Slave craton, Canada. *Canadian Journal of Earth Sciences*, 53(1), 41-58.
- Ogawa, Y., Ichiki, M., Kanda, W., Mishina, M., & Asamori, K. (2014). Three-dimensional magnetotelluric imaging of crustal fluids and seismicity around Naruko volcano, NE Japan. *Earth, Planets and Space*, 66(1), 158.

References

- Oldenburg, D. W. (1981), Conductivity structure of oceanic upper mantle beneath the Pacific plate, *Geophys. J. R. Astron. Soc.*, *65*, 359–394.
- O'Reilly, S. Y., & Griffin, W. L. (2010). The continental lithosphere–asthenosphere boundary: can we sample it?. *Lithos*, *120*(1-2), 1-13.
- Pearson, D. G., Boyd, F. R., Haggerty, S. E., Pasteris, J. D., Field, S. W., Nixon, P. H., & Pokhilenko, N. P. (1994). The characterisation and origin of graphite in cratonic lithospheric mantle: a petrological carbon isotope and Raman spectroscopic study. *Contributions to Mineralogy and Petrology*, *115*(4), 449-466.
- Pearson, N.J., Griffin, W.L., Doyle, B.J., O'Reilly, S.Y., VanAchterbergh, E., Kivi, K., 1999. Xenoliths from kimberlite pipes of the Lac de Gras area, Slave craton, Canada. In: Gurney, J.J., et al. (Eds.), Proceedings of the 7th international Kimberlite conference. P.H. Nixon, vol. 2. Red Roof Design, Cape Town, pp. 644–658.
- Pehrsson, S. J., Chacko, T., Pilkington, M., Villeneuve, M. E., & Bethune, K. (2000). Anton terrane revisited: Late Archean exhumation of a moderate-pressure granulite terrane in the western Slave Province. *Geology*, *28*(12), 1075-1078.
- Percival, J. A., Clowes, R., & Cook, F. A. (Eds.). (2012). Tectonic styles in Canada: the LITHOPROBE perspective. Geological Association of Canada.
- Peslier, A. H., & Luhr, J. F. (2006). Hydrogen loss from olivines in mantle xenoliths from Simcoe (USA) and Mexico: Mafic alkalic magma ascent rates and water budget of the sub-continental lithosphere. *Earth and Planetary Science Letters*, *242*(3-4), 302-319.
- Peslier, A. H., Woodland, A. B., Bell, D. R., & Lazarov, M. (2010). Olivine water contents in the continental lithosphere and the longevity of cratons. *Nature*, *467*(7311), 78.
- Pinto, L. G. R., de Pádua, M. B., Ussami, N., Vitorello, Í., Padilha, A. L., & Braitenberg, C. (2010). Magnetotelluric deep soundings, gravity and geoid in the south São Francisco craton: Geophysical indicators of cratonic lithosphere rejuvenation and crustal underplating. *Earth and Planetary Science Letters*, *297*(3-4), 423-434.

References

- Poudjom Djomani, Y. H., Griffin, W. L., O'Reilly, S. Y., & Doyle, B. J. (2005a). Lithospheric domains and controls on kimberlite emplacement, Slave Province, Canada: Evidence from elastic thickness and upper mantle composition. *Geochemistry, Geophysics, Geosystems*, 6(10).
- Poudjom Djomani, Y. H., O'Reilly, S. Y., Griffin, W. L., Natapov, L. M., Pearson, N. J., & Doyle, B. J. (2005b). Variations of the effective elastic thickness (T_e) and structure of the lithosphere beneath the Slave Province, Canada. *Exploration Geophysics*, 36(3), 266-271.
- Power, M., & Hildes, D. (2007). Geophysical strategies for kimberlite exploration in northern Canada. In *Proceedings of Exploration* (Vol. 7, pp. 1025-1031).
- Power, M., Belcourt, G., & Rockel, E. (2004). Geophysical methods for kimberlite exploration in northern Canada. *The Leading Edge*, 23(11), 1124-1129.
- Rader, E., Emry, E., Schmerr, N., Frost, D., Cheng, C., Menard, J., ... & Geist, D. (2015). Characterization and petrological constraints of the midlithospheric discontinuity. *Geochemistry, Geophysics, Geosystems*, 16(10), 3484-3504.
- Reed, L. E., & Witherly, K. E. (2007). 50 years of kimberlite geophysics: A review. In *Proceedings of Exploration 07: Fifth Decennial International Conference on Mineral Exploration*(pp. p679-p689).
- Rippe, D., Unsworth, M. J., & Currie, C. A. (2013). Magnetotelluric constraints on the fluid content in the upper mantle beneath the southern Canadian Cordillera: Implications for rheology. *Journal of Geophysical Research: Solid Earth*, 118(10), 5601-5624.
- Rodi, W., & Mackie, R. L. (2001). Nonlinear conjugate gradients algorithm for 2-D magnetotelluric inversion. *Geophysics*, 66(1), 174-187.
- Sack, R. O., & Ebel, D. S. (2006). Thermochemistry of sulfide mineral solutions. *Reviews in Mineralogy and Geochemistry*, 61(1), 265-364.
- Saha, S., Dasgupta, R., & Tsuno, K. (2018). High Pressure Phase Relations of a Depleted Peridotite Fluxed by CO₂-H₂O-Bearing Siliceous Melts and the Origin of Mid-Lithospheric Discontinuity. *Geochemistry, Geophysics, Geosystems*, 19(3), 595-620.

References

- Schilling, F. R., Partzsch, G. M., Brasse, H., & Schwarz, G. (1997). Partial melting below the magmatic arc in the central Andes deduced from geoelectromagnetic field experiments and laboratory data. *Physics of the Earth and Planetary Interiors*, 103(1-2), 17-31.
- Schrauder, M., & Navon, O. (1994). Hydrous and carbonatitic mantle fluids in fibrous diamonds from Jwaneng, Botswana. *Geochimica et Cosmochimica Acta*, 58(2), 761-771.
- Schultz, A., Kurtz, R.D., Chave, A.D., Jones, A.G., 1993. Conductivity discontinuities in the upper mantle beneath a stable craton. *Geophys. Res. Lett.* 20, 2941–2944
- Selway, K. (2014). On the causes of electrical conductivity anomalies in tectonically stable lithosphere. *Surveys in Geophysics*, 35(1), 219-257.
- Selway, K. (2018). Electrical discontinuities in the continental lithosphere imaged with magnetotellurics. *Lithospheric Discontinuities*, 239, 89.
- Selway, K., Ford, H., & Kelemen, P. (2015). The seismic mid-lithosphere discontinuity. *Earth and Planetary Science Letters*, 414, 45-57.
- Selway, K., Yi, J., & Karato, S. I. (2014). Water content of the Tanzanian lithosphere from magnetotelluric data: Implications for cratonic growth and stability. *Earth and Planetary Science Letters*, 388, 175-186.
- Shankland, T. J., R. J. O'Connell, and H. S. Waff (1981), Geophysical constraints on partial melt in the upper mantle, *Rev. Geophys. SpacePhys.*, 19, 394–406.
- Simpson, F., & Bahr, K. (2005). *Practical magnetotellurics*. Cambridge University Press.
- Siripunvaraporn, W., Egbert, G., Lenbury, Y., & Uyeshima, M. (2005). Three-dimensional magnetotelluric inversion: data-space method. *Physics of the Earth and planetary interiors*, 150(1-3), 3-14.
- Snyder, D. B., & Grütter, H. S. (2010). Lithoprobe's impact on the Canadian diamond-exploration industry. *Canadian Journal of Earth Sciences*, 47(5), 783-800.

References

- Snyder, D. B., Hillier, M. J., Kjarsgaard, B. A., de Kemp, E. A., & Craven, J. A. (2014). Lithospheric architecture of the Slave craton, northwest Canada, as determined from an interdisciplinary 3-D model. *Geochemistry, Geophysics, Geosystems*, *15*(5), 1895-1910.
- Snyder, D. B., Humphreys, E., & Pearson, D. G. (2017). Construction and destruction of some North American cratons. *Tectonophysics*, *694*, 464-485.
- Snyder, D. B., Rondenay, S., Bostock, M. G., & Lockhart, G. D. (2004). Mapping the mantle lithosphere for diamond potential using teleseismic methods. *Lithos*, *77*(1-4), 859-872.
- Spratt, J. E., Jones, A. G., Jackson, V. A., Collins, L., & Avdeeva, A. (2009). Lithospheric geometry of the Wopmay orogen from a Slave craton to Bear Province magnetotelluric transect. *Journal of Geophysical Research: Solid Earth*, *114*(B1).
- Stagno, V., & Frost, D. J. (2010). Carbon speciation in the asthenosphere: Experimental measurements of the redox conditions at which carbonate-bearing melts coexist with graphite or diamond in peridotite assemblages. *Earth and Planetary Science Letters*, *300*(1-2), 72-84.
- Thiel, S., & Heinson, G. (2013). Electrical conductors in Archean mantle—Result of plume interaction?. *Geophysical Research Letters*, *40*(12), 2947-2952.
- Thomas, M. D. (1992). Ancient collisional continental margins in the Canadian shield: geophysical signatures and derived crustal transects. In *Basement Tectonics 8* (pp. 5-25). Springer, Dordrecht.

References

- Thorpe, R. I., Cumming, G. L., & Mortensen, J. K. (1992). A significant Pb isotope boundary in the Slave Province and its probable relation to ancient basement in the western Slave Province. *Geological Survey of Canada Open File*, 2484, 179-184.
- Thybo, H. (2006). The heterogeneous upper mantle low velocity zone. *Tectonophysics*, 416(1-4), 53-79.
- Thybo, H., & Perčuč, E. (1997). The seismic 8 discontinuity and partial melting in continental mantle. *Science*, 275(5306), 1626-1629.
- Türkoğlu, E., Unsworth, M., & Pana, D. (2009). Deep electrical structure of northern Alberta (Canada): implications for diamond exploration. *Canadian Journal of Earth Sciences*, 46(2), 139-154.
- Viejo, G. F., Clowes, R. M., & Amor, J. R. (1999). Imaging the lithospheric mantle in northwestern Canada with seismic wide-angle reflections. *Geophysical Research Letters*, 26(18), 2809-2812.
- Waff, H. S. (1974). Theoretical considerations of electrical conductivity in a partially molten mantle and implications for geothermometry. *Journal of Geophysical Research*, 79(26), 4003-4010.
- Wang, D., Guo, Y., Yu, Y., & Karato, S. I. (2012). Electrical conductivity of amphibole-bearing rocks: influence of dehydration. *Contributions to Mineralogy and Petrology*, 164(1), 17-25.
- Wang, D., Karato, S. I., & Jiang, Z. (2013). An experimental study of the influence of graphite on the electrical conductivity of olivine aggregates. *Geophysical Research Letters*, 40(10), 2028-2032.
- Wang, D., Mookherjee, M., Xu, Y., & Karato, S. I. (2006). The effect of water on the electrical conductivity of olivine. *Nature*, 443(7114), 977.
- Wang, E. (2019) Multidimensional magnetotelluric studies of the Precambrian Alberta Basement (Doctoral dissertation). University of Alberta, Edmonton, Canada.

References

- Watson, H. C., Roberts, J. J., & Tyburczy, J. A. (2010). Effect of conductive impurities on electrical conductivity in polycrystalline olivine. *Geophysical Research Letters*, *37*(2).
- Weiss, Y., McNeill, J., Pearson, D. G., Nowell, G. M., & Ottley, C. J. (2015). Highly saline fluids from a subducting slab as the source for fluid-rich diamonds. *Nature*, *524*(7565), 339.
- Yang, X. (2011). Origin of high electrical conductivity in the lower continental crust: a review. *Surveys in geophysics*, *32*(6), 875.
- Yoshino, T. (2010). Laboratory electrical conductivity measurement of mantle minerals. *Surveys in Geophysics*, *31*(2), 163-206.
- Yoshino, T., Gruber, B., & Reinier, C. (2018). Effects of pressure and water on electrical conductivity of carbonate melt with implications for conductivity anomaly in continental mantle lithosphere. *Physics of the Earth and Planetary Interiors*, *281*, 8-16.
- Yoshino, T., Matsuzaki, T., Shatskiy, A., & Katsura, T. (2009). The effect of water on the electrical conductivity of olivine aggregates and its implications for the electrical structure of the upper mantle. *Earth and Planetary Science Letters*, *288*(1-2), 291-300.
- Yoshino, T., Matsuzaki, T., Shatzkiy, A., & Katsura, T. (2014). Corrigendum to "The effect of water on the electrical conductivity of olivine aggregates and its implications for the electrical structure in the upper mantle"[*Earth Planet. Sci. Lett.* *288* (2009) 291-300]. *Earth and Planetary Science Letters*, *391*, 135-136.
- Yoshino, T., Matsuzaki, T., Yamashita, S., & Katsura, T. (2006). Hydrous olivine unable to account for conductivity anomaly at the top of the asthenosphere. *Nature*, *443*(7114), 973.
- Yoshino, T., McIsaac, E., Laumonier, M., & Katsura, T. (2012). Electrical conductivity of partial molten carbonate peridotite. *Physics of the Earth and Planetary Interiors*, *194*, 1-9.
- Zhang, B., & Yoshino, T. (2017). Effect of graphite on the electrical conductivity of the lithospheric mantle. *Geochemistry, Geophysics, Geosystems*, *18*(1), 23-40.

Appendix

A.1 Initial 3-D Resistivity Models of the Slave Craton

Initial inversion models of the Slave craton attempted to use all available data collected in the SNORCLE and Slave to Bear Province data sets, however, the resulting models were too memory intensive and required a spatial decimation of the magnetotelluric data. To compensate for memory requirements, every other station along the S2B profile and the winter road surveys was removed, which allowed for modelling the largest region possible. A coarse mesh was used in the preliminary models of with 112, 106 and 39 cells in the x, y and z directions. The initial resistivity model had a uniform resistivity of 100 Ωm . The full impedance tensor was inverted using the ModEM inversion algorithm (Kelbert et al., 2014) and the model used an irregular rectilinear mesh with the width of the cells in the x and y direction being 10 km by 10 km. The central mesh was surrounded by 13 padding cells that geometrically increased in size by a factor of 1.5 extending to a total distance of ~ 5800 km in the horizontal direction. The vertical mesh started with a layer thickness of 100 m and increased geometrically by a factor of 1.3 to a total thickness of 611 km. Error floors of 10% were applied to all models. The only parameter tested for the early models was covariance, which determines smoothness of the model. Other parameters were not investigated as it was determined early on in the modelling that spatially decimating the data resulted in low-resolution models, which would not be sufficient for interpretation.

A.2 Varying Parameters in the initial 3-D inversions

A.2.1 Effect of Varying Covariance

A 3-D inversion can apply spatial smoothing to the resistivity model in the x, y and z direction and the smoothing does not have to be equal in each direction. In the ModEM inversion package (Kelbert et al., 2014), the covariance parameter is in the range 0 to 1, but for practical purposes is only varied between 0.1 and 0.9. The covariance parameter is analogous to the tau parameter in the 2-D inversion that was discussed in section 6.6.1 in that a higher covariance results in a smoother model while a lower covariance results in a rougher model. Thus, an ideal 3-D inversion uses a covariance parameter that honours the data while not over smoothing the model. However, 3-D inversions are much more computationally intensive than 2-D inversions, which mean that it is often not feasible to test every covariance parameter and generate an L-curve.

Hence, in the preliminary models four representative covariance parameters were tested rather than testing covariances increasing by 0.05 or 0.1 intervals. The resulting models are shown in as a horizontal slice at a depth of 75 km in Figure A.1 and vertical slices on a central profile are shown in Figure A.3. A covariance parameter of 0.3 was found to produce the best resistivity model as it does not smear the resistivity model significantly as seen for values of 0.6 and 0.9, but is not leave the model too rough as seen with a covariance of 0.1.

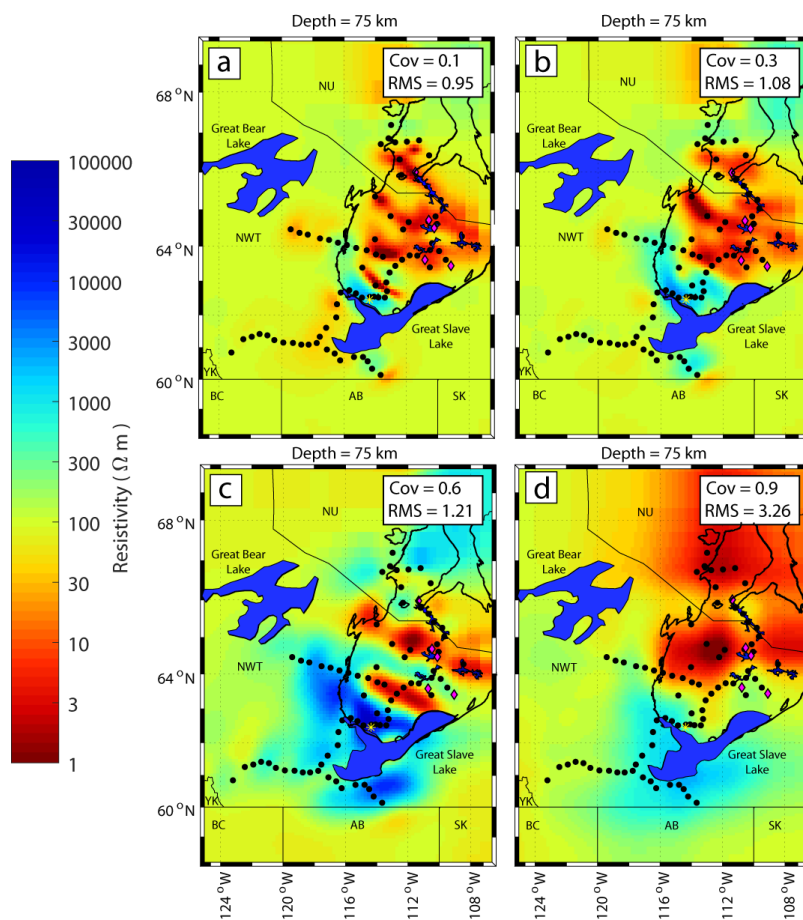


Figure A.1 Horizontal slices of inversion models produced by varying the covariance parameter for early inversions. Horizontal model slices at 75 km depth produced using a covariance parameter of (a) 0.1, (b) 0.3, (c) 0.6, (d) 0.9. The preferred model uses a covariance of 0.3 and is shown in (b). NU = Nunavut. NWT = Northwest Territories. BC = British Columbia. YK = Yukon. SK = Saskatchewan. AB = Alberta.

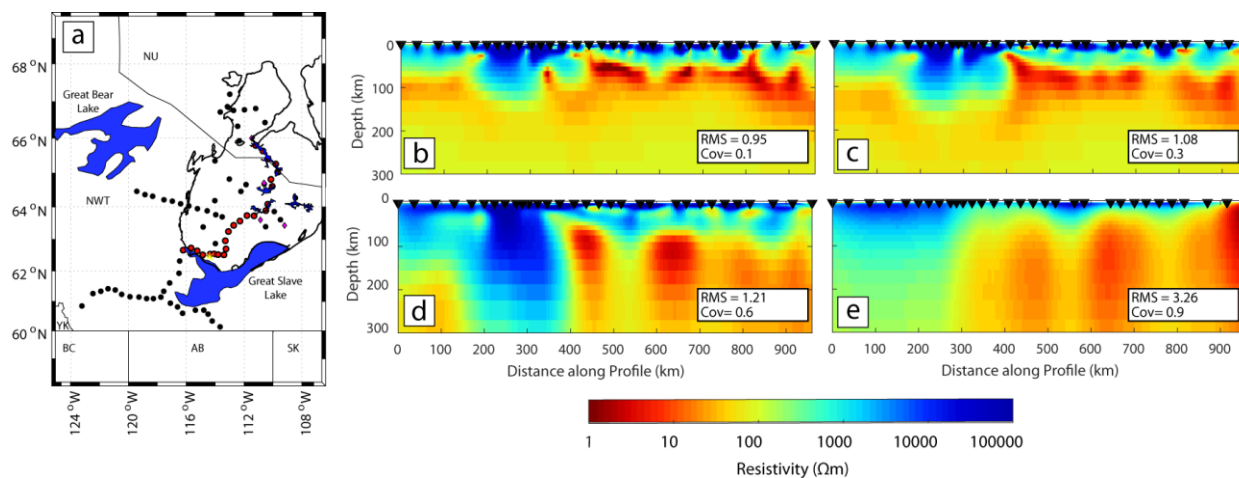


Figure A.2 Model depth slices produced by varying the covariance parameter for early inversions. Stations along the depth slices are highlighted in red on (a) the base map. Resistivity models are shown that were produced using a covariance parameter of (b) 0.1, (c) 0.3, (d) 0.6, and (e) 0.9. The preferred model uses a covariance parameter of 0.3 and is shown in (c). NU = Nunavut. NWT = Northwest Territories.

A.3 Focussed Resistivity Models of the Slave Craton

In the previous section, the decimated inversion results were discussed and it was apparent that spatially decimating the data resulted in a low resolution model, which was insufficient for accurately mapping the lithosphere of the Slave craton. To improve the resolution of the model the stations south of the craton were removed allowing for a higher station density within the Slave craton. The mesh was $112 \times 106 \times 39$ with a $100 \Omega\text{m}$ starting model. The full impedance tensor was inverted using the ModEM inversion algorithm (Kelbert et al., 2014) and the model uses an irregular rectilinear mesh with the width of the cells in the x and y direction being 10 km by 10 km. The central mesh is surrounded by 13 padding cells that geometrically increase in size by a factor of 1.5 extending to a total distance of ~ 5800 km in the horizontal direction. Resolution was also improved by using a finer vertical mesh than in early models and fixing the cell width in the area of interest. The vertical cell thickness were increased geometrically by a factor of 1.2 until a depth of 27 km where they are held constant at 5 km thickness for the subsequent 130 km to increase resolution in the upper mantle. At ~ 155 km depth the mesh again begins to geometrically increase by 1.2 until a total vertical cell count of 70 is achieved, which corresponded to a depth of ~ 1780 km. The starting model and covariance were investigated for this set of inversions.

A.4 Varying Parameters

A.4.1 Effect of Varying Starting Models

The resistivity of the starting models was varied by 5 orders of magnitude for 1, 10, 100, 1000 and 10000 Ωm to test the effect on the final inversion model. The results show that starting models of 1, 10 and 10000 Ωm produce models with little structural detail and relatively high r.m.s. misfits. These models are clearly not acceptable as they appear geologically unreasonable and do not fit the data well as indicated by the r.m.s. misfits. The poor model results using the aforementioned starting models could be a result of the ModEM inversion algorithm encountering a local minimum in the data fit due to these starting models being far away from the average resistivity value in the data. Indeed, resistivity values in the crust of the Slave craton exceed 100000 Ωm (e.g., Jones and Ferguson, 2001), which suggests that very low resistivity starting models of 1 and 10 Ωm are inadequate in this geological environment. On the other hand, a resistivity of 10000 Ωm for the starting model may be too far away from the low resistivities found in the CSMC ($\sim 10 \Omega\text{m}$) causing the inversion difficulty in finding a suitable resistivity model to accommodate this contrast in resistivities. The 100 and 1000 Ωm models are preferable compared to the 1, 10 and 100000 Ωm models as the r.m.s. misfits are low (< 1.3) and there is more structural detail. The r.m.s. misfit is the lowest for the 1000 Ωm model, however, it is not clear if this model is better than the 100 Ωm model as the mesh becomes very coarse at the depth that the 1000 Ωm model begins to place a conductor resulting in a poor resolution. Interestingly, the 1000 Ωm model is able to fit the data similarly to the 100 Ωm model by placing the conductor much deeper ($\sim 120 \text{ km}$) in the resistivity model compared to the 100 Ωm model ($\sim 75 \text{ km}$). For this reason, the difference between the 100 Ωm and 1000 Ωm starting model was further investigated using synthetics in Section 7.5.1 and in later inversions which is discussed in Section 7.5.2. It is also worth noting that the 100 and 1000 Ωm starting models produced the most desirable results in the 2-D inversions (Section 6.6.4).

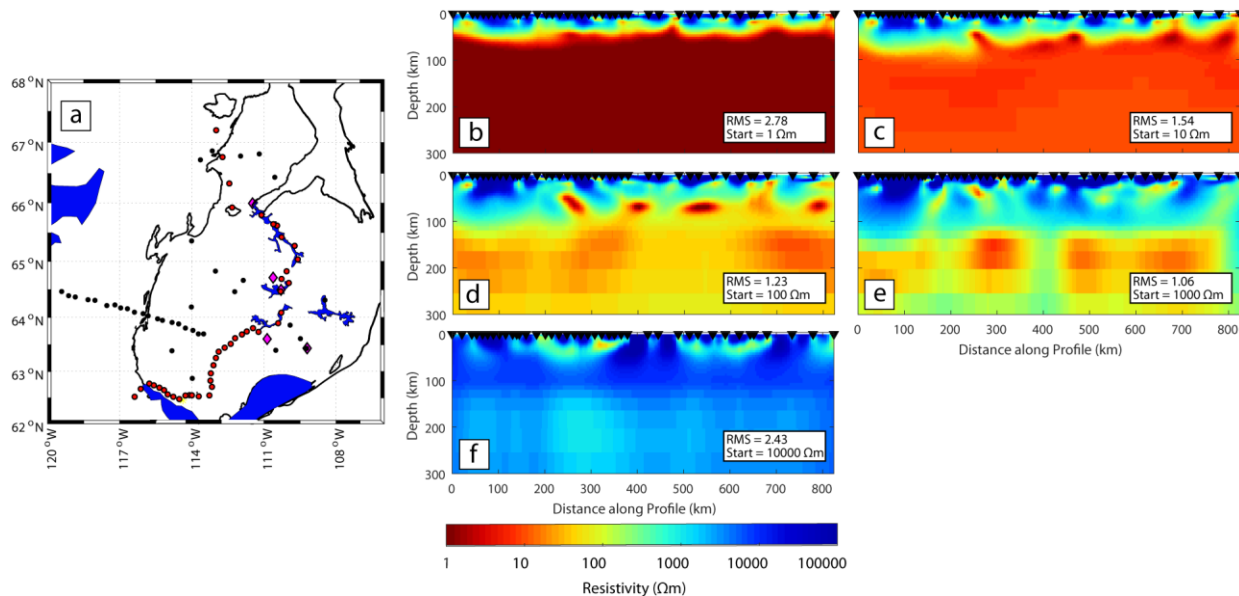


Figure A.3 Model depth slices produced by varying the starting model used in the inversion. Stations along the depth slices are highlighted in red on the base map. Resistivity models are shown that were produced using starting models of (a) 1 Ωm , (b) 10 Ωm , (c) 100 Ωm , (d) 1000 Ωm and 10000 Ωm . The preferred model is used a starting model of 1000 Ωm and is shown in (d). NU = Nunavut. NWT = Northwest Territories.

A.4.2 Effect of Varying Covariance

The covariance parameter was tested again on the focussed inversions to determine if a covariance of 0.3 was optimal as was found in early inversion models. Representative covariance values of 0.3, 0.4, 0.5, 0.6 and 0.9 were tested to determine the optimal covariance for the focussed inversions. A covariance of 0.3 was again found to be optimal as this model resulted in a low r.m.s. misfit of 1.23, but did not smear out features such that resolution was reduced in the resistivity models. The effect on the model can be seen in Figure A.4 and Figure A.5.

Appendix

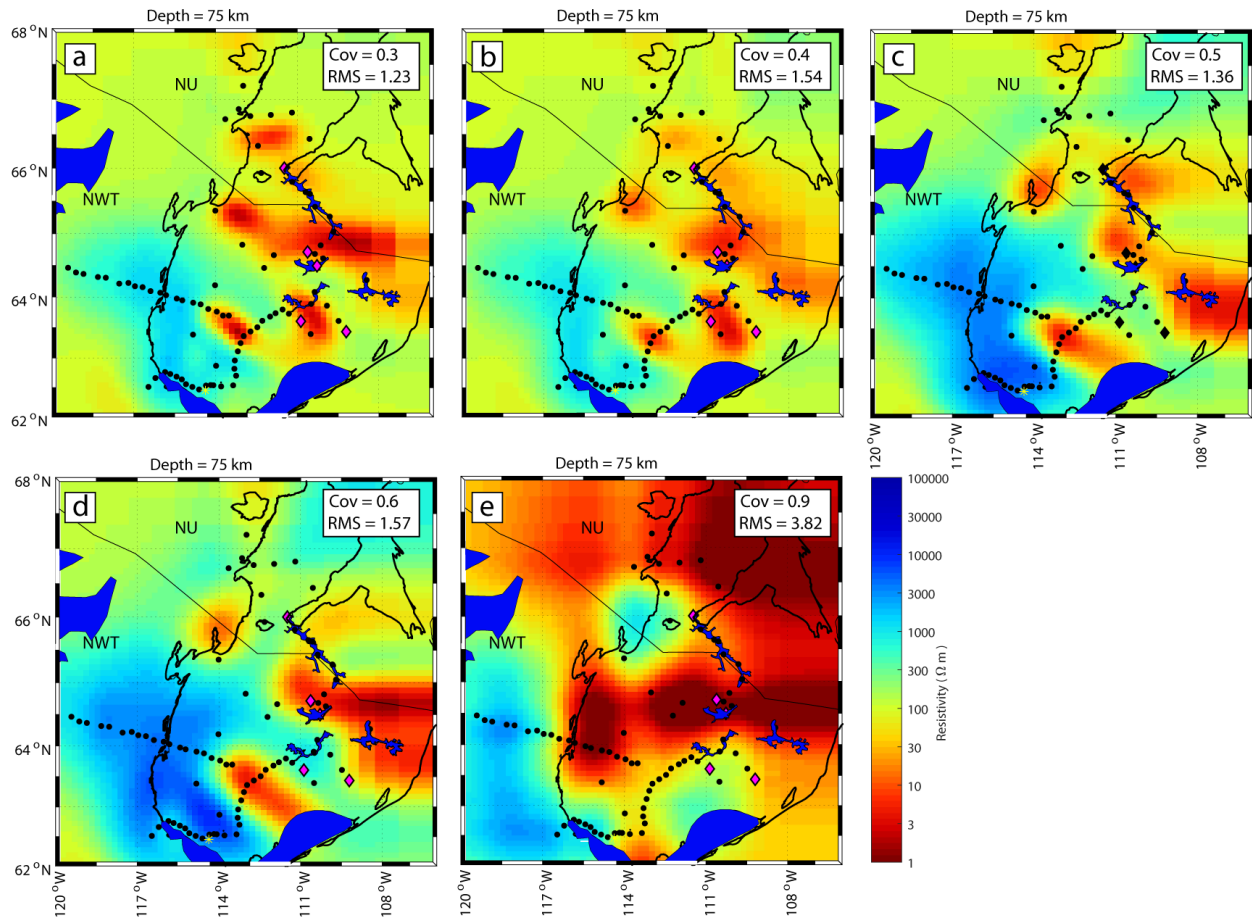


Figure A.4 Horizontal slices of inversion models produced by varying the covariance parameter for inverting the magnetotelluric data. Horizontal model slices at 100 km depth produced using a covariance parameter of (a) 0.3, (b) 0.4, (c) 0.5, (d) 0.6 and (e) 0.9. The preferred model uses a covariance of 0.3 and is shown in (a).

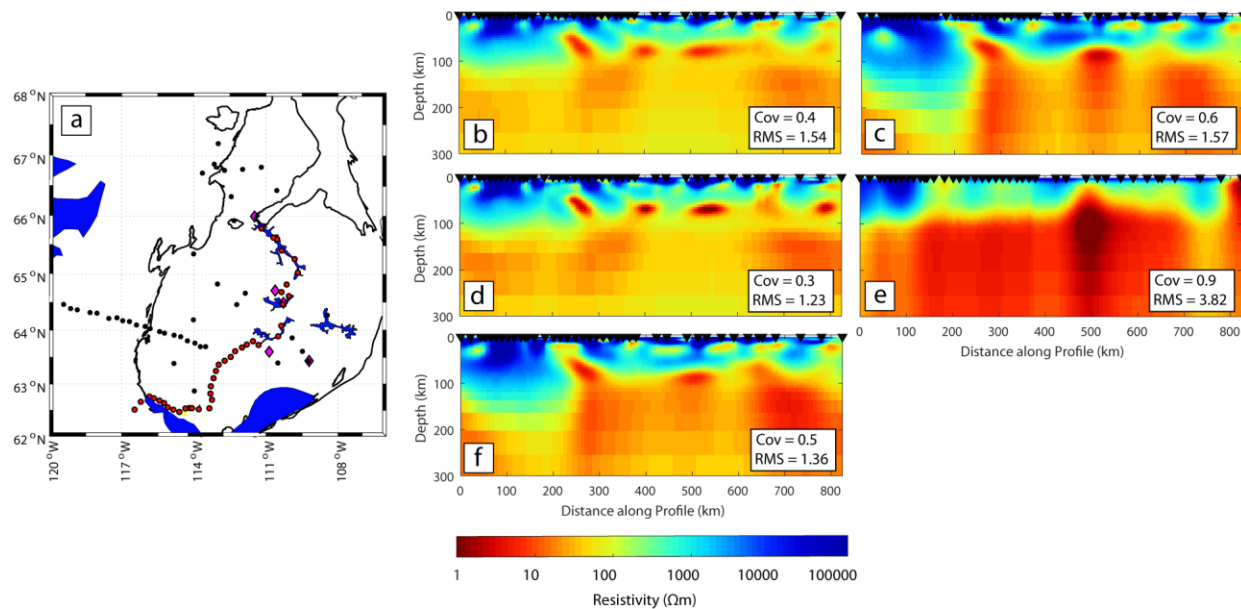


Figure A.5 Model depth slices produced by varying the covariance parameter used in the inversion. Stations along the depth slices are highlighted in red on (a) the base map. Resistivity models are shown that were produced using starting models of (b) 0.4, (c) 0.6, (d) 0.3, (e) 0.9 and (f) 0.5. The preferred model is used a covariance parameter of 0.3 and is shown in (d). NU = Nunavut. NWT = Northwest Territories.

A.5 Investigating the Resolution of Upper Mantle Conductors

The sensitivity of the inversion to resolve upper mantle conductors is tested by placing four conductors of 1 and 10 Ωm labelled as C1, C2, C3 and the CSMC at 100 - 140 km depth in a 1000 Ωm halfspace (Figure A.6(a,b)). The goal of this exercise is to (1) test the robustness of the prominent conductors C2 and the CSMC in the preferred resistivity model (s92p21r8) and (2) to determine the resolution of the inversion in regions of the model with sparser station spacing by recovering hypothetical conductors denoted as C1 and C3. The conductors C2 and the CSMC were made to have similar geometries as found in the preferred resistivity model and the conductors C1 and C3 are arbitrary in spatial extent, but are the same thickness (40 km) as C2 and the CSMC. Recovering C1 and C3 serves the purpose of testing resolution in regions with sparse station coverage in the preferred resistivity model (i.e. the central Slave craton west of Lac de Gras and the northern Slave craton).

The synthetic inversion models show that the CSMC is recovered well with the current station distribution, however, the inversion is unable to recover the southernmost extent of the conductor in the region without stations (Figure A.6(c,d)). Therefore, the southernmost extent of the CSMC in the preferred model (Figure 7.6) is likely not well defined and could be an artefact.

A second notable result is that under the current station distribution for conductors of 1 and 10 Ωm the CSMC is recovered an order of magnitude more resistive than its input resistivity suggesting that the resistivity of the CSMC in the preferred model could be an upper bound of its true resistivity. Thus, the synthetic inversion model suggests that the CSMC is a robust feature, but that its true resistivity may be underestimated. Additionally, C1, C2 and C3 are not recovered well with the current station distribution (Figure A.6(c,d)). This suggests that (1) C2 is not a robust feature in the preferred model in agreement with the synthetic forward models discussed in Section 7.6.1.2 and (2) the northern Slave craton and the central Slave craton west of Lac de Gras are not well constrained in the preferred resistivity model (s92p21r8).

Adding synthetic stations to the inversion results in better resolution for C1, C2, C3 and the CSMC (Figure A.6(e,f)). In particular, with the proposed station distribution the CSMC is recovered closer to its true resistivity (10 Ωm) while conductors C1, C2 and C3 are recovered as differentiable conductors with a resistivity of 100 Ωm rather than being undetected when recovered under the current station distribution.

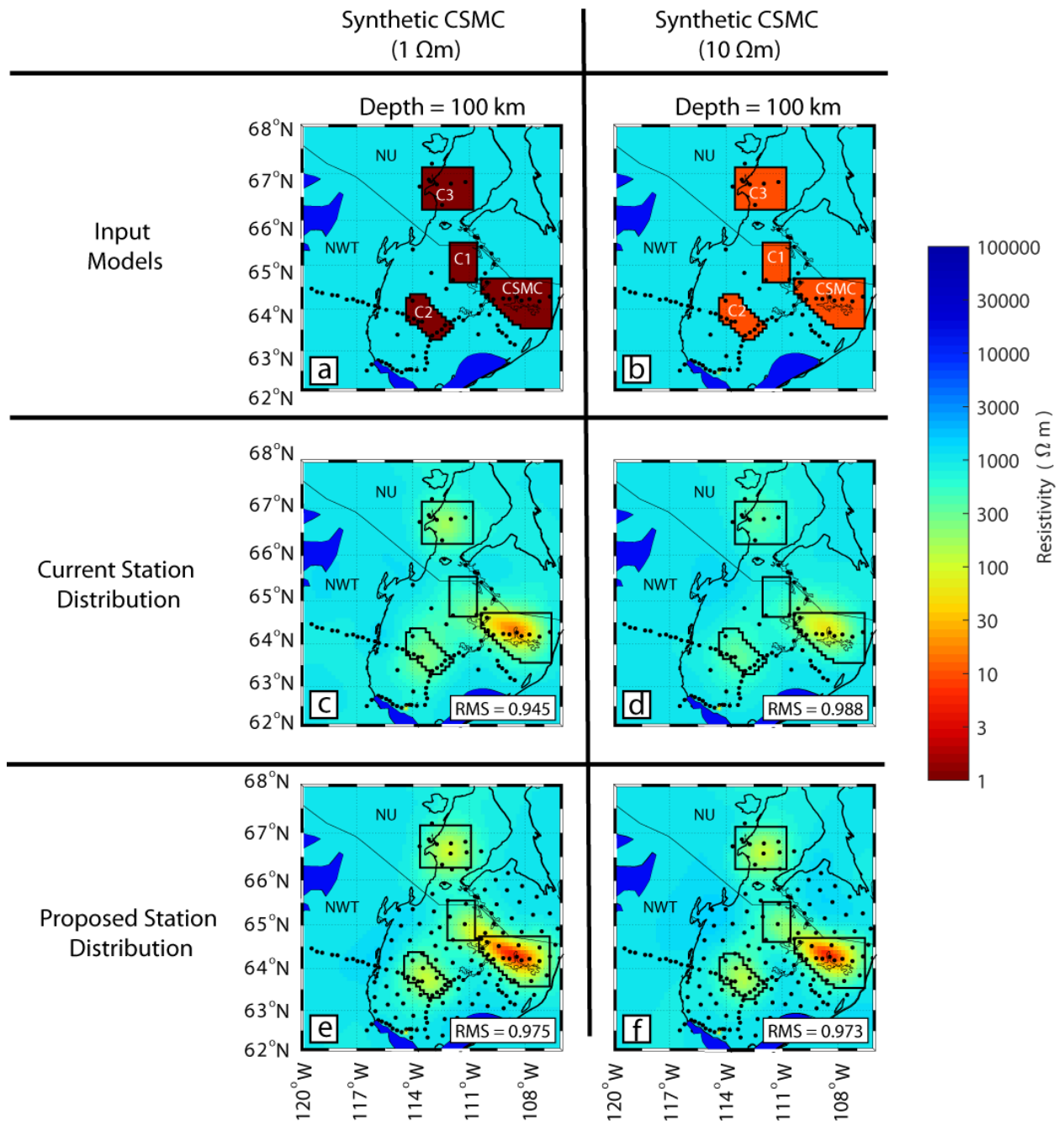


Figure A.6 Synthetic inversion recovering four upper mantle conductors. A black line in each panel outlines the extent of the input model.